

# **NUMERICAL ANALYSIS OF SHALLOW CIRCULAR FOUNDATIONS ON SANDS**

**By**  
**NOBUTAKA YAMAMOTO**



A thesis submitted for the degree of  
**Doctor of Philosophy**  
at  
The University of Western Australia

School of Civil and Resource Engineering  
May 2006

## **ABSTRACT**

This thesis describes a numerical investigation of shallow circular foundations resting on various types of soil, mainly siliceous and calcareous sands. An elasto-plastic constitutive model, namely the MIT-S1 model (Pestana, 1994), which can predict the rate independent behaviour of different types of soils ranging through uncemented sands, silts and clays, is used to simulating the compression, drained triaxial shear and shallow circular foundation responses. It is found that this model provides a reasonable fit to measured behaviour, particularly for highly compressible calcareous sands, because of the superior modelling of the volumetric compression.

The features of the MIT-S1 model have been used to investigate the effects of density, stress level (or foundation size), inherent anisotropy and material type on the response of shallow foundations. It was found that the MIT-S1 model is able to distinguish responses on dilatant siliceous and compressible calcareous sands by relatively minor adjustment of the model parameters. Kinematic mechanisms extracted from finite element calculations show different deformation patterns typical for these sands, with a bulb of compressed material and punching shear for calcareous sand, and a classical rupture failure pattern accompanied by surface heave for siliceous sand. Moreover, it was observed that the classical failure pattern transforms gradually to a punching shear failure pattern as the foundation size increases. From this evidence, a dimensional transition between these failure mechanisms can be defined, referred to as the critical size.

The critical size is also the limiting foundation size to apply conventional bearing capacity analyses. Alternative approaches are needed, focusing mainly on the soil compressibility, for shallow foundations greater than the critical size. Two approaches, 1-D compression and bearing modulus analyses, have been proposed for those foundation conditions. From the validations, the former is applicable for extremely large foundations, very loose soil conditions and highly compressible calcareous materials, while the latter is suitable for moderate levels of compressibility or foundation size. It is suggested that appropriate assessment of compression features is of great importance for shallow foundation analysis on sand.

## **ACKNOWLEDGEMENT**

I express my sincere appreciation to my supervisor, Professor Mark Randolph, who always gave valuable advice and special guidance during my study period. Although I often digressed from the main objective of this study, he always pulled me back on track with his enormous encouragement. He also gave valuable comments and corrections of this thesis. I am extremely grateful to have worked with him.

I also wish to express my profound gratitude to my co-supervisor, Dr. Itai Einav, for his persistent guidance, appropriate suggestions and encouragement, which enabled me to accomplish this thesis. Especially, his great mathematical ability helped to solve numerical problems of this study.

I am grateful to all staff in the Centre for Offshore Foundation Systems and School of Civil and Resource Engineering. They always gave support on technical and personal matters and refreshed me through some sports events. I wish to give special thanks to Ms. Monica Mackman for helping me in many administrative matters throughout my candidate. Special thanks are also due to past and current administrative staff. The additional financial support from COFS and the School of Civil and Resource Engineering is also acknowledged.

I would like to express my grateful thanks to group mates and visitors. I often received interesting ideas not only for my study but also for my life from them. I will never forget their kindness and friendship.

Moreover, I express my sincere gratitude to Professor Andrew Whittle and Dr. Yo-Ming Hsieh for providing the MIT-S1 model in the form of an ABAQUS user-defined subroutine. I could not have completed this study without their help.

Finally, the most grateful thanks must be given to my wife, Tomomi, and my parents. Their unbounded love, encouragement and moral support has always helped me. Especially, I must give my great sincere appreciation for my parents in providing financial support for my entire candidate. This thesis is dedicated to them in gratitude.

## **DECLARATION**

I hereby declare that except where specific reference is made in the text to the work of others, the contents of this thesis are original and have not been submitted to any other university.

Nobutaka Yamamoto

14 May 2006

## **CONTENTS**

|   |            |
|---|------------|
| <b>ABSTRACT .....</b>   | <b>i</b>   |
| <b>ACKNOWLEDGEMENT .....</b>  | <b>ii</b>  |
| <b>DECLARATION .....</b>  | <b>iii</b> |
| <b>CONTENTS .....</b>   | <b>iv</b>  |
| <b>NOTATION .....</b>   | <b>ix</b>  |
| <br>  |            |
| <b>1 INTRODUCTION .....</b>   | <b>1</b>   |
| <b>1.1 Background .....</b>   | <b>1</b>   |
| <b>1.2 Objectives of the Study .....</b>  | <b>2</b>   |
| <b>1.3 Outline of the Thesis .....</b>  | <b>3</b>   |
| <br>  |            |
| <b>2 LITERATURE REVIEW .....</b>  | <b>7</b>   |
| <b>2.1 Introduction .....</b>   | <b>7</b>   |
| <b>2.2 Comparison between Siliceous and Calcareous Sands .....</b>                    | <b>8</b>   |
| <b>2.2.1 Features .....</b>   | <b>8</b>   |
| <b>2.2.2 Properties .....</b>   | <b>9</b>   |
| <b>2.2.3 Compression behaviour .....</b>  | <b>10</b>  |
| <b>2.2.4 Shear behaviour .....</b>  | <b>11</b>  |
| <b>2.2.5 Critical state .....</b>   | <b>12</b>  |
| <b>2.2.6 Foundation responses .....</b>   | <b>13</b>  |
| <b>2.2.7 Summary .....</b>  | <b>14</b>  |
| <b>2.3 Bearing Capacity of Shallow Foundations on Sand .....</b>                      | <b>14</b>  |
| <b>2.3.1 Introduction to the bearing capacity equation .....</b>                      | <b>15</b>  |
| <b>2.3.2 Mode of bearing capacity failure .....</b>                                   | <b>16</b>  |
| <b>2.3.3 Foundation size effects of bearing capacity of shallow Foundations .....</b> | <b>17</b>  |
| <b>2.3.4 Other aspects of bearing capacity of shallow foundations .....</b>           | <b>20</b>  |
| <b>2.3.5 Bearing capacity of shallow foundations on calcareous sands .....</b>        | <b>21</b>  |
| <b>2.3.6 Summary .....</b>  | <b>23</b>  |
| <b>2.4 Constitutive Models for Sands .....</b>  | <b>24</b>  |
| <b>2.4.1 Modelling the compression behaviour .....</b>                                | <b>24</b>  |
| <b>2.4.2 Modelling the shear behaviour .....</b>                                      | <b>26</b>  |
| <b>2.4.3 Summary .....</b>  | <b>27</b>  |

---

|   |           |
|---|-----------|
| <b>3 DETERMINATION OF MIT-S1 MODEL PARAMETERS FOR VARIOUS SOILS .....</b>                 | <b>41</b> |
| <b>3.1 Introduction .....</b>   | <b>41</b> |
| <b>3.2 Model Parameters .....</b>   | <b>42</b> |
| <b>3.3 Model Predictions for Goodwyn Calcareous Sand .....</b>                            | <b>43</b> |
| 3.3.1 Compression parameters ( $\rho_c, p'_{ref}, \theta$ ) .....                         | 43        |
| 3.3.2 Small strain parameters ( $C_b, \omega_s$ ) .....                                   | 44        |
| 3.3.3 $K_0$ and swelling parameters ( $K_{0NC}, \mu'_0, \omega$ ) .....                   | 45        |
| 3.3.4 Shear and critical state parameters ( $\phi'_{cs}, m, \phi'_{mr}, np, \psi$ ) ..... | 46        |
| 3.3.5 Prediction for triaxial isotropic undrained shear tests .....                       | 47        |
| 3.3.6 Predictions for triaxial isotropic drained shear tests .....                        | 47        |
| 3.3.7 Summary .....   | 48        |
| <b>3.4 Model Predictions for Dogs Bay Calcareous Sand .....</b>                           | <b>49</b> |
| 3.4.1 Compression parameters ( $\rho_c, p'_{ref}, \theta$ ) .....                         | 49        |
| 3.4.2 Small strain parameters ( $C_b, \omega_s$ ) .....                                   | 49        |
| 3.4.3 $K_0$ and swelling parameters ( $K_{0NC}, \mu'_0, \omega$ ) .....                   | 50        |
| 3.4.4 Shear and critical state parameters ( $\phi'_{cs}, m, \phi'_{mr}, np, \psi$ ) ..... | 50        |
| 3.4.5 Prediction for triaxial isotropic undrained shear tests .....                       | 51        |
| 3.4.6 Predictions for triaxial isotropic drained shear tests .....                        | 51        |
| 3.4.7 Prediction for $p'$ constant shear tests .....                                      | 51        |
| 3.4.8 Summary .....   | 52        |
| <b>3.5 Model Predictions for Goodwyn Calcareous Silt .....</b>                            | <b>52</b> |
| 3.5.1 Compression parameters ( $\rho_c, p'_{ref}, \theta$ ) .....                         | 53        |
| 3.5.2 Small strain parameters ( $C_b, \omega_s$ ) .....                                   | 53        |
| 3.5.3 $K_0$ and swelling parameters ( $K_{0NC}, \mu'_0, \omega$ ) .....                   | 53        |
| 3.5.4 Shear and critical state parameters ( $\phi'_{cs}, m, \phi'_{mr}, np, \psi$ ) ..... | 53        |
| 3.5.5 Prediction for triaxial isotropic undrained shear tests .....                       | 54        |
| 3.5.6 Summary .....   | 54        |
| <b>3.6 Conclusions .....</b>  | <b>54</b> |
| <br>  |           |
| <b>4 MIT-S1 MODEL PREDICTIONS FOR THE BEHAVIOUR OF SHALLOW CIRCULAR FOOTINGS .....</b>    | <b>81</b> |
| <b>4.1 Introduction .....</b>   | <b>81</b> |

|  |            |
|--|------------|
| <b>4.2 Finite Element Calibrations .....</b>   | <b>81</b>  |
| 4.2.1 Geometry of finite element mesh .....  | 82         |
| 4.2.2 Mesh size .....  | 83         |
| 4.2.3 Step control .....   | 83         |
| 4.2.4 Void ratio variation with depth .....  | 84         |
| <b>4.3 A Study of Shallow Circular Footings on Siliceous and Calcareous Sands Using Various Constitutive Models .....</b>              | <b>85</b>  |
| 4.3.1 Additional constitutive models used in the current study .....   | 85         |
| 4.3.2 Input parameters of the constitutive models .....  | 86         |
| 4.3.3 Bearing responses .....  | 87         |
| 4.3.4 Discussion .....   | 88         |
| <b>4.4 A Comparison between Numerical and Physical Model Tests of Shallow Circular Footings on Various Soils .....</b>                 | <b>89</b>  |
| 4.4.1 Toyoura siliceous sand .....   | 89         |
| 4.4.2 Goodwyn calcareous sand .....  | 90         |
| 4.4.3 Dogs Bay calcareous sand .....   | 91         |
| 4.4.4 Goodwyn calcareous silt .....  | 91         |
| 4.4.5 Discussion .....   | 92         |
| <b>4.5 Sensitivity analysis on the Effect of the MIT-S1 Model Parameters on the Behaviour of Shallow Circular Footings .....</b>       | <b>93</b>  |
| 4.5.1 Compression parameters ( $\rho_c$ , $\theta$ , $p'_{ref}$ ) .....  | 93         |
| 4.5.2 Shear parameters with small strain measurement ( $C_b$ , $\omega_s$ ) .....  | 94         |
| 4.5.3 Shear parameters with large strain measurement ( $\phi'_{cs}$ , $m$ , $\phi'_{mr}$ , $np$ , $\psi$ ) .....                       | 94         |
| 4.5.4 Discussion .....   | 95         |
| <b>4.6 Conclusions .....</b>   | <b>96</b>  |
| <b>5 THE EFFECTS OF SOIL AND FOUNDATION PROPERTIES ON SHALLOW FOUNDATION PERFORMANCE .....</b>   | <b>123</b> |
| <b>5.1 Introduction .....</b>  | <b>123</b> |
| <b>5.2 The Effects of Stress Level and Density on Compression and Strength Characteristics on Siliceous and Calcareous Sands .....</b> | <b>123</b> |
| 5.2.1 Compression behaviour .....  | 124        |
| 5.2.2 Shear behaviour .....  | 124        |

|            |  |            |
|------------|--|------------|
| 5.2.3      | Peak friction angle and dilatancy .....  | 125        |
| 5.2.4      | Discussion .....   | 126        |
| <b>5.3</b> | <b>A Comparison of the Responses for Small Scale Shallow Foundations on Siliceous and Calcareous Sands .....</b> | <b>127</b> |
| 5.3.1      | Pressure-displacement curves .....   | 127        |
| 5.3.2      | Deformation mechanisms .....   | 128        |
| 5.3.3      | Comparison of incremental horizontal displacement contours and characteristic mesh .....                         | 129        |
| 5.3.4      | Volumetric strain distributions .....  | 129        |
| 5.3.5      | Integration point outputs .....  | 130        |
| 5.3.6      | Effects of void ratio and $K_0$ .....  | 131        |
| 5.3.7      | Discussion .....   | 132        |
| <b>5.4</b> | <b>A Comparison of the Responses for Large Scale Shallow Foundations on Siliceous and Calcareous Sands .....</b> | <b>133</b> |
| 5.4.1      | Pressure-displacement curves .....   | 133        |
| 5.4.2      | Deformation mechanisms .....   | 134        |
| 5.4.3      | Incremental horizontal displacement contours .....   | 134        |
| 5.4.4      | Volumetric strain distributions .....  | 135        |
| 5.4.5      | Void ratio and mean effective stress relationship from integration points .....                                  | 135        |
| 5.4.6      | Effects of void ratio and $K_0$ .....  | 136        |
| 5.4.7      | Parametric study .....   | 136        |
| 5.4.8      | Discussion .....   | 137        |
| <b>5.5</b> | <b>The Effect of Foundation Size on Bearing Capacity Factor, <math>N_\gamma</math> .....</b>                     | <b>138</b> |
| 5.5.1      | Siliceous sand .....   | 138        |
| 5.5.2      | Calcareous sand .....  | 139        |
| 5.5.3      | $N_\gamma$ - D relationship for various sands .....  | 140        |
| 5.5.4      | Discussion .....   | 141        |
| <b>5.6</b> | <b>Conclusions .....</b>   | <b>142</b> |
| <b>6</b>   | <b>ANALYTICAL METHODS FOR SHALLOW FOUNDATION RESPONSES ON CALCAREOUS SOIL .....</b>                              | <b>187</b> |
| <b>6.1</b> | <b>Introduction .....</b>  | <b>187</b> |
| <b>6.2</b> | <b>A Comparison of the Bearing Capacity Factor <math>N_\gamma</math> from Equations,</b>                         |            |

|   |                           |            |
|---|---------------------------|------------|
| <b>Plastic Solutions and Finite Element Results .....</b>   | <b>187</b>                |            |
| 6.2.1 $N_y - \phi'$ relationship for siliceous sand .....   | 188                       |            |
| 6.2.2 $N_y - \phi'$ relationship for calcareous sand .....  | 190                       |            |
| 6.2.3    Problems associated with the choice of friction angle .....                                  | 190                       |            |
| <b>6.3 One-dimensional Compression Analysis for Shallow Foundations on<br/>Calcareous Sand .....</b>  | <b>191</b>                |            |
| <b>6.4 Bearing Modulus Analysis for Shallow Foundations on Calcareous<br/>Sand .....</b>              | <b>192</b>                |            |
| 6.4.1    Bearing modulus, M .....   | 193                       |            |
| 6.4.2    Bearing modulus analysis for Goodwyn calcareous sand .....                                   | 193                       |            |
| 6.4.3    Bearing modulus analysis for Dogs Bay calcareous sand and<br>Goodwyn calcareous silt .....   | 194                       |            |
| 6.4.4    Relationship between bearing modulus equation and MIT-S1<br>compression parameters .....     | 195                       |            |
| <b>6.5 Discussion .....</b>   | <b>195</b>                |            |
| <b>6.6 Conclusions .....</b>  | <b>196</b>                |            |
| <br>  |                           |            |
| <b>7 CONCLUSIONS .....</b>  | <b>209</b>                |            |
| <b>7.1 Conclusions .....</b>  | <b>209</b>                |            |
| 7.1.1    MIT-S1 model .....   | 209                       |            |
| 7.1.2    Effects of soil properties and foundation designs on shallow<br>foundation performance ..... | 210                       |            |
| 7.1.3    Analytical methods for shallow foundations on calcareous sands                               | 211                       |            |
| <b>7.2 Recommendations for Further Research .....</b>   | <b>212</b>                |            |
| <br>  |                           |            |
| <b>APPENDIX</b>   | <b>MIT-S1 MODEL .....</b> | <b>215</b> |
| <b>REFERENCES .....</b>   |                           | <b>227</b> |

## NOTATION

\* *Italic descriptions are associated with the MIT-S1 model*

|                  |  |
|------------------|--|
| A                | material constant (Equation 3.1)   |
| a                | <i>shape constant controlling the spacing of the LCC</i>                                   |
| B                | footing width  |
| <b>b</b>         | <i>orientation vectors for the bounding surface</i>  |
| $B_{\text{ref}}$ | reference width (Equation 2.3)   |
| $c'$             | cohesion   |
| $C_b$            | <i>small strain stiffness parameter</i>  |
| CID              | triaxial isotropic drained shear test  |
| CIU              | triaxial isotropic undrained shear test  |
| CSL              | critical state line  |
| $C_u$            | coefficient of uniformity ( $= D_{60}/D_{10}$ )  |
| D                | 1) diameter<br>2) <i>constant for volumetric hysteresis behaviour for clay</i>             |
| $D_{50}$         | mean particle size   |
| $D_r$            | relative density   |
| $D_{\text{ref}}$ | reference diameter ( $= 1 \text{ m}$ ) (Equation 6.7)                                      |
| E                | Young's modulus  |
| e                | current void ratio   |
| $e_0$            | initial (preshear or ground surface) void ratio  |
| $e_c$            | void ratio at loading condition (Equation 2.4)   |
| $e_{\text{cs}}$  | reference void ratio at $p' = 1 \text{ kPa}$ for critical state line                       |
| $e_{\max}$       | maximum void ratio   |
| $e_{\min}$       | minimum void ratio   |
| $e_{\text{NC}}$  | reference void ratio at $p' = 1 \text{ kPa}$ for normally consolidated line (Equation 2.4) |
| $e_{\text{OC}}$  | reference void ratio at $p' = 1 \text{ kPa}$ for overconsolidated line (Equation 2.5)      |
| $e_s$            | void ratio at unloading condition (Equation 2.5)   |
| f                | yield function   |
| G                | current shear modulus  |
| $G_{\max}$       | maximum shear modulus  |
| H                | <i>elasto-plastic hardening modulus</i>  |

|            |   |
|------------|---|
| $h$        | <i>material constant controlling irrecoverable plastic strains in unload-reload cycles</i>  |
| $K$        | current bulk modulus  |
| $K_{\max}$ | maximum bulk modulus  |
| $K_0$      | coefficient of earth pressure at rest   |
| $K_{0NC}$  | <i>coefficient of earth pressure at rest in the LCC</i>   |
| LCC        | <i>limit compression curve</i>  |
| $M$        | bearing modulus (Equation 6.4)  |
| $m$        | 1) degradation parameter for overconsolidationd<br>2) <i>geometric parameter of the bounding surface</i>  |
| $m^*$      | degradation parameter for cementation   |
| $N_c$      | bearing capacity factor for cohesion  |
| NCL        | normally consolidated line  |
| $n_h$      | exponential constant for horizontal effective stress (Equation 3.1)   |
| $n_p$      | <i>constant for maximum friction angle, <math>\phi'_m</math></i>  |
| $N_q$      | bearing capacity factor for surcharge   |
| $n_v$      | exponential constant for vertical effective stress (Equation 3.1)   |
| $N_\gamma$ | bearing capacity factor for self-weight   |
| $P$        | <i>direction of plastic strain increments</i>   |
| $p'$       | mean effective stress at current state  |
| $p'_0$     | mean effective stress at initial (or pre-shear) state   |
| $p_a$      | atmospheric pressure ( $\sim 100$ kPa)  |
| $p'_b$     | <i>mean effective stress on the hydrostatic LCC</i>   |
| $p'_{cs}$  | mean effective stress at critical state   |
| $p'_f$     | mean effective stress at failure  |
| $p'_y$     | mean effective stress at yield state  |
| $p'_{ref}$ | 1) reference mean effective stress (Equation 2.3, 6.5, 6.6, 6.7)<br>2) <i>reference mean effective stress of the hydrostatic LCC at unit void ratio</i> |
| $Q$        | <i>gradient of bounding surface</i>   |
| $q$        | deviatoric stress   |
| $\bar{q}$  | effective surcharge at foundation level   |
| $q_b$      | bearing pressure  |
| $r$        | 1) spacing ratio for yield surface ( $= p'_y/p'_{cs}$ ) (SU model)<br>2) <i>control parameter for volumetric hysteresis behaviour for clay</i>          |

---

|                       |  |
|-----------------------|--|
| R                     | size ratio of subloading surface to superloading surface ( $= p'_{\text{sub}}/p'_{\text{super}}$ ) (Asaoka model)    |
| $R^*$                 | size ratio of yield surface to superloading surface ( $= p'/p'_{\text{super}}$ ) (Asaoka model)                      |
| $\mathbf{s}$          | <i>shear stress vector</i>   |
| U                     | coefficient for bearing modulus analysis (Equation 6.10)   |
| <br>                  |  |
| $\alpha$              | fitting coefficient (Equation 6.4)   |
| $\alpha'$             | <i>size of bounding surface</i>  |
| $\alpha'_e$           | <i>mean effective stress at the hydrostatic LCC for the current void ratio</i>                                       |
| $\alpha'_o$           | <i>size of the current loading surface</i>   |
| $\alpha'_{oi}$        | <i>size of the loading surface at the initial state</i>  |
| $\beta$               | power coefficient (Equation 2.3, 6.5, 6.7)   |
| $\delta$              | vertical displacement for footing penetration  |
| $\delta_b$            | <i>dimensionless distance between <math>\alpha'</math> and <math>\alpha'_e</math></i>                                |
| $\delta_{HS}$         | <i>dimensionless distance between <math>p'</math> and <math>p'_b</math> at the current void ratio</i>                |
| $\delta_{1D}$         | <i>dimensionless distance between <math>\sigma'_v</math> and <math>\sigma'_{vb}</math> at the current void ratio</i> |
| $\epsilon_a$          | axial strain   |
| $\epsilon_s$          | shear strain   |
| $\epsilon_v$          | volumetric strain  |
| $\epsilon_v^e$        | elastic volumetric strain  |
| $\epsilon_v^p$        | plastic volumetric strain  |
| $\phi'$               | effective friction angle   |
| $\phi_{cs}$           | critical state friction angle  |
| $\phi_m'$             | <i>maximum friction angle</i>  |
| $\phi_{mr}'$          | <i>maximum friction angle at unit void ratio</i>   |
| $\phi_p'$             | peak friction angle  |
| $\phi_{ref}'$         | reference friction angle (Equation 2.3, 6.5, 6.6, 6.7)   |
| $\gamma_{\text{dry}}$ | effective unit weight of soil  |
| $\gamma'$             | effective unit weight of soil  |
| $\boldsymbol{\eta}$   | <i>current stress ratio vector</i>   |
| $\kappa$              | swelling index (Equation 2.5)  |
| $\dot{\Lambda}$       | <i>scalar controlling magnitude of plastic strain increment</i>  |
| $\lambda$             | compression index (Equation 2.4)   |

|                  |  |
|------------------|--|
| M                | stress ratio at critical state   |
| $\mu'_0$         | <i>Poisson's ratio</i>   |
| $\theta$         | <i>transition parameter of the first loading curve in <math>lne-lnp'</math> space</i>    |
| $\rho_c$         | <i>slope of the LCC regime in <math>lne-lnp'</math> space</i>                            |
| $\rho_r$         | <i>parameter defining the current elastic volumetric stiffness</i>                       |
| $\sigma'$        | normal effective stress (Figure 5.7)   |
| $\sigma'_h$      | horizontal effective stress  |
| $\sigma'_r$      | reference stress (= 1 kPa) (Equation 3.1)  |
| $\sigma'_v$      | vertical effective stress  |
| $\sigma'_{vb}$   | <i>vertical effective stress on the one dimensional LCC</i>                              |
| $\sigma'_{vref}$ | <i>reference vertical effective stress of the one-dimensional LCC at unit void ratio</i> |
| $\tau$           | shear stress (Figure 5.7)  |
| $\omega$         | <i>control parameter for non-linear Poisson's ratio</i>                                  |
| $\omega_s$       | <i>small strain non-linearity during undrained shearing</i>                              |
| $\psi$           | 1) dilation angle<br>2) rate of evolution of anisotropy                                  |

# Chapter 1

## Introduction

### 1.1 BACKGROUND

Shallow foundation systems with dimensions over 100 m and base area in excess of 10,000 m<sup>2</sup> such as large gravity based structures are used extensively in offshore engineering (Watt, 1978; Randolph and Erbrich, 2000). A common type of gravity base structure as shown in **Figure 1.1** has been widely adopted, e.g. Gullfaks in North Sea, UK and Wandoo on the North-West Shelf, Australia. It comprises a large cellular base supporting three or four concrete towers and is generally equipped with a skirt system at the base. Such large foundations are sufficiently stable under the severe loading applied in the offshore environment. Moreover, large raft foundations are frequently used on calcareous sediments rather than driven pile foundations because the skin friction for piles in calcareous sand is extremely low (Fahey, 1993).

The well known superposition formula for bearing capacity calculation (Terzaghi, 1943) is used almost universally for the shallow foundation design, because it provides an estimate of the load carrying capacity of shallow foundations on sand through a single parameter, friction angle. Although the approach has proved adequate for relatively small foundations on siliceous sand, it has obvious limits for particular design conditions, such as large shallow foundations (De Beer, 1963) and for calcareous materials (Dutt and Ingram, 1988). The bearing capacity measured under those conditions is generally much lower than estimated using the standard bearing capacity approach.

Physical model tests provide good insight into the response of foundation systems on sands and have inspired modifications of the bearing capacity formula (e.g., Kusakabe et al., 1991; Murff et al., 1992; Ueno et al., 1998). However, the potential of centrifuge modelling has a limit in simulating large prototype scales. The modelling for calcareous

sand has also problems due to the strong spatial variability in effective particle size and in the repeatability of the materials due to high crushability of the particles.

Numerical modelling must often be relied on in assessing the performance of shallow foundations. A constitutive model is needed that can simulate the different aspects of sand behaviour, including compressibility of sand, dilatancy and non-associativity, and combining these features properly. If the model provides successful simulation featuring these aspects, then it will be able to distinguish between the shallow foundation responses on dilative siliceous and compressive calcareous sands, to assess the effect of soil compressibility on bearing capacity, and to support the development of design issues from a numerical approach.

## **1.2 OBJECTIVES OF THE STUDY**

The principal scope of this study is to analyse numerically the behaviour of shallow foundations on sands. It is anticipated that the knowledge gained from this study can promote better understanding of the uncertainties in respect of shallow foundation responses on sands. It is believed that the investigations of this study can aid in development of better design guidelines for shallow offshore foundations, in particular extremely large foundations or foundations on compressible calcareous sands.

The specific aims of this research are to:

1. find a constitutive model that can simulate both compression and shear behaviour of sands within the model framework;
2. determine model parameters for the chosen constitutive model from compression and shear tests for various sands and explore the sensitivity to different parameters;
3. highlight advantages and disadvantages of the chosen model in terms of numerical simulations for shallow foundations, by comparison with simulations using other constitutive models and to physical model results on various sands;

4. examine shallow foundation responses with different soil properties and foundation designs on siliceous and calcareous sands and summarise the influence of those factors on the foundation behaviour;
5. comprehend difficulties in applying the conventional bearing capacity formulae for estimating shallow foundation capacity and modify the formula or propose new approaches, focusing especially on soil compressibility.

### **1.3 OUTLINE OF THE THESIS**

Following this chapter, which has described the aims and scopes of this research work, **Chapter 2** specifies further the main objectives of this study by reviewing past literature under three headings, mechanical features of sands, bearing capacity of shallow foundations, and constitutive models.

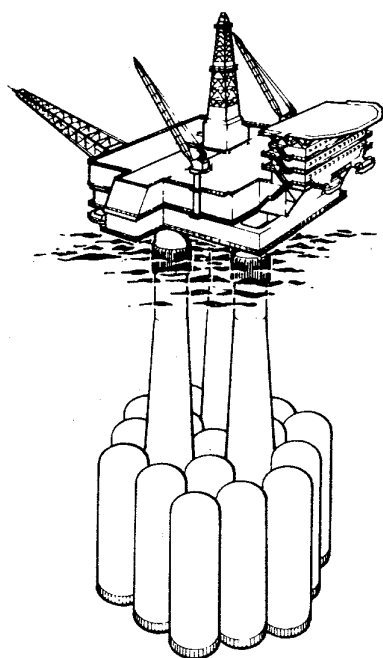
**Chapter 3** determines input parameters for the chosen constitutive model, the MIT-S1 model, for various soils. Pestana (1994) has proposed a determination procedure for this model using an extensive experimental database for soils and extracted the model parameters for Toyoura siliceous sand. This chapter follows the proposed process for determining calcareous material parameters.

**Chapter 4** proves a predictive capability of the MIT-S1 model for shallow foundation problems on sands. Three investigations, a comparison with other constitutive model predictions, a comparison with physical model tests on various soils, and a sensitivity analysis for the MIT-S1 model parameters, are carried out. Calibrations for the finite element mesh and its boundary conditions, and methods for calculation stability are described beforehand.

**Chapter 5** examines effects of soil properties and foundation conditions on the shallow foundation response for siliceous and calcareous sands. Geometrical results and stress-strain relationships extracted from numerical simulations are presented and compared between small and large foundations on siliceous and calcareous sands. Influence factors found in this study are described in terms of the bearing capacity factor for the self-weight component,  $N_\gamma$ .

**Chapter 6** firstly identifies difficulties in applying conventional bearing capacity methods for foundation conditions dominated by compression behaviour. Other alternative approaches for assessing these conditions are proposed based on the effect of soil compressibility. The estimation methods are validated through finite element results.

The major contributions and findings of this study are summarised in **Chapter 7**. Some recommendations for further research required in this area are also presented.



**Figure 1.1: Gravity base structure platform (Watt, 1978)**



# **Chapter 2**

## **Literature Review**

### **2.1 INTRODUCTION**

The main objective of this study is to analyse numerically the behaviour of shallow foundations on sandy deposits. Three questions from this objective arise such as what types of sands are analysed, what background information exists for bearing capacity and settlement of shallow foundations on sand, and which constitutive model should be used. This chapter develops possible answers to those questions by reviewing what features have been found in the past literature.

The first section examines experimental results for various types of sand from the literature and summarises their physical and mechanical differences. This study will take two generic types of sand: siliceous and calcareous sands. A typical difference between these two types of sands is the particle strength; a silica particle requires extremely high pressure for crushing, while calcareous sand particles are highly susceptible to breakage or crushing, even under very low pressure. This feature will result in significant differences in their fundamental behaviour, especially the compression behaviour.

The second section addresses the bearing capacity problem for shallow foundations on sandy deposits. This has been discussed extensively in the past in terms of various alternative expressions for bearing capacity (e.g. Terzaghi, 1943; Meyerhof 1953, Brinch Hansen, 1961). In fact, many researchers have revealed that the classical bearing capacity equation of Terzaghi (1943) is appropriate for specific conditions such as vertically loaded strip footings on dilative materials although a large number of correction factors have been proposed (e.g. Zadroga, 1995).

Based on the arguments in the first two sections, the third section will discuss the selection of constitutive models. In fact, most constitutive models for sands have been

developed based on the behaviour of dilative sands, and are not suitable for predicting the behaviour of compressible sands. The ideal model for this study should be chosen so that different types of sands may be distinguished by relatively minor variations in the input parameters.

## **2.2 COMPARISON BETWEEN SILICEOUS AND CALCAREOUS SANDS**

In the geotechnical field, sand is classified as a granular material in which greater than 85 % (by volume) of the individual particles have diameters in the range 0.05 to 2 mm. However, a wide variety of characteristics, such as the strength or angularity, may be attributed to the individual particles within such categorisation of sands. This section compares experimental results of two typical sands, siliceous and calcareous sands. The siliceous sands generally comprise stronger particles than the calcareous sands although the greater angularity of calcareous sand particles leads to higher friction angles than for siliceous sand at small strain level.

### **2.2.1 Features**

Siliceous sand can be found along rivers and coasts where grains are originally derived from the land, especially by erosive action (so-called terrigenous soils). It is relatively easy to make uniform reconstituted samples in any case for laboratory testing. Thus, siliceous sands have generally been performed as standard sands for research purposes. The mechanical behaviour of siliceous sands from different sites is generally similar, thus spatial variability is usually not a major concern.

On the other hand, calcareous sand deposits are derived mostly from the sedimentation of the carbonate skeletons of different varieties of marine organisms. They can be found along the coasts and the continental shelves in tropical regions where marine biological activity would have occurred in the past. Calcareous sand is mainly composed of calcium carbonate ( $\text{CaCO}_3$ )<sup>1</sup> (Milliman, 1974). High angularity and compressibility of soil skeleton are the main features of calcareous sands. The presence of high inter-

---

<sup>1</sup> Two terms are often used in the available literature to describe this soil: “calcareous” and “carbonate”. According to [Fookes \(1988\)](#), calcareous soils are classified as soils that are predominantly containing Calcium Carbonate ( $\text{CaCO}_3$ ), whereas carbonate soils embrace other less common carbonate minerals such as Magnesium Carbonate ( $\text{MgCO}_3$ ).

particle voids due to the angularity of the soil grains and the presence of intra-particle voids due to hollow skeletal soil particles lead to relatively high void ratios. Deposits of calcareous sands are therefore highly susceptible to damage, even under practical levels of loading. Environmental conditions such as temperature, salinity, sunlight and water clarity also provide significant differences in their forms (spatial variability) even for samples at the same site. Semple (1988) and Coop and Airey (2003) provide clear summaries for calcareous materials.

### 2.2.2 Properties

**Table 2.1** summarises the basic properties of typical siliceous and calcareous sands from the literature. From the table, higher maximum and minimum void ratios,  $e_{\max}$  and  $e_{\min}$ , for calcareous sands are found. The high  $e_{\max}$  values arise from the high angularity of most calcareous sands and the presence of intra-particle voids. The high compressibility of calcareous sands, at only moderate stress levels, is consistent with the wide void ratio range, ( $e_{\max} - e_{\min}$ ). Moreover, the yield pressure,  $p'_y$ , can be calculated using Cam Clay model parameters for the soils. The  $p'_y$  values in the table are calculated based on the samples with initial relative density of 90 % at  $p' = 1$  kPa. The  $p'_y$  values for calcareous sands are significantly lower than that for siliceous sands. Such lower  $p'_y$  values suggest that the deformation on calcareous sand show significant compression even at lower stress level.

In fact,  $e_{\max}$  and  $e_{\min}$  for calcareous sand are very sensitive to heterogeneities within the sample. For example, Finnie (1993), Ismail (2000), and Sharma (2003) conducted density tests on Goodwyn calcareous sand and obtained 1.97, 2.32, and 2.04 for  $e_{\max}$  and 0.941, 1.27, and 1.41 for  $e_{\min}$ , respectively. Such irregularity is frequently observed in the investigation of calcareous sands and may be explained by spatial variability. This has contributed to inconsistent information for calcareous samples and additional complexity for shallow foundation design.

**Figure 2.1** shows grain size distributions of typical siliceous and calcareous sands. It can be seen that the gradation of Dogs Bay calcareous sand is almost equivalent to that of Ham River siliceous sand and the mean particle size is apparently larger than Toyoura siliceous sand. Goodwyn sand is relatively well graded with 30% fines content.

The gradations of other sands can be distinguished using the value of uniformity coefficient,  $C_u$  and mean particle size,  $D_{50}$  in **Table 2.1**. The  $C_u$  and  $D_{50}$  values for calcareous sands show quite wide variation, while those for siliceous sands are almost identical.

### 2.2.3 Compression behaviour

**Figure 2.2** compares triaxial isotropic compression tests on Toyoura siliceous sand (Miura et al, 1984; Verdugo and Ishihara, 1996), Goodwyn calcareous sand (Ismail, 2000) and Dogs Bay calcareous sand (Coop, 1990) in void ratio and mean effective stress space. Those samples are uncemented, freshly deposited and tested up to very high pressures.

It is observed that the curves for Toyoura sand samples with two different initial densities eventually tend to merge into a unique asymptotic line as the stress level increases. The principal mechanism of this phenomenon involves particle crushing, while volume change at low stress level is due to rearrangement of the particles themselves (e.g. Roberts and DeSouza, 1958). Pestana and Whittle (1995) described this convergent state as a Limiting Compression Curve (LCC). Its uniqueness has to be confirmed, though, for both one-dimensional loading conditions and isotropic compression (Coop and Lee, 1993; Joer et al., 2000).

The compression behaviour of calcareous sands is significantly different from siliceous sands. The initial void ratios of Goodwyn and Dogs Bay sands are very high but their relative densities are similar to the loose sample of Toyoura sand. Then, the results show significant non-linear volumetric reduction over a wide range of stress, independent of the initial density. This is due to the loose contacts between particles and fragile angular grains with excessive intra-particle voids (Coop and Airey, 2003). Such high compressibility is the most distinctive feature of calcareous sand. The interpretation of compression behaviour is one of the most significant aspects for the selection of physical properties or the development of suitable constitutive models.

## 2.2.4 Shear behaviour

**Figure 2.3** shows triaxial undrained shear (CIU) tests for Goodwyn calcareous (Sharma, 2004) and Toyoura siliceous sands (Ishihara, 1993) for similar initial relative density (63%). Also **Figure 2.4** compares CIU tests for Dogs Bay calcareous (Coop, 1990) and Leighton Buzzard siliceous sand (Golightly and Hyde, 1988). These figures reveal that samples at similar relative densities show totally different behaviour: a strong dilative behaviour in siliceous sand (dilatancy) and a dilative-contractive behaviour in calcareous sand (particle crushing).

Siliceous sand in a loose state forms an assemblage of the particles with points of contact and large gaps between the particles. When shear stress is applied, inter-granular contacts are dislocated and the particles tend to fill the gaps (contractive behaviour). By contrast, as the material densities and the initial gaps have become sufficiently filled by the particles, further shearing leads to rearrangement of the formation and the volume tends to increase<sup>1</sup>. This shear-induced volume increase is termed dilatancy. Evaluating dilatancy is one of the most important aspects for modelling the behaviour of sand.

On the other hand, the grains of calcareous sands tend to crush relatively easily even under moderate stress levels. As seen in **Figure 2.3(a)**, the stress path for the Goodwyn sample shows somewhat dilative behaviour after the phase transformation stage<sup>2</sup>. Then after showing a peak stress at relatively large strain level, it reverts back towards residual strength (critical state). It is physically expected that although calcareous particles start to rearrange their formation at the initial stage of loading (pre-peak dilation), they are easily crushed by inter-granular contacts, and hence fragments of particles would fill the gap (post-peak contraction). Note that the steeper CSL for calcareous sand is due to the high angularity of the grains, and thus higher friction angle.

The difference in shear mechanisms is also evidenced from the relationship of pore water pressure measurement. From the pore water pressure measurements for a dense

<sup>1</sup> For undrained conditions, strain softening and strain hardening behaviour result from the contractive and dilative behaviour. The tendency for contraction and dilation are actually indicated by generation of positive pore pressure and negative pore pressure, respectively.

<sup>2</sup> Ishihara et al. (1975) indicated the phase transformation state as the point of minimum effective mean stress along undrained stress paths for sand. From that point, dilatancy behaviour changes from contractive (strain softening) to dilative (strain hardening).

sample in **Figure 2.4(b)**, significant reduction of pore water pressure occurs for siliceous sand due to dilative behaviour with suppressed volume expansion. On the other hand the pore water pressure for calcareous sand tends to increase due to contractive behaviour. It is interesting to note that the relative density of Dogs Bay sand is over 100%, implying that the initial density was increased by the very high confining stress.

**Figures 2.5** and **2.6** compare triaxial drained shear (CID) tests for calcareous and siliceous sands under low confining pressure (Goodwyn calcareous (Finnie, 1993) vs Leighton Buzzard siliceous (Golightly and Hyde, 1988)) and high confining pressure (Dogs Bay calcareous (Coop, 1990) vs Toyoura siliceous (Miura and Yamanouchi, 1975)), respectively. From the stress-strain relationships, the initial stiffness of siliceous sand samples is relatively higher than that of calcareous sand samples. Surprisingly, the shear strength of the calcareous sands is eventually higher than for the siliceous sands. It is deduced that the fragments of crushed calcareous sand particles are easily compacted under pressure, leading to increasing stiffness and strength, while the siliceous sample tends to shear along localised bands at high deviatoric stress. **Figure 2.5(b)** shows that for similar density samples, negative volumetric strain (volume expansion) is developed in the siliceous sand, while positive volumetric strain (volume reduction) is developed in the calcareous sand. Note that the pre-shear void ratios for calcareous sands are lower than their  $e_{min}$  values (e.g. Goodwyn  $e_{min} = 1.41$ ) which implies that particles are, indeed, crushed during the consolidation stage.

### 2.2.5 Critical state

The critical state concept (Schofield and Wroth, 1968) provides an excellent framework for capturing a limit state in terms of the Critical State Line (CSL). Based on this concept, the CSL can be drawn as a linear line on  $e$ - $Inp'$  plane, parallel to the Normally Consolidated Line (NCL). Recent studies, however, have revealed that the critical state line on  $e$ - $Inp'$  for sand is not a straight line on  $e$ - $Inp'$  plane but rather slightly curved at moderate stress levels (e.g. Been et al., 1991). The CSLs for Toyoura siliceous sand (Ishihara, 1993; Miura et al., 1984) and Dogs Bay calcareous sand (Coop, 1990) on the  $e$ - $Inp'$  plane are shown in **Figure 2.7**. These critical state envelopes collect results from undrained and drained shear tests with different initial void ratios and confining

pressures. In Dogs Bay sand, the void ratio values show some scatter and the total envelope is nearly linear, as opposed to Toyoura sand where the envelope becomes curved at about 2000 kPa. While the CSL seems phenomenologically unique for the siliceous sand, it looks rather scattered for the calcareous sand. Again severe crushing of calcareous particles changes the inherent grain size distribution. It is probably not possible to obtain a unique CSL for the calcareous sand due to the variety of individual particle strengths even if throughout every test particular attention is paid to obtaining the same density and grain size distribution. This suggests there are limitations in describing the strength and characteristics of calcareous sand with a constitutive model based on a unique CSL concept, like the Cam Clay model.

### 2.2.6 Foundation responses

The difference between siliceous and calcareous sands could also be observed in shallow foundation responses. **Figure 2.8** shows centrifuge model results of circular footings resting on Toyoura siliceous sand (Okamura, et al. 1997), Dogs Bay calcareous sand (Klotz and Coop, 2001) and Goodwyn calcareous sand and silt (Finnie, 1993), although Dogs Bay tests were based on the results from jacked pile models<sup>1</sup>. The footing diameter in all case is 3 m. The high initial stiffness and clear ultimate capacity in siliceous sand, and the lower initial stiffness and linearly increase of bearing pressure without reaching an ultimate state for calcareous sand, are evident. These features reflect somewhat similar behaviour from triaxial drained shear results (**Figure 2.5** and **2.6**). This is because the analysis of bearing response on sand is normally considered under drained conditions, where siliceous sand exhibits dilative behaviour, while calcareous sand exhibits contract behaviour.

The bearing response of Goodwyn calcareous sand is significantly weaker than that of Dogs Bay calcareous sand. Apart from some differences in the testing details, the amount of fines content and variation in strength of the calcareous particles might explain their different behaviour. As indicated by the grain size distribution shown in **Figure 2.1**, Goodwyn sand has about 30 % fines content, while the Dogs Bay sample comprises coarse grains only.

---

<sup>1</sup> The equivalent final penetration depth for their pile tests was up to 60 m. Here, though, only the initial penetration response, up to a maximum of half a diameter, is considered in detail.

### **2.2.7 Summary**

A brief comparison of siliceous and calcareous sand based on experimental results from the literature has been presented. Although both sands are categorised uniquely as ‘sand’ in the geotechnical classification, they present significant differences in their behaviour:

1. calcareous sand is mainly composed of very weak grains, of calcium carbonate ( $\text{CaCO}_3$ ), while siliceous sand mainly contains very hard quartz ( $\text{SiO}_2$ ) grains;
2. significant spatial variability is attributed to the calcareous sand in its natural state, but less significant for siliceous sand deposits;
3. large volume change in calcareous samples occurs under compression loading even at moderate stress level, while the siliceous sand undergoes only a small volume change for stresses up to about 10 MPa;
4. strong dilatancy in siliceous sand but greater compressibility in calcareous sand is associated with shear loading;
5. the CSL (or  $\phi'_{cs}$ ) for calcareous sand is higher than for siliceous sand;
6. the CSL of siliceous sand is curved in the  $e-\ln p'$  plane and seems unique, while it is more scattered for calcareous sand.

These behavioural characteristics will also affect the foundation response on these sands. The following section will review the bearing capacity problem for siliceous and calcareous sands, mainly focusing on the applicability of conventional bearing capacity calculations.

## **2.3 BEARING CAPACITY OF SHALLOW FOUNDATIONS ON SAND**

A large quantity of research has been directed towards evaluating the mechanical behaviour and the bearing capacity of shallow foundations on granular materials. Kusakabe (1995) summarised experimental results (mainly from centrifuge modelling) of shallow foundations on different materials and under different conditions from the literature. It was found that many uncertainties for the bearing capacity problem have not yet been answered.

For example, the Terzaghi (1943) bearing capacity equation has been widely used for shallow foundation design for a long period. However, it is found that this equation is applicable only for uniform, incompressible and moderate frictional granular materials. Randolph et al. (2004) pointed out that the greatest sources of uncertainty in applying the conventional equation to shallow foundations on sand are: a) an appropriate choice of friction angle for the bearing capacity equation; and b) allowance for soil compressibility.

The following subsection begins with a brief explanation of the Terzaghi bearing capacity equation and failure mode of shallow foundations. Then limitations in application of the bearing capacity equation will be discussed in terms of foundation size and shallow foundation response on calcareous or other compressible sands. Finally, existing problems of shallow foundation analysis in the context of this study are summarised.

### 2.3.1 Introduction to the bearing capacity equation

The well known bearing capacity formula proposed by Terzaghi (1943) comprises superposition of three terms, representing the contributions from cohesion, surcharge and self-weight, expressed as:

$$q_b = c' N_c + \bar{q} N_q + \frac{\gamma' B}{2} N_\gamma \quad (2.1)$$

where  $c'$  is the cohesion (or the undrained shear strength for ideal total stress analysis),  $\bar{q}$  is the effective surcharge at foundation level,  $\gamma'$  is the unit weight of soil and  $B$  is the footing width.  $N_c$ ,  $N_q$  and  $N_\gamma$  are bearing capacity factors, given as functions of the friction angle,  $\phi'$ . This equation is quite simple and is still widely used in practical design with some modifications (e.g. Brinch Hansen, 1961, 1970).

In fact, the first and second terms of the right hand side of **Equation 2.1** are often negligible for analysing surface foundations on sand, as the cohesion,  $c'$ , can be

assumed zero and the effective surcharge,  $\bar{q}$ , is zero when the foundation is on the ground surface. Thus, **Equation 2.1** degenerates for surface foundations on sand to:

$$q_b = \frac{\gamma' B}{2} N_\gamma \quad (2.2)$$

According to this equation, the bearing capacity factor  $N_\gamma$  could be obtained directly from experimental surface foundation tests on sand. Zadroga (1994) summarised several empirical equations for  $N_\gamma$  from the literature. The problem is that those equations are not only dependent on  $\phi'$ , but also appear to depend on the size of foundation (e.g. De Beer, 1963).

Furthermore, the bearing capacity equation is not appropriate for highly compressible materials like calcareous sands, especially given their high friction angle. The approach leads to enormously high bearing capacity factors which are unrealistic in practice. **Table 2.2** compares the bearing capacity factors between siliceous and calcareous sands. It can be seen that the high friction angle for calcareous sand gives a factor of more than 100 for the bearing capacity factor. The range of the values is also very wide.

### 2.3.2 Mode of bearing capacity failure

The bearing response of shallow foundations at large displacements may be classified into one of three failure modes (Vesić, 1975). **Figure 2.9** illustrates those three modes (from Das, 1995, after Vesić, 1973).

The general shear failure mode (**Figure 2.9(a)**) occurs for incompressible material, dense sand, or clays under rapid loading (undrained conditions). The ultimate bearing capacity is mobilised at relatively small settlement accompanied by clearly formed shear planes and heave around the foundation.

The local shear failure mode (**Figure 2.9(b)**) is observed for more compressible material of moderate density. Slight heave occurs, but the rupture surface does not extend to the soil surface. Large settlements may be necessary for a clear rupture

surface to form, and the bearing capacity continues to increase as the settlement increases.

The punching shear failure mode (**Figure 2.9(c)**) occurs in very loose sands, soils with low particle strength, multi-layered ground where a thin crust is underlain by soft soil, or clays under very slow loading (drained conditions). No heave and slip line are observed and there is no ultimate bearing capacity or well-defined yield point. Instead, large settlements occur due to the high compressibility of the soil and the bearing pressure continuously increases with penetration depth.

In the case of granular material deposits, the failure mode of shallow foundations depends mainly on the relative density or the crushability of the particles. Foundations on dense incompressible ground will induce a general shear mode behaviour, whereas a punching shear mechanism will dominate the foundation response on crushable materials or loose compressible sands.

In fact, Terzaghi's equation is based on the bearing capacity of incompressible (uncrushable) granular materials, which typically show a general shear failure pattern (**Figure 2.9(a)**). Thus it is not suitable for highly compressible materials such as calcareous sand. When this equation is applied for the analysis of foundation response on compressible material, the bearing capacity must be defined as the bearing pressure at some nominal displacement, conventionally taken as 5 or 10 % of the foundation diameter (Randolph et al., 2004).

### 2.3.3 Foundation size effects of bearing capacity of shallow foundations

Early bearing capacity studies of small model foundations on granular material tested at 1 g revealed that the bearing capacity factor,  $N_y$ , decreased with increasing footing width, widely recognised as a 'foundation size effect<sup>1</sup>' (De Beer, 1963). Based on accumulated observations, especially the development of centrifuge modelling over the past forty years, the foundation size effect has been recognised as a considerable issue in coarse-grained granular soils (Ovesen, 1975; Yamaguchi et al., 1976; Kimura et al.,

<sup>1</sup> Foundation size effect is generally called 'scale effect'. However, the term 'scale' is often confused with 'scale effect' in the centrifuge tests (Taylor, 1995) which refer to the relative size of soil particles and foundation. To avoid such confusion, the term 'foundation size effect' is used hereafter.

1985; Hettler and Gudehus 1988; Pu and Ko, 1988; Kusakabe et al., 1991; Aiban, 1994; Okamura et al., 1997; Zhu et al. 1998).

Cerato (2004) summarised this foundation size effect for circular and square footings in the literature (**Figure 2.10**). The trend of decreasing  $N_y$  with increasing footing width is observed for both circular and square footings. In spite of considerable scatter, it can be seen that there is a gradual reduction in  $N_y$  particularly for foundations exceeding 0.1 m diameter or width (e.g. cone penetration devices) and relatively constant  $N_y$  over 3 m diameter (e.g. piles, shallow footings). Note, however, that **Figure 2.10** may not give a clear picture regarding the foundation size effect because it is plotted for a number of different sand types and varying densities. Kimura et al. (1985) conducted centrifuge tests for different widths of strip foundations on Toyoura siliceous sand. Different degradation curves for the  $N_y$  - B relationship were found for different densities (**Figure 2.11**). The  $N_y$  value for the same sand is therefore dependent on the width of the strip foundation as well as the density of the sand. This may also occur for circular foundations.

Kusakabe (1995) suggested that the foundation size effect on  $N_y$  may be interpreted from two different points of view: progressive failure (Yamaguchi et al., 1976) and stress dependency (De Beer, 1963; Hettler and Gudehus, 1988; Kusakabe et al., 1991).

The first explanation is that progressive failure may dominate when the size of foundation increases. Yamaguchi et al. (1976) presented shear strain distributions of two different prototype scale foundations at different stages of settlement (**Figure 2.12**). Final slip lines detected by radiography of the centrifuge box were also shown. It is clearly observed that shear strains developed along the slip line and their area spread from beneath the foundation. It was also shown that the region of high shear strain is apparently larger beneath large foundations than that for small footings. They concluded that the foundation size effect could be reasonably explained by progressive failure and the assumption of constant shearing strain adopted in existing bearing capacity theories may not be valid.

The second explanation (De Beer, 1963) suggested that the foundation size effect is due to a non-linear failure envelope rather than the conventional Mohr-Coulomb envelope

which is used for the development of bearing capacity equations. Such a non-linear envelope arises because of the stress dependency of dilation, particle rearrangement and crushing (Lee and Seed, 1967). This observation has been recognized for a long period and a large number of friction angle equations allowing for the stress-dependent nature of this quantity have been proposed (e.g. De Beer, 1963; Baligh, 1975; Bolton, 1986; Hettler and Gudehus, 1988; Ueno, 1998, 2002).

For example, Hettler and Gudehus (1988) addressed the foundation size effect due to the stress dependency of  $\phi'$ . They expressed  $\phi'$  as a power law of mean effective stress and the  $N_\gamma$  as a function of the footing width as follows:

$$\sin \phi' = \frac{\sin \phi'}{(p'/p'_{ref})^\beta + \sin \phi'_{ref} [1 - (p'/p'_{ref})^\beta]} \quad (2.3a)$$

$$\frac{p'}{p'_{ref}} = \frac{B}{B_{ref}} \frac{N_\gamma}{N_{\gamma ref}} \quad (2.3b)$$

$$N_\gamma = \exp(5.71(\tan \phi')^{1.15}) - 1 \quad (\text{Gudehus, 1981}) \quad (2.3c)$$

where  $B$  is the foundation size and  $p'$  is the mean effective stress given by **Equation 2.3b**:  $\phi'_{ref}$ ,  $B_{ref}$ ,  $p'_{ref}$  and  $N_{\gamma ref}$  are reference values. From test results, a set of  $B_{ref}$  and  $N_{\gamma ref}$  can be obtained and  $p'_{ref}$  and  $\phi'_{ref}$  are then defined using **Equation 2.3b and 2.3c**, respectively. The friction angle  $\phi'$  as well as  $N_\gamma$  for a given  $B$  can be determined by an iterative procedure. This method agrees well with the centrifuge test results given by Kimura et al. (1985) (**Figure 2.11**).

Moreover, there are several numerical approaches for assessing the influence of the bearing capacity factor,  $N_\gamma$ , using non-associated constitutive models (i.e. where the dilation angle is not equal to the friction angle). Frydman and Burd (1997) and Erickson and Drescher (2002) studied the dilation angle effect on  $N_\gamma$  for strip and circular footings respectively, using a non-associated Mohr-Coulomb model. They found that the effect of dilation angle is negligible at low friction angles. However, it cannot be neglected for friction greater than  $35^\circ$ , especially for rough circular foundations.

In summary, it is clear that the foundation size has a significant influence on the bearing capacity factor,  $N_\gamma$ . A large number of centrifuge tests and numerical investigations have contributed to evaluating this effect. However, the numerical studies are somewhat limited in quantifying this issue satisfactorily. One of the reasons is that the Mohr-Coulomb model does not capture sufficiently the stress and density state dependency of sand behaviour or the compressibility of sands. It is believed that analyses should follow an appropriate constitutive model capturing these effects and this is one of the objectives of the present study.

### 2.3.4 Other aspects of bearing capacity of shallow foundations

Kimura et al. (1985) conducted centrifuge tests for rough and smooth based strip footings resting on dense siliceous sand. It was observed that the bearing capacity of smooth footings is reduced to as low as a half of that of rough footings (**Figure 2.13**), with the effect greater for smaller foundations. Potts and Zdravkovic (2001) carried out numerical simulations in terms of the roughness effect using a non-associated Mohr-Coulomb model representing granular materials. The results of predicted load-settlement curves are shown in **Figure 2.14**. Significant bearing capacity reduction from rough to smooth foundation base can be found. It is interesting to note that the dilation angle does not affect greatly the ultimate bearing capacity but influences the settlement required to mobilise this capacity.

Ueno et al. (1994) suggested that increasing  $K_0$  might lead to an increase in the bearing capacity, based on centrifuge results.

Certain numerical problems of the finite element analysis may often induce significant errors in the results of calculations, e.g. mesh geometry (coarse or fine, boundary length and depth), type of discretised element, calculation step size, and so forth. Frydman and Burd (1995) examined the effect of finite difference mesh refinement using FLAC (1993), and of calculation step size in terms of the bearing capacity factor,  $N_\gamma$  (**Figure 2.15**). They concluded that the value of  $N_\gamma$  depends critically on the number of load steps but is relatively insensitive to the number of elements in the mesh. On the other hand, Sloan and Randolph (1982) reported that locking of low-order finite elements can lead to errors in the calculation of undrained bearing capacity, with similar problems

arising for drained analyses with constant dilation. However it should be noted that the post-failure behaviour in FLAC is treated differently than in finite element analysis.

### 2.3.5 Bearing capacity of shallow foundations on calcareous sands

The discussion above reflects that most of the design methods for bearing capacity problems have been based on the behaviour of siliceous sands, rather than highly compressible frictional materials such as calcareous sands. This means that special attention and modification of the design methods is required for the analysis of foundations on calcareous sands.

There are some published works, however, on shallow foundation analyses on calcareous sands. Poulos and Chua (1985) carried out 1g model tests for shallow foundations on calcareous sand with comparison to siliceous sand. The bearing resistance on calcareous sand was significantly lower than for siliceous sand at small displacement levels. However, the bearing resistance of calcareous sands increases continuously with increasing penetration and can eventually give higher mobilised bearing pressures than the level of ultimate bearing capacity for siliceous sand. The same conclusion was arrived at based on centrifuge model tests performed by Nauroy and Golightly (1991) (**Figure 2.16** as well as a previous figure **Figure 2.8**). Mechanical features such as dilatancy of siliceous sand and compressibility of calcareous sand would contribute to the differences in shallow foundation responses. Quasi-linear increase in bearing resistance of calcareous sand with penetration depth, with no clear ultimate state, has also been reported in the literature (Le Tirant et al., 1988; Finnie, 1993; Finnie and Randolph, 1994a, 1994b). Dutt and Ingram (1988) noticed that the conventional bearing capacity model based on the general failure mode was inappropriate for predicting the quasi-linear bearing response of calcareous sand.

Smith et al. (1988) simulated the results of drained plate load tests on calcareous sand using the Molenkamp model (Molenkamp, 1981) and other constitutive models (Drucker-Prager and crush-up model by Sweet (1988)) (**Figure 2.17**). Non-linear load-displacement curves were predicted and agreed reasonably with results from large-scale 1g plate load tests. However, they commented that those numerical predictions were for undrained problems, where ‘collapsing’ or ‘liquefying’ behaviour was of major concern.

Numerical complexity and a large number of parameters (21 parameters for the Molenkamp model) would not necessarily lead to any greater ability for curve fitting of field measurement. Islam (1999) predicted the behaviour of circular footings on calcareous sand using the Cam Clay model with non-associated flow rule (SU model). The results agreed reasonably well with results from centrifuge model tests (Finnie, 1993) and small-scale 1g footing tests. Although this model added an additional constant for varying the size of the yield surface, it should, in fact, be taken as a variable that depends on initial density.

The quasi-linear bearing response of calcareous sand is now widely accepted as resulting from punching shear failure due to compressive volumetric strains, in contrast to the general shear type of failure observed for most siliceous sand. Randolph and Erbrich (2000) explained this phenomenon in terms of the separate variation of three strain components: volumetric strains due to change in mean effective stress,  $p'$  (consolidation settlement), volumetric strains due to changes in mobilised deviatoric stress ratio,  $q/p'$ , and shear strains also due to changes in  $q/p'$ . **Figure 2.18(a)** illustrates how the components affect the bearing pressure and settlement curve. The ‘consolidation settlement’ response will show an increasing stiffness with increasing bearing pressure, reflecting a higher bulk modulus with increasing effective stress level. Conversely, the shear stress induced volumetric and shear strain components will show a decreasing stiffness with increasing bearing pressure, due to the increase in applied shear stress ratio. Dilative material such as siliceous sand is strongly dominated by the shear strain component and will indicate a clear ultimate behaviour, whereas compressive material such as calcareous sand results in a continuously increasing bearing resistance due to dominance of the volumetric component.

They also commented on the interesting results from shallow footing tests on uncemented calcareous sand performed by Finnie (1993), for which the bearing response was insensitive to foundation size (**Figure 2.19**). The consolidation settlement increased steadily with increasing diameter, because of the decreasing ratio of the stress change at any depth beneath the foundation to the ambient stress level. The volumetric and shear strains caused by shear stresses would be largest for the smallest foundations and would reduce to very small values for the largest foundations (see **Figure 2.18(b)**). This hypothesis might be applicable for dilative material, meaning that the response of

very large foundations on any type of material would be mainly dominated by the consolidation settlement.

Although some constitutive models were able to predict the quasi-linear bearing response of calcareous sands, the effect of compression characteristics was normally neglected. If a model is developed to describe the compression behaviour appropriately, it should be possible to characterise the shallow foundation responses of siliceous and calcareous sands, to explore the effect of soil compressibility, and to support the development of design issues using numerical methods.

### 2.3.6 Summary

The bearing response of shallow foundations on various sands has been reviewed. The conventional bearing capacity equations and the factor,  $N_\gamma$ , should be used carefully for the following reasons:

1. Highly frictional materials: the range of the friction angle of calcareous sands (frequently  $> 40^\circ$ ) leads to an unrealistic  $N_\gamma$  value.
2. Soil compressibility: the conventional bearing capacity equations were developed based on an assumption of dilatant granular materials which generally show a general shear failure pattern. Thus it is not suitable for highly compressible materials such as calcareous sand that shows a completely different failure mechanism, known as a punching shear mechanism.
3. Foundation size effect: the  $N_\gamma$  value decreases with increasing footing size. Although this has been revealed by extensive research using centrifuge model tests, these cannot be extended to very large sizes of shallow foundation ( $> 30$  m). The current literature indicates that the foundation size effect (see **Figure 2.10 to 2.12**) does not lead to significant changes in the  $N_\gamma$  value at large diameters. However, there are still uncertainties for large foundation sizes, particularly when dealing with compressible soil types.

Further evaluation of the bearing capacity problem by means of experimental investigation is limited by cost. The obvious alternative is then to use numerical analysis of shallow foundation behaviour, using a constitutive model that successfully simulates

the different aspects of sand behaviour. Such a model should be able to distinguish between the shallow foundation responses of siliceous and calcareous sands, to assess the effect of soil compressibility on the bearing capacity problem, and to support the development of design issues from a numerical approach. The next section will review constitutive models from the literature and discuss the suitability for the aims of this study.

## **2.4 CONSTITUTIVE MODELS FOR SAND**

In the previous sections, experimental results from the literature highlighted several mechanical features of sand behaviour. A large number of factors influence the behaviour and are difficult to be captured by simple constitutive models. A great number of constitutive models have therefore been proposed to account for the different types of soil.

This section evaluates the abilities of existing constitutive models developed to capture the behaviour of sand. As mentioned earlier, an interpretation of the compression behaviour is a key issue for the development of suitable constitutive models in this study. From an experimental standpoint, for example, the initial state at the end of consolidation dictates the level of dilatancy. The compression characteristics such as non-linearity in  $e$ - $\ln p'$  space would also affect the shear behaviour. Therefore, when the model is validated, it should be focused on how the model accounts for the compression behaviour. Other aspects such as the dilatancy and non-associativity of sand are also discussed.

### **2.4.1 Modelling the compression behaviour**

The compression curves in **Figure 2.2** show different levels of volume change between siliceous and calcareous sands. Also, the curves for siliceous samples with different initial densities tend to merge as the stress level increases, showing that the effect of the initial density is gradually eliminated at high pressure.

The relationship between the void ratio,  $e$ , and the stress,  $p'$ , is frequently described in terms of the critical state parameters,  $\lambda$  and  $\kappa$ , for loading and unloading:

$$e_c = e_{NC} - \lambda \ln p' \text{ (loading)} \quad (2.4)$$

$$e_s = e_{OC} - \kappa \ln p' \text{ (unloading)} \quad (2.5)$$

where,  $e_{NC}$  and  $e_{OC}$  are the intersections of the normally consolidated line (NCL) and overconsolidated line (OCL) at the reference stress (normally taken as  $p' = 1$  kPa). The  $\lambda$ ,  $\kappa$  and  $e_{NC}$  values for various soils are reported in **Table 2.1**. Moreover, the yield pressure,  $p'_y$ , can be calculated using **Equation 2.4** and **2.5**. **Table 2.1** shows the  $p'_y$  values for the samples with initial relative density at unit mean effective stress ( $p' = 1$  kPa) of 90 %. The  $p'_y$  values for calcareous sands are significantly lower than that for siliceous sands. It suggests that calcareous sands attain the yield state at relatively low stress levels and then yield continuously thereafter.

**Equation 2.4** and **2.5** represent a simple elasto-plastic model that has a clear distinct yield point. It has a conceptual limit to describing the compression behaviour for sand which generally has no clear yield point but deforms asymptotically to the plastic state. Furthermore, it is possible to envisage an infinite number of the NCLs over a wide range of stress and density levels for sand, depending on the initial properties (Ishihara et al, 1975; Jefferies and Been, 1987). Those NCLs are believed to be non-linear in  $e - \ln p'$  space but tend to merge at large stress levels (Joer et al., 2000), implying that there is probably a state which is independent of the initial density.

Pestana and Whittle (1995) proposed a compression model that can describe the compression behaviour of freshly deposited cohesionless soils over a wide range of stress levels and densities. This model is based on the postulation of the existence of an infinity of NCLs and unique ‘particle crushing’ state, the Limit Compression Curve (LCC). The compression behaviour of this model assumes that:

1. the soil experiences some plastic strain throughout its loading history, so that irrecoverable volumetric strains are developed during first loading;
2. the degree of curvature for the first loading response can be controlled using a mapping distance from the LCC (Dafalias and Herrmann, 1982);
3. all NCLs merge to a unique LCC at large stress levels.

At low stress levels, volume changes can be explained as elastic compression of the soil skeleton, while, at large stress levels, it is principally controlled by not only particle crushing but also particle rearrangement. A large number of simulations for different sands have demonstrated the predictive capabilities of this model (Pestana, 1994; Pestana and Whittle, 1995; Joer et al., 2000).

#### **2.4.2 Modelling the shear behaviour**

The first important aspect for modelling the shear behaviour of sand is to provide a better prediction of the dilatancy response, especially for siliceous sand. In critical state soil mechanics, for example, when the shear stress reaches its critical state (i.e. the plastic volumetric strain increment ( $d\varepsilon_v^p$ ) becomes zero) on  $p'$ - $q$  space, the behaviour becomes neutral and the stresses remain steady. When the constitutive model is applied to simulate sand behaviour, it should be modified to express the dilative behaviour satisfactorily.

A large number of phenomenological constitutive models for sand have been proposed: e.g. the double-hardening model (Nova and Wood, 1979; Molenkamp, 1981), the Bounding Surface model for sand (Bardet, 1986; Crouch et al. 1994), the Cam Clay model for sand (Basaran, 1994; Gutierrez, 2003), Nor-sand model (Jefferies, 1993), Superior sand model (Drescher and Mroz, 1997), the two-surface model (Manzari and Dafalias, 1997), Severn-Trent sand model (Gajo and Muir Wood, 1999), and the sub- and super-loading surface model (Asaoka et al, 2000). Most of the constitutive models showed good predictions of contractive-dilative behaviour of sand under undrained loading. However, some models were only valid for predicting the undrained behaviour because their input parameters depend on the initial density state (Nova and Wood, 1979; Bardet, 1987; Basaran, 1994; Gutierrez, 2003) and most of models were incapable of describing the effect of compressibility for granular materials.

The MIT-S1 model (Pestana and Whittle, 1999) represents a particular model that can simulates both the compression and shear behaviour of sands within the model framework, as already mentioned. Isotropic hardening of the yield surface (bounding surface) of this model is controlled by mapping the distance to the LCC regime. The

shear behaviour can be characterised as the response inside the LCC, while compressibility becomes dominant when the state is on the LCC.

Moreover, evidence from experimental results on sand has revealed that the vector of plastic strain increment on the yield surface is not perpendicular to the tangent of the yield surface and hence the normality rule is not appropriate (e.g. Miura et al., 1984; Huang, 1994). A non-associated flow rule is therefore required for the prediction of sand response. For example, Yu (1998) and Islam (1999) adopted non-associated flow rules for the Cam clay model using an additional input parameter

#### 2.4.3 Summary

A brief introduction to some of the existing constitutive models (particularly those featuring sand behaviour) has been presented. The MIT-S1 model has been found suitable for our purposes for the following reasons:

1. it is capable of accounting for the compression aspects in sands;
2. it allows combining of the compression and shear features;
3. it describes the dilatancy and the non-associativity of sands under shear loading;

This model, therefore, is fit for the research purpose in this study, the assessment of the bearing response of highly frictional and compressible calcareous sands. Full details of the model can be found in Pestana's thesis (Pestana, 1994) and a subsequent journal paper (Pestana and Whittle, 1999). Formulae of the model and a numerical implementation in the finite element method are described in the **Appendix**.

**Table 2.1: Properties and critical state parameters for various sands**

| Sands                          | D <sub>50</sub> | C <sub>u</sub> | e <sub>max</sub> | e <sub>min</sub> | Cam Clay parameter |       | p' <sub>y</sub> *<br>(MPa) |      |
|--------------------------------|-----------------|----------------|------------------|------------------|--------------------|-------|----------------------------|------|
|                                |                 |                |                  |                  | λ                  | κ     |                            |      |
| <b><i>Calcareous sands</i></b> |                 |                |                  |                  |                    |       |                            |      |
| Dogs Bay                       | 0.30            | 2.06           | 2.21             | 1.48             | 0.335              | 0.013 | 3.80                       | 1.07 |
| Goodwyn                        | 0.10            | 4.60           | 2.04             | 1.41             | 0.290              | 0.017 | 3.30                       | 0.81 |
| Ledge Point                    | 0.27            | 1.84           | 1.22             | 0.88             | 0.185              | 0.006 | 2.50                       | 7.05 |
| North Rankin                   | 0.23            | 3.75           | 1.79             | 1.22             | 0.220              | 0.014 | 2.67                       | 0.86 |
| Rottnest                       | 0.17            | 1.50           | 1.21             | 0.84             | 0.192              | 0.019 | 2.40                       | 6.66 |
| Quiou                          | 0.70            | 4.50           | 1.20             | 0.78             | 0.152              | -     | 2.02                       | 4.61 |
| <b><i>Siliceous sands</i></b>  |                 |                |                  |                  |                    |       |                            |      |
| Ham River                      | 0.31            | 1.55           | 0.92             | 0.59             | 0.160              | 0.013 | 2.17                       | 37.2 |
| Leighton Buzzard               | 0.12            | 1.48           | 0.84             | 0.51             | -                  | -     | -                          | -    |
| Ottawa                         | 0.28            | 1.5            | 0.75             | 0.48             | 0.130              | -     | 1.94                       | 154  |
| Sacramento River               | 0.21            | 1.50           | 1.03             | 0.61             | 0.200              | -     | 2.50                       | 16.8 |
| Ticino                         | 0.53            | 1.60           | 0.97             | 0.53             | 0.189              | 0.020 | 2.46                       | 70.2 |
| Toyoura                        | 0.17            | 1.50           | 0.98             | 0.62             | 0.141              | 0.018 | 2.13                       | 160  |

\* p'<sub>y</sub> is calculated based on the sample with relative density of 90 % at p' = 1 kPa and κ value for unavailable materials is assumed as 0.01.

## Reference:

- |                   |                           |
|-------------------|---------------------------|
| Dogs Bay:         | Coop and Lee (1993)       |
| Goodwyn:          | Sharma (2004)             |
| Ledge Point:      | Sharma (2004)             |
| North Rankin:     | Allman and Poulos (1988)  |
| Rottnest:         | Ismail (2000)             |
| Quiou:            | Pestana (1994)            |
| Ham River:        | Coop and Lee (1993)       |
| Leighton Buzzard: | Golightly and Hyde (1988) |
| Ottawa:           | Pestana(1994)             |
| Sacramento River: | Lee and Seed (1967)       |
| Ticino:           | Pestana(1994)             |
| Toyoura:          | Ishihara (1993)           |

**Table 2.2 Terzaghi's bearing capacity factors for siliceous and calcareous sands**

| Sands           | $c'$ | $\phi'(^{\circ})$ | $N_q^3$ | $N_c^4$ | $N_y^5$ | Failure mode <sup>6</sup> |
|-----------------|------|-------------------|---------|---------|---------|---------------------------|
| Siliceous sand  | 0    | $30\pm 2^1$       | 15-23   | 26-36   | 11-21   | General                   |
| Calcareous sand | 0    | $40\pm 5^2$       | 33-135  | 46-134  | 48-272  | Punching shear            |

<sup>1</sup> Leighton Buzzard (Golightly and Nauroy, 1988), Toyoura (Miura et al. 1984)

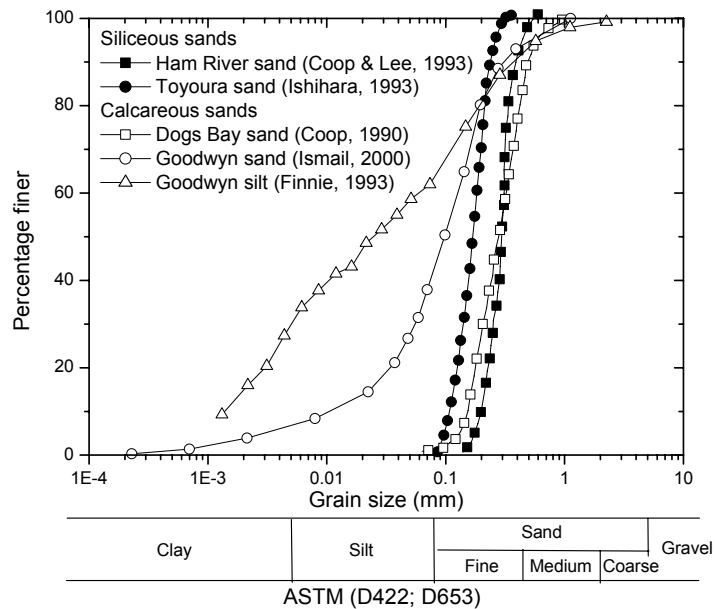
<sup>2</sup> Bombay, Coral Algae, Dogs Bay (Golightly and Nauroy, 1988), Goodwyn (Sharma, 2004)

$$^3 N_q = \exp(\pi \tan \phi') \cdot \tan^2 \left( \frac{\pi}{4} + \frac{\phi'}{2} \right)$$

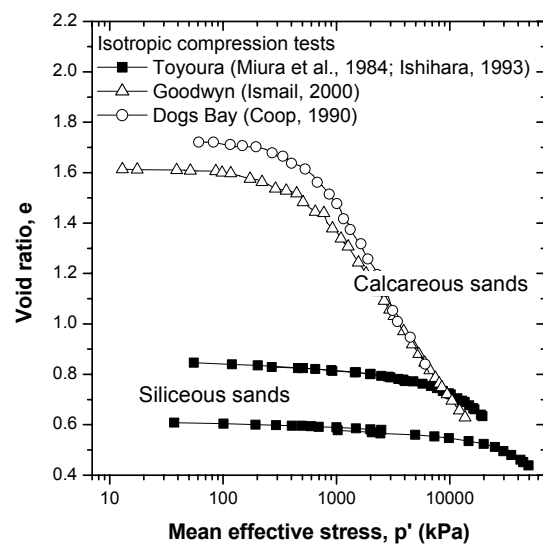
$$^4 N_c = \frac{N_q - 1}{\tan \phi'}$$

$$^5 1.5(N_q - 1) \tan \phi' (\text{Brinch Hansen, 1970})$$

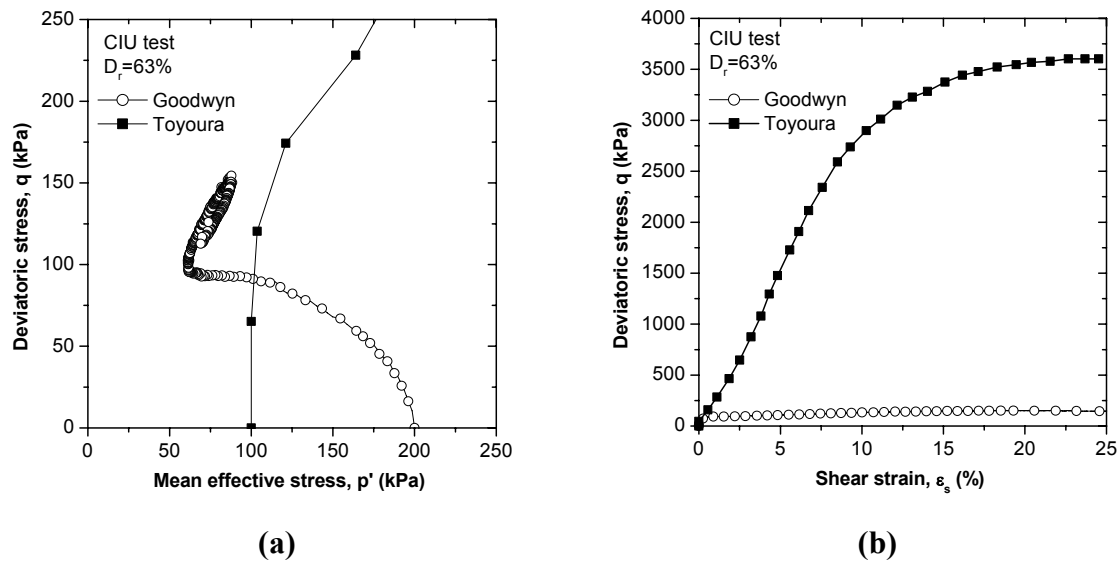
<sup>6</sup> As in **Figure 2.9**



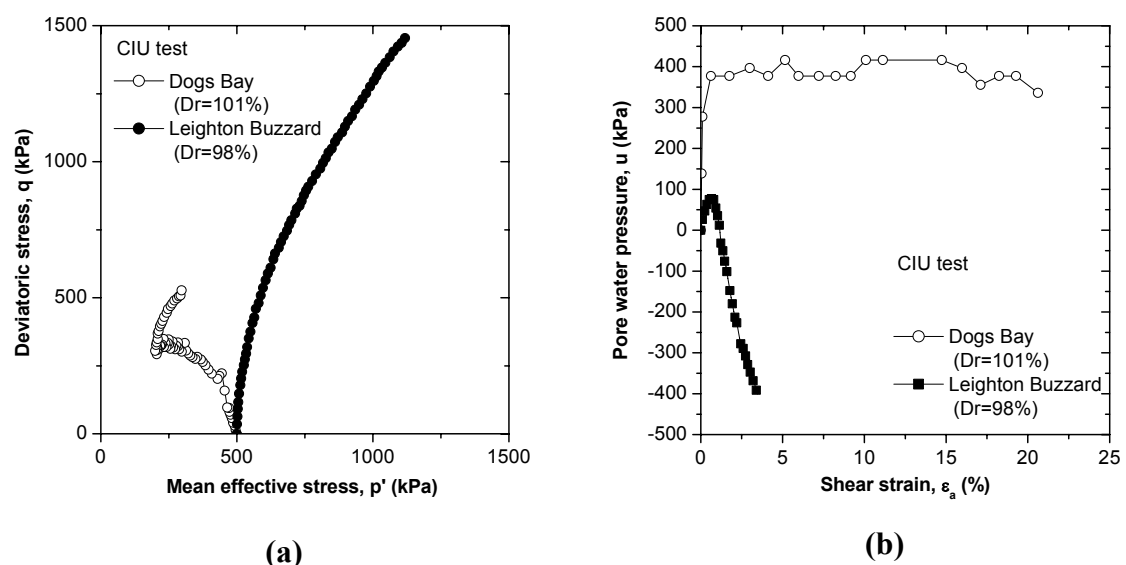
**Figure 2.1: Grain size distributions for siliceous and calcareous soils**



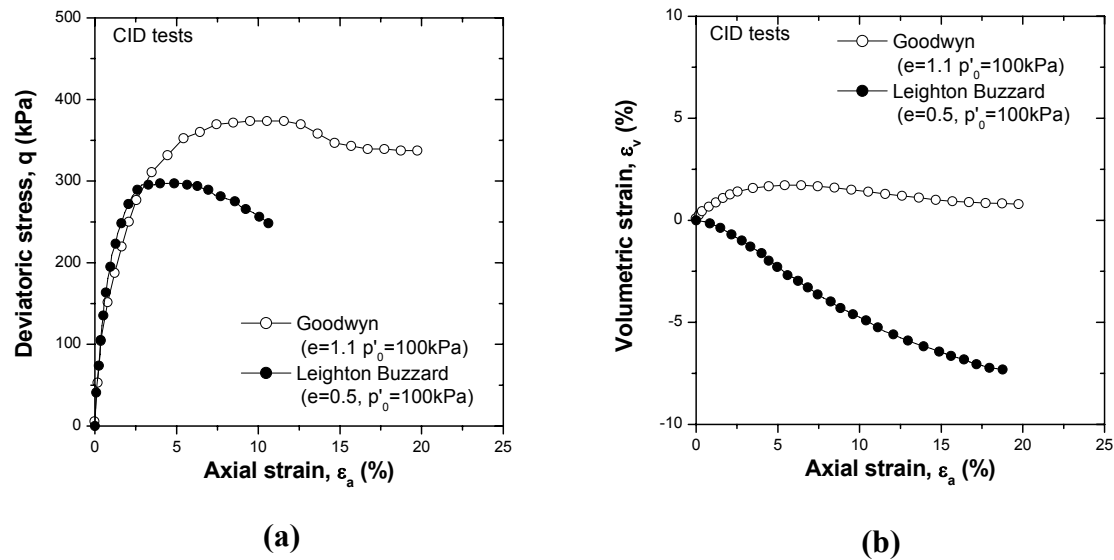
**Figure 2.2: Consolidation curves for siliceous and calcareous sands**



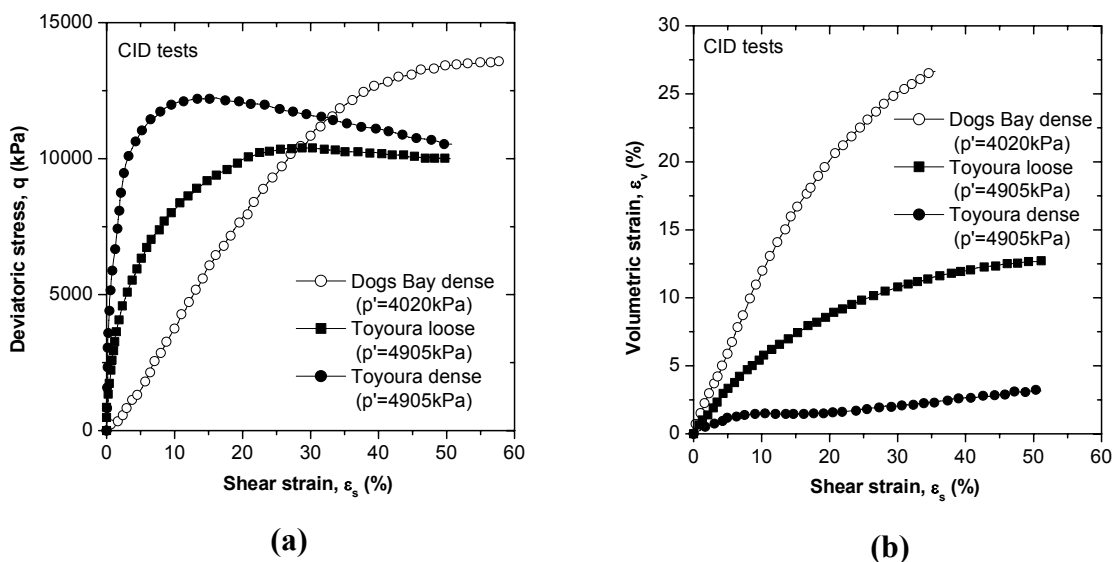
**Figure 2.3: Triaxial undrained shear tests for Goodwyn calcareous (Sharma, 2004) and Toyoura siliceous sands (Ishihara, 1993)**



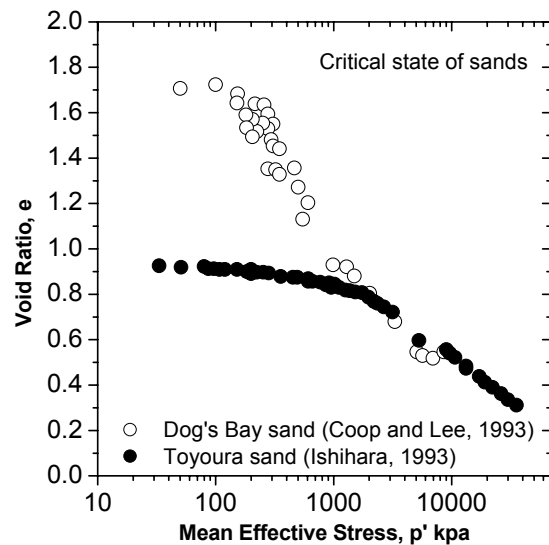
**Figure 2.4: Triaxial undrained shear tests for Dogs Bay calcareous (Coop, 1990) and Leighton Buzzard siliceous sands (Golightly and Hyde, 1988)**



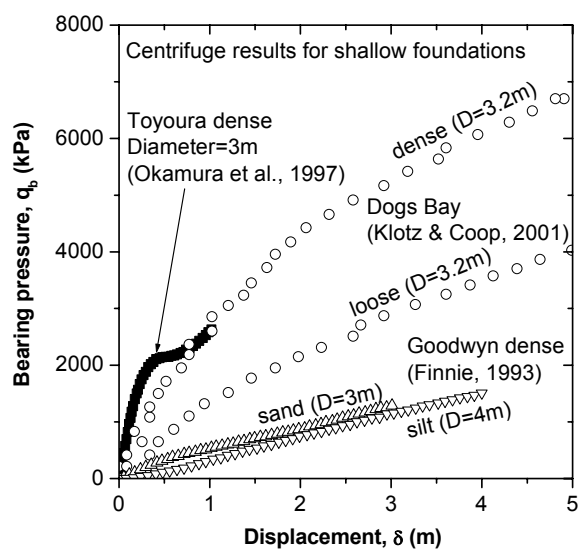
**Figure 2.5: Low-confined triaxial drained shear tests for Goodwyn calcareous (Finnie, 1993) and Leighton Buzzard siliceous (Golightly and Hyde, 1988) sands**



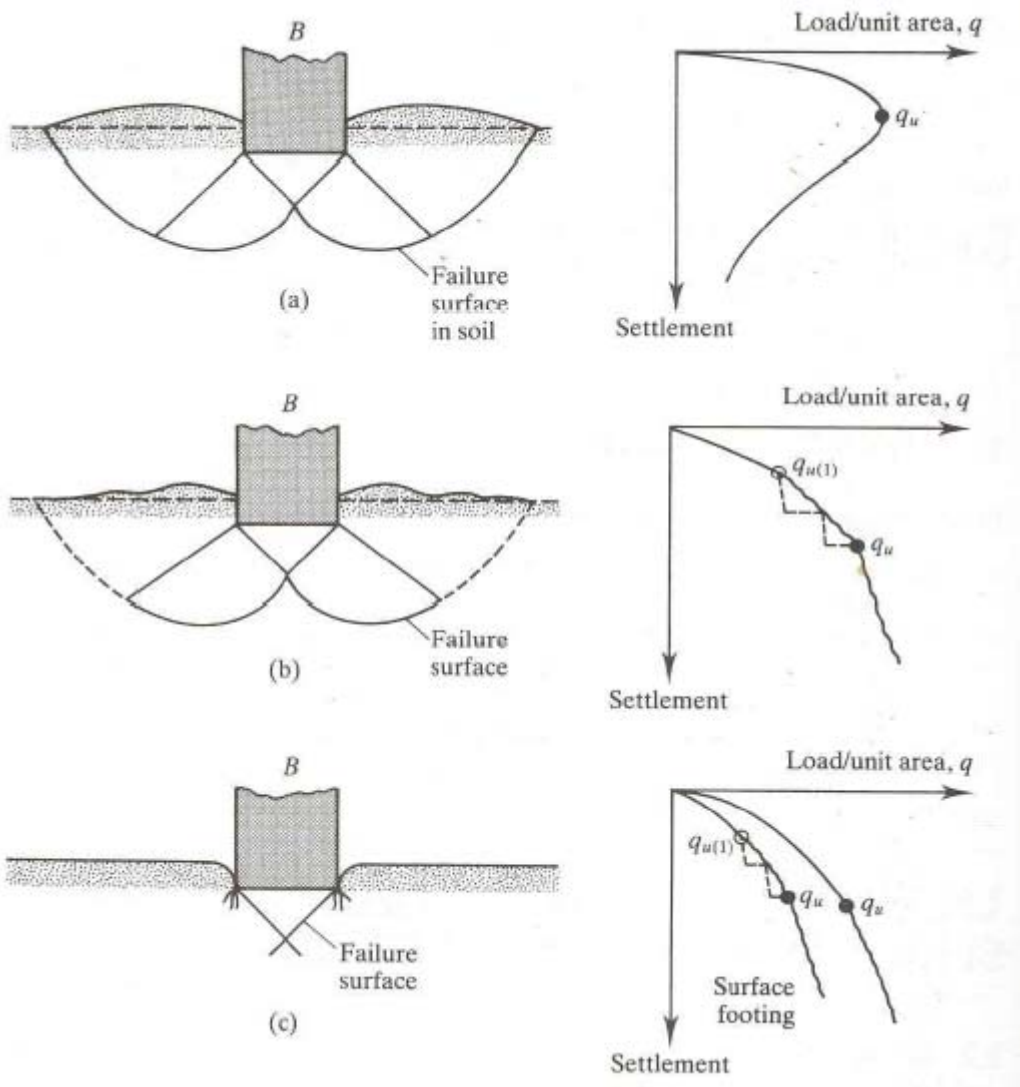
**Figure 2.6: High-confined triaxial drained shear tests for Dogs Bay calcareous (Coop, 1990) and Toyoura siliceous (Ishihara, 1993) sands**



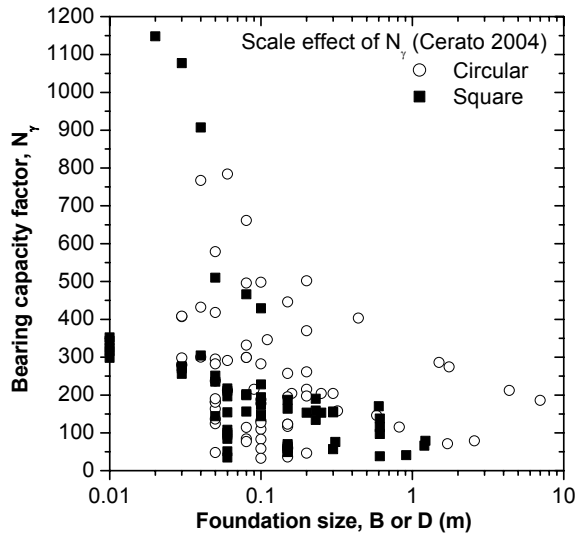
**Figure 2.7: Critical state line for granular materials on  $e$ - $\ln p'$  plane**



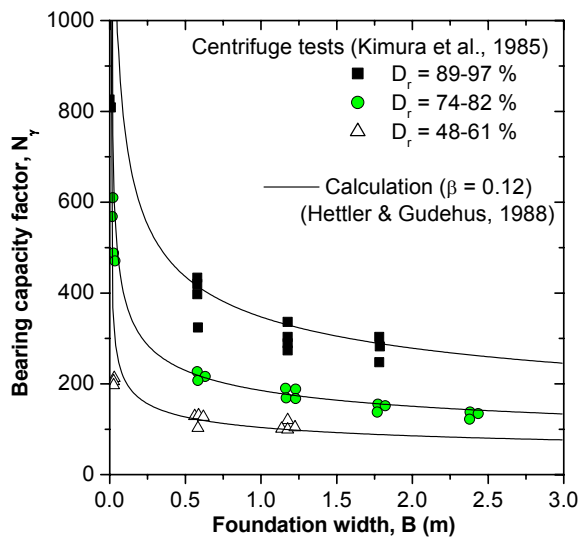
**Figure 2.8: Bearing responses for siliceous and calcareous sands**



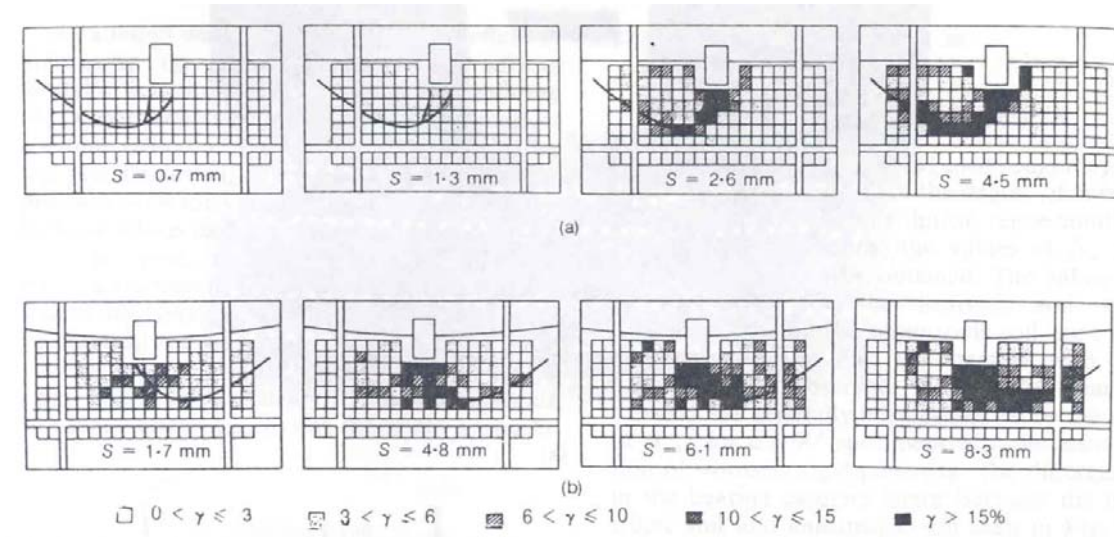
**Figure 2.9: Three modes of Bearing Capacity Failures: (a) General Shear, (b) Local Shear, (c) Punching Shear (from Das 1995, after Vesic. 1973)**



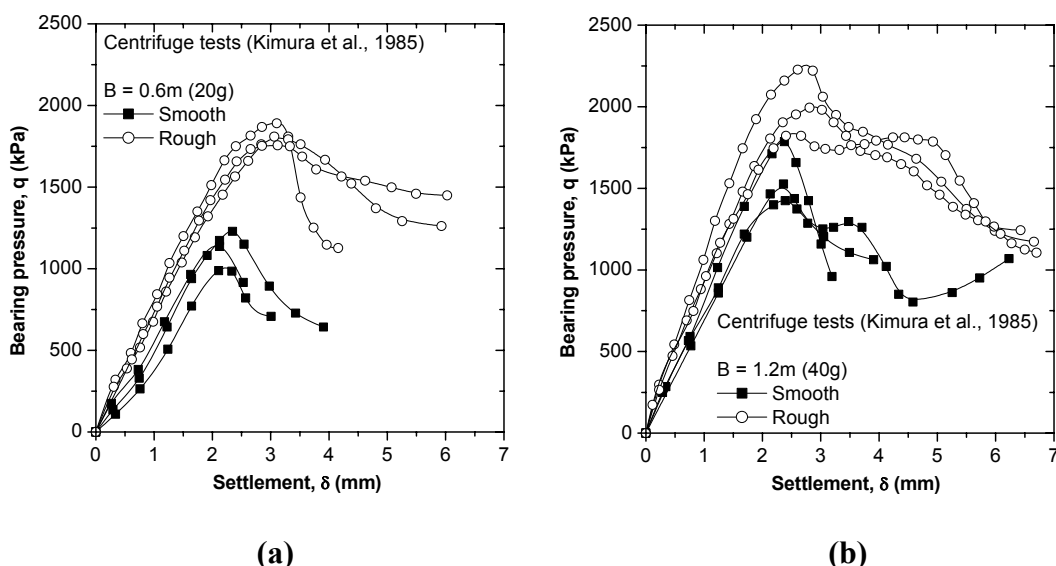
**Figure 2.10: Bearing capacity factor  $N_\gamma$  as a function of foundation size (after Cerato 2004)**



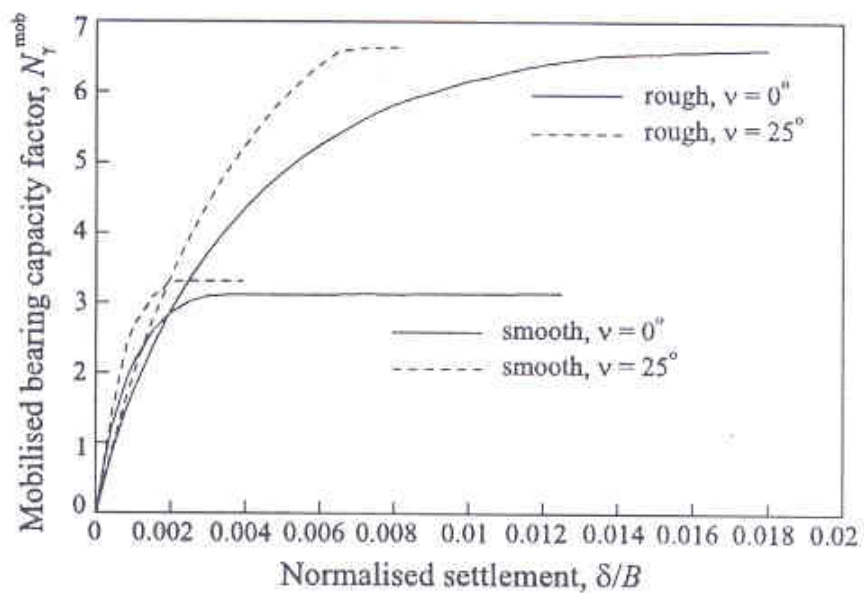
**Figure 2.11:  $N_\gamma$  versus  $B$  in terms of density effect: centrifuge tests (Kimura et al., 1985) and calculations (Hettler and Gudehus, 1988)**



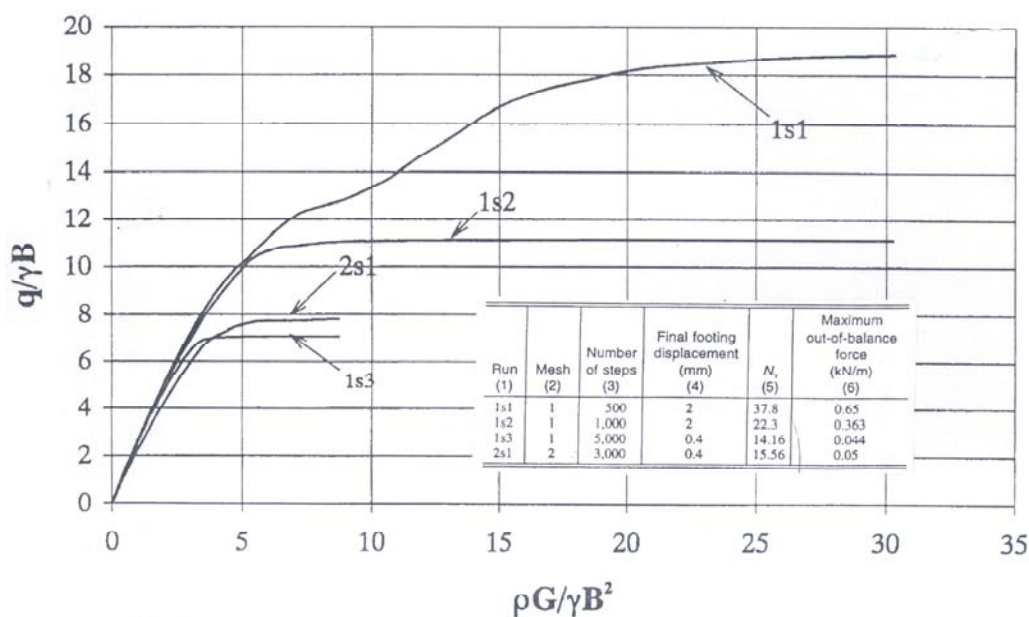
**Figure 2.12: Shear strain distribution from the centrifuge tests with the final slip lines: (a)  $B = 0.03\text{m}$ , (b)  $B=1.2\text{m}$  (Yamaguchi et al., 1976)**



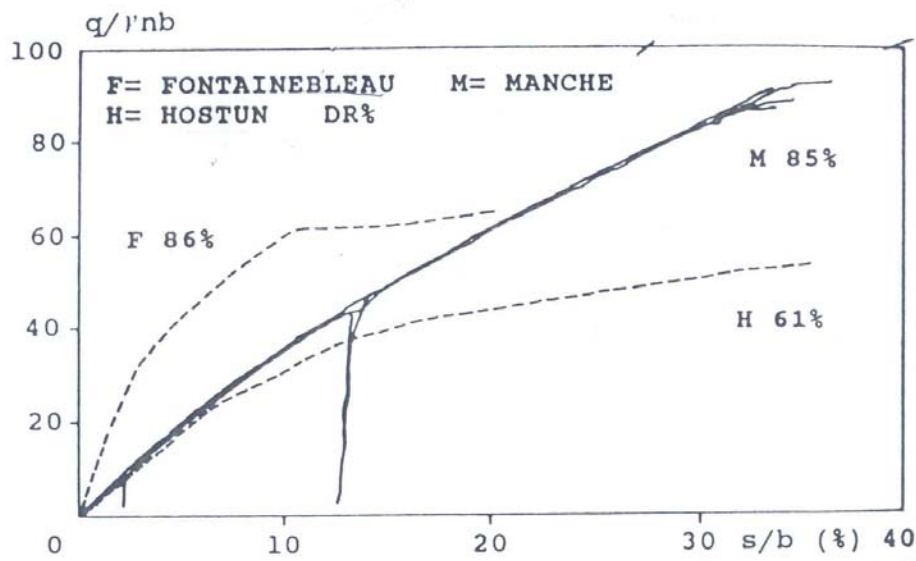
**Figure 2.13: Roughness effect of the bearing capacity in centrifuge tests: (a)  $B = 0.6\text{m}$ , (b)  $B = 1.2\text{m}$  (after Kimura et al., 1985)**



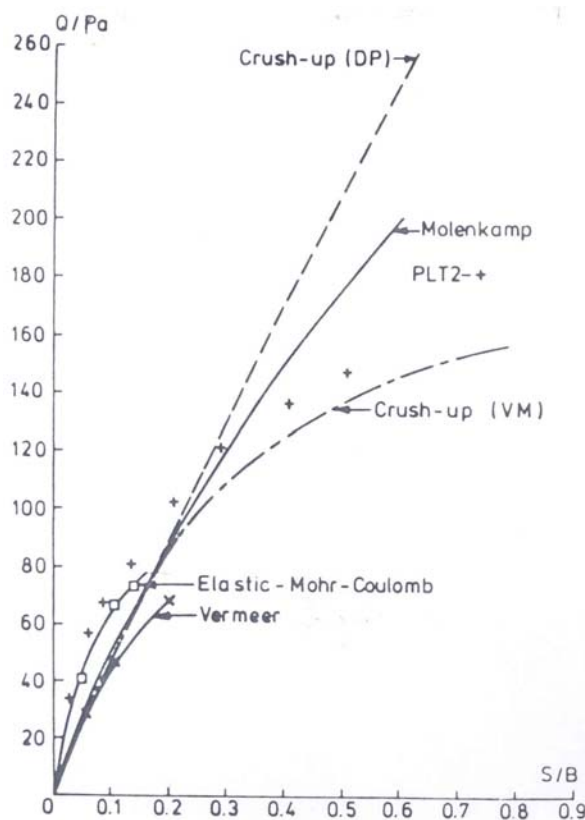
**Figure 2.14: Roughness and associativity effect of the bearing capacity factor in numerical analyses (Potts and Zdravković, 2001)**



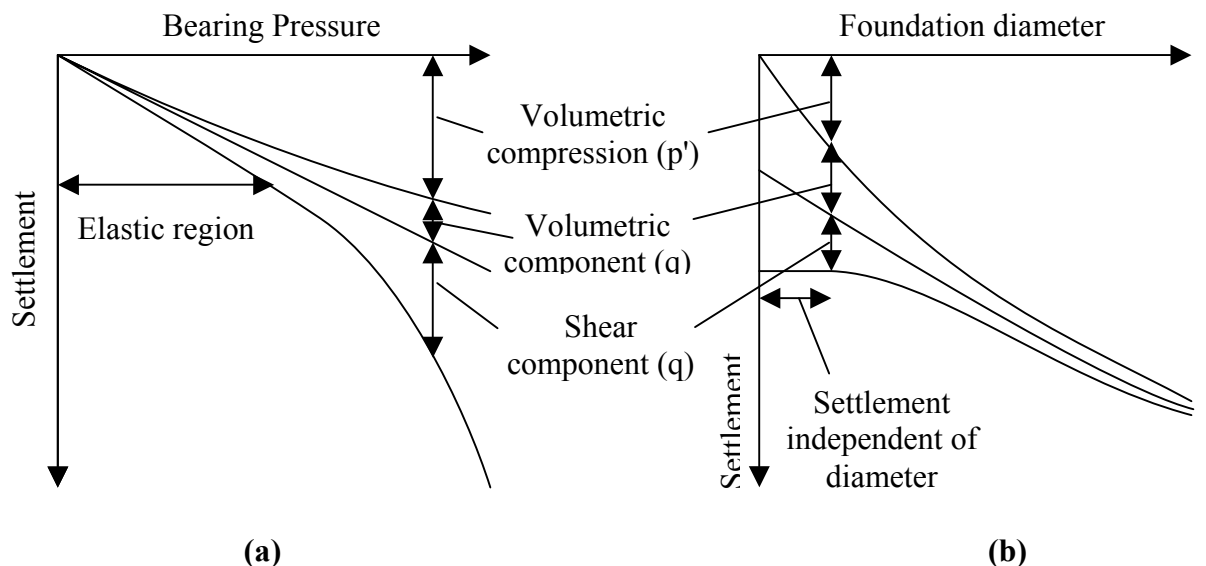
**Figure 2.15: Relationship between  $N_y$  and  $B$  in terms of FE technique effect: the number of steps and mesh geometry (1: coarse, 2: fine) (Frydman and Burd, 1997)**



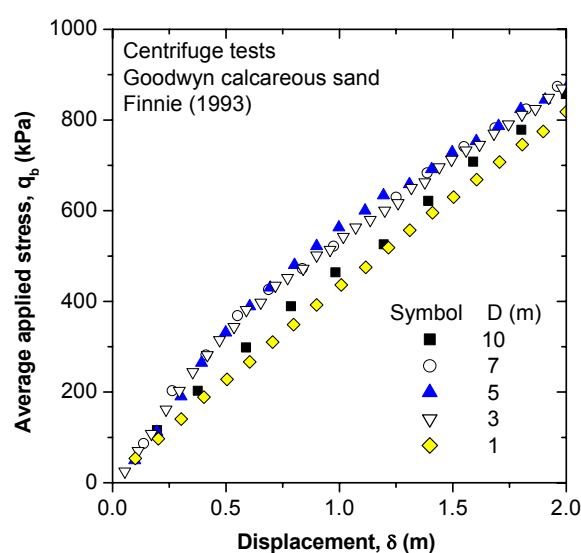
**Figure 2.16: Relationship between  $N_g$  and B in terms of different sands: siliceous (Fontainebleau, Hostun) and calcareous (Manche) (Nauroy and Golightly, 1991)**



**Figure 2.17: Predictions of 1g model test on calcareous sand by various soil models (Smith et al., 1988)**



**Figure 2.18: Components of settlement with bearing pressure and foundation diameter (after Randolph and Erbrich 2000)**



**Figure 2.19: Bearing responses of different footing diameters on calcareous sand (after Finnie 1993)**



# Chapter 3

## Determination of MIT-S1 Model Parameters for Various Soils

### 3.1 INTRODUCTION

There are a great number of constitutive models to predict the behaviour of sand, mainly focused on dilatancy driven mechanisms under shear loading. However, only a few models have managed to combine the characteristics of both dilatancy and compressibility of sands. The MIT-S1 constitutive model (Pestana, 1994; Pestana & Whittle, 1999) is an example of such a model, requiring only a single set of material parameters to model sand response over a wide range of density and confining stress. Subsequently, Pestana et al. (1994, 2002a, 2002b) validated the MIT-S1 model against experimental results for both sands and clays. Although the model requires an extensive experimental database for the determination of the input parameters, reasonable agreement with various laboratory experimental results has been achieved.

A brief introduction to the MIT-S1 model, formulae and the numerical implementation in the finite element code, ABAQUS, is described in the **Appendix**. For full details about the model, readers should refer to the original thesis by Pestana (1994) or the subsequent journal paper (Pestana & Whittle, 1999).

This chapter describes the determination of the MIT-S1 model parameters for various soils. Pestana (1994) (or Pestana et al. (2002a)) has described determination of the model parameters for Toyoura siliceous sand. This chapter will not describe the determination procedure for this sand. Instead, the relevant set of parameters obtained by Pestana is merely listed (**Table 3.1**). However, the determination process of the model parameters will be presented for other materials such as Goodwyn calcareous sand, Dogs Bay calcareous sand and Goodwyn calcareous silt. Finally a discussion of

the main differences between the parameters obtained from the various soils will be given.

### **3.2 MODEL PARAMETERS**

For freshly deposited sands, The MIT-S1 model requires 13 parameters, all potentially derived from an extensive experimental database. Those parameters are:

From compression tests

- slope of the Limit Compression Curve (LCC)<sup>1</sup> in  $\ln e - \ln p'$  space:  $\rho_c$
- reference stress of the LCC at unit void ratio:  $p'_{ref}$
- the transition curvature parameter of the first loading curve:  $\theta$

From  $K_0$  compression and swelling tests

- coefficient of lateral earth pressure at rest measured on the LCC:  $K_{0NC}$
- initial Poisson's ratio at load reversal:  $\mu'_0$
- the Poisson's ratio non-linearity during unloading:  $\omega$

From shear tests with small strain measurements

- small strain stiffness parameter:  $C_b$
- small strain non-linearity parameter in shear:  $\omega_s$

From shear tests with large strain measurements

- critical state friction angle:  $\phi'_{cs}$
- geometric parameter of the yield surface:  $m$
- maximum friction angle at unit void ratio:  $\phi'_{mr}$
- constant of maximum friction angle:  $np$
- rate of evolution of anisotropy:  $\psi$

Each test must include:

1. isotropic or one-dimensional compression tests at very high confining pressures reaching to the LCC ( $> 10$  MPa);
2. a high pressure  $K_0$  compression test with swelling from the LCC;

---

<sup>1</sup> The Limit Compression Curve is suggested to represent a unique void ratio-effective stress state in which all freshly deposited samples converge to, as proposed by Pestana (1994). Further details about this curve are given in the **Appendix**.

3. shear wave velocity measurements for defining the maximum elastic shear modulus,  $G_{\max}$ . This may also be obtained from resonant column tests as well as triaxial tests with local strain;
4. undrained and drained shear tests over a wide range of stresses and densities. The data also requires (at relatively large strains, >20 %) that the critical state is reached.

The database that satisfies the above requirements has been gradually increased over the years following an enormous effort to establish it for various soils using advanced equipment and measurement (e.g. Miura and Yamanouchi, 1975; Ishihara, 1993; Cuccovillo and Coop, 1997; Jovicic and Coop, 2000; Ismail, 2000; Sharma, 2004). This information will be used in the following to establish the MIT-S1 model parameters.

### 3.3 MODEL PREDICTIONS FOR GOODWYN CALCAREOUS SAND

Goodwyn sand is selected as a representative calcareous sand, partly because of the existence of sufficient laboratory test database (Ismail, 2000; Sharma; 2004), but also because it has direct applicability to offshore design on the North-West Shelf of Australia (where the Goodwyn ‘A’ platform is located). The main properties of Goodwyn sand are listed in **Table 3.2**. The grain size distribution reported by Finnie (1993) is shown in **Figure 3.1**.

#### 3.3.1 Compression parameters ( $\rho_c$ , $p'_{ref}$ , $\theta$ )

Finnie (1993) reports a one-dimensional compression test of uncemented Goodwyn calcareous sand, taken up to only 500 kPa, which was not enough to reach the LCC state. In order to demonstrate this, the isotropic compression curve of the same material, this time with sufficiently high pressure (Ismail (2000)), is plotted together in **Figure 3.2**. In this case,  $K_0 = 0.49$  measured by Ismail (2000), which described in the later section, is used for the 1-D compression test result plotting the equivalent effective stress. For the compression prediction, the required parameters are  $C_b$ ,  $\rho_c$ ,  $p'_{ref}$ , and  $\theta$ . Pestana (1994) suggested that the small strain stiffness parameter,  $C_b$ , should, if available, be obtained from undrained triaxial tests with small strain measurements or resonant column tests,

---

as will be described in the next subsection. The computed result for hydrostatic compression agrees with the measured data when the parameters are  $C_b = 450$ ,  $\rho_c = 0.35$ ,  $p'_{ref} = 5000$  kPa, and  $\theta = 0.9$ . However, this parameter set does not show a good prediction for the one-dimensional result, where a revised  $p'_{ref} = 2500$  kPa is needed. This predictive difference may be associated with some spatial variability within the calcareous samples. The two values of  $p'_{ref}$ , 2500 kPa and 5000 kPa, are both used later in evaluating further triaxial shear and shallow foundation tests. It will be shown, however, that the smaller  $p'_{ref}$  value appears to be a more reasonable value to use in analysing shallow foundation results performed by Finnie (1993).

### 3.3.2 Small strain parameters ( $C_b$ , $\omega_s$ )

Pestana and Whittle (1995) recommended that the  $C_b$  value should be estimated using the small strain elastic shear modulus,  $G_{max}$ . Small strain measurement systems, e.g. electro-level gauges (Jardine et al., 1984), local deformation transducers (LDTs) (Goto, et al., 1991), and linearly varying differential transducers (LVDTs) (Cuccovillo and Coop, 1997), have been extensively used in the past in the laboratory for deriving  $G_{max}$ . Based on such experiments and in-situ shear wave propagation tests, various empirical expressions for  $G_{max}$  have been proposed (e.g. Jamiolkowski et al., 1994; Shibuya and Tanaka, 1996; Shibuya et al., 1997). As an example, Jamiolkowski et al. (1994) give the following expression:

$$G_{max} = Af(e)\sigma_r^{(1-nv-nh)}\sigma_v^{nv}\sigma_h^{nh} \quad (3.1)$$

where  $A$  is a material constant,  $\sigma_r$  is a reference stress (1 kPa),  $\sigma_v$  and  $\sigma_h$  are vertical and horizontal effective stresses and  $nv$  and  $nh$  are vertical and horizontal exponents. This equation suggests that  $G_{max}$  is dependent upon the void ratio, the confining pressure and the coefficient of lateral earth pressure at rest,  $K_0$ . The MIT-S1 model, on the other hand, is based on an alternative expression for  $G_{max}$  as a function of void ratio, confining pressure, Poisson's ratio and  $C_b$  according to:

$$\frac{G_{max}}{P_a} = \frac{3}{2} C_b \left( \frac{1+e}{e} \right) \left( \frac{1-2\mu'_0}{1+\mu'_0} \right) \left( \frac{p'}{P_a} \right)^{1/3} \quad (3.2)$$

where  $C_b$  replaces the constant  $A$  of **Equation 3.1**. For Goodwyn sand, Sharma (2004) performed a triaxial isotropic undrained test with internal LVDT measurements. The initial pre-shear void ratio was 1.27, the initial confining stress was 200 kPa and the measured  $G_{max}$  was 88.7 MPa. A value of  $C_b = 450$  is achieved from **Equation 3.2** with an initial Poisson's ratio of 0.15 for Goodwyn sand, as obtained in the next subsection. Pestana and Whittle (1995) reported typical values of  $C_b$  as  $450 \pm 50$  for low plasticity clays, and as  $800 \pm 100$  for clean uniform sands. **Figure 3.3** shows the secant shear modulus degradation against the shear strain and the stress-strain responses for various  $C_b$  in the range of 400 to 500. This shows that the initial stiffness level of Goodwyn calcareous sand is in the range of low plasticity clays.

The parameter  $\omega_s$  controls the degradation of  $G$  at small strain level. **Figure 3.4** shows the model predictions of  $G-\epsilon_s$  and  $q-\epsilon_s$  relationships for Goodwyn sand with  $\omega_s = 1, 3, 5$ . It is observed that varying  $\omega_s$  does not affect  $G_{max}$  but affects the shape of the degradation curve of the shear modulus. The result for  $\omega_s = 1$  is quite close to the measured degradation curve but slightly overestimates the stress strain curve. Thus, a value of  $\omega_s = 3$  is chosen for Goodwyn sand.

### 3.3.3 $K_0$ and swelling parameters ( $K_{0NC}$ , $\mu'_0$ , $\omega$ )

The  $K_{0NC}$  is obtained from  $K_0$ -consolidation tests in a triaxial apparatus with applying pressure up to the LCC regime. Ismail (2000) performed a triaxial  $K_0$ -consolidation test up to 670 kPa and obtained  $K_{0NC} = 0.49$  for Goodwyn sand. The same value was obtained from preliminary investigations in the Goodwyn 'A' project (W.O.P., 1988).

In the MIT-S1 model, the parameters  $\mu'_0$  and  $\omega$  describe the tangential slope along an unloading effective stress path and its degree of non-linearity, respectively. The  $K_0$  is given as a function of  $K_{0NC}$ ,  $\mu'_0$  and  $\omega$  (Pestana, 1994), by:

$$K_0 = K_{0NC} \text{OCR} - \left( \frac{9\mu'_0 + \omega(1 + \mu'_0)\xi_s}{9(1 - \mu'_0) + \omega(1 + \mu'_0)\xi_s} \right) (\text{OCR} - 1) \quad (3.3)$$

where

$$\xi_s = \frac{3\sqrt{6}(K_0 - K_{0NC})}{(1 + 2K_{0NC})(1 + 2K_0)} \quad (3.4)$$

**Figure 3.5** shows a triaxial  $K_0$  unloading test result for uncemented North Rankin sand plotted on normalised vertical and horizontal effective stress (Huang, 1994)<sup>1</sup>. The initial dry unit weight of the specimen was 13 kN/m<sup>3</sup>. A consolidation pressure was applied up to 20 MPa, which is sufficient pressure to reach the LCC state. From this figure, the values of  $\mu'_0$  and  $\omega$  were estimated as 0.15 and 2, respectively. It is noted that  $\mu'_0 = 0.15$  is relatively small compared to siliceous sand (e.g. 0.233 for Toyoura sand).

### 3.3.4 Shear and critical state parameters ( $\phi'_{cs}$ , $m$ , $\phi'_{mr}$ , $np$ , $\psi$ )

The shear parameters  $m$ ,  $\phi'_{mr}$ ,  $np$ , and  $\phi'_{cs}$  determine the location of the CSL in e- $p'$  space. **Figure 3.6(a)** to **3.10(a)** show the CSLs using **Equation A.37** in **Appendix** varying the parameters,  $\phi'_{cs}$ ,  $m$ ,  $\phi'_{cs}$ ,  $np$ , and  $p'_{ref}$ . They compare the analytical critical state envelope with undrained and drained triaxial tests of uncemented Goodwyn sand by Sharma (2004) and Finnie (1993). **Figure 3.6(b)** to **3.10(b)** show the effect of those parameters on the shape of yield surface. The  $\phi'_{cs}$  of 39.6° is in fact obtained from the undrained stress paths of Goodwyn sand reported by Finnie (1993), Ismail (2000) and Sharma (2004). It is found that the parameters  $\phi'_{mr}$  and  $np$  affect the shape of the CSL only at high void ratio ( $e > 1$ ), while the position of the CSL shifts along the  $p'$  axis with different  $\phi'_{cs}$  and  $m$ . The parameters do not affect the shape of the yield surface, except the parameter  $m$ . Input parameters  $m = 0.35$ ,  $\phi'_{cs} = 60.0^\circ$ , and  $np = 2$  for Goodwyn sand are obtained.

Moreover, as discussed in the context of the compression parameters and based on Finnie (1993) results,  $p'_{ref}$  should be selected as 2500 kPa rather than 5000 kPa. **Figure 3.10** shows the effect of  $p'_{ref}$  on the CSL and the LCC. As seen in **Figure 3.10(a)**, the CSL calculated by  $p'_{ref} = 2500$  kPa is shifted towards the lower pressure side. This aspect agrees well with two critical state results (black square dots) that were obtained from triaxial tests by Finnie (1993).

---

<sup>1</sup> Triaxial  $K_0$  unloading test for Goodwyn sand was not found. Although the  $K_{0NC}$  value for North Rankin sand was measured as 0.42, it should not affect determination of the parameters,  $\mu'_0$  and  $\omega$ .

Finally, the parameter  $\psi$  controls the rate of rotation of the yield surface. **Figure 3.11** shows model predictions with the measured behaviour of a CIU test on a medium dense Goodwyn sand with  $e_0 = 1.67$  and  $p'_0 = 200$  kPa (Sharma, 2004). The stress-strain behaviour in the range of  $0.2\% \leq \varepsilon_s \leq 20\%$  is significantly affected by the rotation rate parameter. All the predictions result in initial peaks at  $\varepsilon_s = 2\%$  followed by strain softening then strain hardening until reaching critical state conditions at around  $\varepsilon_s = 20\%$ . The prediction based on  $\psi = 50$  is deemed closest to the experimental results and has therefore been chosen to represent the Goodwyn sand in the following analysis.

### 3.3.5 Prediction for triaxial isotropic undrained shear tests

Sharma (2004) reported a series of CIU tests on uncemented Goodwyn calcareous sand at confining pressures ranging from 50 to 600 kPa, and at various density from loose ( $\gamma_{dry} = 8.83$  kN/m<sup>3</sup>) to dense ( $\gamma_{dry} = 10.8$  kN/m<sup>3</sup>). **Figures 3.12** and **3.13** compare the model predictions against the results from the CIU tests for loose and dense Goodwyn samples, respectively. The model agrees reasonably with the measured undrained stress paths but not with the stress-strain curves. In **Figures 3.11(a)** to **3.15(a)** the critical state of calcareous sand samples is not unique. However, the MIT-S1 model is based on a unique CSL which may explain why it is difficult to attain precise predictions of both the peak and the critical state for calcareous samples.

**Figure 3.14** shows a CIU test performed by Finnie (1993) and presents the model predictions using two different  $p'_{ref}$  values of 2500 kPa and 5000 kPa. Neither of the calculations is in agreement with the experimental data which shows much stronger dilation induced negative pore pressures at low stress level. The present study is mainly concerned with the drained behaviour of calcareous sand. Thus, although the ability of the model to predict undrained behaviour is important, greater emphasis is placed here on fitting results for drained conditions.

### 3.3.6 Predictions for triaxial isotropic drained shear tests

Sharma (2004) reported two CID tests on uncemented Goodwyn calcareous sand at confining pressures of 50 and 200 kPa with corresponding pre-shear void ratios of 1.44

and 1.42 as shown in **Figure 3.15**. Finnie (1993) also conducted a CID test on Goodwyn sand at a confining pressure of 100 kPa and a pre-shear void ratio of 1.1 as shown in **Figure 3.16**. The model agrees reasonably with the measured stress-strain curves, though always underestimating the extent of the volumetric strain. The volumetric strain for all the samples remains positive due to the high compressibility of calcareous materials. Tests at low confining stress (50 kPa and 100 kPa) show a slight volumetric strain reduction (dilative behaviour) at large shear strain. **Figure 3.16** shows an additional prediction using  $p'_{\text{ref}} = 2500$  kPa. It is found that while the stress-strain curve decreases, the volumetric strain - shear strain result increases with decreasing  $p'_{\text{ref}}$  value.

### 3.3.7 Summary

**Table 3.1** summarises the selected MIT-S1 model parameters for Goodwyn calcareous sand and for Toyoura siliceous sand. Significant differences in the parameters are noticed compared to the Toyoura siliceous sand parameters.

Firstly, in the shear parameters, the Goodwyn sand shows higher friction angles,  $\phi_{\text{cs}}$  and  $\phi'_{\text{mr}}$ , than the siliceous sand. In the conventional bearing capacity analysis, as the friction angle is higher, the bearing capacity would increase. However, the physical model tests in **Figure 2.8** reveal that the bearing response for Goodwyn sand is much softer than that for Toyoura sand. Such inconsistency may be perpetuated by finite element analyses using constitutive models that are solely dependent on the friction angle (e.g. the Mohr-Coulomb model).

Secondly, in the compression parameters, change in the  $p'_{\text{ref}}$  and  $\theta$  values affects significantly the behaviour. In particular,  $p'_{\text{ref}}$  is the key parameter in defining the material stiffness. The smaller value of  $p'_{\text{ref}}$  for Goodwyn sand shifts the LCC and the CSL towards lower stress levels. The larger  $p'_{\text{ref}}$  value for Toyoura sand leads to higher shear stress required to reach the CSL, especially when samples are dense. The parameter  $\theta$  that represents the curvature of the virgin compression line is also responsible for changing the material stiffness. In shallow foundation analysis, the compression parameters that relate to softer material response (low  $p'_{\text{ref}}$ , high  $\theta$ , low  $C_b$ ) are expected to reduce the bearing response. This aspect will be discussed in the next chapter.

### 3.4 MODEL PREDICTIONS FOR DOGS BAY CALCAREOUS SAND

Another calcareous sand, Dogs Bay sand, from the west of the Republic of Ireland, will be analysed in this thesis. A large database is available due to the extensive experimental programme conducted for understanding the behaviour of frictional piles in calcareous soils by Coop and co-authors (Coop, 1990; Coop and Lee, 1993; Jovicic and Coop, 1997; Coop, 2000; Coop and Airey, 2003). They include not only various types of laboratory tests such as hydrostatic and  $K_0$  compression tests, CIU, CID and constant  $p'$  tests (CPD), but also physical model tests on driven piles (Klotz and Coop, 2001). The index properties of Dogs Bay sand are summarised in **Table 3.2** and a typical grain size distribution is shown in **Figure 3.1**. As is seen the distribution is poorly graded ( $C_u = 2.06$ ) with higher mean size of grain than the Toyoura sand.

#### 3.4.1 Compression parameters ( $\rho_c$ , $p'_{ref}$ , $\theta$ )

Several hydrostatic and 1-D compression tests for Dogs Bay sand were carried out by Coop (1990). The initial void ratios were around 1.6 to 1.7 and confining pressures were applied up to 10 MPa. **Figure 3.17** shows the MIT-S1 model simulations of hydrostatic compression curves together with the measurements. The computed results are in good agreement with the measured compression behaviour over a wide range of densities. The compression parameters are chosen as  $\rho_c = 0.35$ ,  $p'_{ref} = 4000$  kPa, and  $\theta = 0.4$ . Note that the parameter  $\theta$  is slightly higher (due to the stiffer response) than that for Goodwyn sand. This is probably associated with a poorly graded grain size distribution (low fine grain content).

#### 3.4.2 Small strain parameters ( $C_b$ , $\omega_s$ )

Jovicic and Coop (1997) conducted CIU tests on compacted Dogs Bay sand for measurement of  $G_{max}$  using LVDTs. Void ratios were not reported, thus the pre-shear void ratios were selected from the MIT-S1 compression prediction. **Table 3.3** summarises the  $G_{max}$  values obtained from **Equation 3.2** using Poisson's ratio  $\mu'_0$  of 0.2. The calculated  $G_{max}$  values using  $C_b = 750$  are in relatively good agreement for samples with low confining pressure, but underestimate the measured value from the high

confining pressure sample (650 kPa). By contrast, the  $G_{\max}$  prediction using  $C_b = 1000$  is closer to the data for the highest confining stress, whereas the rest of the results are highly overestimated.

**Figure 3.18** and **3.19** show the predictions of shear modulus degradation curves with  $C_b$  of 750 and 1000, respectively. Neither set of predicted curves agrees well with the measurements.  $C_b = 750$  and  $\omega_s = 2.5$ , which are the same as for the Toyoura sand, are chosen for the small strain parameters for Dogs Bay sand, as at least the  $q - \epsilon_s$  curve is nicely predicted.

#### **3.4.3 $K_0$ and swelling parameters ( $K_{0NC}$ , $\mu'_0$ , $\omega$ )**

Coop (1990) carried out several tests of  $K_0$ -compression and determined  $K_0 = 0.51$  for Dogs Bay sand. No results for a  $K_0$  swelling test were available so parameters  $\mu'_0$  and  $\omega$  are assumed as 0.2 and 1, respectively. Those parameters are believed not to affect the drained behaviour under monotonic loading condition.

#### **3.4.4 Shear and critical state parameters ( $\phi'_{cs}$ , $m$ , $\phi'_{mr}$ , $np$ , $\psi$ )**

**Figure 3.20** shows undrained stress paths for Dogs Bay sand after Coop (1990). Coop defined the critical state parameter,  $M$ , as 1.65, based on the envelope of points at minimum  $p'$ . This value corresponds to a critical state friction angle,  $\phi'_{cs}$  of  $40^\circ$ . However the submerged undrained stress paths all lie beyond this CSL. The value of  $46^\circ$ , which corresponds to the maximum stress ratio, is, therefore, chosen as an alternative  $\phi'_{cs}$  value for Dogs Bay sand.

The shear parameters,  $m$ ,  $\phi'_{mr}$ ,  $np$  and  $\phi'_{cs}$  are defined from the measured critical state envelope for Dogs Bay sand in an  $e$ - $\ln p'$  plot. **Figure 3.21** shows the MIT-S1 model CSLs using two different  $\phi'_{cs}$  values of  $40^\circ$  and  $46^\circ$ . The parameters are  $m = 0.5$ ,  $\phi'_{mr} = 60^\circ$ ,  $np = 2$ , for  $\phi'_{cs} = 40^\circ$  and  $m = 0.55$ ,  $\phi'_{mr} = 80^\circ$ ,  $np = 2$ , for  $\phi'_{cs} = 46^\circ$ . Because of the strong scatter in the results constituting the CSL, it is possible that the entire concept of a unique CSL for calcareous sand should be questioned. However, for practical purposes and since the MIT-S1 model requires it, this dilemma is ignored in the following.

**Figure 3.22** compares model predictions using different values of the parameter  $\psi$  to the measured CIU test on Dogs Bay sand ( $e_0 = 1.47$  and  $p'_0 = 500$  kPa).  $\psi = 50$  seems to yield the best agreement with the measurements. It is also noted that high  $\psi$  induces a smaller peak of the pore water pressure.

#### 3.4.5 Prediction for triaxial isotropic undrained shear tests

The following prediction is based on results from low stress ( $p' = 500$  kPa) and high stress ( $p' = 7422$  kPa) tests which were performed by Coop (1990). With respect to the low stress test in **Figure 3.23**, the use of the parameter  $\phi'_{cs} = 40^\circ$  slightly underestimates the measured shear stress. However, the predictions using the value  $\phi'_{cs} = 46^\circ$  give better agreement. In regard to the high stress test in **Figure 3.24**, however, either of the parameter values leads to an overestimation of the peak stress and underestimation of the pore pressure development.

Both parameters are also evaluated against results from experimental undrained stress paths (Coop, 1990). **Figure 3.25** shows the MIT-S1 predictions using  $\phi'_{cs} = (a) 40^\circ$  and (b)  $46^\circ$  parameter sets with comparison to five CIU test results. The calculated results using a value of  $\phi'_{cs} = 40^\circ$  underestimate all the measured stress paths, while those using  $\phi'_{cs} = 46^\circ$  are in fair agreement.

#### 3.4.6 Predictions for triaxial isotropic drained shear tests

**Figure 3.26** shows the model predictions for a CID test result under high confining pressure ( $p' = 4020$  kPa), based on data from Coop (1990). The predictions using both  $\phi'_{cs} = 40^\circ$  and  $46^\circ$  do not fit the measured response although the use of  $\phi'_{cs} = 46^\circ$  gives marginally better agreement.

#### 3.4.7 Prediction for $p'$ constant shear tests

Coop (1990) conducted a number of CID tests, maintaining the initial mean effective stress constant ( $p'$ -constant test). The scheme is particularly useful for investigating the dilatancy behaviour of soils with respect to the effect of shear strain component. **Figure**

**3.27** and **3.28** show two  $p'$  constant tests, one under low confining pressure ( $p' = 100$  kPa) and the other under high confining pressure ( $p' = 3286$  kPa), together with the MIT-S1 predictions based on two values of  $\phi'_{cs}$ . The low stress test shows a high initial stiffness and a negative volumetric strain development (dilative behaviour), while the higher stress test behaves with a relatively lower initial stiffness and positive volumetric strain development (contractive behaviour). In **Figure 3.27**, the prediction using a value of  $\phi'_{cs} = 40^\circ$  slightly underestimates the measured stress-strain curve, while that using  $\phi'_{cs} = 46^\circ$  is in good agreement. Neither prediction agrees with the volumetric strain measurements. In **Figure 3.28**, both of the two  $\phi'_{cs}$  values lead to underestimation of the stress-strain and the volumetric strain measurements.

#### **3.4.8 Summary**

**Table 3.1** shows the MIT-S1 model parameters for Dogs Bay calcareous sand. It is noticed that Dogs Bay sand has higher friction angles than the Toyoura siliceous sand and stiffer compression parameters than the Goodwyn calcareous sand. This suggests that the bearing response may not be reduced due to the compression parameters. Therefore, it is presumed that the load-displacement response for Dogs Bay sand would be stronger than that for Toyoura sand, simply because of the higher friction angles. In fact, physical model results in **Figure 2.8** have confirmed the stronger bearing response for Dogs Bay sand.

### **3.5 MODEL PREDICTIONS FOR GOODWYN CALCAREOUS SILT**

Finally, Goodwyn calcareous silt is chosen as the finest-grained material for analysis. It was taken from a layer immediately below the Goodwyn calcareous sand layer. The main properties of this material and the grain size distribution are shown in **Table 3.2** and **Figure 3.1**, respectively (Finnie, 1993). As seen in **Figure 3.1**, compared with the grain size distributions of typical calcareous materials, the Goodwyn silt is quite different with large fines content. It will be interesting to distinguish the effect of fines content in the context of this thesis. Laboratory tests on Gorgon calcareous silt (150 km East from the Goodwyn site) by Mao (2000) provide complementary data. The determination of the model parameters will not be discussed in detail, though key points will be mentioned.

### 3.5.1 Compression parameters ( $\rho_c$ , $p'_{ref}$ , $\theta$ )

**Figure 3.29** shows the MIT-S1 model predictions of one-dimensional compression curves and measured data for Goodwyn silt (Finnie, 1993). The final pressure in this test was insufficient for getting reliable MIT-S1 model parameters. Therefore, in a complementary manner, compression tests on Gorgon silt (Mao, 2000) will be used. The computed results are consistent with the measured compression behaviour over the wide void ratio range of the other soils. The compression parameters are selected as  $\rho_c = 0.25$ ,  $p'_{ref} = 2000$  kPa (as  $K_{0NC} = 0.45$  described later), and  $\theta = 0.9$ . The values of these parameters, compared relatively to the other materials, indicate that this is the softest material.

### 3.5.2 Small strain parameters ( $C_b$ , $\omega_s$ )

$G_{max}$  measurements using LVDTs or bender elements were not found. Therefore, the  $C_b$  is assumed to be the same as Goodwyn sand (450), which is the lowest  $C_b$  suggested by Pestana (1994). The parameter  $\omega_s$  is also assumed based on Goodwyn sand as 3.

### 3.5.3 $K_0$ and swelling parameters ( $K_{0NC}$ , $\mu'_0$ , $\omega$ )

Based on  $K_0$ -consolidation tests on Gorgon silt, Mao (2002) deduced a  $K_0$  value of 0.45. It is, however, necessary to assume the parameters  $\mu'_0$  and  $\omega$  as 0.2 and 2 because  $K_0$  unloading was not applied.

### 3.5.4 Shear and critical state parameters ( $\phi'_{cs}$ , $m$ , $\phi'_{mr}$ , $np$ , $\psi$ )

The critical state friction angle  $\phi'_{cs}$  of  $40^\circ$  is obtained from several triaxial tests on Goodwyn and Gorgon silt. The parameters,  $m$ ,  $\phi'_{mr}$  and  $np$  are defined from the critical state envelope for Gorgon and Goodwyn sands plotted on  $e$ - $Inp'$  space as shown in **Figure 3.30**. Despite the high scatter in the obtained critical state values, the parameters are defined uniquely as  $m = 0.3$ ,  $\phi'_{mr} = 72^\circ$  and  $np = 2$ . The parameter  $\psi$  was set as 50 to agree with all the previous sands introduced before.

### **3.5.5 Prediction for triaxial isotropic undrained shear tests**

Finnie (1993) carried out three CIU tests for Goodwyn silt with different levels of confining pressure. Details of stress-strain and pore pressure-strain curves of only one sample confined to 50 kPa were presented. **Figure 3.31** compares the MIT-S1 model predictions with the CIU test data. All of the computed results agree well with the undrained stress paths. The prediction slightly overestimates the pore pressure behaviour in the 50 kPa test. However, the trend of significant reduction of pore water pressure with increasing strain is in agreement with the measurement.

### **3.5.6 Summary**

**Table 3.1** lists the MIT-S1 model parameters for Goodwyn calcareous silt. It is found that the compression parameters (in particular  $p'_{ref}$ ,  $\theta$  and  $C_b$ ) of the Goodwyn sand and silt are almost identical. The MIT-S1 predictions for shallow foundations on those soils are thus expected to show similar behaviour as will be discussed in the next chapter. This aspect also agrees with the results of the physical modelling as shown in **Figure 2.8**.

## **3.6 CONCLUSIONS**

This chapter has described determination of the MIT-S1 model parameters for various soils, which will be utilised in the present thesis, using standard and advanced laboratory test data. Although Pestana (1994) (or Pestana et al. (2002a)) have described the model parameters for Toyoura siliceous sand, in this chapter parameters are determined for Goodwyn calcareous sand and silt and Dogs Bay calcareous sand. It is found that calcareous sand has much higher friction angle parameters compared with Toyoura sand. Also, Toyoura and Dogs Bay sands are defined as relatively stiff material, while the Goodwyn sand and silt are classified as softer materials with respect to the compression parameters.

Particular attention has been paid to identifying which parameters would be the most significant with respect to the present study of shallow foundation response. It is found

that primary attention should be given to the selection of the friction angles,  $\phi'_{cs}$  and  $\phi'_{mr}$ , and the compression parameters,  $p'_{ref}$  and  $\theta$ , while the remaining parameters are likely to be of secondary importance. This conclusion will be confirmed when the bearing capacity problem is analysed using the finite element method as will be described in the next chapter.

**Table 3.1 MIT-S1 model parameters for various soils**

| Test type                                 | Symbol       | Physical meaning   | Siliceous     |         | Calcareous** |         |
|---|--------------|--|---------------|---------|--------------|---------|
|   |              |  | Toyoura sand* | GW sand | DB sand      | GW silt |
| Compression test                          | $\rho_c$     | Compressibility at large stresses (LCC regime)           | 0.370         | 0.350   | 0.350        | 0.250   |
|   | $p'_{ref}$   | Reference stress at unity void ratio for the H-LCC (kPa) | 5500          | 2500    | 4000         | 2000    |
| $K_0$ consolidation test                  | $\theta$     | First loading curve transition parameter                 | 0.200         | 0.900   | 0.400        | 0.900   |
|   | $K_{0NC}$    | $K_0$ in the LCC regime                                  | 0.490         | 0.490   | 0.510        | 0.450   |
|   | $\mu'_0$     | Poisson's ratio  | 0.233         | 0.150   | 0.200        | 0.200   |
| Shear test                                | $\omega$     | Parameter for non-linear Poisson's ratio                 | 1.00          | 2.00    | 1.00         | 2.00    |
|   | $\phi_{cs}$  | Critical state friction angle (°)                        | 31.0          | 39.6    | 46.0         | 40.0    |
|   | $\phi'_{mr}$ | Peak friction angle as a function of void ratio (°)      | 28.5          | 60.0    | 80.0         | 72.0    |
|   | $n_p$        | Constant of peak friction angle                          | 2.45          | 2.00    | 2.00         | 2.00    |
| Shear test with local measurement systems | $m$          | Geometry of bounding surface                             | 0.55          | 0.35    | 0.55         | 0.30    |
|   | $\psi$       | Rate of evolution of anisotropy                          | 50.0          | 50.0    | 50.0         | 50.0    |
|   | $C_b$        | Small strain stiffness parameter                         | 750           | 450     | 750          | 450     |
|   | $\omega_s$   | Small strain non-linearity parameter                     | 2.50          | 3.00    | 2.50         | 3.0     |

\* Pestana (1994)

\*\*: GW = Goodwyn; DB = Dogs Bay

**Table 3.2: Index properties of Siliceous and Calcareous sands**

| Property                          | Siliceous                         |                               | Calcareous                    |                               |
|-----------------------------------|-----------------------------------|-------------------------------|-------------------------------|-------------------------------|
|                                   | Toyoura sand                      | Goodwyn sand                  | Dogs Bay sand                 | Goodwyn silt                  |
| Mineralogy                        | Quartz,<br>Feldspar,<br>magnetite | Calcium<br>carbonate<br>(94%) | Calcium<br>carbonate<br>(98%) | Calcium<br>carbonate<br>(94%) |
| Grain shape                       | subangular                        | Skeletal<br>grain             | Skeletal<br>grain             | Skeletal<br>grain             |
| Specific Gravity, $G_s$           | 2.65                              | 2.72                          | 2.75                          | 2.77                          |
| Mean particle size, $D_{50}$ (mm) | 0.16-0.20                         | 0.1-0.2                       | 0.2                           | 0.03                          |
| Coefficient of uniformity, $C_u$  | 1.3-1.7                           | 10-15                         | 2.06                          | 45                            |
| Maximum void ratio, $e_{max}$     | 0.98                              | 2.32-1.97                     | 2.21-1.83                     | 2.40                          |
| Minimum void ratio, $e_{min}$     | 0.61-0.58                         | 1.41-0.94                     | 1.48-0.98                     | 1.21                          |

Reference:

Toyoura sand: Miura et al (1984); Ishihara (1993)

Goodwyn sand: Finnie and Randolph (1994); Ismail (2000); Sharma (2004)

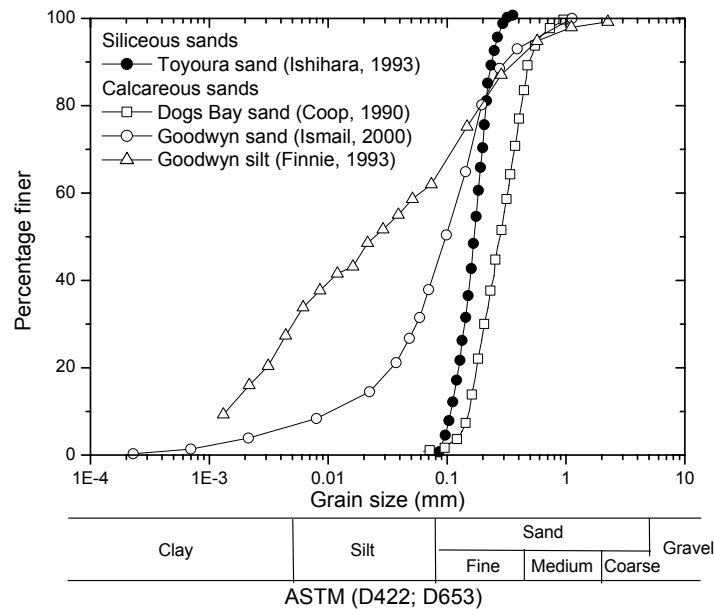
Dogs Bay sand: Golightly and Hyde (1988); Houlsby et al (1988); Coop and Lee (1993)

Goodwyn silt: Finnie and Randolph (1994)

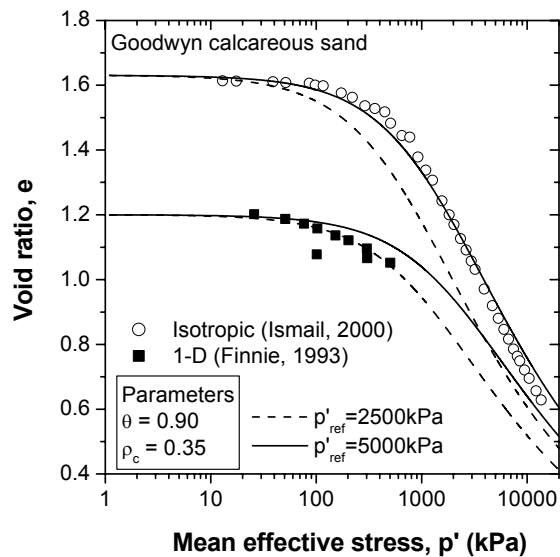
**Table 3.3:  $G_{max}$  predictions for Dogs Bay sand**

| p'<br>(kPa) | e*   | Measured | $G_{max}$ (MPa) |             |              |
|-------------|------|----------|-----------------|-------------|--------------|
|             |      |          | Equation 3.2    |             |              |
|             |      |          | $C_b = 500$     | $C_b = 750$ | $C_b = 1000$ |
| 63          | 1.46 | 73.1     | 54.2            | 81.2        | 108          |
| 150         | 1.44 | 112      | 72.7            | 109         | 146          |
| 250         | 1.42 | 137      | 86.7            | 130         | 174          |
| 650         | 1.36 | 278      | 121             | 182         | 243          |

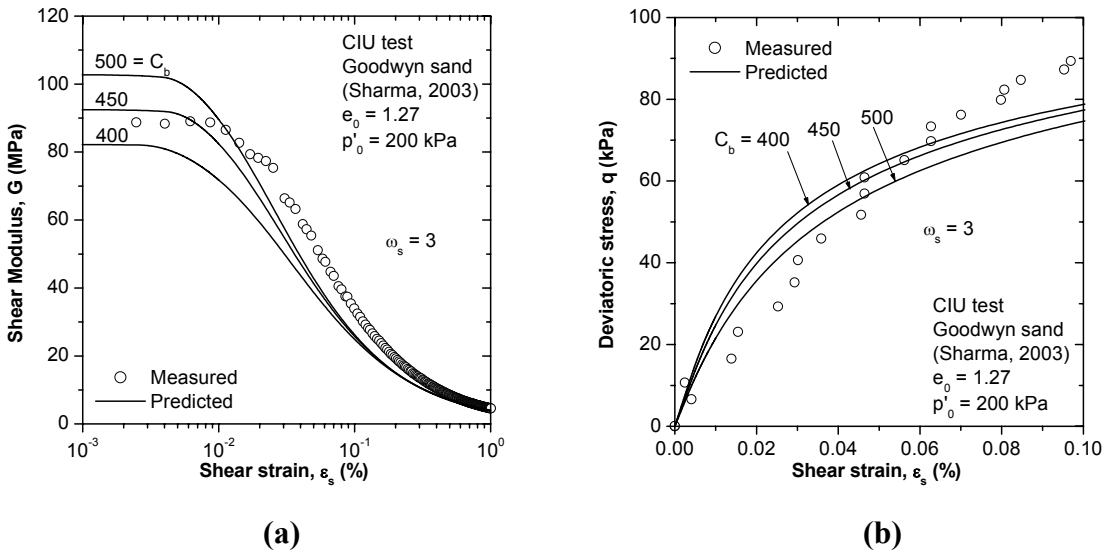
\* void ratio is obtained from MIT-S1 compression model



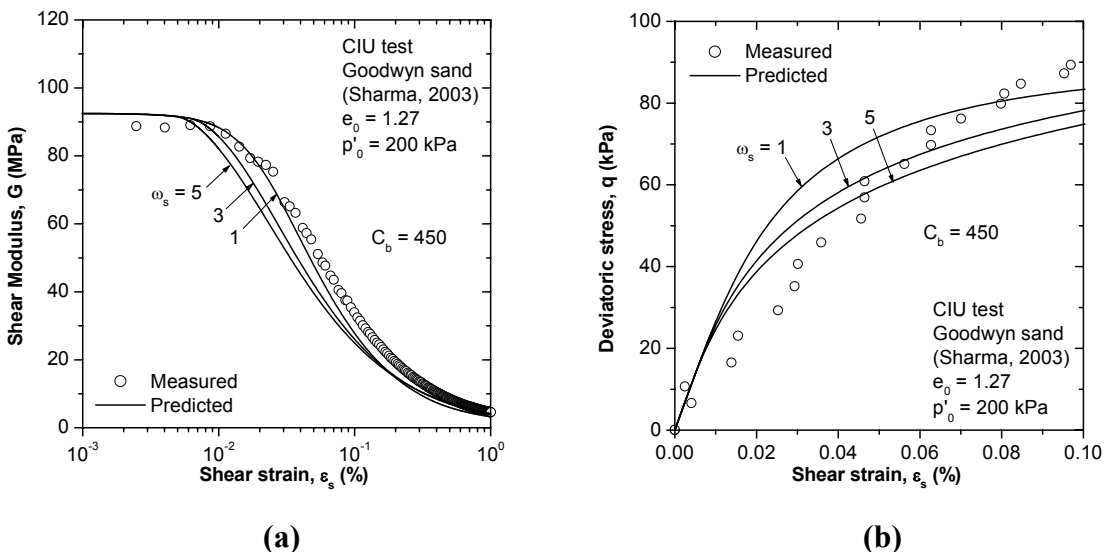
**Figure 3.1: Grain size distribution for various soils**



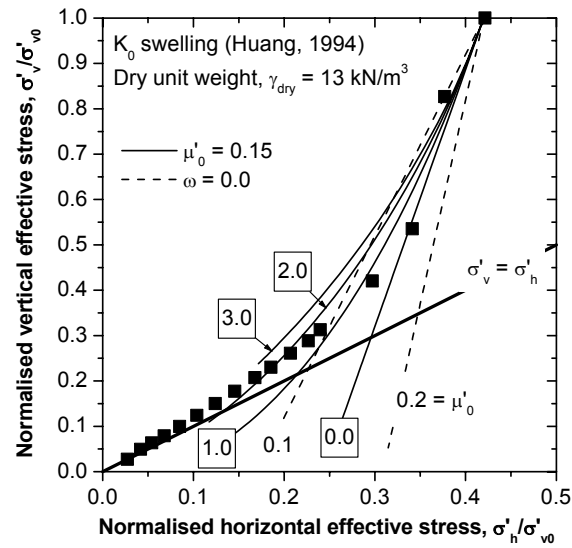
**Figure 3.2: Compression tests for Goodwyn calcareous sand**



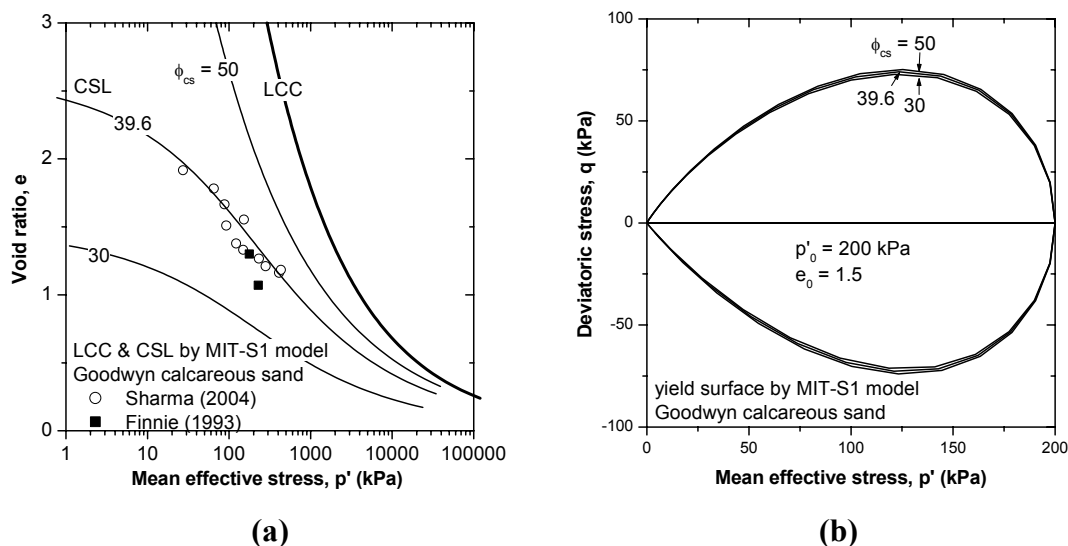
**Figure 3.3: Estimation of MIT-S1 model parameter  $C_b$  from small strain measurement of undrained shear test for Goodwyn calcareous sand ( $e_0 = 1.27$ ,  $p'_0 = 200$  kPa)**



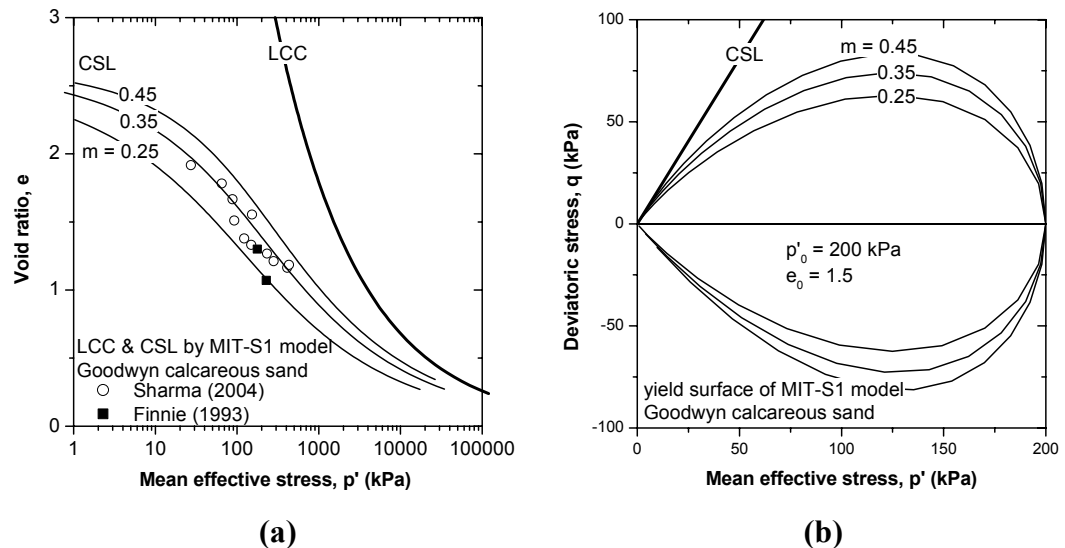
**Figure 3.4: Estimation of MIT-S1 model parameter  $\omega_s$  from small strain measurement of undrained shear test for Goodwyn calcareous sand ( $e_0 = 1.27$ ,  $p'_0 = 200$  kPa)**



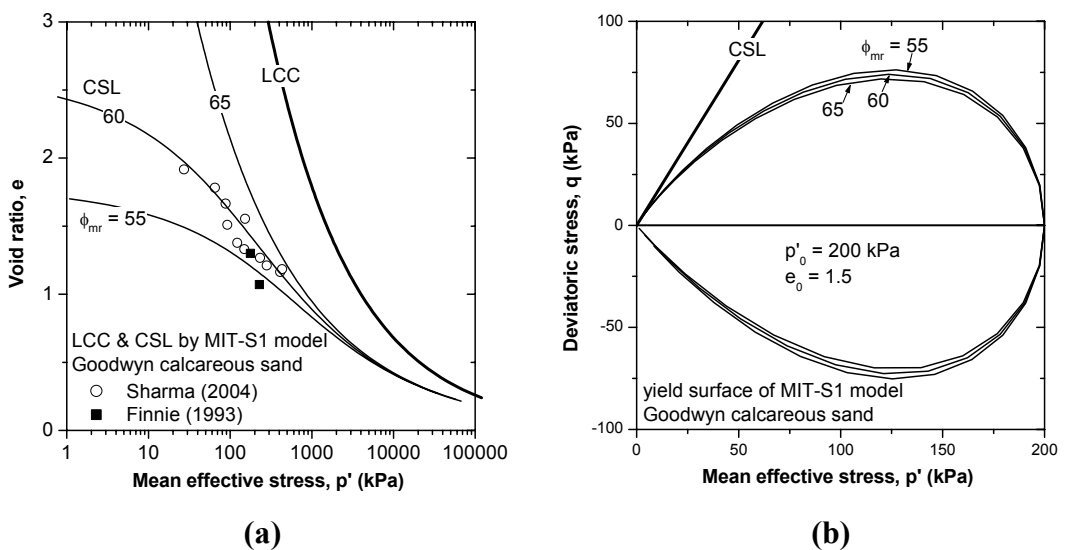
**Figure 3.5: Estimation of MIT-S1 model parameter  $\mu'_0$  and  $\omega$  from  $K_0$  unloading test of North Rankin calcareous sand (Huang, 1994)**



**Figure 3.6: Estimation of MIT-S1 model parameter  $\phi_{cs}$  for Goodwyn calcareous sand: (a) CSL, (b) yield surface**



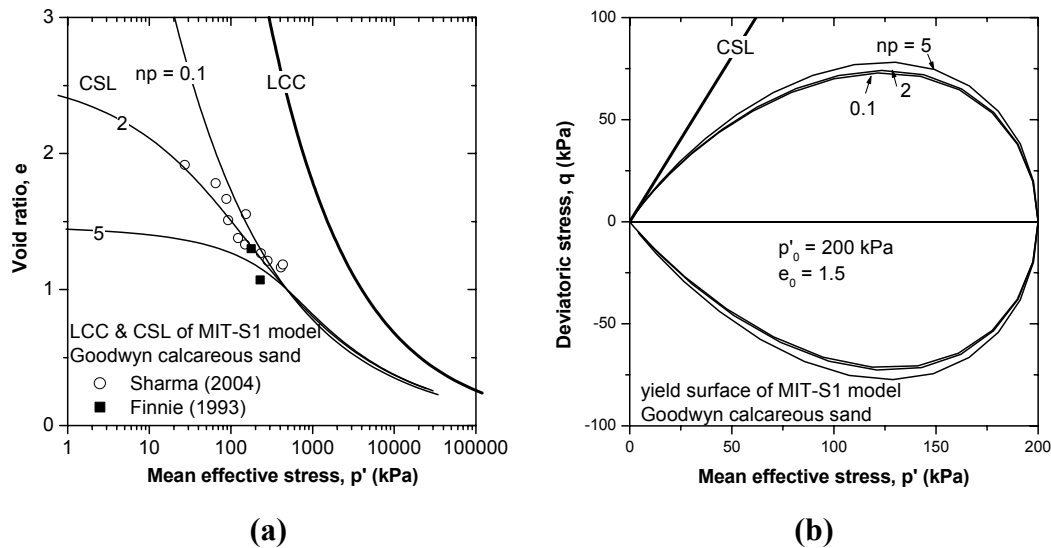
**Figure 3.7: Estimation of MIT-S1 model parameter  $m$  for Goodwyn calcareous sand: (a) CSL, (b) yield surface**



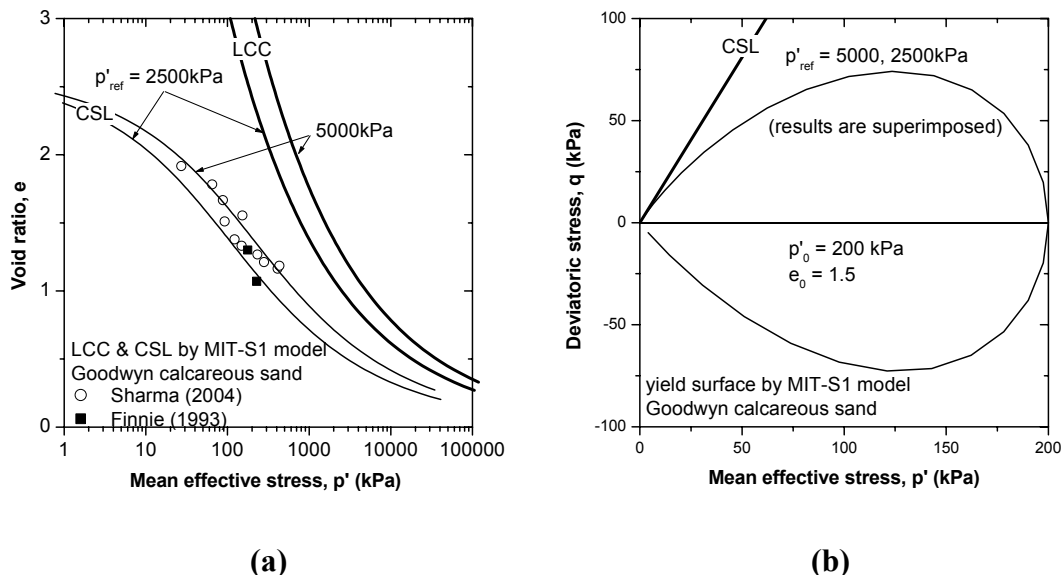
**Figure 3.8: Estimation of MIT-S1 model parameter  $\phi'_{mr}$  for Goodwyn calcareous sand: (a) CSL, (b) yield surface**

### 3. MIT-S1 model parameters

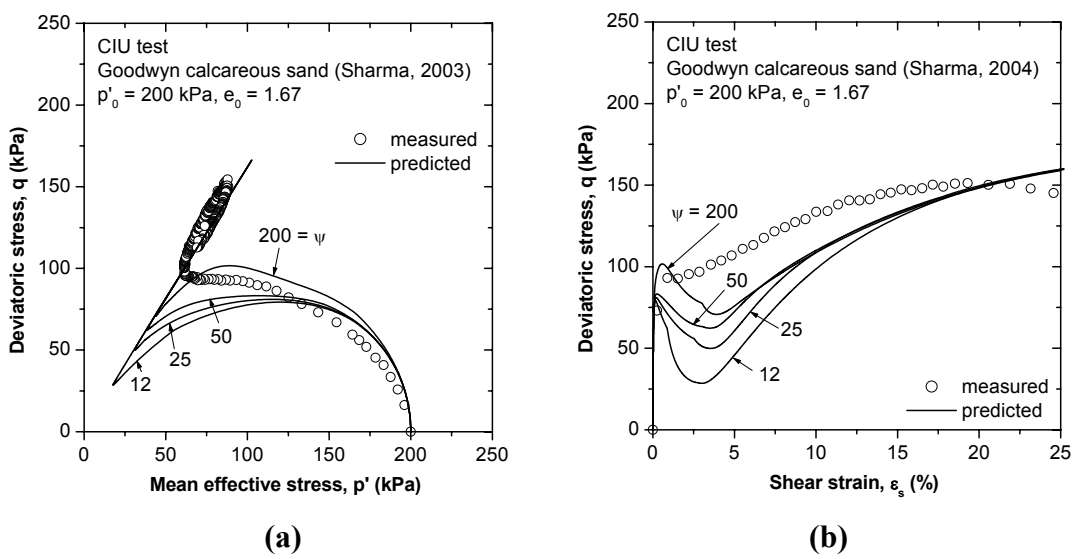
---



**Figure 3.9: Estimation of MIT-S1 model parameter  $np$  for Goodwyn calcareous sand: (a) CSL, (b) yield surface**



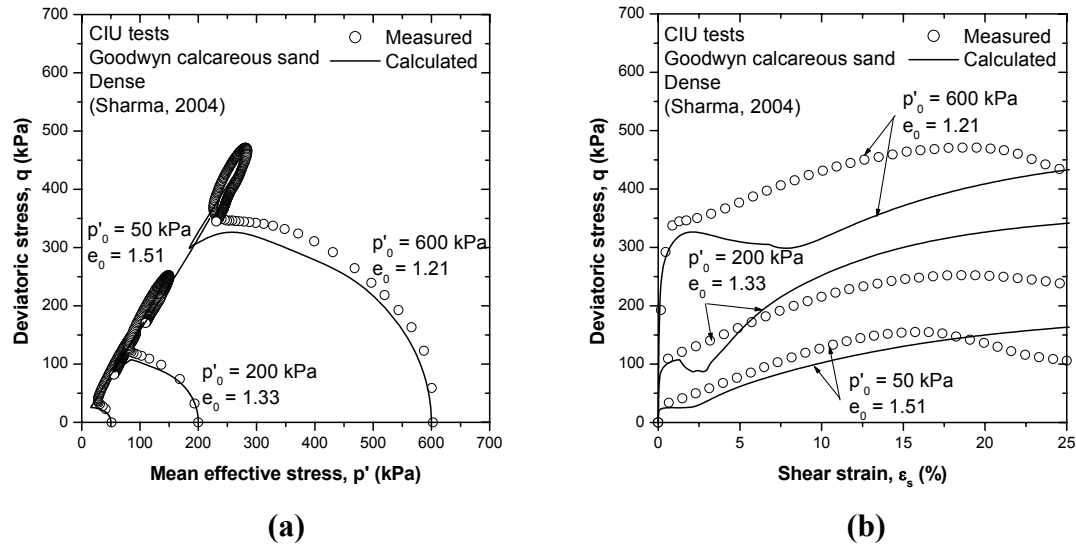
**Figure 3.10: Estimation of MIT-S1 model parameter  $p'_{ref}$  for Goodwyn calcareous sand: (a) CSL, (b) yield surface**



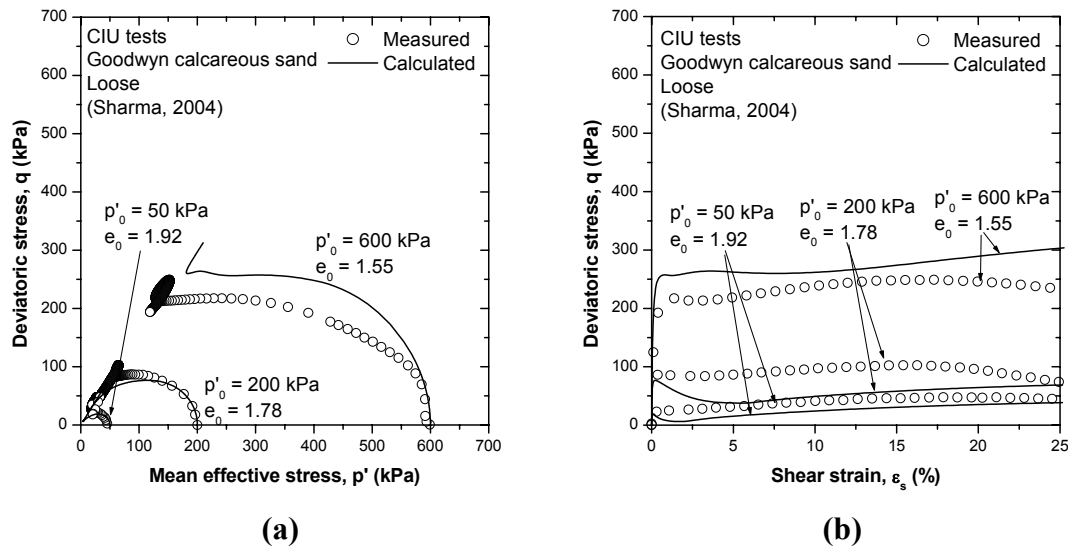
**Figure 3.11: Estimation of MIT-S1 model parameter  $\psi$  from undrained test for Goodwyn calcareous sand**

### 3. MIT-S1 model parameters

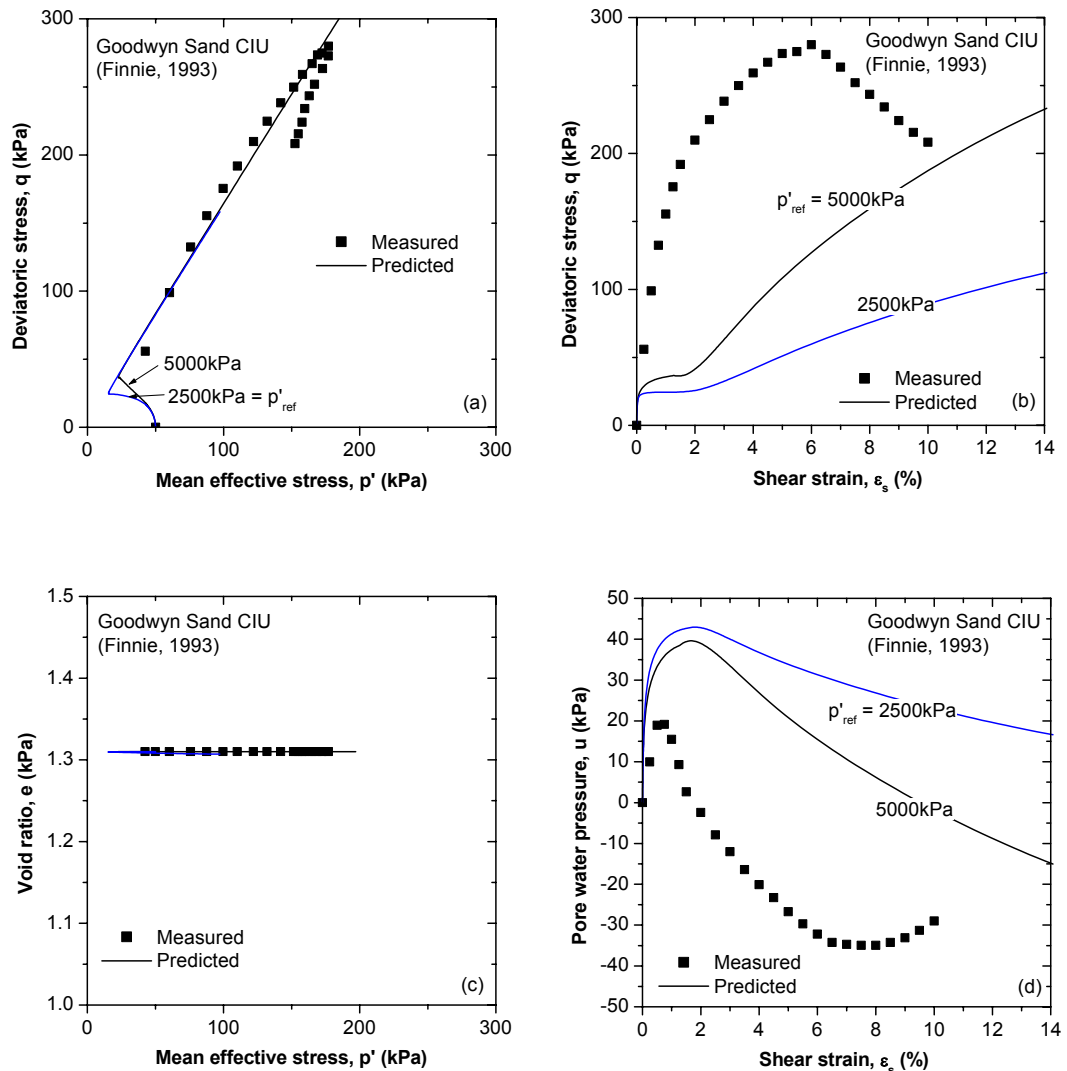
---



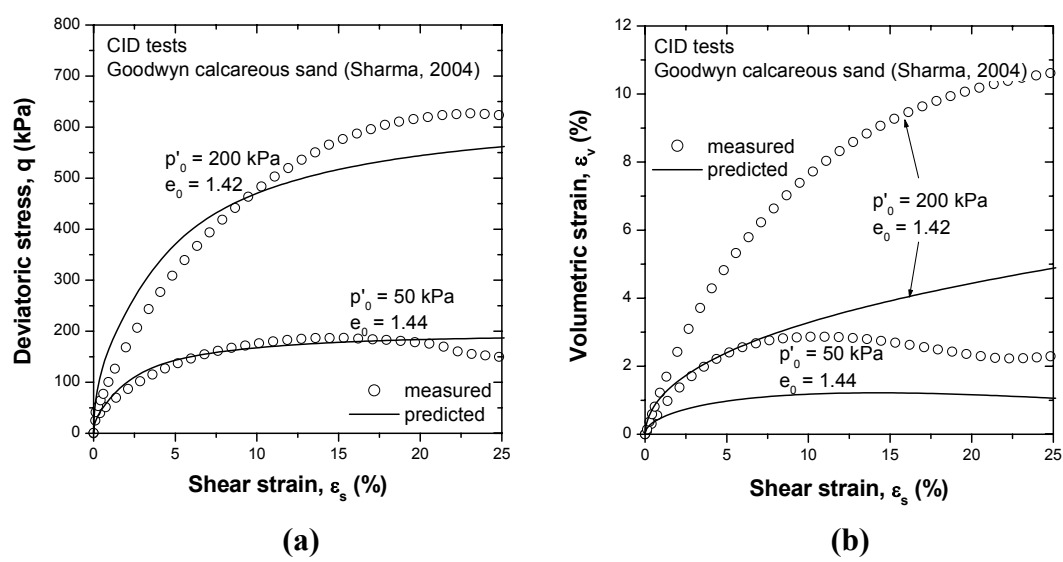
**Figure 3.12: MIT-S1 model predictions for CIU tests of dense Goodwyn calcareous sand**



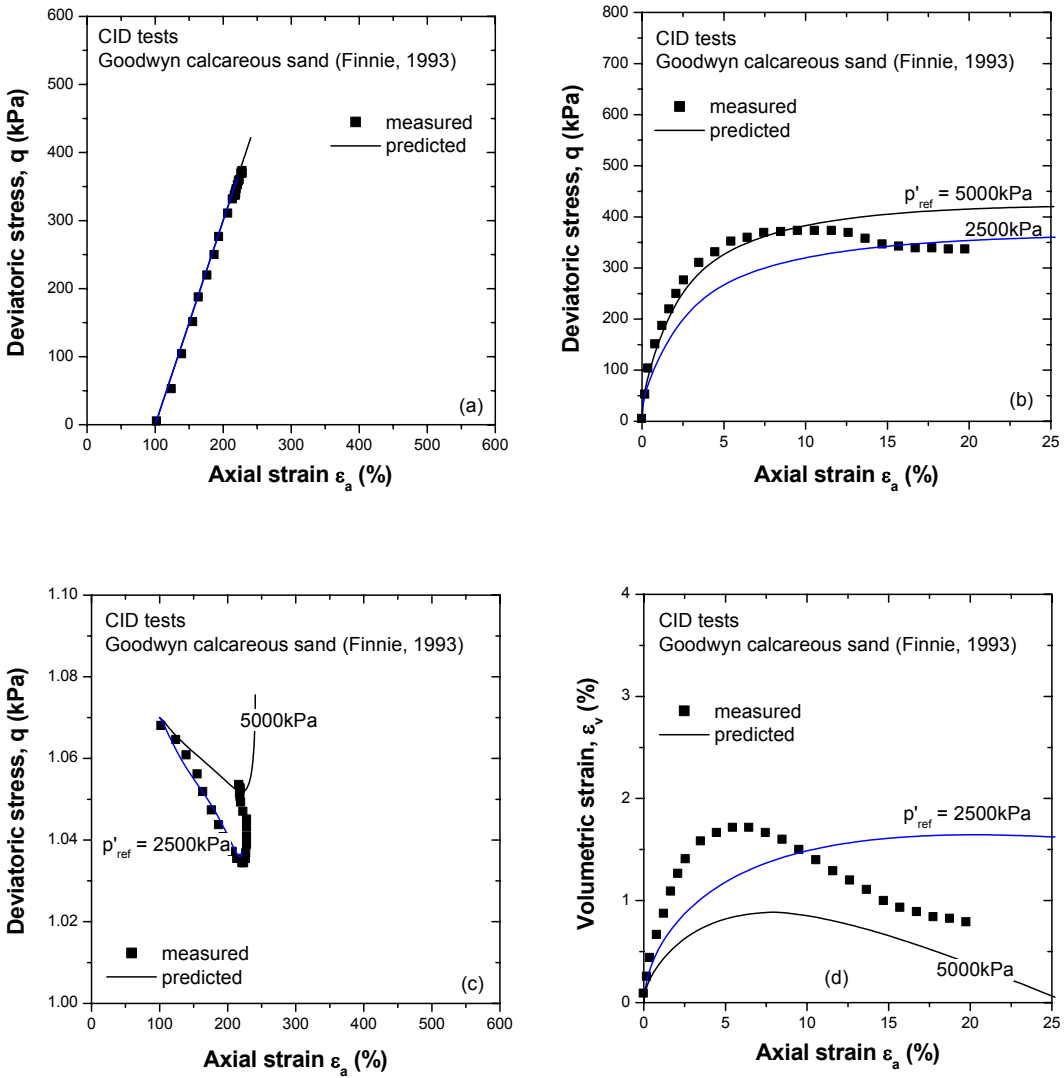
**Figure 3.13: MIT-S1 model predictions for CIU tests of loose Goodwyn calcareous sand**



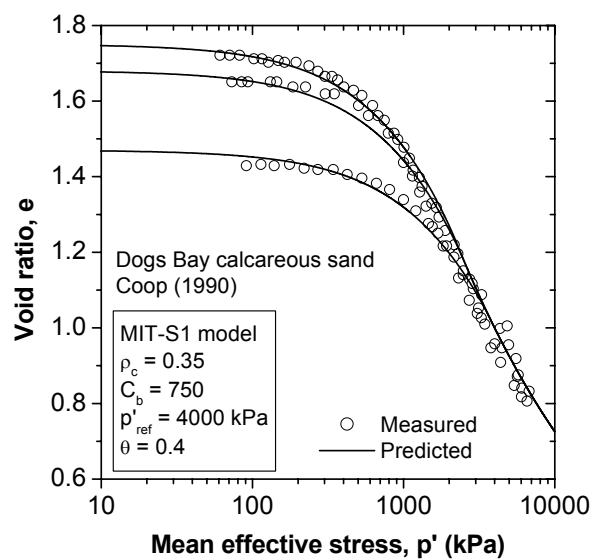
**Figure 3.14: MIT-S1 model predictions for a CIU test of Goodwyn calcareous sand ( $p'_0 = 50 \text{ kPa}$ ,  $e_0 = 1.31$ )**



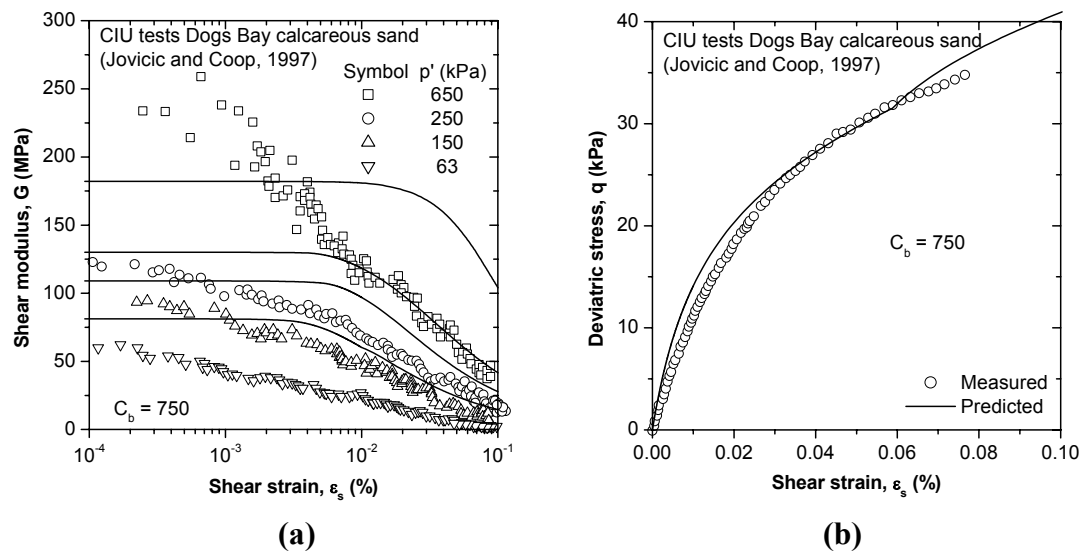
**Figure 3.15: MIT-S1 model predictions for CID tests of Goodwyn calcareous sand (Sharma, 2004)**



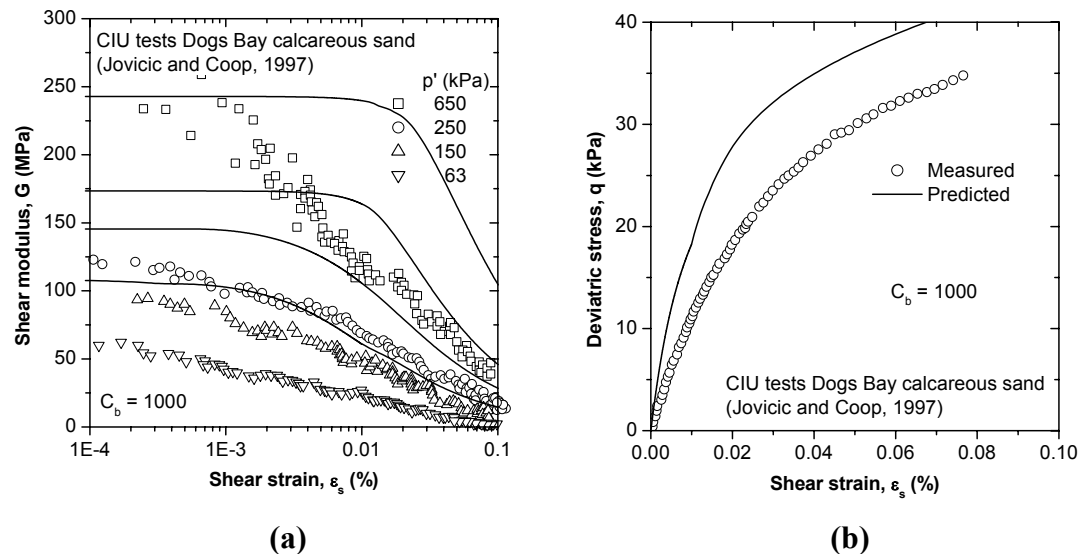
**Figure 3.16: MIT-S1 model predictions for a CID test of Goodwyn calcareous sand (Finnie, 1993)**



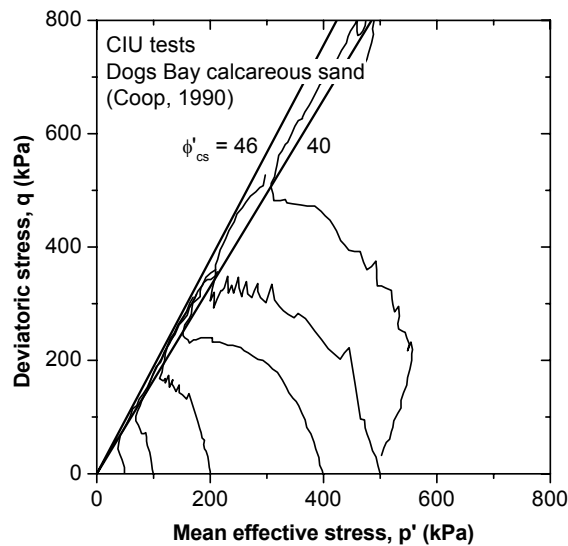
**Figure 3.17: Compression tests for Dogs Bay calcareous sand**



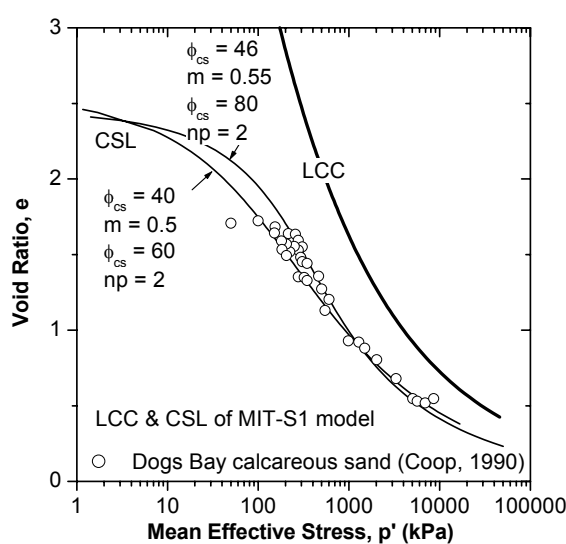
**Figure 3.18: Estimation of MIT-S1 model parameter  $C_b$  (= 750) from small strain measurement of undrained shear test for Dogs Bay calcareous sand**



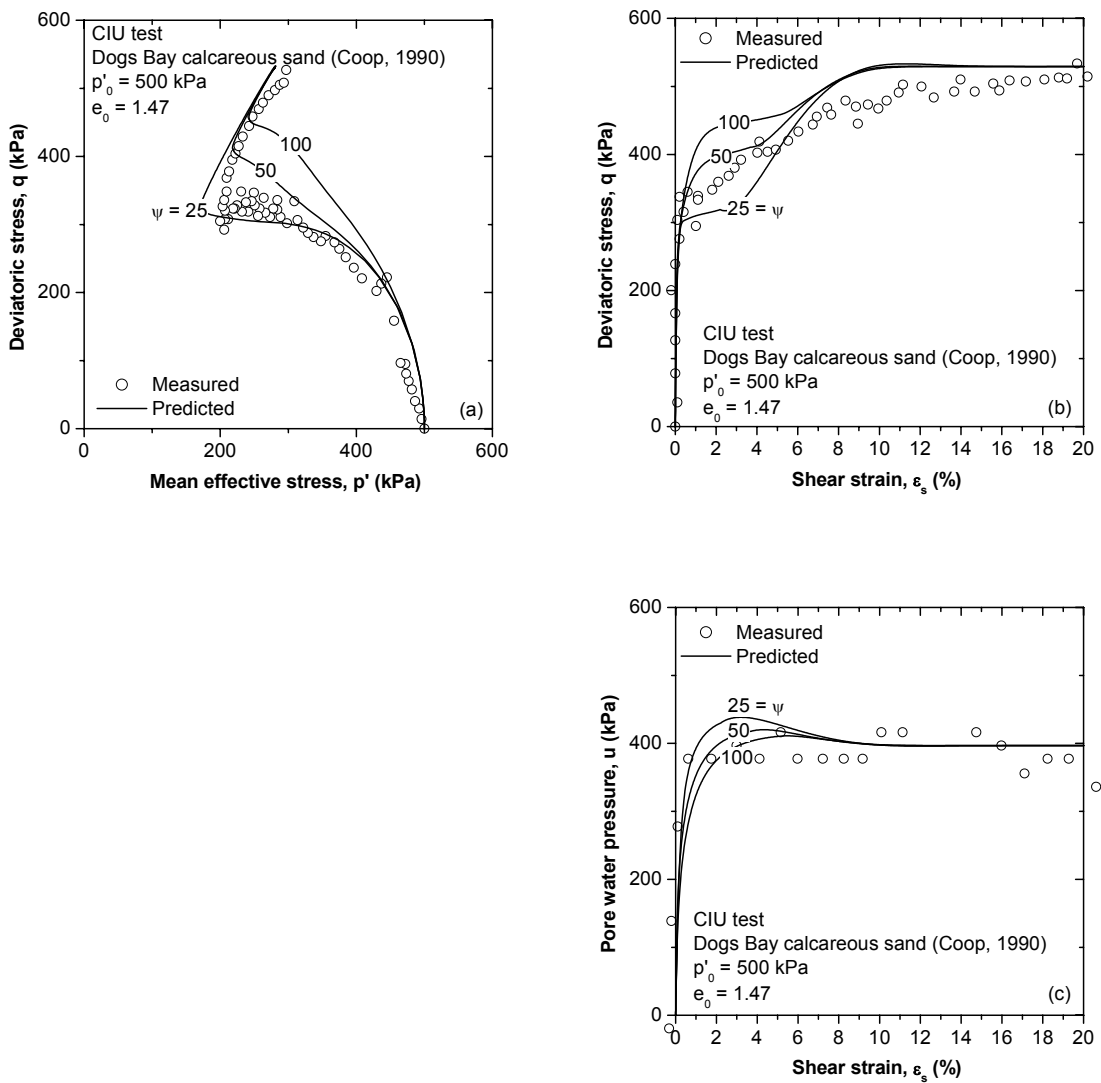
**Figure 3.19: Estimation of MIT-S1 model parameter  $C_b$  (= 1000) from small strain measurement of undrained shear test for Dogs Bay calcareous sand**



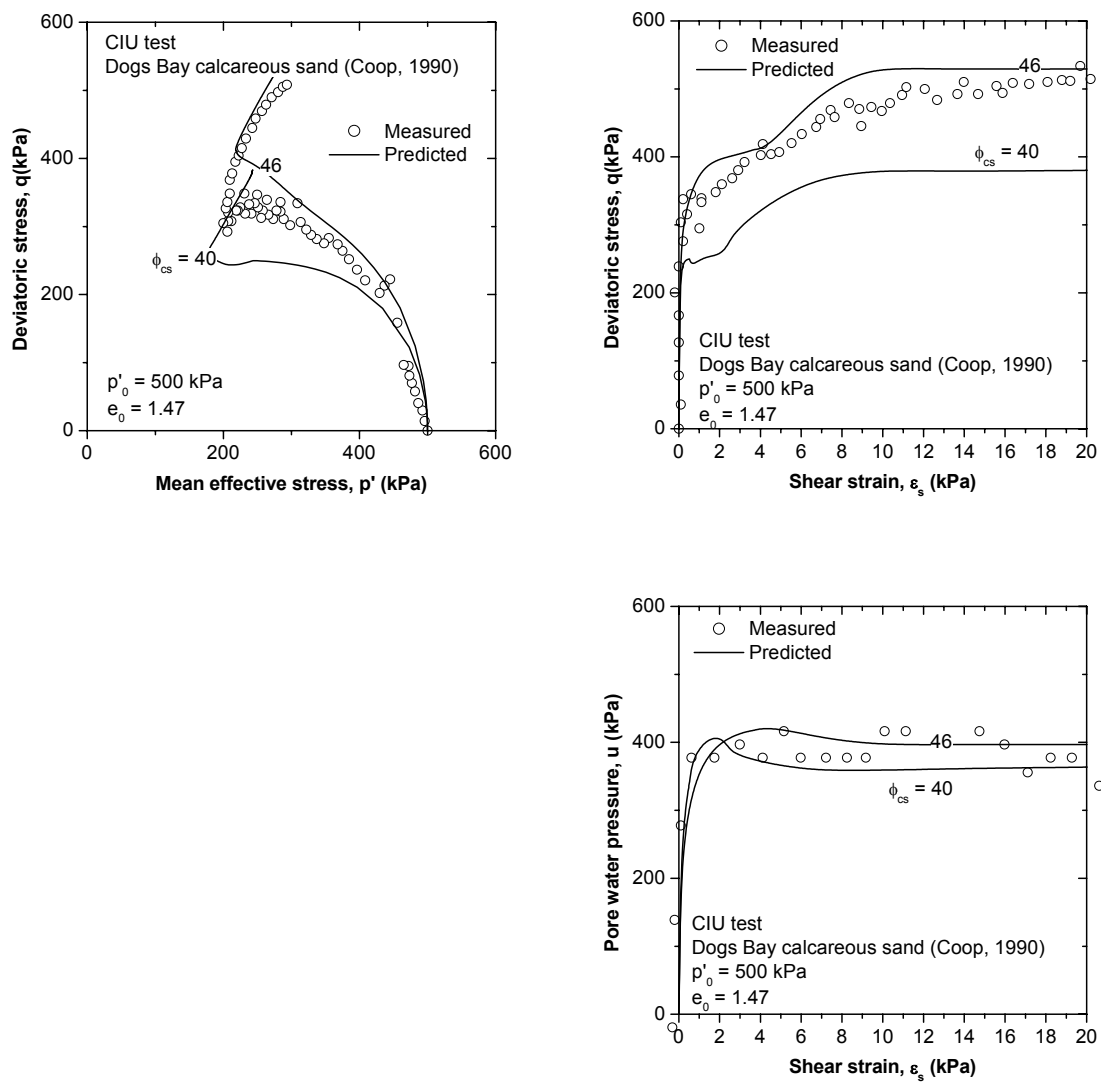
**Figure 3.20: Undrained stress path of Dogs Bay calcareous sand**



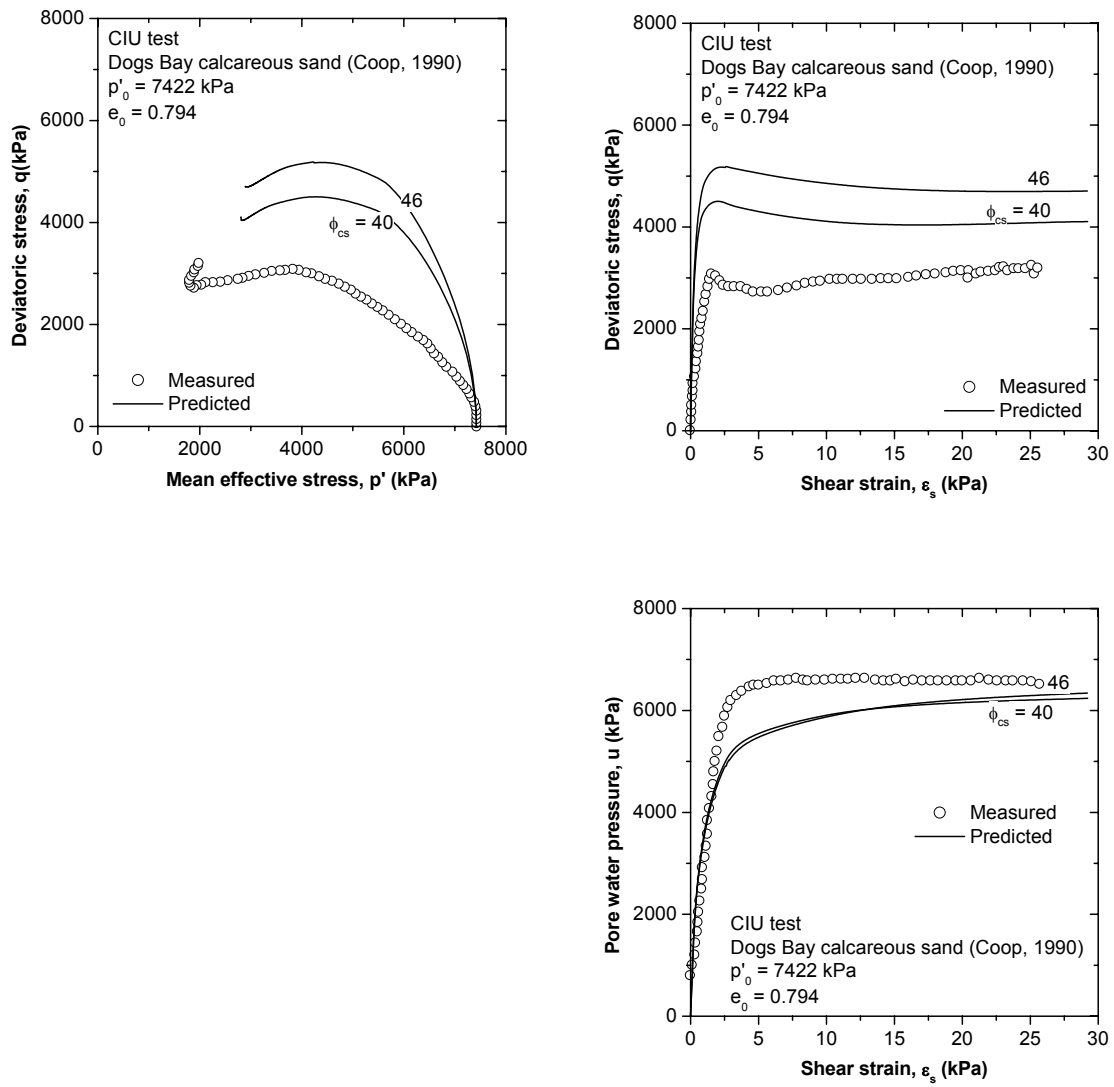
**Figure 3.21: Estimation of critical state line for Dogs Bay calcareous sand**



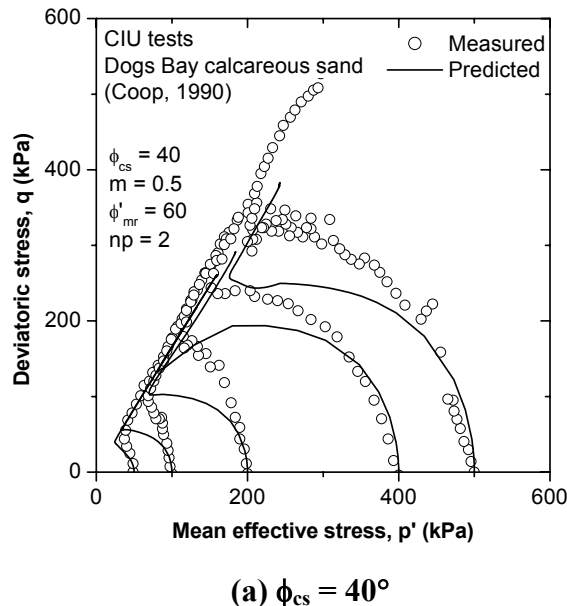
**Figure 3.22: Estimation of MIT-S1 model parameter  $\psi$  from undrained test for Dogs Bay calcareous sand**



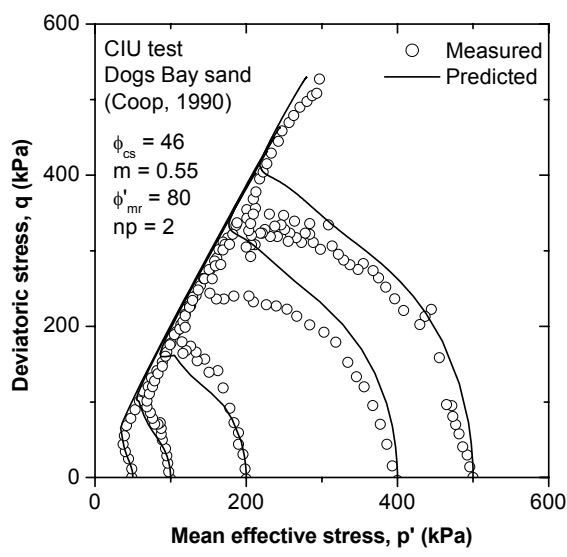
**Figure 3.23: MIT-S1 model predictions for CIU tests of low confined Dogs Bay calcareous sand**



**Figure 3.24: MIT-S1 model predictions for CIU tests of high confined Dogs Bay calcareous sand**

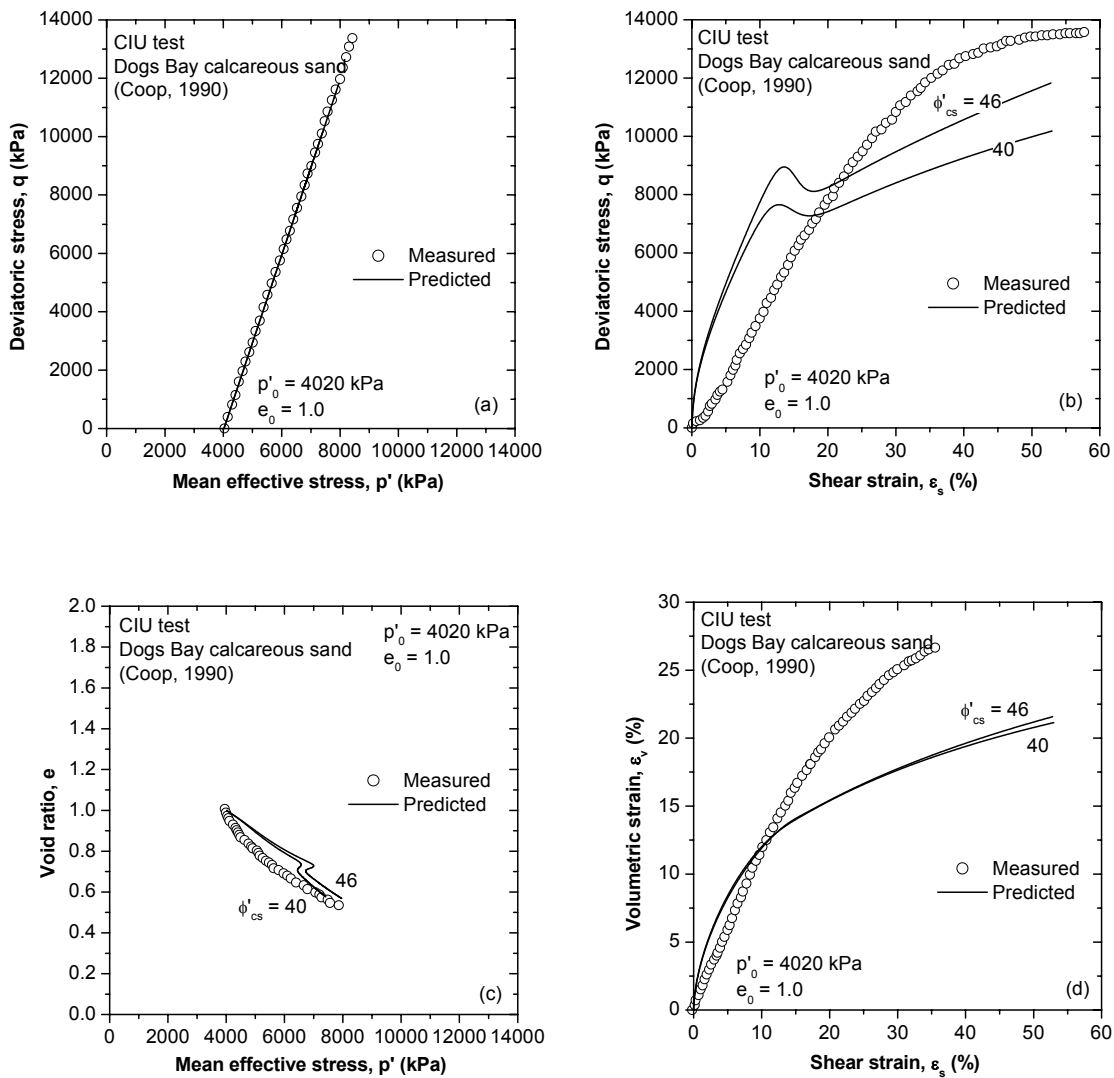


(a)  $\phi_{cs} = 40^\circ$

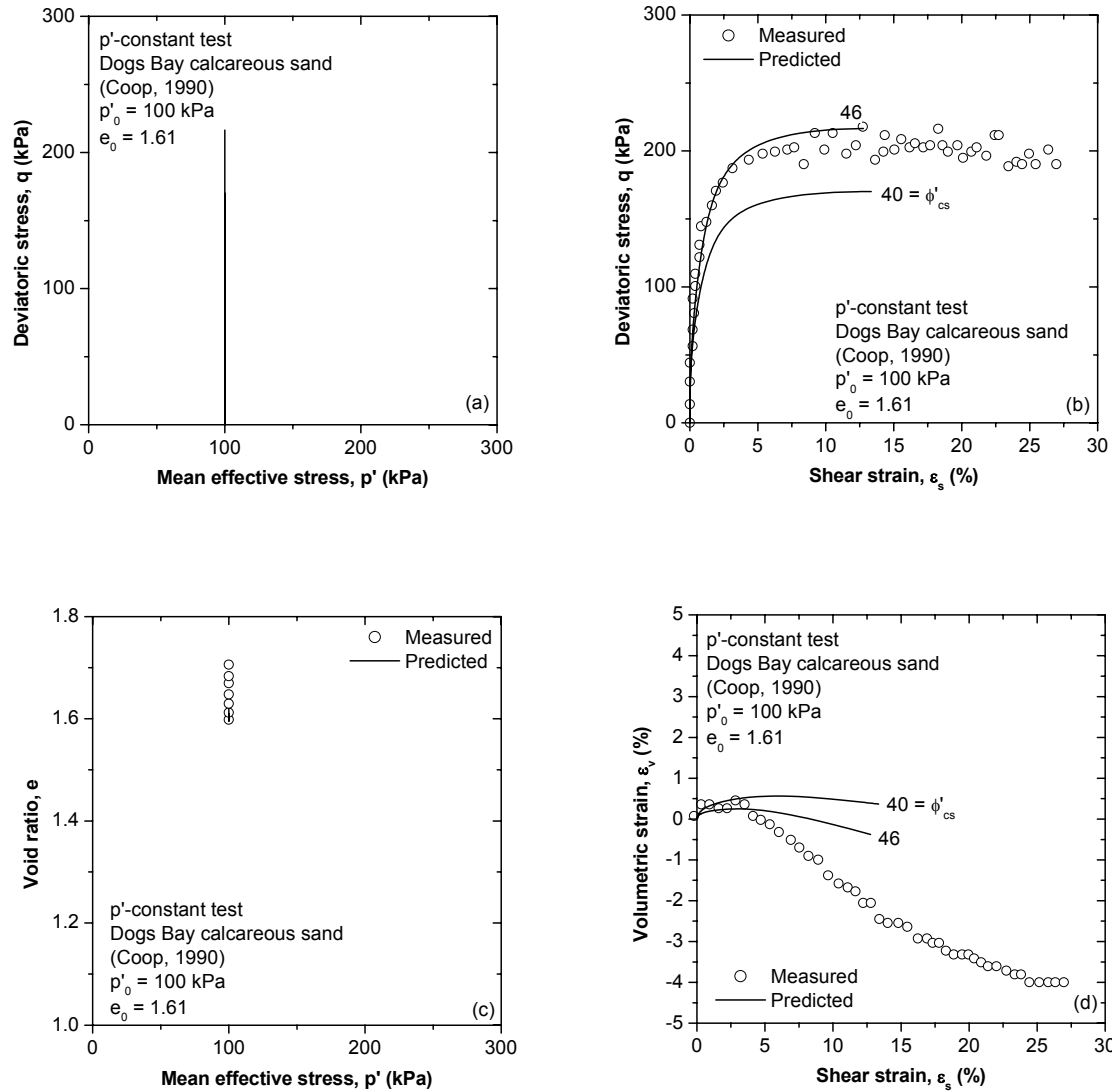


(a)  $\phi_{cs} = 46^\circ$

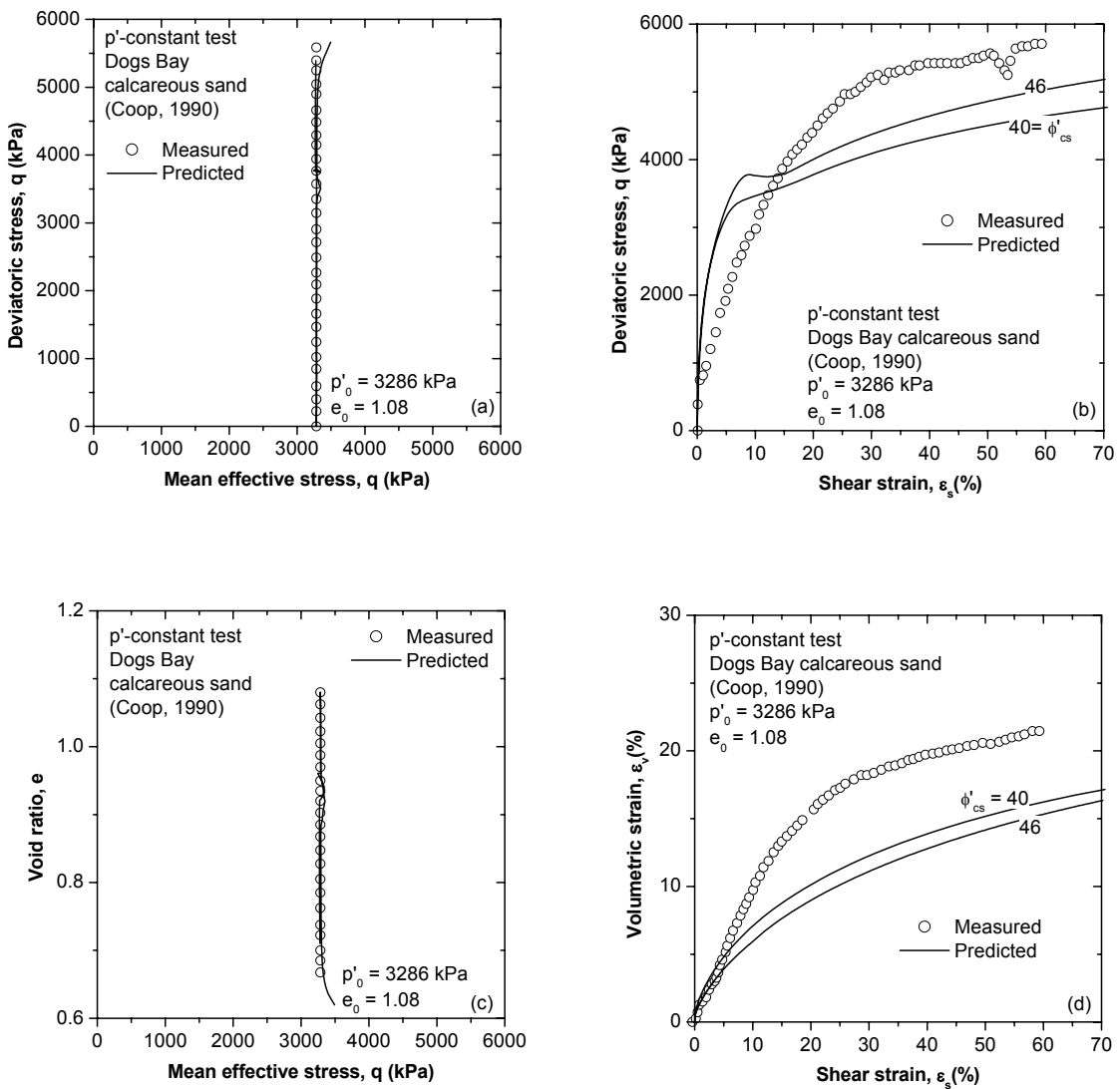
**Figure 3.25: Predictions for undrained stress path of Dogs Bay calcareous sand**



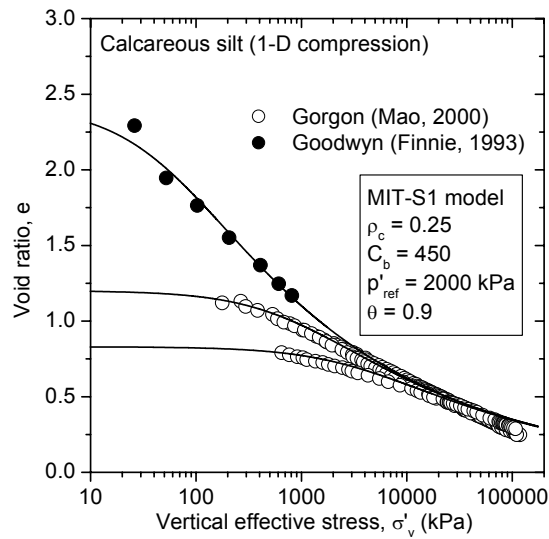
**Figure 3.26: MIT-S1 model predictions for a CID test of high confined Dogs Bay calcareous sand**



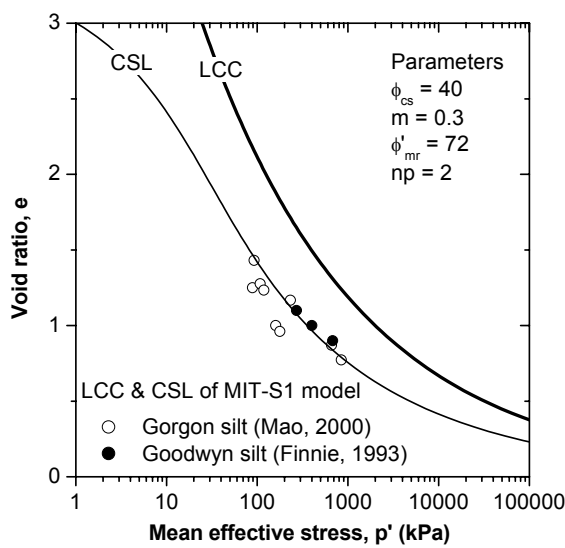
**Figure 3.27: MIT-S1 model predictions for a  $p'$ -constant test of low confined Dogs Bay calcareous sand**



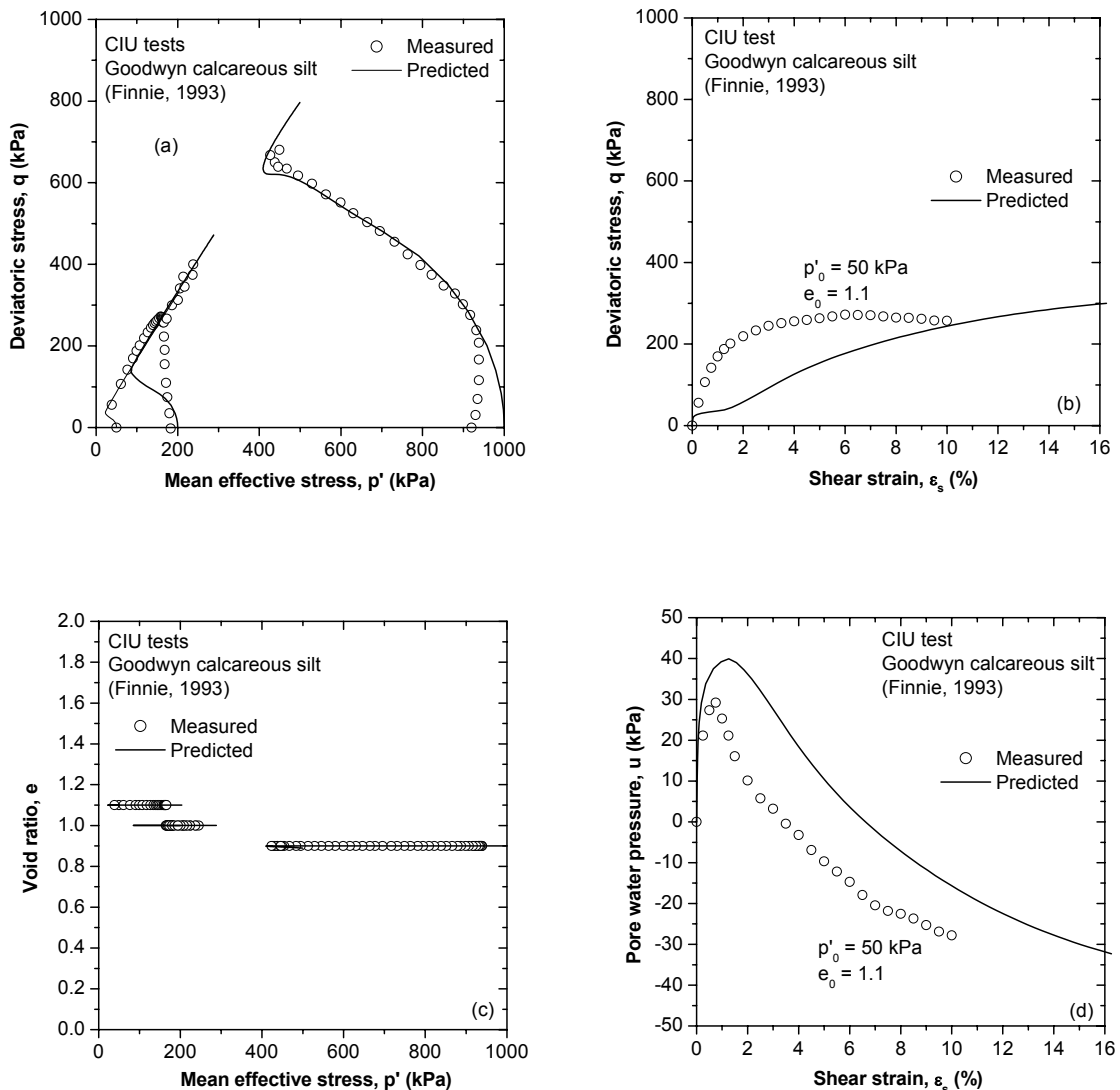
**Figure 3.28: MIT-S1 model predictions for a  $p'$ -constant test of high confined Dogs Bay calcareous sand**



**Figure 3.29: Compression tests for Goodwyn and Gorgon calcareous silt**



**Figure 3.30: Estimation of critical state line for Goodwyn calcareous silt**



**Figure 3.31: MIT-S1 model predictions for CIU tests of Goodwyn calcareous silt**



# **Chapter 4**

## **MIT-S1 Model Predictions for the Behaviour of Shallow Circular Footings**

### **4.1 INTRODUCTION**

It was argued in **Section 2.4** that the MIT-S1 model, which combines well both the compression and shear features of sands, would be suitable for the purposes of this study. This chapter demonstrates this potential, using the MIT-S1 model to predict the bearing response of shallow foundations on siliceous and calcareous sands. Three examinations will be conducted. Firstly, results from the use of the MIT-S1 model will be compared with other constitutive model predictions. This will highlight the advantages of the MIT-S1 model for the analysis of shallow foundations. Secondly, physical model tests on various soils, corresponding to the model parameters obtained in **Chapter 3**, will be used for validating the MIT-S1 model. In the final stage, a sensitivity analysis on the MIT-S1 model parameters is presented, confirming which parameters are the most effective and significant for analysing shallow foundations on sand.

Before commencing the finite element analysis, a finite element mesh must be established and the effect of domain size, mesh density and boundary must be investigated. It was also found that many finite element analyses terminated prematurely using the MIT-S1 model, probably due to the complexity of the model formulation. Techniques in the ABAQUS finite element code are described, which help to avoid such terminations.

### **4.2 FINITE ELEMENT CALIBRATIONS**

This section describes the calibration of the two different finite element (FE) methods that are going to be used throughout the thesis. The first FE code which will be applied

in this thesis is ABAQUS (ABAQUS, 2003), and this will be adopted for any calculations using the MIT-S1 model. The techniques in ABAQUS for improving the calculation stability will be evaluated simultaneously. The second FE code is AFENA (Carter and Balaam, 1995), and this has been adopted for analyses with the other constitutive models, as is discussed in **Section 4.3**.

The following conditions are fixed for all analyses in this study:

1. circular footing (axisymmetric analysis);
2. perfectly rigid footing (displacement control);
3. fully drained conditions;
4. freshly deposited (normally consolidated) conditions.

#### **4.2.1 Geometry of finite element mesh**

In the ABAQUS analyses, 8 node quadrilateral isoparametric elements with quadratic interpolation functions and 9 Gaussian integration points are used to construct the finite element mesh for the footing problem. The choice of the 8 node isoparametric element was made in order to give best results for the general analysis of dilatant solids under either plane strain or axisymmetric conditions. **Figure 4.1** illustrates the typical mesh geometry used in the ABAQUS analyses. Finer mesh divisions are provided in the areas of highest strain beneath and immediately adjacent to the footing.

In the AFENA analyses, 8 node quadrilateral isoparametric elements with 9 Gaussian integration points were also used. **Figure 4.2** shows a typical mesh geometry used in the AFENA analyses. Finer mesh divisions are given beneath and around the edge of the footing, but the mesh is not graded in the same way as for the ABAQUS analyses.

The effect of the mesh fineness around the loading area for the ABAQUS analyses was examined. Similar analysis was conducted using AFENA, but for brevity will not be detailed here. Generally, a finer mesh will lead to more accurate calculations and smoother stress and strain contours. **Figure 4.3** shows typical MIT-S1 model predictions for the bearing response of shallow foundations on siliceous and calcareous sands calculated based on the different meshes. The different fineness of the mesh is

quantified by the number of elements directly beneath the footing, which ranged from 5 to 14 (Mesh 5 to Mesh 14). It is found that the mesh fineness affects the measured ultimate capacity of the siliceous sand, which decreases with increasing fineness of the mesh. On the other hand, the pressure-settlement response on the calcareous sand is insensitive to the mesh fineness. Mesh 10 for the siliceous sand and Mesh 7 for the calcareous sand are taken as minimum element density to avoid any mesh effect.

#### 4.2.2 Mesh size

In both the ABAQUS and AFENA meshes, left and right boundaries of the mesh are restrained in the horizontal direction, while the base of the mesh is not allowed to move in either the vertical or the horizontal directions. The depth and length of the calculation meshes give at least 5 diameters for the ABAQUS mesh and at least 4 diameters for the AFENA mesh (**Figure 4.1** and **4.2**).

One of the main objectives of this study was to examine the effect of foundation size on the shallow foundation response. The numerical predictions in this case used a single mesh, but artificially varied the magnitude of the soil unit weight (similar to varying the acceleration level in a centrifuge model). **Figure 4.4** compares two calculations, one with the mesh scaled to a 10 m diameter footing (as in **Figure 4.1**) with a soil effective unit weight of 8 kN/m<sup>3</sup>, while the other uses a scaled version of the same mesh, corresponding to a footing of 1 m diameter, but with a soil effective unit weight of 80 kN/m<sup>3</sup>. The results for the siliceous and calcareous sands are perfectly identical. Thus, this numerical technique is found reliable for the analysis of different foundation sizes.

It should be noted that, using this method, the variation of foundation size simply results in a change in the initial stress level. In other words, the examination of the effect of foundation size corresponds to the effect of initial in-situ stress level.

#### 4.2.3 Step control

Most of the finite element analyses (including those for the AFENA analyses) have been based on an incremental Euler integration scheme, which assumes that the tangent stiffness at the beginning of an increment is a linear approximation of the incremental

response. This method needs very small increments to obtain an accurate solution and consequently consumes very large computation times. The ABAQUS code also has the capability for an automatic stepping control option to avoid calculation instability and minimise computation time. If the calculation fails to find an approximate equilibrium configuration at the end of each time increment using the Newton method, it repeats the analysis but reducing the increment size. If the iterative procedure achieves a solution in equilibrium with a given tolerance, then the calculation goes to the next stage, increasing the increment size. The user is able to declare a tolerance for the allowable equilibrium solution. The effect of the tolerance on the pressure-displacement response on the siliceous and calcareous sands using the MIT-S1 model is examined in **Figure 4.5**. Higher tolerance values are expected to give increasing errors. However no error in the pressure-deflection curves, up to a tolerance of 1, is observed for both sand conditions. The coarsest tolerance will thus be used only when calculation instability is encountered, otherwise it keeps a default value.

#### **4.2.4 Void ratio variation with depth**

In a naturally deposited ground or seabed, the soil normally becomes denser with increasing depth (due to variation of void ratio with depth). In the models that incorporate compression capabilities the initial density may be defined using the model's void ratio-stress relationship. In the MIT-S1 model, the initial density is calculated independently by the MIT-S1 compression model. **Figure 4.6** compares the pressure-displacement curves using either varied or constant void ratio with depth for siliceous and calcareous sands. The  $e$ - $\ln p'$  relationships from integration points at different depths are also shown. The different conditions do not dramatically affect the bearing response although significant differences in the  $e$ - $\ln p'$  results may be noticed. This agreement may result from the fact that the void ratios are quite similar at shallow depths, which are critical for the foundation response. The effect of the initial void ratio values might become more significant as the foundation size (or initial in-situ stress level) increases. All calculation results in the present study are based on a varying initial void ratio condition.

### 4.3 A STUDY OF SHALLOW CIRCULAR FOOTINGS ON SILICEOUS AND CALCAREOUS SANDS USING VARIOUS CONSTITUTIVE MODELS

This section compares the MIT-S1 model with other available constitutive models in terms of the shallow foundation response on siliceous and calcareous sands. Three additional models are examined, namely the classical elastic-perfect plastic Mohr-Coulomb model, the SU model (Islam, 1999) and the Asaoka model (Asaoka et al., 2000). The latter two are both elasto-plastic models based on critical state concepts with improvements to the shear characteristics. The following comparison highlights the advantages of the MIT-S1 model for the current set of analyses.

The following subsections briefly introduce the additional selected models and the input parameters. The shallow foundation response on siliceous and calcareous sands is then evaluated using the AFENA finite element code (Carter and Balaam, 1995). Analytical capabilities and limitations of the models are also discussed.

#### 4.3.1 Additional constitutive models used in the current study

The *Mohr-Coulomb model* has been widely used for design applications involving foundation response on sand. The model uses a classical Mohr-coulomb yield criterion: a straight line in the shear stress-normal stress plane and an irregular hexagonal section in the deviatoric plane. It allows the material to harden or soften isotropically. The straight line is defined by an angle of friction,  $\phi'$ . However, this model cannot predict the volumetric behaviour of soils, which is the main point to study in this thesis.

The *Sydney University (SU) model* (Islam, 1999) was developed based on the Cam Clay model<sup>1</sup>. The stress-dilatancy relations and the plastic potential function of the SU model are the same as for the Cam clay model. The flow rule is non-associated with the yield function differing from the potential function by incorporating a spacing ratio of the yield stress ( $p'_y$ ) for  $q = 0$  to the mean effective stress on the CSL ( $p'_{cs}$ ) (see **Figure 4.7**). This model was developed particularly for investigation of calcareous soil behaviour. It

---

<sup>1</sup> There were two SU models. The SU1 model was based on the original Cam Clay model, while the SU2 model was based on the modified Cam Clay model

was shown that the SU2 model predictions were in agreement with results from triaxial tests as well as from plate loading tests on calcareous sand. However, the spacing ratio depends on the stress level and density, and must therefore be chosen with care for any given application.

The *Asaoka model* (Asaoka et al., 2000) is a model which adds sub- and super-loading surfaces into the Cam Clay model using Hashiguchi's sub-loading surface theory (Hashiguchi, 1989). The sub-loading surface was incorporated within the real yield surface to capture the non-linear behaviour of overconsolidated soils, while the super-loading surface is positioned exterior to the yield surface to predict the structured or aged behaviour of soils (see **Figure 4.8**). Additional parameters allow the introduction of similarity ratios for those surfaces with respect to the yield surface and revolution rates of the two surfaces. This enhances the ability to predict the dilatancy behaviour of sand. The similarity ratios are dependent on the stress level and density.

#### 4.3.2 Input parameters for the constitutive models

The required input parameters for the Mohr-Coulomb, SU2 and Asaoka models are summarised in **Tables 4.1, 4.2** and **4.3**, respectively. Detailed explanations of the input parameters are not included here but full descriptions of the models and their parameters may be obtained from the relevant publications. The compression parameters of the SU2 and Asaoka models are determined using **Figures 4.9** and **4.10**, respectively. Clear distinct point can be observed in compression prediction from SU2 model, while Asaoka model can predict smooth transition of compression curve. Parameter  $\lambda$  is obtained from an isotropic compression test performed by Ismail (2000), while Parameter  $e_{cs}$  is obtained from a 1-D compression test by Finnie (1993). SU2 model predictions for CIU and CID tests for siliceous and calcareous sands are compared with experimental results as shown in **Figures 4.11** and **4.12**. The prediction curves with clear distinction between elastic and plastic response do not fit the smooth curved measurements well. Asaoka model predictions for CIU and CID tests for siliceous and calcareous sands with comparison to the same experimental results are shown in **Figures 4.13** and **4.14**. The smooth prediction curves are in good agreement with some of the measurements, in particular CIU tests for siliceous sand and CID tests for calcareous sands.

### 4.3.3 Bearing responses

This section describes analyses of vertically loaded shallow circular footings using different constitutive models representing Toyoura siliceous and Goodwyn calcareous sands. The footing loading is controlled by displacing the interface nodes vertically down, while allowing them to move freely in the horizontal direction, thus simulating rigid and smooth footings. The results of pressure-displacement curves as well as incremental displacement vectors are presented, focusing mainly on a 10 m diameter circular footing.

First of all, the predictions using the Mohr-Coulomb model are detailed. The analyses on siliceous and calcareous sands are based on two types of soil stiffness conditions. In the first the stiffness is kept constant with depth, while in the second it varies with depth. The pressure-displacement curves in **Figure 4.15** show that the calcareous sand exhibits quantitatively higher bearing response than the siliceous sand due to higher friction angle ( $39.6^\circ$ ). The incremental displacement vectors at a displacement of 1 m ( $\delta/D = 10\%$ ) for all analyses are presented. It is found that the deformation mechanism for the Mohr-Coulomb model for both siliceous and calcareous sands, exhibits a classical failure mechanism.

The SU2 model, on the other hand, predicts relatively acceptable results for the calcareous sand behaviour but not for siliceous sand. **Figure 4.16** compares the SU2 model predictions of the surface circular footings on siliceous and calcareous sands. Initial void ratios,  $e$ , and spacing ratios,  $r$ , are 0.8 (yield pressure,  $p'_y = 22.2$  MPa) and 5 for the siliceous sand and 1.3 ( $p'_y = 1.41$  MPa) and 15.0 for the calcareous sand. In contrast to the Mohr-Coulomb model, the response of the calcareous sand is significantly lower than that of the siliceous sand and the incremental displacement vectors show a punching-shear type of deformation owing to the compression component. For the siliceous sand analysis, however, the response increases exponentially and an extremely large stress level is needed to reach the yield state. The incremental displacement vectors do not show the general deformation pattern for the siliceous sand. The predictive incapability for the siliceous sand is an intrinsic problem of the SU2 (Cam Clay) model.

The other Cam Clay based model, the Asaoka model, is also not in agreement with the siliceous sand but produced comparable results with the experiments on calcareous sand. The model prediction is relied on values of the parameter, R and R\* and their variations with depth, dR and dR\*. The values are  $R = 0.015$ ,  $R^* = 1.0$ ,  $dR = 0.00213$ ,  $dR^* = -0.0025$  for the siliceous sand and  $R = 0.1$ ,  $R^* = 0.9$ ,  $dR = 0.00875$ ,  $dR^* = -0.00875$  for the calcareous sand. The pressure-settlement curves for the siliceous and calcareous sand analyses in **Figure 4.17** show quasi-linear responses. However, the lowest mobilised bearing pressures compared to the other model results are achieved. The incremental displacement vectors show a degree of surface heave for the siliceous sand analysis, but this does not develop into a full failure mechanism.

In light of the above demonstration it will be shown that the MIT-S1 model would serve this thesis well in distinguishing between the behaviour of compressible and dilative sands by relatively minor adjustment of the model parameters (see **Table 3.1**). The pressure-displacement curves in **Figure 4.18** reveal that a clear ultimate bearing capacity is shown in the siliceous sand analysis, whereas a quasi-linear response with no peak pressure is exhibited in the calcareous sand analysis. The results of the incremental displacement vectors nicely show the ability of the MIT-S1 model to produce reliable failure patterns, with a bulb of compressed material and punching failure for the calcareous sand, and the classical rupture pattern accompanied by surface heave for the siliceous sand. A proper combination of the compression and shear capabilities might be the reason of this successful distinction.

#### 4.3.4 Discussion

From the comparisons, several analytical capabilities and limitations of the selected constitutive models are found. The Mohr-Coulomb model, which does not consider the compression characteristics of natural sands, derives higher mobilised bearing capacity when the material has a higher friction angle. The SU2 model, which is based on the Cam Clay compression model, agrees only slightly with the general shape of bearing response for the calcareous sand. The Asaoka model allows simulating the smooth compression curves. However the lowest mobilised bearing pressures for siliceous and calcareous sands are measured.

The balance between the compression and shear responses appears to be fundamental to the different foundation responses observed for siliceous and calcareous sands. The MIT-S1 model is able to simulate this significant difference in the bearing responses and the deformation mechanisms for siliceous and calcareous sands, due to its superior modelling of the non-linear volumetric behaviour of freshly deposited sand. It is deduced that the parameter  $\theta$ , which represents the curvature of the compression curve, may be the most effective in achieving this goal. Lower  $\theta$  (0.2 for Toyoura siliceous sand) leads to stiffer response in compression and results in a distinct yield point in the bearing response, whereas higher  $\theta$  (0.9 for Goodwyn calcareous sand) gives greater compressibility and predicts a mildly non-linear bearing response with a punching failure mode. Further investigations of the contribution of the MIT-S1 compression component and the effect of the MIT-S1 model parameters on the bearing response is described in the following sections.

#### 4.4 A COMPARISON BETWEEN NUMERICAL AND PHYSICAL MODEL TESTS OF SHALLOW CIRCULAR FOOTINGS ON VARIOUS SOILS

Research based on physical modelling using centrifuge facilities has been increasing rapidly over the last several decades. This section presents results from physical model tests of circular foundations resting on uncemented normally consolidated Toyoura siliceous sand, Goodwyn calcareous sand, Dogs Bay calcareous sand and Goodwyn calcareous silt. Finite element calculations for the behaviour of shallow foundations on the above soils using the MIT-S1 model are also presented and compared with the physical model results. The comparison will explore the ability of the MIT-S1 model to predict the results. The input parameters for the soils have been determined in **Chapter 3** and were listed in **Table 3.1**.

##### 4.4.1 Toyoura siliceous sand

Okamura et al. (1997) reported results from centrifuge model tests of surface circular footings on uniformly deposited Toyoura siliceous sand. Their experiments encompassed three different footing diameters (1.5, 2, 3 m), tested at various levels of gravitational acceleration. Sand was glued on the base of the footing, to represent a fully

rough interface. The relative density of all samples was roughly 85 % ( $e_0 \approx 0.65$ ). **Figure 4.19(a)** shows the pressure-settlement curves for footings with different diameters. Ultimate bearing capacities are clearly observed and increase with increasing foundation size.

Unfortunately, the finite element analysis of small diameter foundations (< 3 m) on dense siliceous sands terminated prematurely before showing the ultimate capacity (**Figure 4.19(b)**). However, the calculations on loose ( $e_0 = 0.8$ ) or medium loose ( $e_0 = 0.7$ ) samples using a rough mesh (Mesh 5) attained limiting bearing resistances.

#### 4.4.2 Goodwyn calcareous sand

Finnie (1993) and Finnie and Randolph (1994a; 1994b) reported physical model results for circular flat foundations on homogeneous, normally consolidated and uncemented Goodwyn calcareous sand. Their analyses modelled the effect of variation in foundation diameter (3, 5, 7, 10 m). The average void ratio at the end of consolidation on the centrifuge was 1.3. The results of the pressure-displacement curves are shown in **Figure 4.20**. The most noticeable features are 1) quasi-linearity of the responses, and 2) relatively small dependency on the foundation size. These features contrast significantly with the results for siliceous sand. Randolph & Erbrich (2000) suggested that the shear strain component dominates the settlement of small foundations ( $D < 10$  m) (**Figure 2.18**). The absolute settlement of the small diameter foundations, for a given bearing pressure, will then stay approximately constant, i.e. independent of the diameter. They also argued that the domination of the consolidation component would gradually increase with increasing foundation diameter.

The MIT-S1 model predictions are superimposed in **Figure 4.20**. The initial properties are a void ratio of 1.3 (dense) and effective unit weight of 7 kN/m<sup>3</sup>. For convenience, the numerical predictions for different foundation sizes were achieved by artificially varying the magnitude of the soil unit weight as discussed in **Section 4.2.3**. The predicted pressure-settlement curves agree reasonably with the physical model results. However, the predicted bearing resistance decreases slightly with increasing foundation size, which is not entirely consistent with the measured results.

#### 4.4.3 Dogs Bay calcareous sand

Klotz and Coop (2001) carried out a series of model pile tests in the centrifuge, driven into Dogs Bay calcareous sand. The diameter of the model pile was 16 mm and centrifugal accelerations of 50, 100 and 200g were applied, thus, leading to simulation of three different prototype diameters (0.8, 1.6, 3.2 m). The densities of the samples were carefully measured by LVDTs installed in the soil sample. **Figure 4.21** shows the pressure-settlement curves of the footings with different diameters and densities. The piles were jacked to a depth of about 60 m at prototype scale. There are clear changes in the bearing responses at a displacement of 5 to 10 m. The mobilised bearing pressures at the yield points (representing a form of ultimate bearing capacity) are extremely high.

The MIT-S1 model results are compared with 3.2 m diameter footings on samples with different densities. The calculations for small size foundations on dense Dogs Bay sand (**Figure 4.21(e) and 4.21(f)**) terminated prematurely at displacement of 3 to 6 % of the diameter, probably for the same reason for in the calculations of Toyoura sand. In the loose Dogs Bay sand analysis (**Figure 4.21(d)**), the prediction agrees reasonably with the physical model results.

#### 4.4.4 Goodwyn calcareous silt

Finnie (1993) (see also subsequent papers by Finnie and Randolph (1994a; 1994b)) conducted physical model tests of circular foundations on Goodwyn calcareous silt. Finnie used different sized footings (4, 6, 8, 15 m) under the same centrifugal acceleration. The average void ratio at the end of centrifugal consolidation was 1.7. The results of the pressure-displacement curves are shown in **Figure 4.22**. The bearing responses are observed to harden with increasing penetration depth. Unlike for Goodwyn sand, the responses depend more obviously on the foundation size.

The MIT-S1 predictions (void ratio at surface of 1.7 (dense) and effective unit weight of 6 kN/m<sup>3</sup>) are also plotted together in **Figure 4.22**. Like the Goodwyn sand analysis, the numerical predictions of the different foundation sizes were calculated by varying the soil effective unit weight. Both the predicted and measured bearing responses show

decreased resistance with increasing size of the foundation. However, the shape of the curves agrees only moderately with the measurements.

#### **4.4.5 Discussion**

Results from physical model tests of circular foundations resting on Toyoura siliceous sand, Goodwyn calcareous sand, Dogs Bay calcareous sand and Goodwyn calcareous silt were presented and compared with the MIT-S1 model predictions using the input parameters defined in **Chapter 3**. For small foundation size and relatively stiff (or dense) material (Toyoura and Dogs Bay sands), the analyses terminated due to numerical problems at an early stage of the loading, generally for displacement between 3 and 6 % of the diameter. The foundation behaviour under those conditions results in significant stress concentrations that appear to lead to numerical instability for complex constitutive models. Particular numerical techniques, such as adaptive mesh refinement, may be necessary to resolve this issue.

Ignoring the failed calculations, the MIT-S1 model simulations using the input parameters obtained from standard laboratory tests in **Chapter 3** are in fair agreement with the physical model measurements. As a typical example, the bearing response on siliceous sand reaches a clear limit pressure, while the analyses for calcareous sand show only mild non-linearity in the responses with no clear yield stress or ultimate bearing capacity.

It should be noted that the interrelation between the shear and compression parameters is of great importance for the bearing capacity analysis on sands. The values of the shear parameters such as friction angle for the calcareous sands are normally higher than for the siliceous sands. For the pressure-settlement curves on calcareous sands, Dogs Bay sand shows higher bearing resistance due to the stiffer compression parameters, while Goodwyn sand exhibits lower resistance due to softer compression parameters.

Moreover, the physical model responses on Goodwyn sand are insensitive to the foundation size, while the predicted resistance decrease somewhat with increasing foundation size. Randolph & Erbrich (2000) suggested that diameter independency of the bearing response would typically occur for smaller diameter foundations ( $D < 10$  m)

because the deformation is dominated by the shear component. It is difficult to evaluate the cause of diameter independency for small foundations using the MIT-S1 model. However, when the foundation size is large, the compression component increasingly dominates the behaviour. It is suggested that the MIT-S1 model provides better analysis of moderate to large shallow foundations, due to its superior modelling of the compression component.

#### **4.5 SENSITIVITY ANALYSIS ON THE EFFECT OF THE MIT-S1 MODEL PARAMETERS ON THE BEHAVIOUR OF SHALLOW CIRCULAR FOOTINGS**

An investigation of the effects of changes in the MIT-S1 model parameters on the behaviour of circular footings on siliceous and calcareous sands is presented here. It was mentioned in the previous chapter that the friction angles,  $\phi'_{cs}$  and  $\phi'_{mr}$ , and the compression parameters,  $p'_{ref}$  and  $\theta$ , are expected to be the most significant, while the rest of the parameters may have less effect. This section will evaluate whether those parameters are in fact the most effective in producing changes in the shallow foundation behaviour.

Toyoura and Goodwyn sand parameters shown in **Table 3.1** are used in the siliceous and calcareous sand analyses, respectively. A diameter of 10 m and a fully smooth footing base are selected. The values of effective unit weight and void ratio are 8 kN/m<sup>3</sup> and 0.8 for siliceous sand and 7 kN/m<sup>3</sup> and 1.3 for calcareous sand. The range of model parameters chosen for the parametric study will be explained below.

##### **4.5.1 Compression parameters ( $\rho_c$ , $\theta$ , $p'_{ref}$ )**

As might be expected, the influence of the parameter  $p'_{ref}$  on the bearing response is found significant in the calcareous sand analysis, but less significant in the siliceous sand analysis (**Figure 4.23(a)**). It is found in **Figure 4.23(b)** that  $p'_{ref}$  controls the compression curves and the CSL. Technically the calcareous samples possess initial states that are always closer to the CSL and the LCC and are thus quite sensitive to changes in the  $p'_{ref}$ , whereas the variations of the CSL and the LCC has little effect on the bearing response on siliceous sand since extremely high pressures are required to

reach them. It is deduced that the effect of  $p'_{\text{ref}}$  would become more significant for siliceous sand as the foundation size increases because the initial stress state becomes closer to the LCC and the CSL.

On the other hand, the parameter  $\theta$  significantly affects the calculated pressure-displacement curves for both siliceous and calcareous sand (**Figure 4.24**). In a similar way to the compression curves, the parameter controls the curvature of the bearing response. The shape of the pressure-settlement curve on siliceous and calcareous samples with  $\theta = 0.2$  is the most curved and these are consistent with the shape of compression curve.

The other compression parameter,  $\rho_c$ , is also examined in **Figure 4.25**. The effect of the parameter is negligibly small for both siliceous and calcareous sand analyses. Ranges of applied values are narrow because calculations by wider range are always terminated.

#### 4.5.2 Shear parameters with small strain measurement ( $C_b$ , $\omega_s$ )

The characteristics at small strain level are expected not to affect the bearing response, which is mainly associated with large strain behaviour. The foundation analyses prove that the effects of  $C_b$  and  $\omega_s$  on the bearing response are negligible for calcareous sand, and relatively slight for siliceous sand at lower displacement level. (**Figure 4.26** and **4.27**). The responses for siliceous sands merge at a displacement of 0.5 m ( $\delta/D = 5\%$ ).

#### 4.5.3 Shear parameters with large strain measurement ( $\phi'_{\text{cs}}$ , $m$ , $\phi'_{\text{mr}}$ , $n_p$ , $\psi$ )

Particular focus should be paid to the selection of the friction angle for the bearing capacity problem. A proper assessment of the friction angle may give rise to distinctive changes in the bearing response on siliceous and calcareous sands.

**Figure 4.28** shows the effect of  $\phi'_{\text{cs}}$  on the bearing response on siliceous and calcareous sands, plotted together with the CSLs in  $e$ - $\ln p'$  space. Unfortunately, calculations except for  $\phi'_{\text{cs}} = 31^\circ$  terminated early and prevented exploring fully the effect of  $\phi'_{\text{cs}}$  on the shallow foundation response on siliceous sand. It can be said that the bearing responses on calcareous sand are insensitive to  $\phi'_{\text{cs}}$  although the CSLs are affected by  $\phi'_{\text{cs}}$ .

The MIT-S1 model simulates variation of the peak friction angle with the stress level and density. For that purpose, the parameters  $\phi'_{mr}$  and  $np$  control the prediction of the peak friction angles in drained shear tests at low confining pressures. **Figure 4.29** and **4.30** show a) the pressure-displacement curves, b) stress-strain curves and c) void ratio-stress curves calculated using different values of  $\phi'_{mr}$  and  $np$ . It can be seen that  $\phi'_{mr}$  dictates the level of dilatancy and influences significantly the bearing response for siliceous sand. The level of dilatancy is more significant as  $np$  changes. The sample initially had  $e_0 = 0.8$  such that  $np$  may clearly reflect both contractive ( $np = 1$ ) and dilative ( $np = 5$ ) responses. This range induces enormous sensitivity in the bearing response. In contrast, the value of  $\phi'_{mr}$  affects less the bearing response on calcareous sand although volume change induced by the location of the CSL is quite significant. Moreover, the effect of  $np$  is negligibly small for the calcareous sand.

The shape factor of the yield surface, controlled by the parameter  $m$ , affects significantly the bearing responses on siliceous and calcareous sands (**Figure 4.31**).

The effect of the parameter  $\psi$ , which controls the rate of induced anisotropy, can be ignored on the bearing response on siliceous and calcareous sands as shown in **Figure 4.32**.

#### 4.5.4 Discussion

A sensitivity analysis on the effects of the MIT-S1 model parameters on the analysis of shallow foundation response has been presented. A summary of the evaluation for the siliceous and calcareous sands is given in **Table 4.4**. Overall, except for the parameter  $m$ , the shear parameters do not affect the analysis on calcareous sand. It may be concluded that the bearing response on calcareous sand is not dominated by the shear component, but rather by the compression component.

In the siliceous sand analysis, the parameters  $\phi'_{mr}$  and  $np$ , which dictate the peak friction angle, lead to significantly different predictions. The main technical aim of those parameters is to prescribe the location of the CSL in the void ratio and pressure relationship. **Figures 4.29** and **4.30** show the significant influence of the CSL position

on the level of dilatancy as well as the bearing response. It is presumed that the effect of the CSL position is important for the estimation of the peak friction angle and the bearing response for given values of  $\phi'_{mr}$  and  $np$ . This effect on the shallow foundation response will be described in the next chapter.

It should be noted, however, that the analyses in this chapter were performed using a 10 m diameter footing. The effect of the MIT-S1 model parameters for larger scale foundation may not be the same as for the smaller foundation. It is anticipated that the effect of the shear parameters for siliceous sand would decrease as the foundation size increases. A parametric study for larger foundations (ignoring those parameters that have negligible effect) will be conducted in the following chapter.

#### 4.6 CONCLUSIONS

This chapter has presented result from finite element analysis of shallow foundations using the MIT-S1 model as well as three other models. It is found that, compared with the other models, the MIT-S1 model allowed distinguishing between the foundation responses on siliceous and calcareous materials based on relatively minor modification of the model parameters. The remaining constitutive models are incapable of simulating the wide range of soil types and properties and are applicable to only a particular class of soil.

The MIT-S1 model analysis of shallow foundations on the various soils has been conducted using the input parameters obtained in **Chapter 3**. The calculations for dense Toyoura and Dogs Bay sands samples cannot be completed beyond a certain load level due to numerical difficulties. However prior to this point, the MIT-S1 predictions agree satisfactorily with the physical model results.

Finally, a sensitivity analysis for the various model parameters on the bearing response on siliceous and calcareous sands has been presented. This study reveals that the compression parameters,  $\theta$  and  $p'_{ref}$  have the greatest effect on the bearing response for both sand types. The shear parameters  $\phi'_{mr}$ , and  $np$  do not affect the response for calcareous sand, but influence the ultimate bearing resistance for siliceous sand because the parameters dictate the magnitude of the peak friction angle.

**Table 4.1: SU2 model parameters for Toyoura and Goodwyn sands**

| Physical meaning            | Symbol          | Siliceous sand | Calcareous sand |
|-----------------------------|-----------------|----------------|-----------------|
| Friction angle              | $\phi' (\circ)$ | 31.0           | 39.6            |
| Dilation angle              | $\psi (\circ)$  | 31.0           | 39.6            |
| Young's modulus (constant)  | E (MPa)         | 447*           | 266*            |
| Young's modulus (variation) | E (MPa/m)       | 40.3           | 23.9            |
| Poisson's ratio             | $\mu'_0$        | 0.233          | 0.150           |

\*:  $E = 2G(1+\mu'_0)$ ;  $G = 181$  MPa for siliceous sand (Ishihara, 1993);  $G = 88.7$  MPa for calcareous sand (Sharma, 2004)

**Table 4.2: SU2 model parameters for Toyoura and Goodwyn sands**

| Physical meaning                           | Symbol    | Siliceous sand | Calcareous sand |
|--|-----------|----------------|-----------------|
| Slope of normally consolidated curve       | $\lambda$ | 0.20           | 0.27            |
| Slope of swelling curve                    | $\kappa$  | 0.02           | 0.02            |
| Critical void ratio at unit pressure       | $e_{cs}$  | 2.41           | 2.93            |
| Poisson's ratio                            | $\mu'_0$  | 0.233          | 0.150           |
| Slope of critical state line on q-p' space | M         | 1.3            | 1.63            |

**Table 4.3: Asaoka model parameters for Toyoura and Goodwyn sands**

| Physical meaning                           | Symbol    | Siliceous sand | Calcareous sand |
|--|-----------|----------------|-----------------|
| Slope of normally consolidated curve       | $\lambda$ | 0.20           | 0.30            |
| Slope of swelling curve                    | $\kappa$  | 0.01           | 0.01            |
| Critical void ratio at unit pressure       | $e_{cs}$  | 2.78           | 3.14            |
| Poisson's ratio                            | $\mu'_0$  | 0.233          | 0.150           |
| Slope of critical state line on q-p' space | M         | 1.3            | 1.63            |
| Degradation parameter of overconsolidation | m         | 0.5            | 0.5             |
| Degradation parameter of cementation       | $m^*$     | 0.5            | 0.5             |

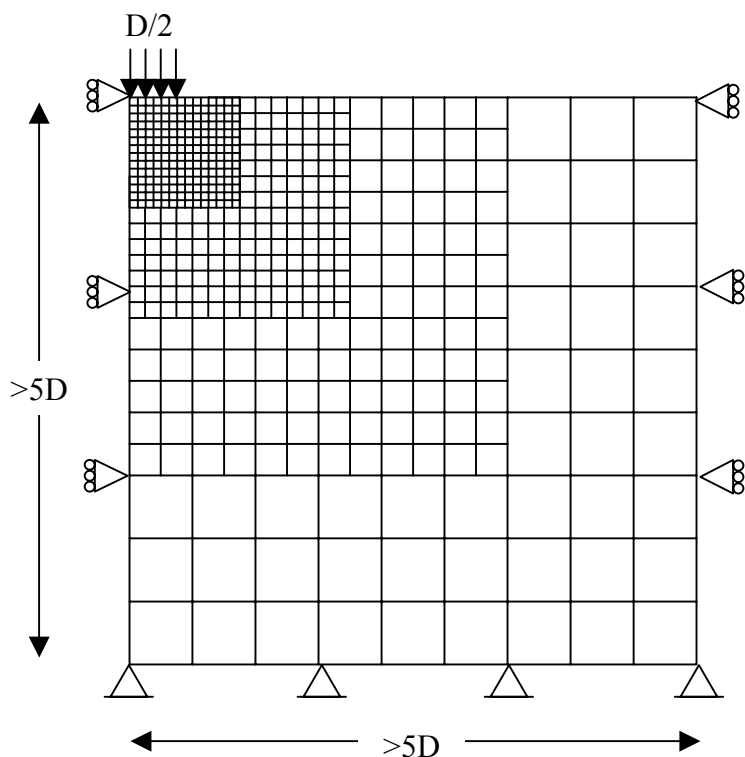
**Table 4.4: Significance of the MIT-S1 model parameters in the shallow foundation analysis**

| Test type                                 | Symbol       | Siliceous sand | Calcareous sand |
|---|--------------|----------------|-----------------|
| Compression test                          | $\rho_c$     | ✗              | ✗               |
|   | $p'_{ref}$   | ○              | ○               |
|   | $\theta$     | ○              | ○               |
| $K_0$ consolidation test                  | $K_{0NC}$    | -              | -               |
|   | $\mu'_0$     | ✗              | ✗               |
|   | $\omega$     | ✗              | ✗               |
| Shear test                                | $\phi_{cs}$  | ✗              | ✗               |
|   | $\phi'_{mr}$ | ○              | △               |
|   | $np$         | ○              | ✗               |
|   | $m$          | ○              | ○               |
|   | $\psi$       | ✗              | ✗               |
| Shear test with local measurement systems | $C_b$        | △              | ✗               |
|   | $\omega_s$   | △              | ✗               |

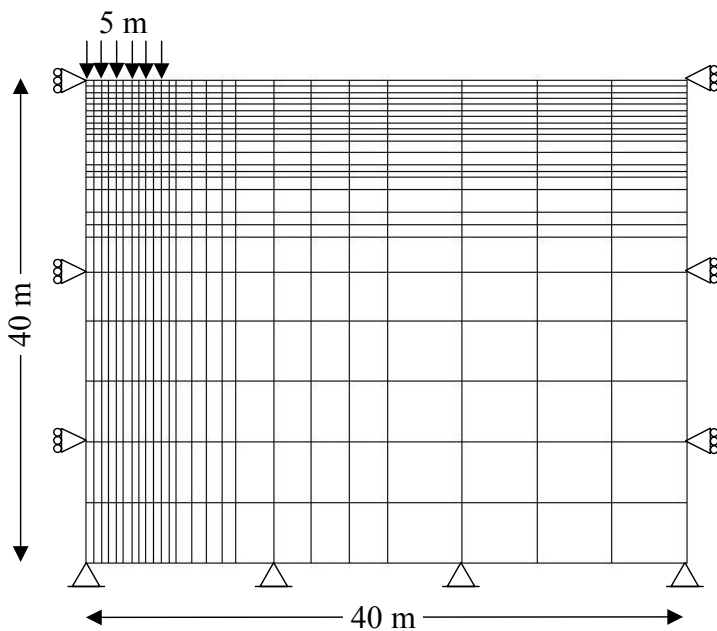
○: significant

△: slight

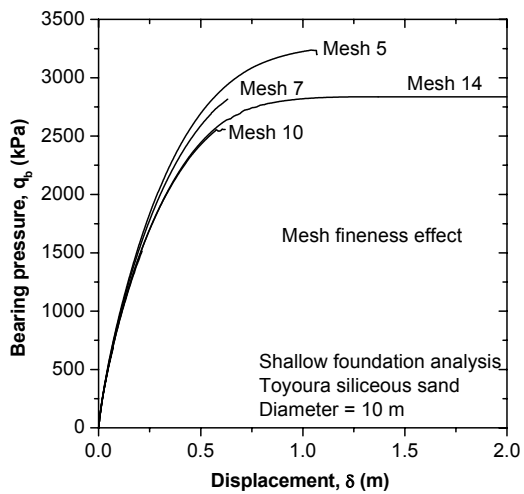
✗: negligible



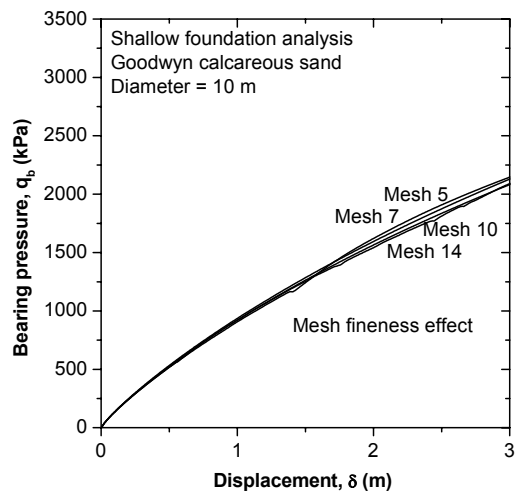
**Figure 4.1:** Finite element mesh for the ABAQUS analysis (MIT-S1 model)



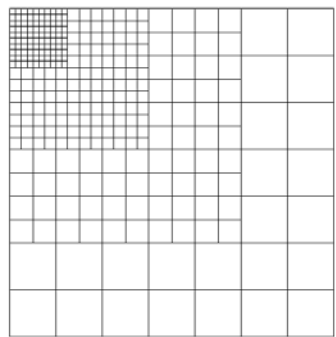
**Figure 4.2:** Finite element mesh for the AFENA analysis (Mohr-Coulomb, SU2 and Asaoka models)



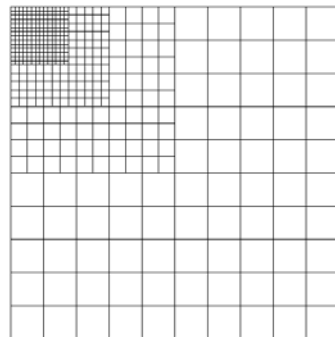
**(a) Siliceous sand**



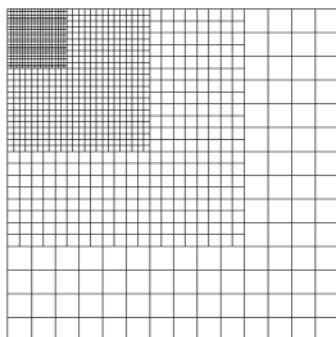
**(b) Calcareous sand**



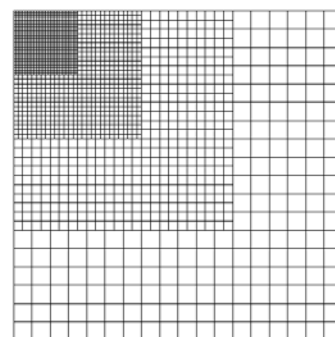
**Mesh 5**



**Mesh 7**



**Mesh 10**



**Mesh 14**

**Figure 4.3: Effect of mesh on bearing response**

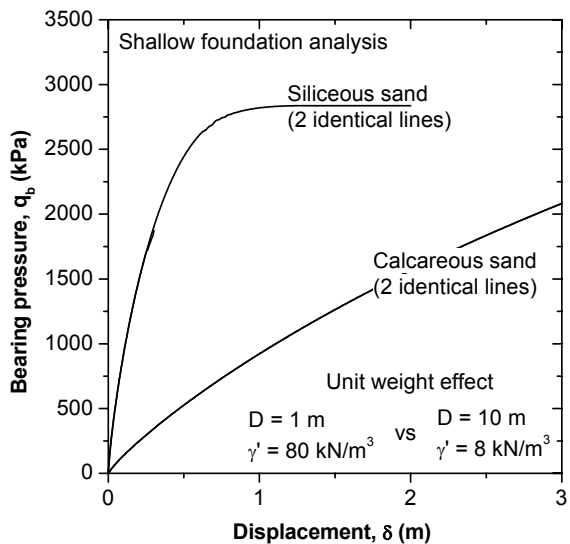


Figure 4.4: Modelling of models effect on bearing response

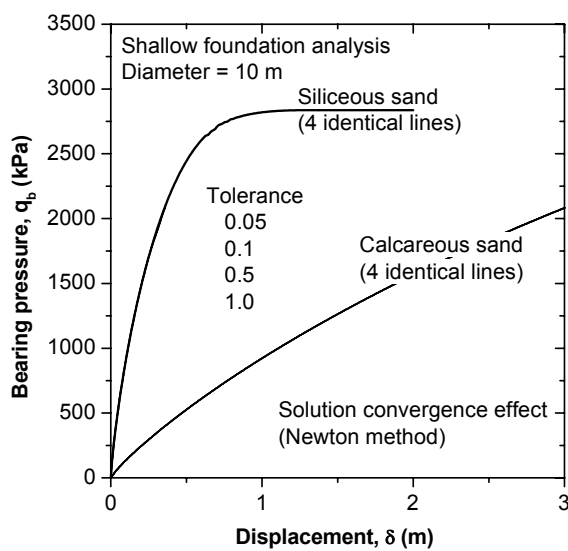
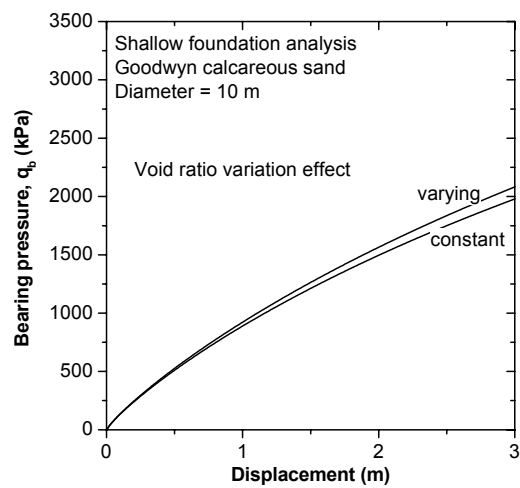
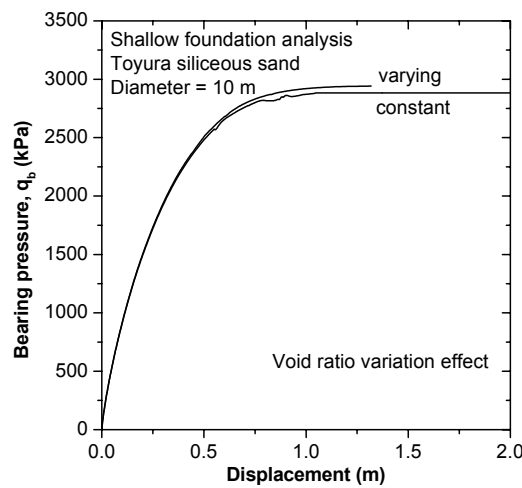
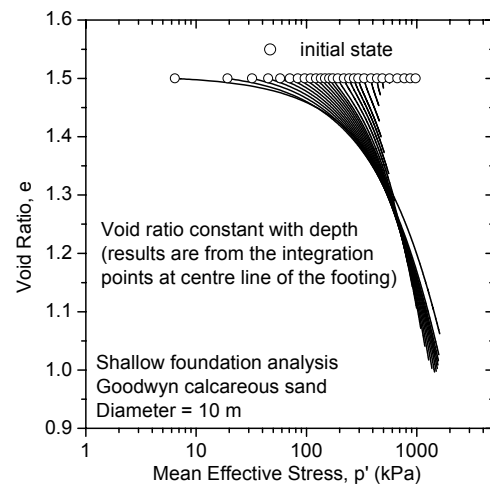
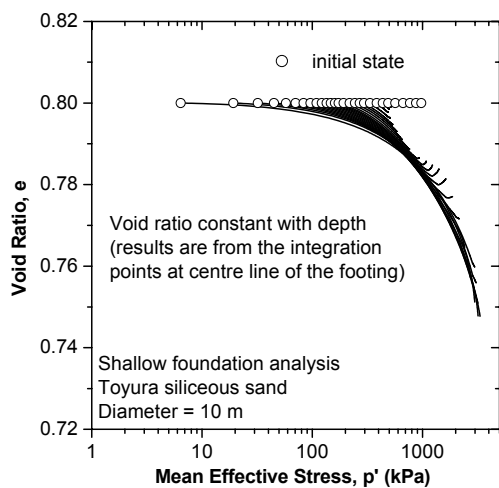


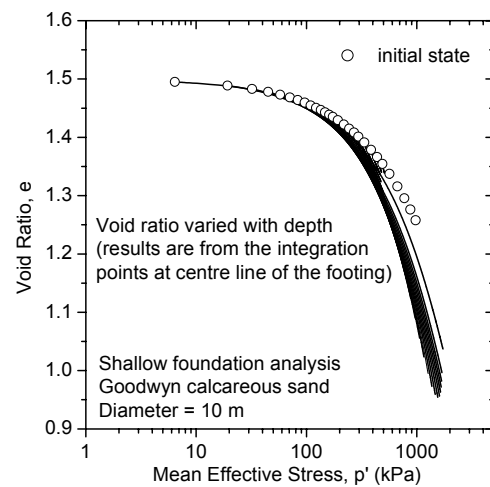
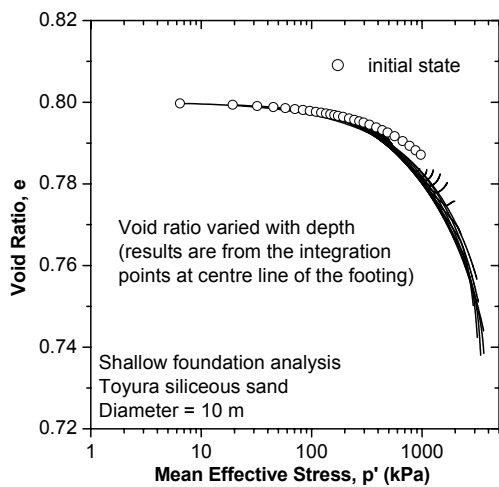
Figure 4.5: Solution convergence effect on bearing response



(a) Pressure-displacement curve

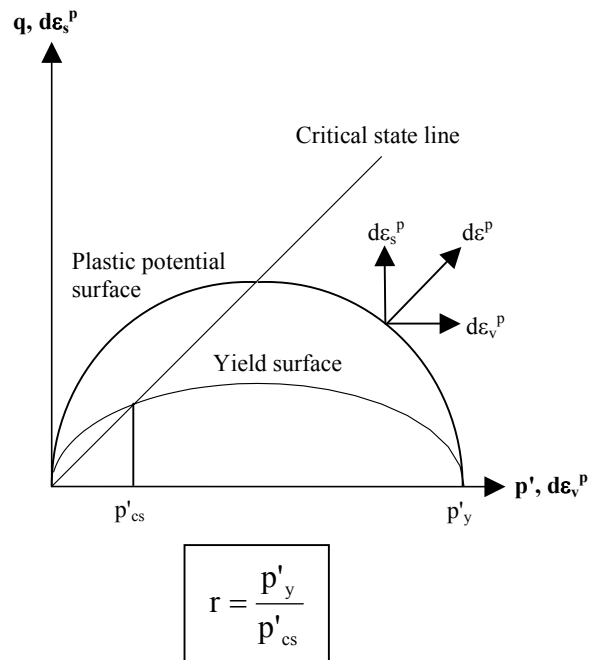


(b) volume change for initially constant void ratio

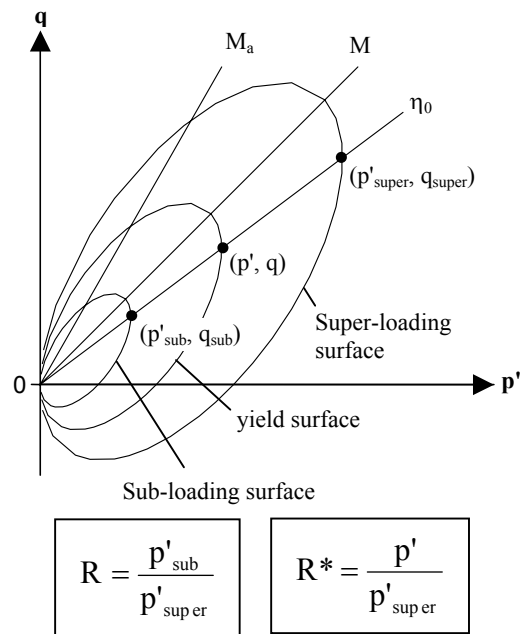


(c) volume change for initially varying void ratio

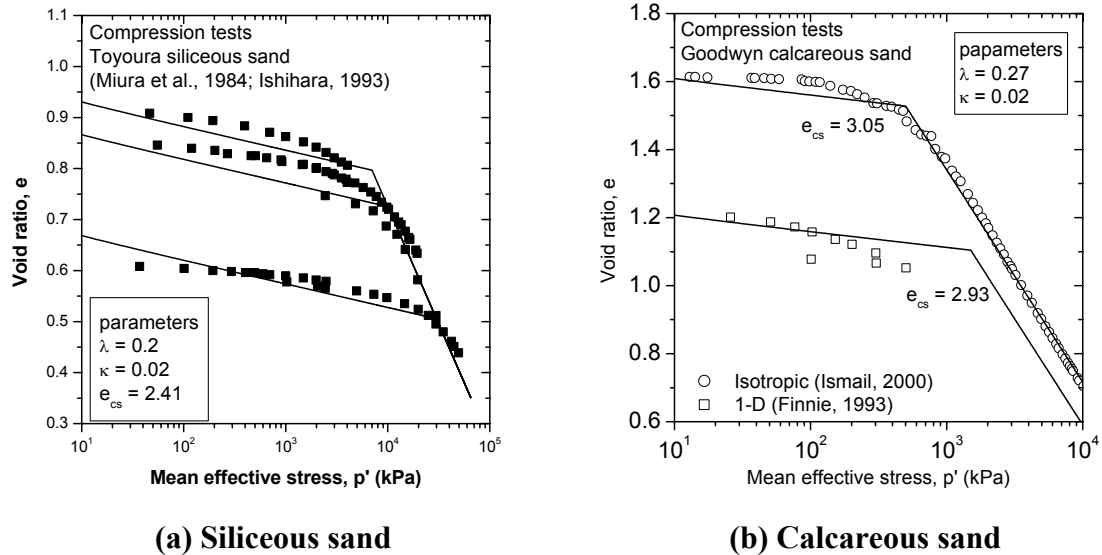
Figure 4.6: Void ratio variation effect on bearing response



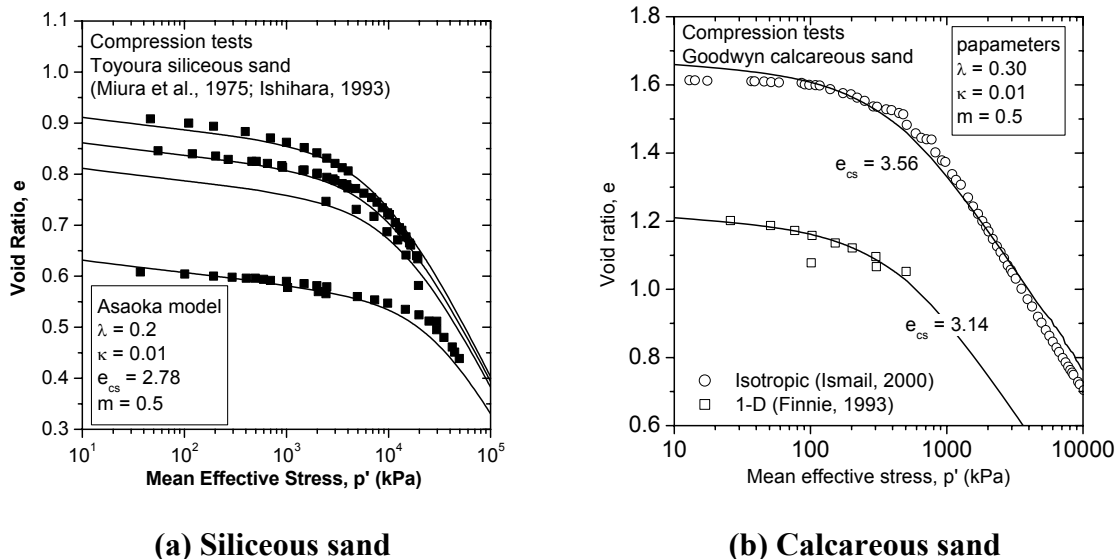
**Figure 4.7: Yield and plastic potential surfaces of SU2 model (after Islam 1999)**



**Figure 4.8: Yield and sub- and super-loading surfaces of Asaoka model (after Asaoka et al. 2002)**



**Figure 4.9: Estimation of compression parameters for SU2 model**



**Figure 4.10: Estimation of compression parameters for Asaoka model**

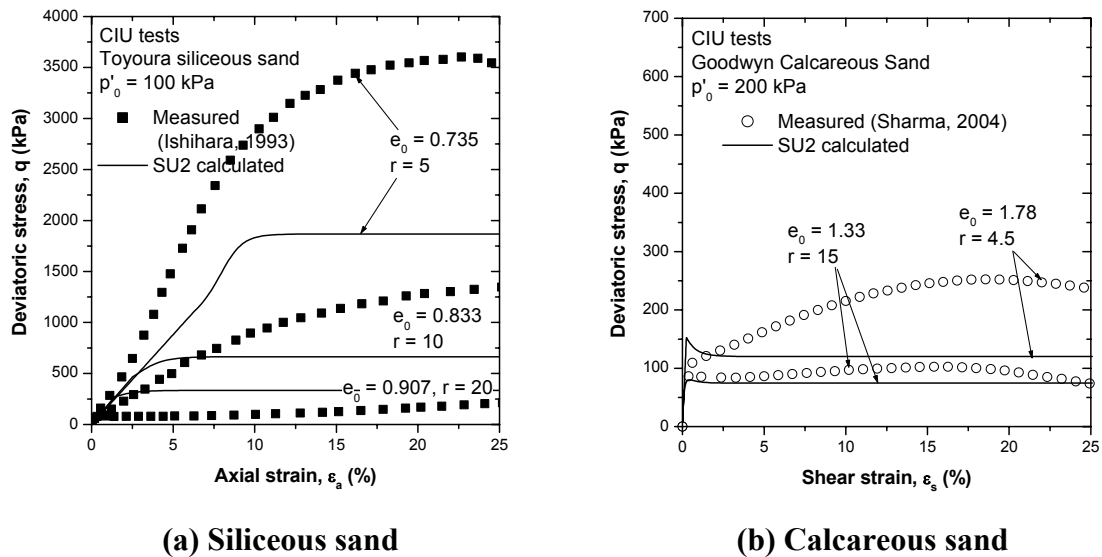


Figure 4.11: SU2 model predictions for CIU tests

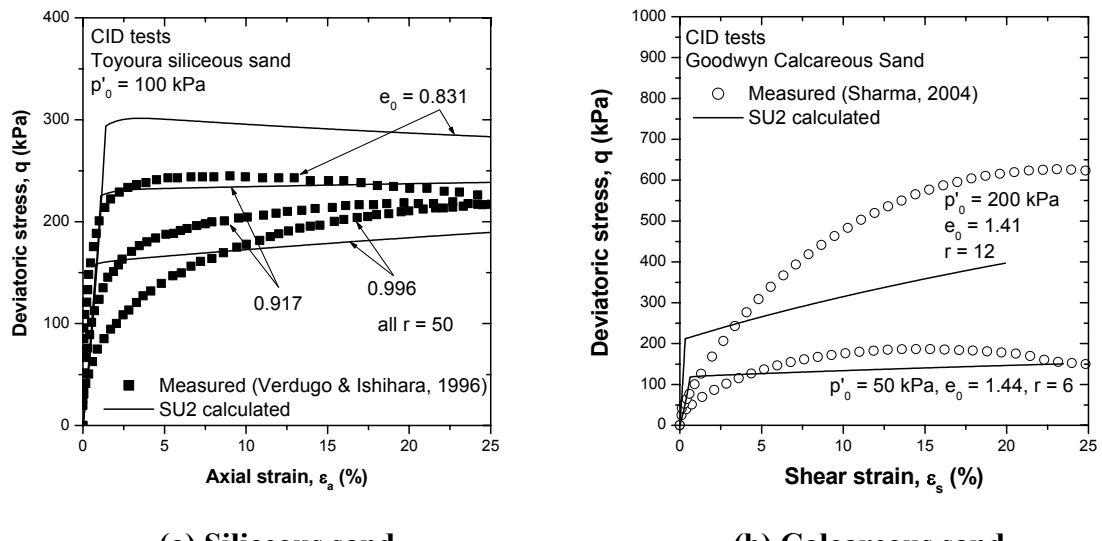
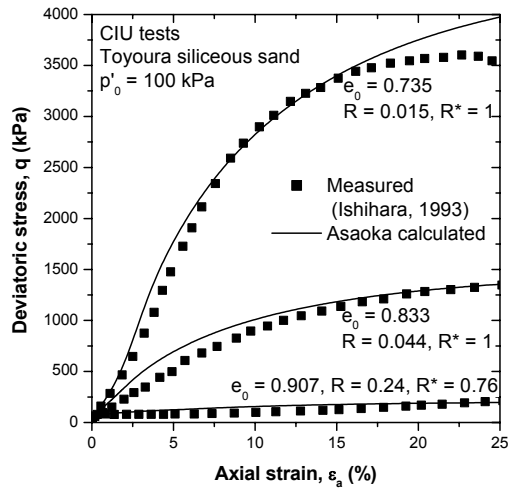
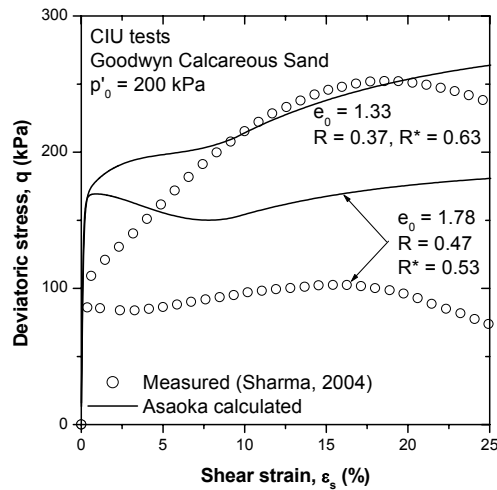


Figure 4.12: SU2 model predictions for CID tests

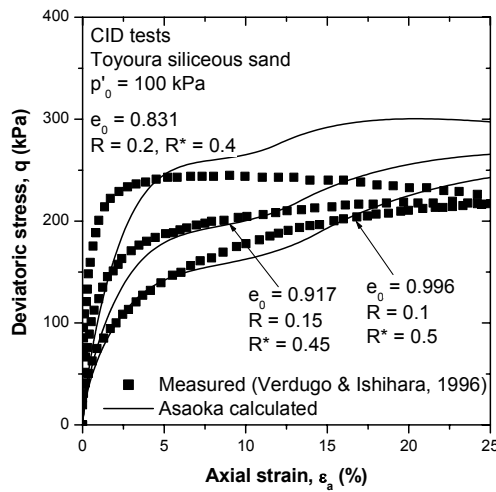


(a) siliceous sand

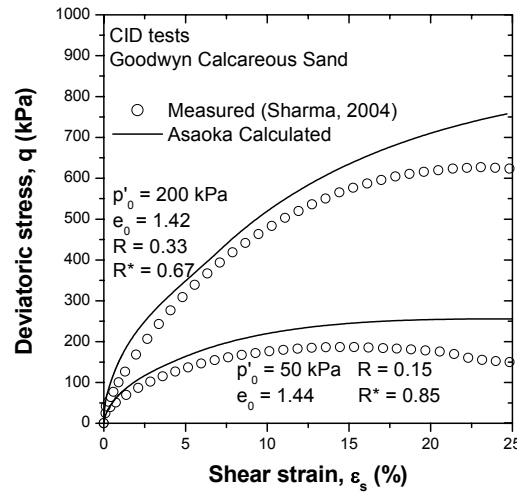


(b) calcareous sand

Figure 4.13: Asaoka model predictions for CIU tests

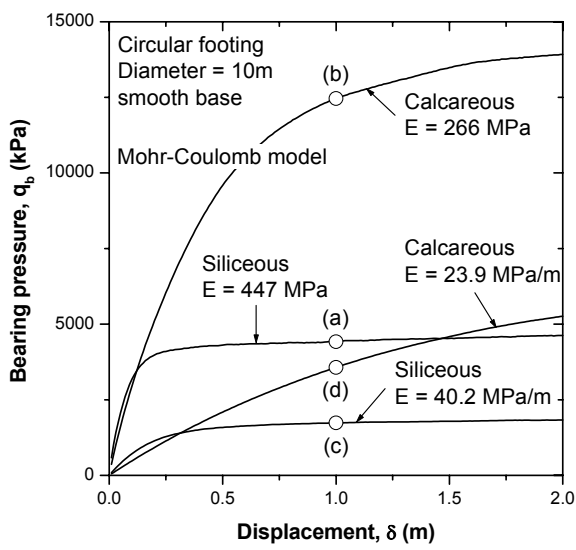
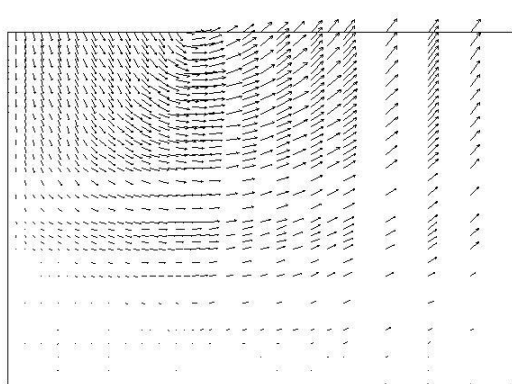
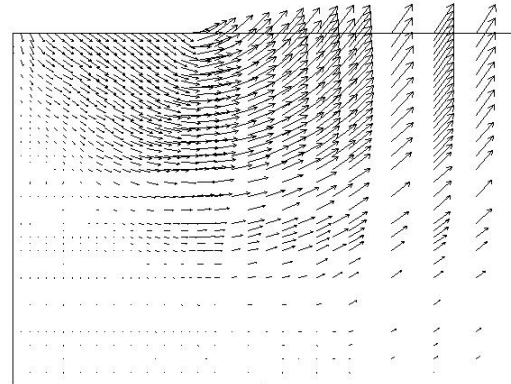
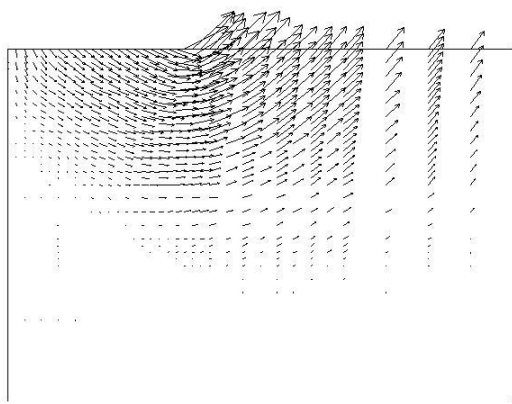
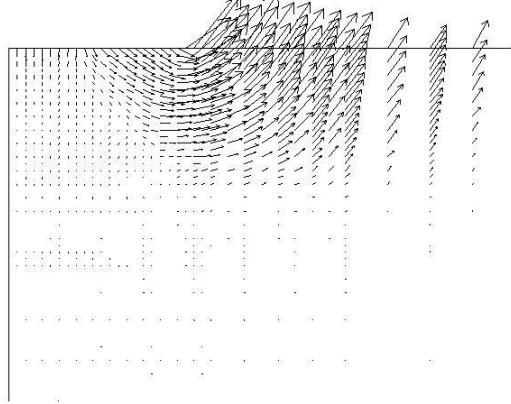


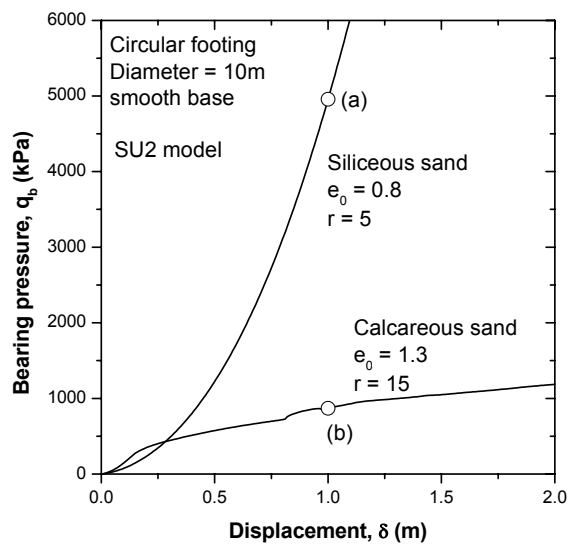
(a) siliceous sand



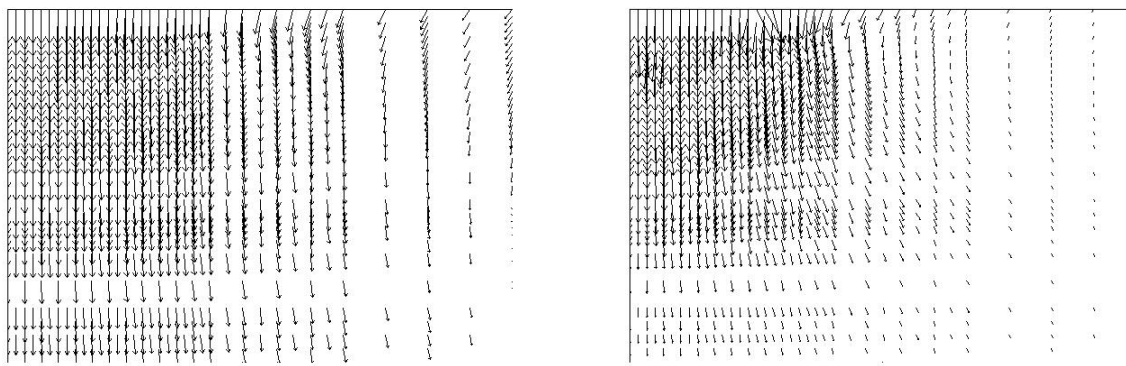
(b) calcareous sand

Figure 4.14: Asaoka model predictions for CID tests

**Pressure-displacement curve****(a) Siliceous, E constant****(b) Calcareous, E constant****(c) Siliceous, E variation****(d) Calcareous, E variation****Incremental displacement vectors****Figure 4.15: Mohr-Coulomb model predictions for shallow circular footings**



**Pressure-displacement curve**

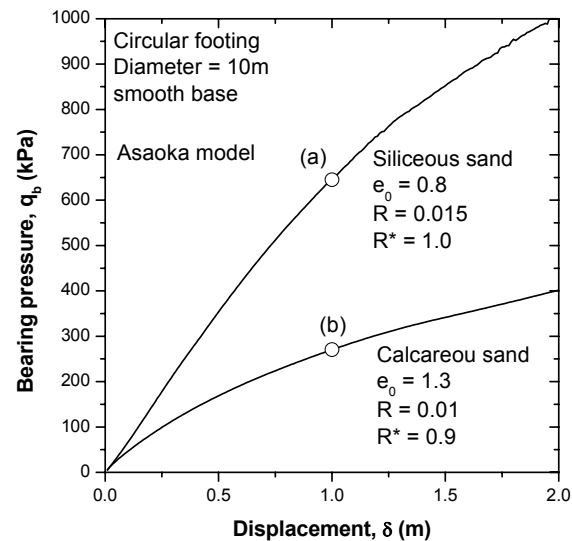


**(a) Siliceous sand**

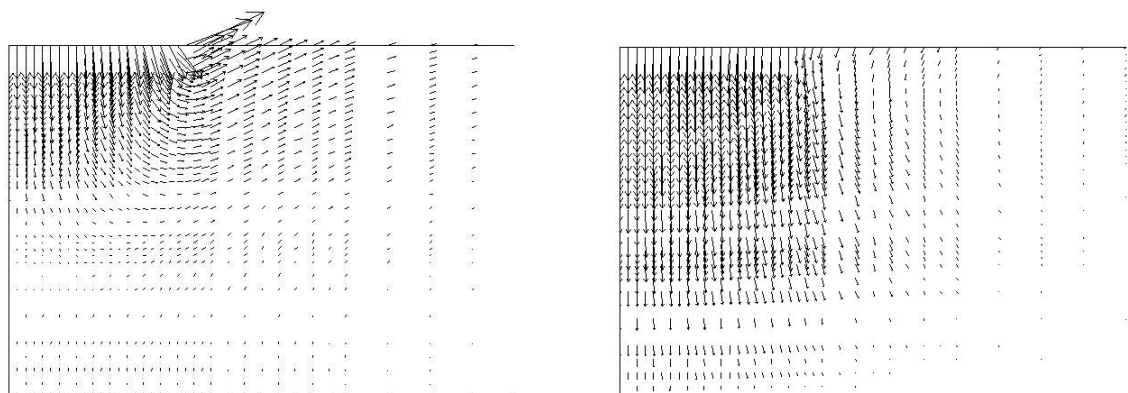
**(b) Calcareous sand**

**Incremental displacement vectors**

**Figure 4.16: SU2 model predictions for shallow circular footings**



**Pressure-displacement curve**

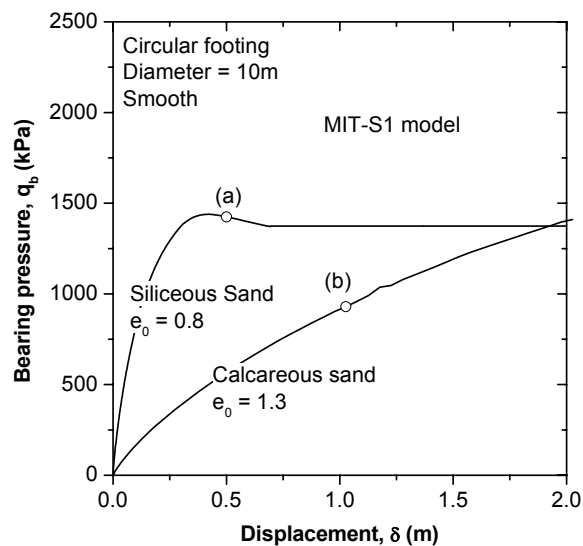


**(a) Siliceous sand**

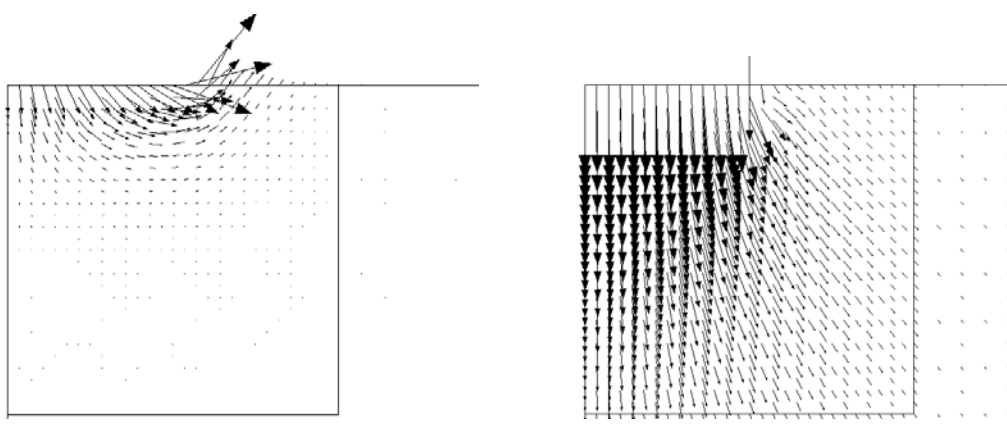
**(b) Calcareous sand**

**Incremental displacement vectors**

**Figure 4.17: Asaoka model predictions for shallow circular footings**



**Pressure-displacement curve**

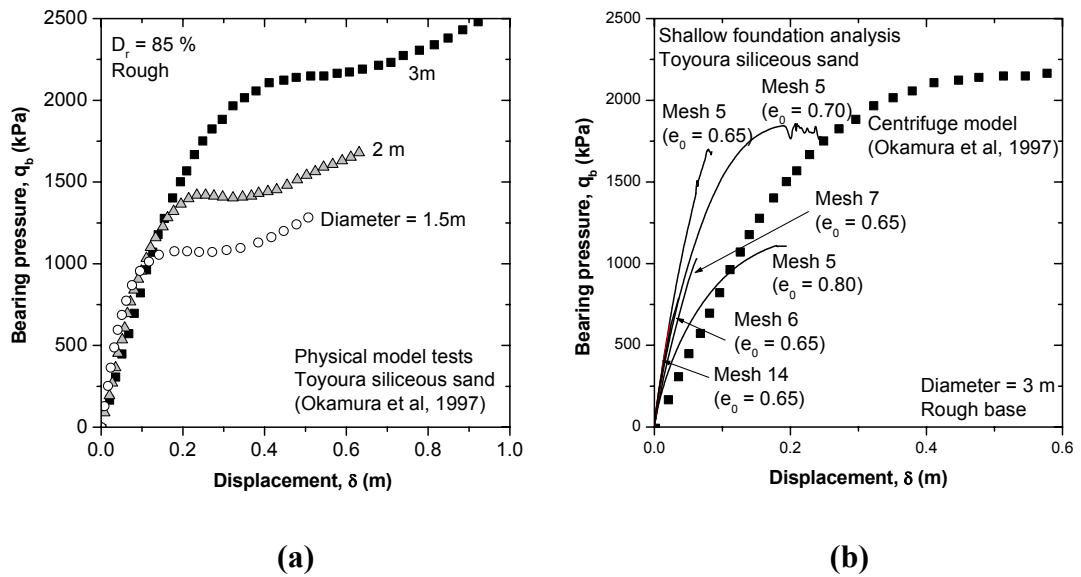


**(a) Siliceous sand**

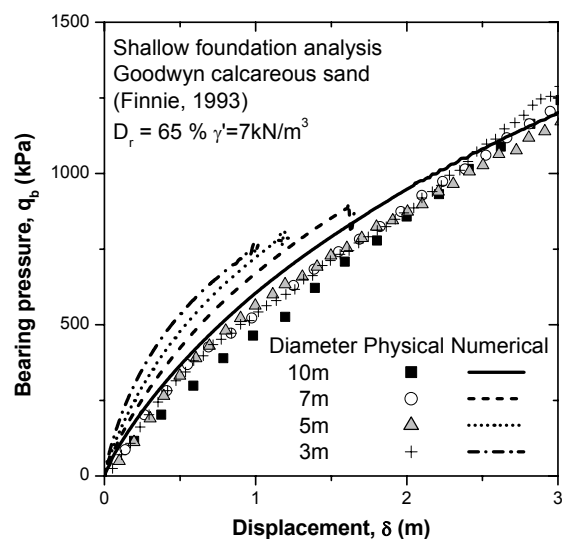
**(b) Calcareous sand**

**Incremental displacement vectors**

**Figure 4.18: MIT-S1 model predictions for shallow circular footings**



**Figure 4.19: MIT-S1 predictions for physical model results on Toyoura siliceous sand**



**Figure 4.20: MIT-S1 predictions for physical model results on Goodwyn calcareous sand**

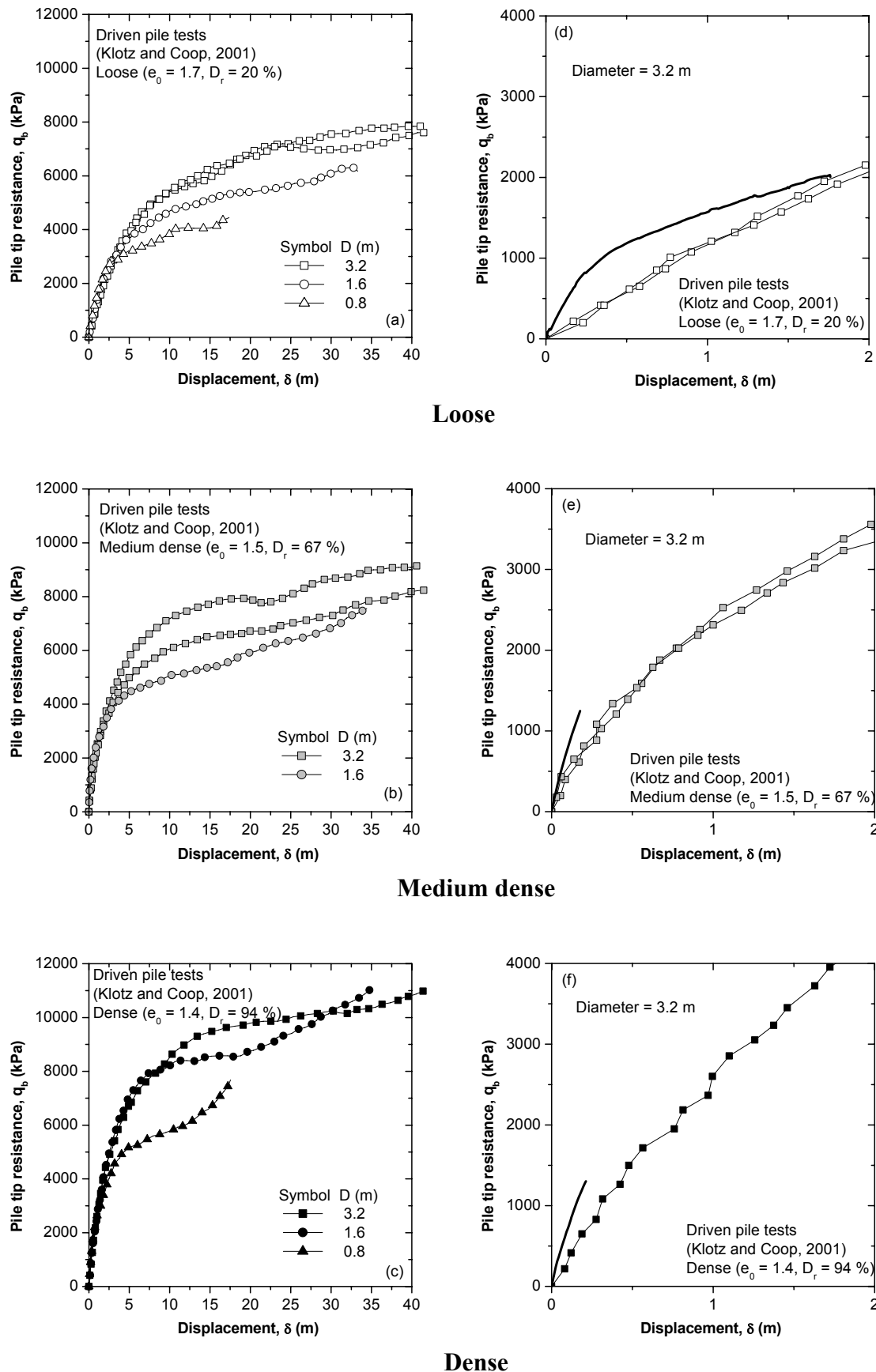
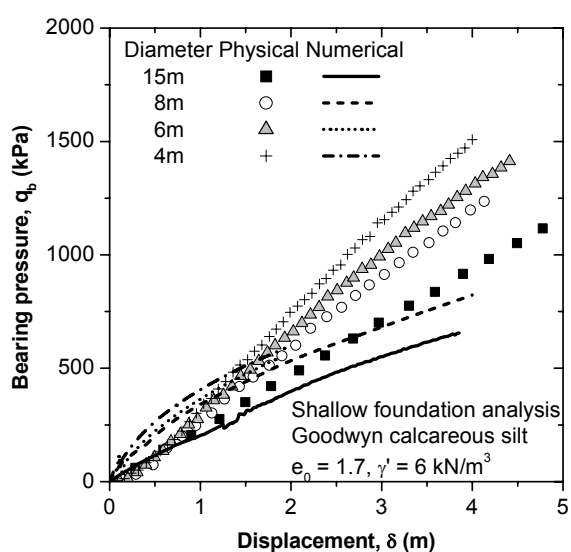
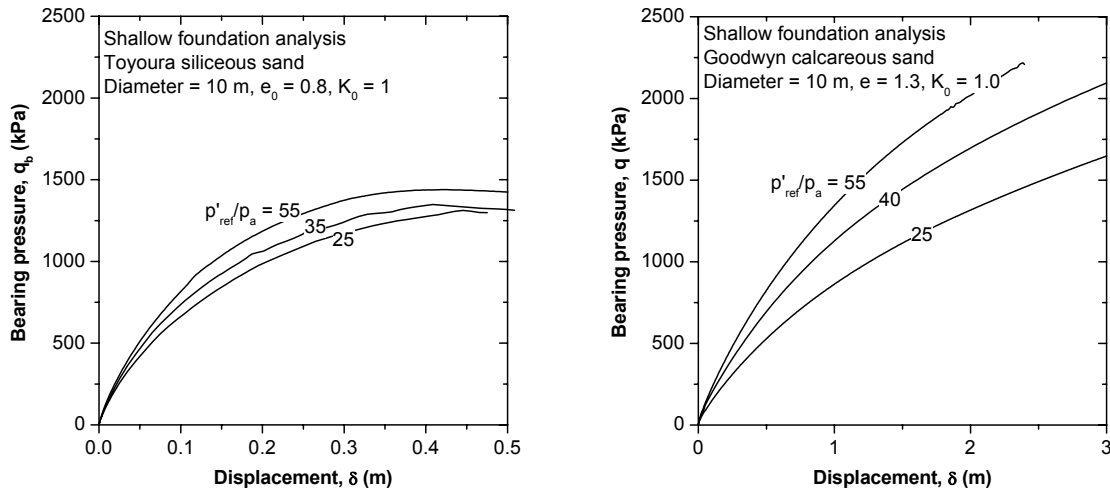


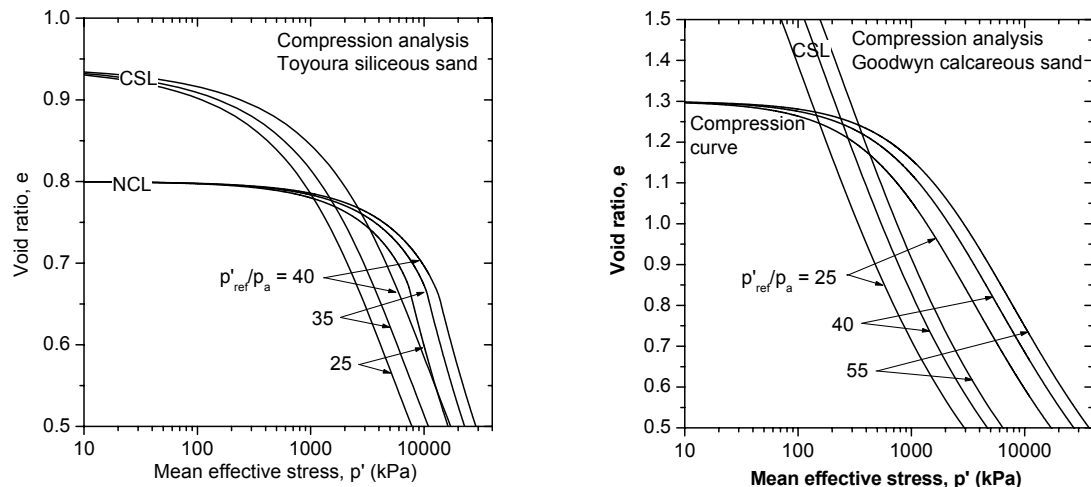
Figure 4.21: MIT-S1 predictions for physical model results on Dogs Bay calcareous sand



**Figure 4.22: MIT-S1 predictions for physical model results on Goodwyn calcareous silt**



(a) Pressure-displacement curve



(b) Compression curve & CSL

Figure 4.23: Effect of  $p'_{ref}$  on bearing response

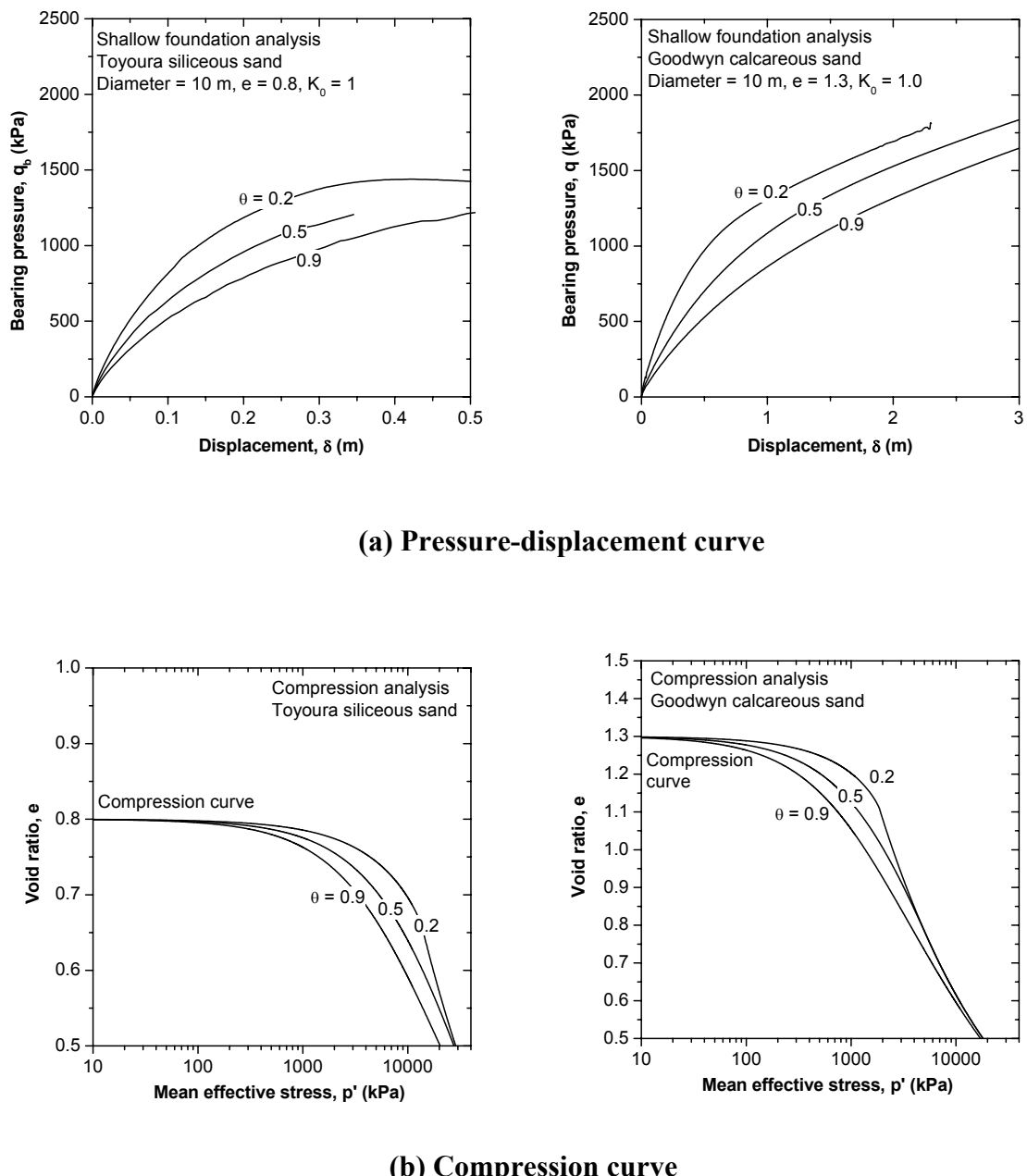


Figure 4.24: Effect of  $\theta$  on bearing response

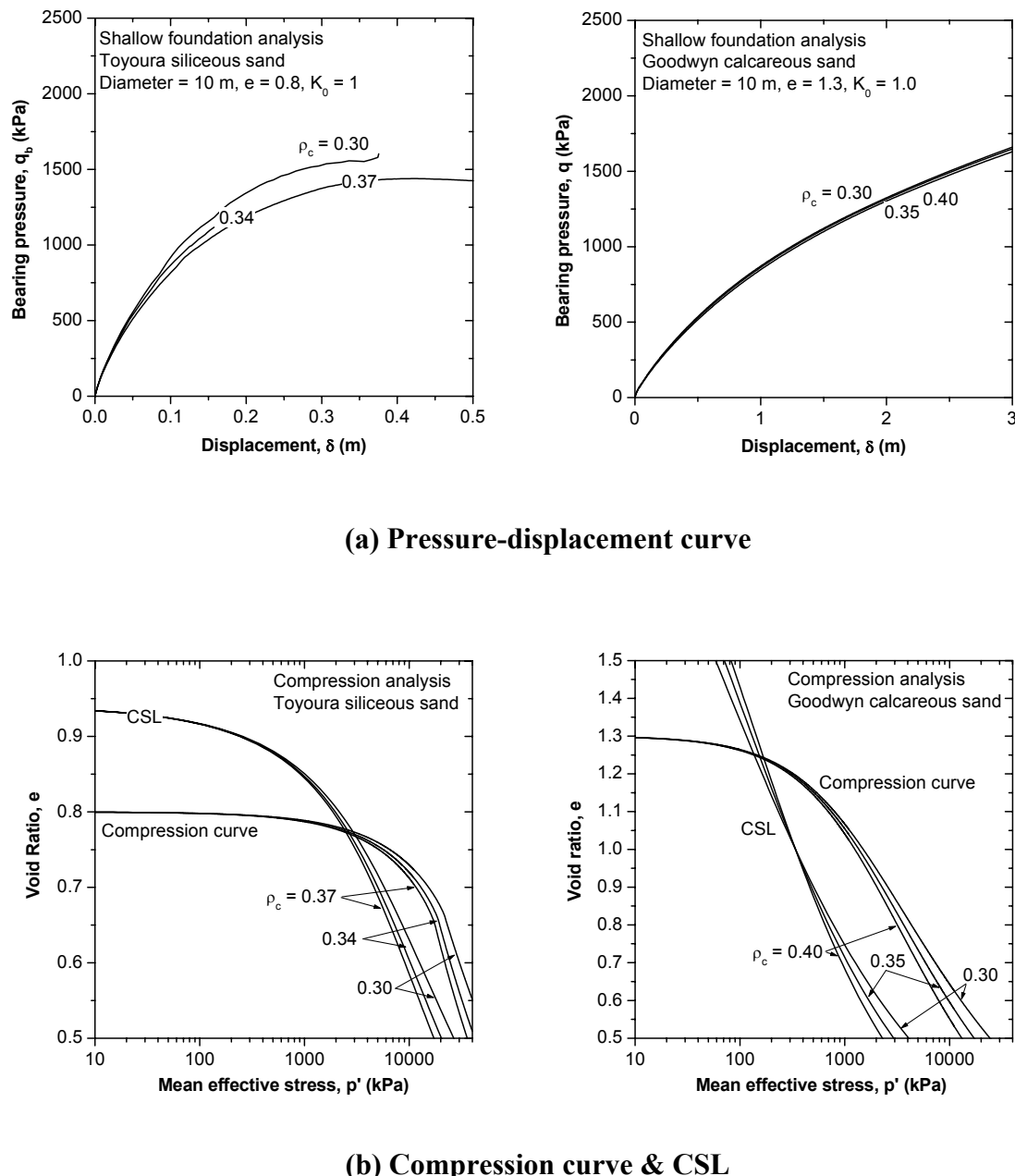
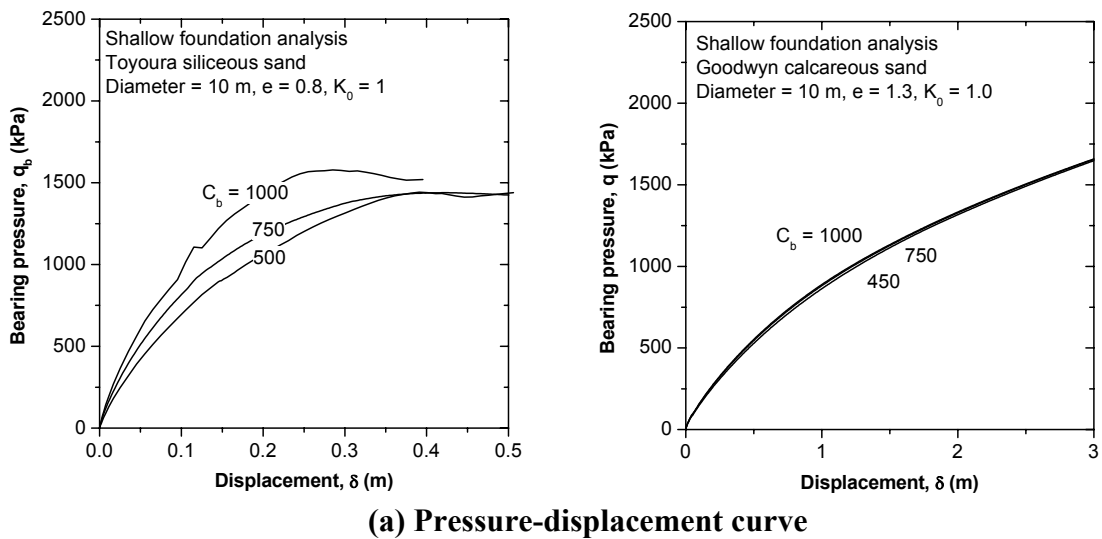
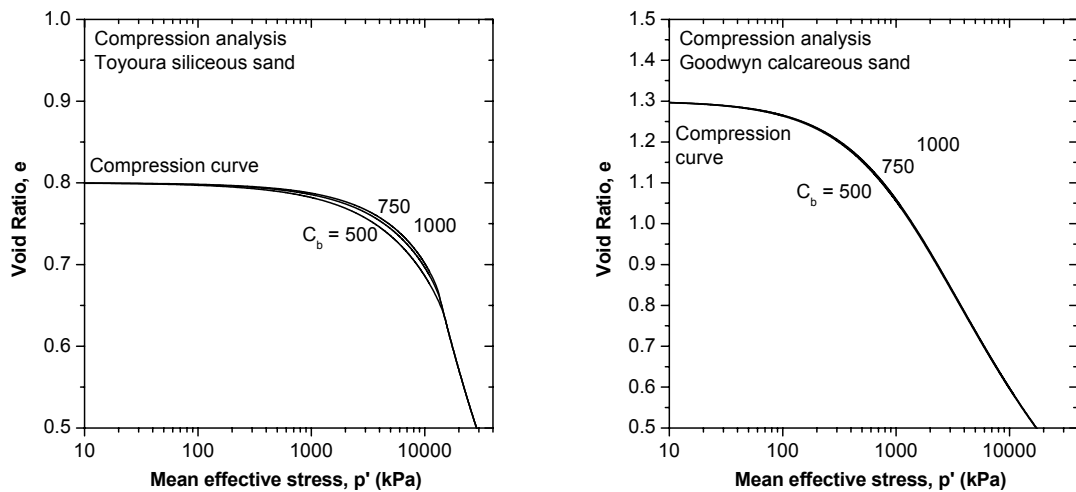


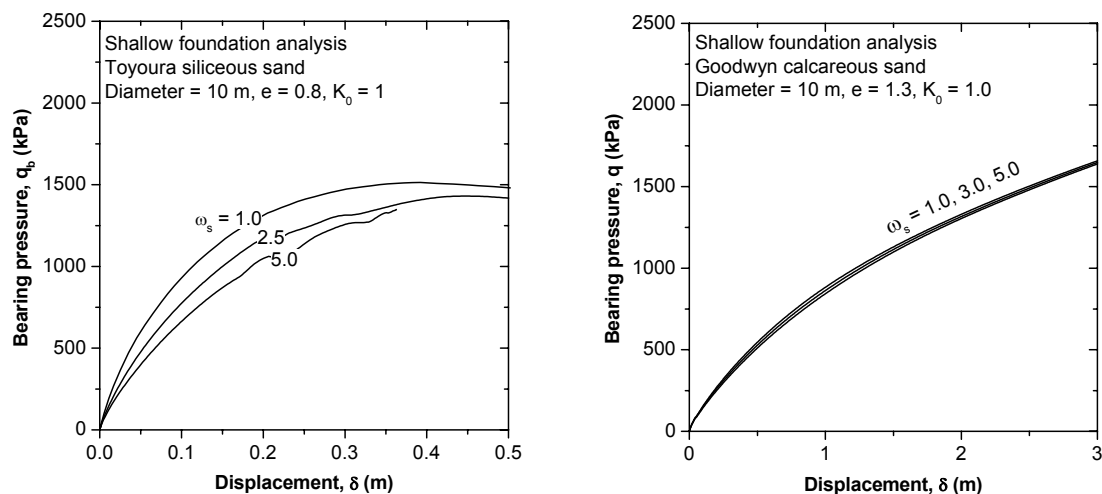
Figure 4.25: Effect of  $\rho_c$  on bearing response

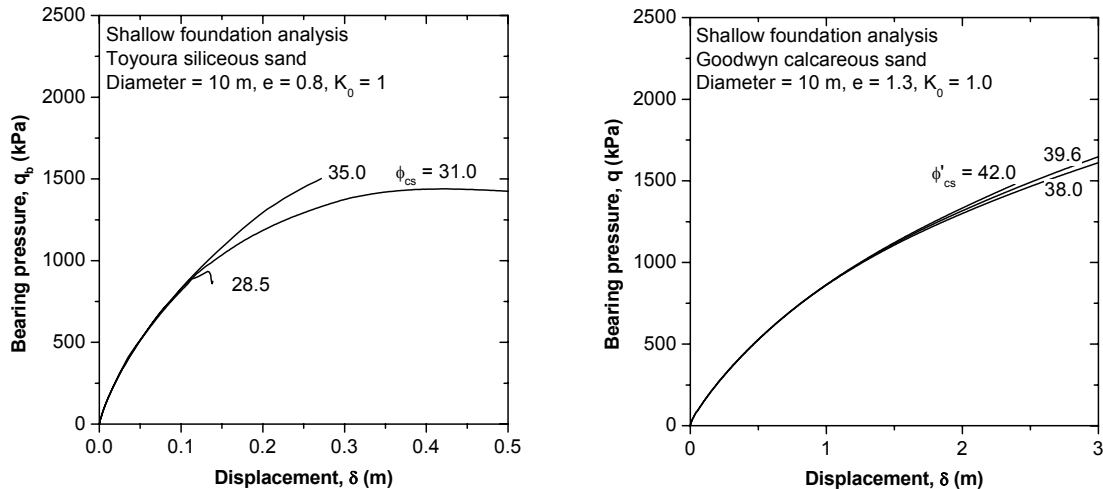


(a) Pressure-displacement curve

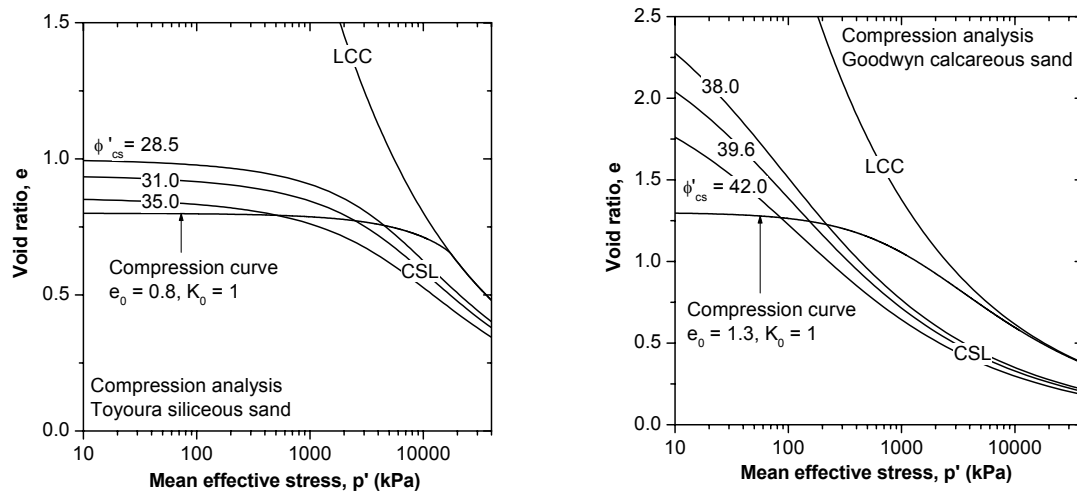


(b) Compression curve

 Figure 4.26: Effect of  $C_b$  on bearing response

 Figure 4.27: Effect of  $\omega_s$  on bearing response

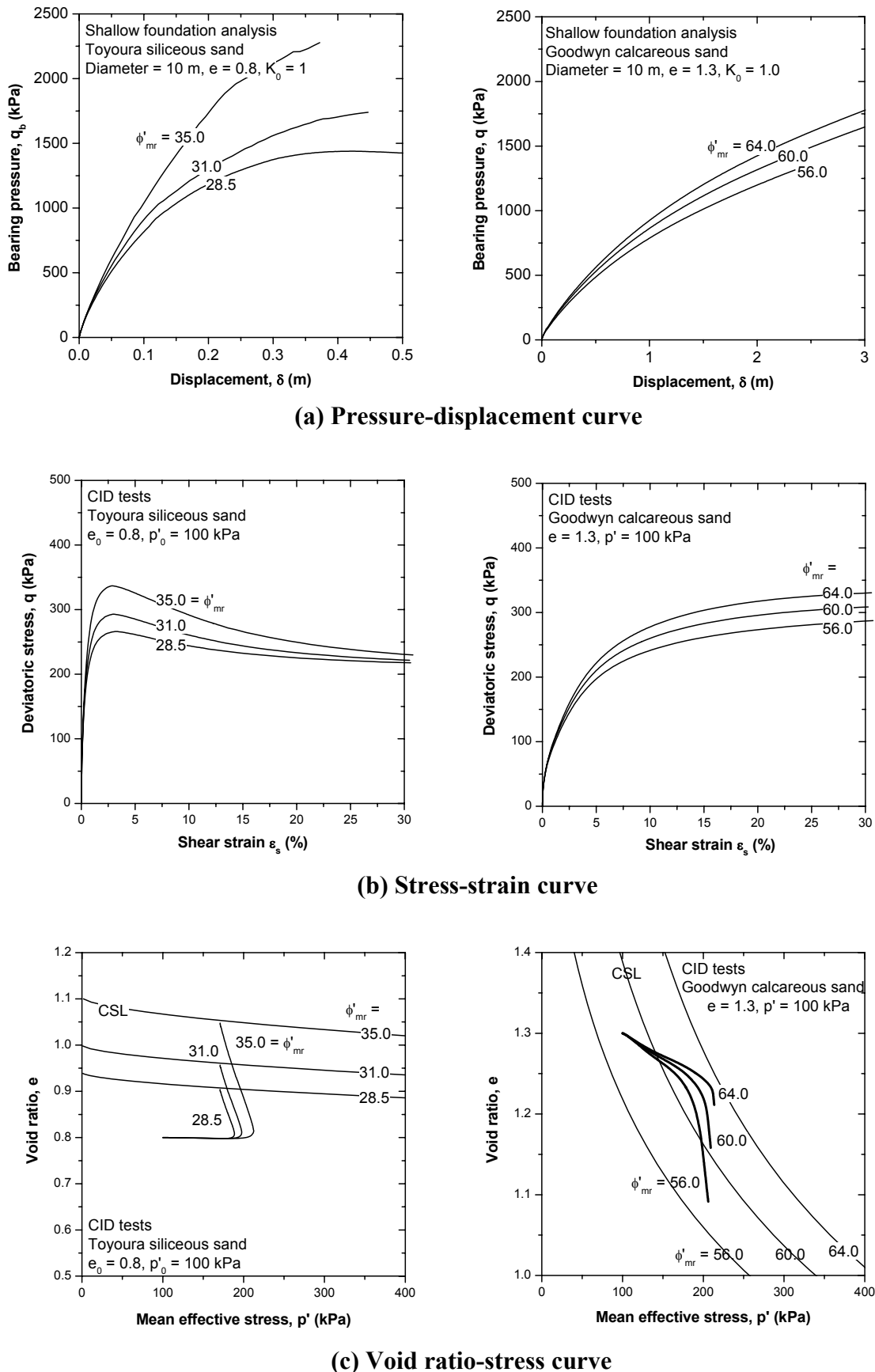


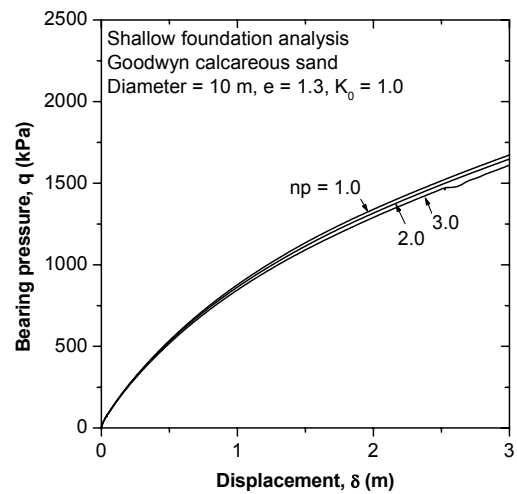
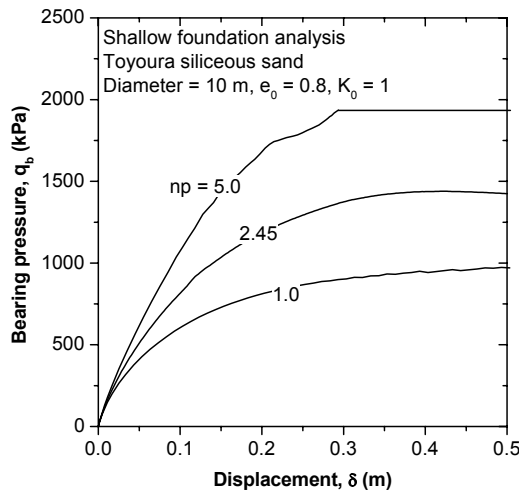
(a) Pressure-displacement curve Siliceous sand



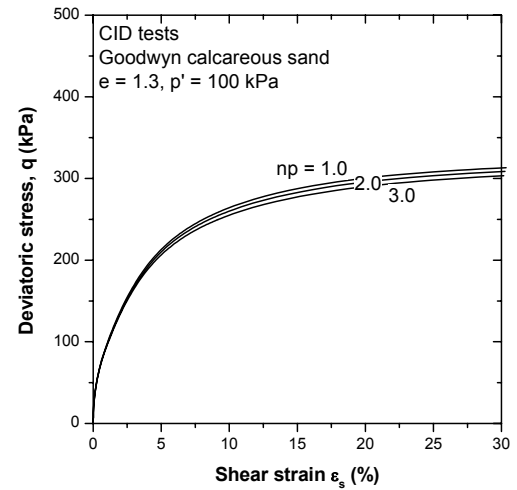
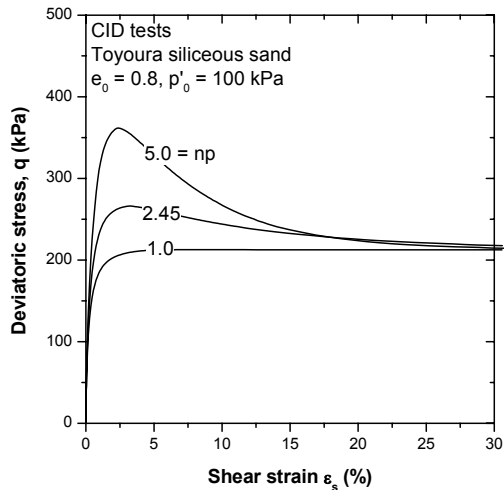
(b) Void ratio-stress curve

Figure 4.28: Effect of  $\phi'_{cs}$  on bearing response

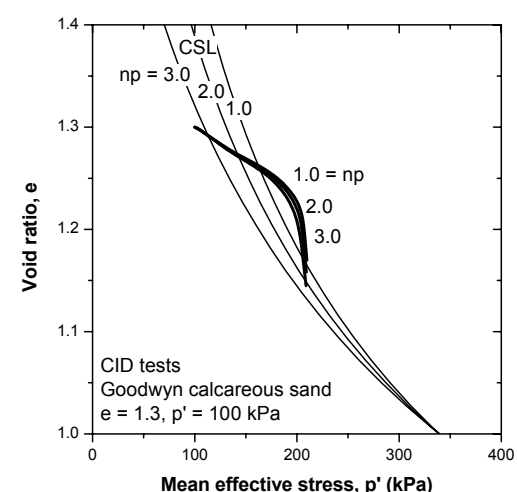
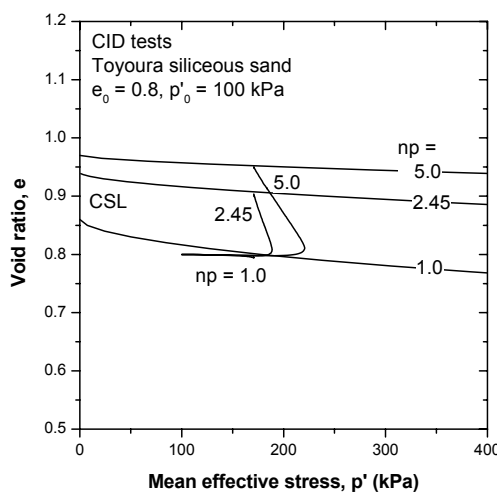
Figure 4.29: Effect of  $\phi'_{mr}$  on bearing response



(a) Pressure-displacement curve

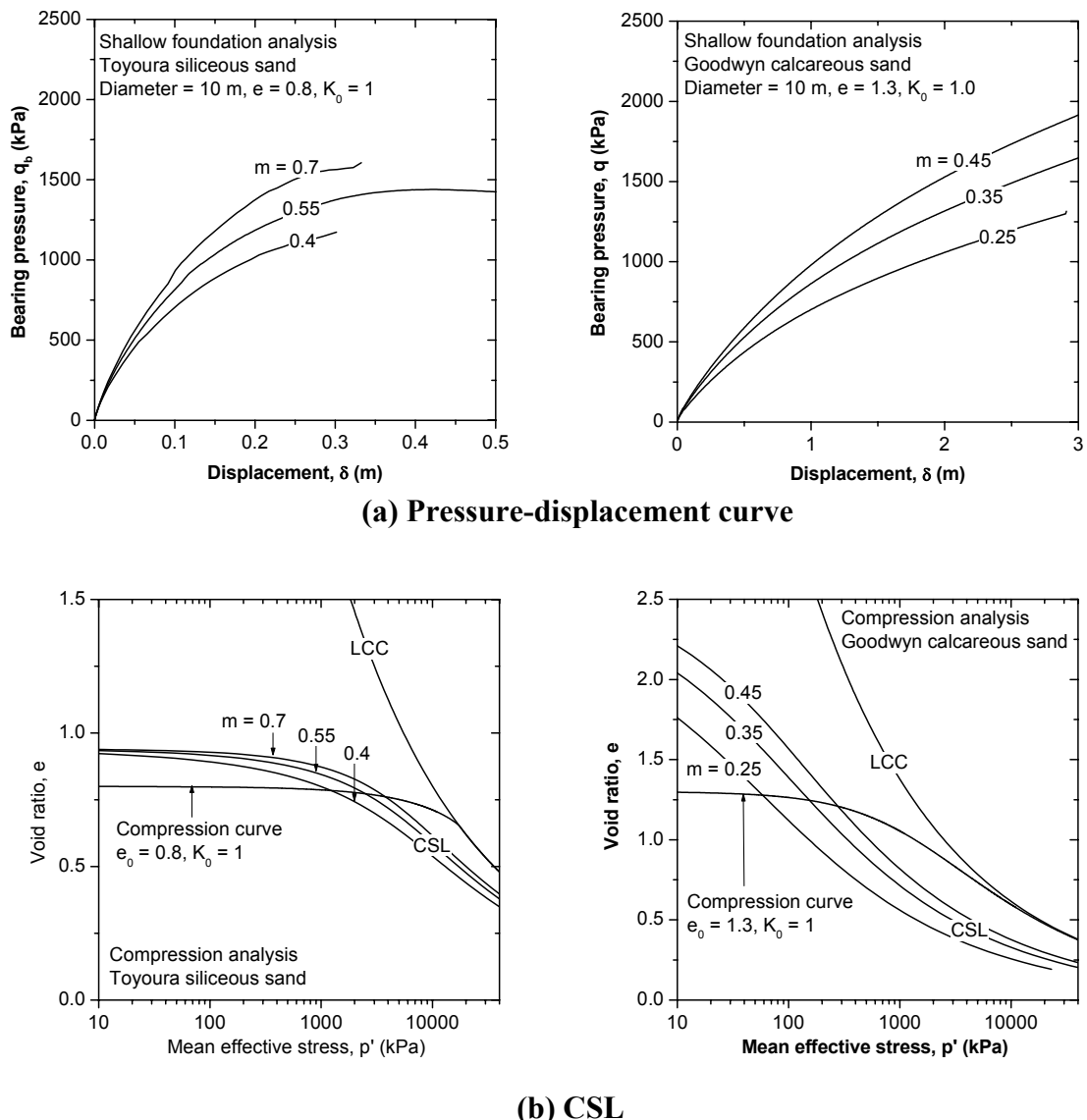
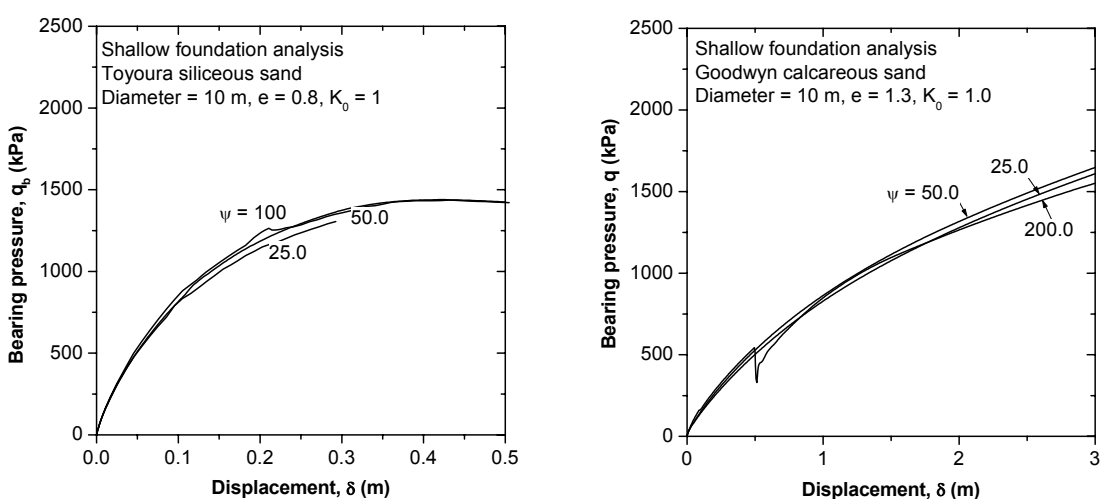


(b) Stress-strain curve



(c) Void ratio-stress curve

Figure 4.30: Effect of  $np$  on bearing response


 Figure 4.31: Effect of  $m$  on bearing response

 Figure 4.32: Effect of  $\psi$  on bearing response



# **Chapter 5**

## **The Effects of Soil and Foundation Properties on Shallow Foundation Performance**

### **5.1 INTRODUCTION**

Among the models explored in the previous chapter, the MIT-S1 model has been found most suitable for the analysis of shallow foundations on sand. The model simulates relatively well both the compression and shear behaviours of natural sands over a wide range of densities,  $K_0$  values and confining pressures using only a single set of the model parameters. **Chapter 4** also showed that this model is able to distinguish between the shallow foundation responses of siliceous and calcareous sands by appropriate choice of the model parameters.

This chapter provides a numerical investigation of the effects of soil and foundation variables on the shallow foundation response on siliceous and calcareous sands using the MIT-S1 model. Before proceeding to examine the shallow foundation problems in detail, effects of stress level, density and  $K_0$  on the strength characteristics of siliceous and calcareous sands using triaxial drained shear test results are discussed. Then, results from shallow foundation simulations using the MIT-S1 model for siliceous and calcareous sands are presented followed by a discussion of the effect of foundation size in terms of the bearing capacity factor for the self-weight component,  $N_\gamma$ .

### **5.2 EFFECTS OF STRESS LEVEL AND DENSITY ON COMPRESSION AND STRENGTH CHARACTERISTICS OF SILICEOUS AND CALCAREOUS SANDS**

This section describes the effects of initial confining pressure and void ratio on isotropic compression and drained triaxial shear tests on siliceous and calcareous sands. Two features are described: a) mechanical distinctions of siliceous and calcareous sands; and

b) stress and density-dependency of the shear strength. The former describes a methodology based on the MIT-S1 model for distinguishing between the strong dilatancy of siliceous sand and the high compressibility of calcareous sand. The latter is discussed in terms of the curvilinear strength envelope in Mohr-Coulomb stress space.

### **5.2.1 Compression behaviour**

The predictions of compression curves using the MIT-S1 model shown in **Figure 5.1** reveal that the initial density states and the location of their terminal state lines, such as the LCC for siliceous and calcareous sands, are significantly different. Calcareous sand samples have initially higher void ratios than siliceous sand samples. During compression, the volume reduction of the calcareous samples is significantly greater than for siliceous samples.

The CSLs of both sands also exhibit significant differences in their locations and shapes. This difference is an important aspect that allows the MIT-S1 model to distinguish between siliceous and calcareous sands. The siliceous samples with  $e_{min}$  and  $e_{max}$  approximately of 0.5 and 1.0 remain in a dilative state (to the left of the CSL) even for extremely high confining pressures. On the other hand, the calcareous sands with a range of initial void ratio from 1 to 2 move rapidly to the contractive side (to the right of the CSL).

### **5.2.2 Shear behaviour**

**Figure 5.2** shows MIT-S1 predictions for CID tests on Toyoura siliceous sand samples with different initial densities but constant confining stress (100 kPa). Apparent peak stresses are found at relatively small strain levels and the stress-strain responses at large strain levels (i.e. at the critical state) (**Figure 5.2(b)**). It is also noticed that loose and extremely loose samples ( $e_0 = 0.8$  and  $0.95$ ) are initially located close to or above the CSL and show contractive behaviour.

On the other hand, all calcareous samples under the same test conditions as the siliceous sand show contractive behaviour because the initial void ratios of all samples stay on the contractive side (**Figure 5.3**). At large strain, the responses do not merge into the

critical state. The difficulty in identifying a critical state condition for calcareous sand from drained triaxial tests has been noted by several authors (Airey et al., 1988; Golightly and Hyde, 1988; Semple, 1988), as indicated in previously presented experimental results (e.g. **Figure 3.6, 3.21 or 3.30**).

CID test results for samples with varying initial confining pressures (**Figure 5.4** and **5.5**) give an additional understanding for the significance of the CSL location. The siliceous sand samples generally dilate up to  $p'_0 = 500$  kPa. However, the calcareous sand samples present contractive behaviour even at very low stress levels (30 kPa).

### 5.2.3 Peak friction angle and dilatancy

The effects of stress level and density can be more clearly described with a relationship of the peak friction angle,  $\phi'_p$ , against either initial confining pressure or void ratio. **Figure 5.6** illustrates the relationship of  $(\phi'_p - \phi'_{cs})$  against the confining stress and void ratio for a) Toyoura siliceous, b) Dogs Bay calcareous and c) Goodwyn calcareous sands.

The peak friction angles at lower stress levels for Toyoura siliceous sand are nearly constant (**Figure 5.6(a)**), as reported experimentally by Fukushima and Tatsuoka (1984). Then they gradually decrease with increasing confining pressure and eventually converge to critical state values (i.e.  $\phi'_p - \phi'_{cs} = 0$ ) at ‘critical stresses’ as suggested by Vesic and Clough (1968). It is noticed that the critical stress decreases as the density decreases. The peak friction angles of calcareous sands (**Figure 5.6(b)** and **5.6(c)**) also depend on the combined influence of the initial void ratio and mean effective stress. However, they are not constant at low stress levels but decrease rapidly with increasing mean effective stress. The critical stresses of calcareous sands are significantly lower than those for siliceous sand.

The relationship of  $(\phi'_p - \phi'_{cs})$  is fully consistent with the familiar curved shear strength envelopes for granular material on shear stress-normal effective stress space (**Figure 5.7**). The  $(\phi'_p - \phi'_{cs})$  values are, in this case, plotted against the mean effective stress at failure,  $p'_f$ . The curvilinear strength envelope in **Figure 5.7(b)** corresponds to the relationship of  $(\phi'_p - \phi'_{cs})$  and  $p'_f$  in **Figure 5.7(a)**. The critical stress essentially reduces

as the density decreases, or the material becomes more compressible, and the curved shear strength envelopes approach asymptotically to the linear critical state friction angle envelope.

#### **5.2.4 Discussion**

Numerical simulations of compression and shear behaviours for calcareous and siliceous sands have been presented. The effects of stress level and density of sands are clearly observed in the relationship of the peak friction angle against the initial mean effective stress and void ratio. It is shown that at a mean effective stress of less than 100 kPa, the peak friction angles of siliceous sand decrease slowly with increasing stresses, while those for calcareous samples decrease dramatically.

The variation of peak friction angle raises questions on the applicability of conventional bearing capacity theories, which are based on constant friction angle with depth (normalised by foundation size). For example, an analysis of a 10 m diameter foundation with practical settlement limits of 5 to 10 % of foundation diameter (or width) may be based on initial stresses of 40 kPa (multiplying half of the diameter, 5 m, by a soil unit weight of 8 kN/m<sup>3</sup>). However, when the same settlement level is applied to a 100 m diameter foundation, the corresponding stress level is simply 10 times (400 kPa) that for the 10 m diameter footing. At that stress level, the peak friction angles are no longer constant with depth. The peak friction angles for calcareous sands are obviously not constant at 40 kPa, thus for this sand the conventional bearing capacity formulae do not fit even for a moderate foundation size.

The relationship of peak friction angle is quite useful. For example, Hsieh et al (2002) examined the predicted peak friction angles using the MIT-S1 model normalised by the state parameter proposed by Been and Jefferies (1985). The results using Toyoura siliceous sand parameters by Pestana (1994) were in good agreement with experimental results. Sharma et al. (2005) conducted a similar study for calcareous sand and found that the results lie completely outside of experimental results obtained mostly from siliceous sand.

### 5.3 COMPARISON BETWEEN THE RESPONSES OF SMALL SCALE SHALLOW FOUNDATIONS ON SILICEOUS AND CALCAREOUS SANDS

This section presents results from parallel numerical analyses for shallow foundations on siliceous and calcareous sands and discusses the kinematic features observed for both sands. Those results provide further information for the mechanical difference between shallow foundation behaviour for siliceous (dilative) and calcareous (contractive) materials. The effect of foundation roughness on the bearing response is explained simultaneously. Using the MIT-S1 model a wide variety of the initial conditions such as densities and anisotropic stress conditions are simulated using only a single set of model parameters and effects of those conditions on the bearing response is described in the following subsections.

#### 5.3.1 Pressure-displacement curves

**Figure 5.8** shows pressure-displacement curves for both fully rough and fully smooth foundations resting on Toyoura siliceous and Goodwyn calcareous sand. Initial void ratios at the surface and effective unit weights are 0.8 (medium dense) and 8 kN/m<sup>3</sup> for the siliceous sand, and 1.3 (dense) and 7 kN/m<sup>3</sup> for the calcareous sand.

The shapes of the curves for siliceous and calcareous sands are significantly different: the former shows stiffer initial bearing stiffness and a clear ultimate bearing capacity, while the latter shows softer bearing stiffness and a quasi-linear response. This difference can be explained well by the Randolph and Erbrich (2000) hypothesis (i.e. **Figure 2.18**) that the shallow foundation deformation for dilative siliceous material is dominated strongly by the shear strain component, whereas that for compressive calcareous material is controlled mainly by the compression component. It is also consistent with the relationship between ( $\phi'_p - \phi'_{cs}$ ) and  $p'$ , which showed that calcareous sand presents a dilative response only at very small stress levels.

Moreover, a significant effect of the foundation roughness on the ultimate bearing capacity can be noticed in the siliceous sand analyses, whereas the calcareous sand

analyses are insensitive to the roughness. An explanation of this fact will be discussed in the following subsection in the context of the deformation mechanisms.

### 5.3.2 Deformation mechanisms

**Figure 5.9** shows incremental displacement vectors for a fully rough circular footing on siliceous sand at four penetration depths a) 0.3 m, b) 1.0 m, and c) 1.32 m (immediately before development of a collapse mechanism) and d) 2.0 m. Due to the kinematic constrain for horizontal movement (i.e. rigid rough soil-structure interface), purely vertical displacement vectors are found immediately below the footing. The development of a rupture failure mechanism and surface heave with increasing penetration depth is clearly observed. The result corresponding to the 2.0 m penetration depth is severely affected by numerical instability problems.

Incremental displacement vectors for a fully smooth footing on siliceous sand are shown in **Figure 5.10**. The results are at penetration depths of a) 0.3 m, b) 0.5 m, c) 0.68 m (before collapse), and d) 2.0 m. Less downward deformation and more horizontal flow and surface heave are evident in the soil beneath the footing.

Significant differences in the deformation pattern is found in analyses of a fully smooth footing on calcareous sand presented in **Figure 5.11** for depths of penetration of a) 0.3 m; b) 1.0 m; c) 1.5 m; d) 2.0 m). It is noticed that the soil underneath the footing deforms compressively at all penetration depths although slight horizontal vectors with minor surface heave are developed when the footing has penetrated to 2.0 m depth. This deformation mechanism is widely referred to as a punching shear mechanism (e.g. Vesic, 1975).

The change in the deformation pattern between siliceous and calcareous sands adds important information in explaining the effect of foundation roughness. For the siliceous sand, outward sliding wedges of soil beneath the foundation are either fully inhibited for the rough footing or permitted freely for the smooth footing. On the other hand, for the calcareous sand the same bulb of compressed material develops beneath either rough or smooth foundations.

### 5.3.3 Comparison of incremental horizontal displacement contours and characteristic mesh

As expected from the previous section, conventional bearing capacity analysis may be suitable for the response of small to moderate sized shallow foundations on siliceous sand because of the stress-independency of the peak friction angle at small stress levels (c.f., **Figure 5.6**). The deformation mechanism for this case may therefore reflect the plastic deformation mechanism based on the method of characteristics.

**Figure 5.12** compares incremental horizontal displacement contours normalised by foundation diameter for the rough footing analysis at a penetration of 1.32 m with the characteristic mesh using a computer software, Analysis of Bearing Capacity, ABC (Martin, 2003). This program can calculate the bearing capacity of strip or circular footings - smooth or rough - on a general cohesive-frictional soil with surcharge and/or self-weight. Input parameters for ABC are zero cohesion, friction angle of 31°, effective unit weight of 8 kN/m<sup>3</sup> and diameter of 10 m. The shape of incremental horizontal displacement contours is consistent with the familiar Prandtl-type stress field generated by the ABC software. Three individual parts, triangle wedges underneath and outside the footing and a conical fan-zone between them are evident.

Contours for smooth foundations on siliceous sand, taken immediately before the failure, are also similar (**Figure 5.13**). The mesh from ABC is recognised as the well-known Hill-type stress field, in particular with no triangle wedge beneath the footing.

However, as expected, the soil deformation mechanisms on calcareous sand totally disagree with the plastic deformation mechanism. The incremental horizontal displacement contours for the smooth footing analysis on calcareous sand in **Figure 5.14** are much smaller than for siliceous sand. This shape is typically shown in shallow foundation behaviour dominated by a punching shear failure pattern.

### 5.3.4 Volumetric strain distributions

Volumetric strain contours provide further explanation for the effect of soil compressibility on the deformation mechanisms. It is noticed that the cumulative

volumetric strains directly beneath rough and smooth footings on siliceous sand are negligibly small (less than 3.5 %) at all penetration levels (**Figure 5.15** and **5.16**). However, significant negative volumetric strains are developed adjacent to the footing edges. This is consistent with the observation of a large amount of surface heave in **Figure 5.9** and **5.10**, and a dilative response of the sand at low stress levels.

In contrast to the siliceous sand calculations, the contours for the calcareous sand reveal that appreciable increasing volumetric compression occurs over a depth of one footing diameter, with a larger bulbous shape of contours (**Figure 5.17**). The negative volumetric strain at the edge of the footing is very small.

### **5.3.5 Integration point outputs**

Results of relationships of  $q-p'$ ,  $q-\varepsilon_s$ ,  $e-p'$  and  $\varepsilon_v-\varepsilon_s$  obtained from chosen integration points are presented in **Figure 5.18** for the rough footing on siliceous sand. The four chosen integration points are down profiles at the centre, edge, and outside (quarter diameter from the edge of the footing) of the footing depths ( $\sim D/25$ ,  $D/4$ ,  $D/2$ ,  $D$ ), and also horizontally at a shallow depth ( $\sim D/25$ ). Large deviatoric stress development within a small shear strain range but small volumetric strain development can be seen for the centre points, while small deviatoric stress development but large volumetric strain reduction with large shear strain can be observed for the edge points. Large dilative behaviours are also found for the surface outputs. Results of the smooth foundation analysis shown in **Figure 5.19** are quite similar to the rough foundation results.

**Figure 5.20** shows integration point results for calcareous sand. The results are plotted up to a normalised settlement of 20 %. Compared with the siliceous sand results, deviatoric stresses for the centre points are much smaller than for siliceous sand. Most of the points show positive volumetric strains except for a surface output at the edge (point 1 for Edge or point 3 for Surface) which develop significant volumetric expansion.

### 5.3.6 Effects of void ratio and $K_0$

The effects of density and inherent anisotropy play important roles in the bearing response of sands. **Figure 5.21** shows the effects of initial void ratio and  $K_0$  on the behaviour of either fully rough or smooth footings on siliceous sands, plotting the bearing capacity factor,  $N_\gamma = 2q_b/\gamma'D$ , against the normalised displacement with diameter,  $\delta/D$ . The results show the significant influence of  $e$  and  $K_0$ . The effect of initial density on the  $N_\gamma - \delta/D$  curves is very evident for the smooth footing analyses although many of the calculations for the rough footing cases are not available due to finite element problems. The bearing responses of higher density samples ( $e_0 = 0.65, 0.7$ ) mobilise the ultimate bearing capacity at relatively small displacement, while large settlement is required to mobilise the capacity for the lower density sample ( $e_0 = 0.9$ ). This is consistent with the drained triaxial behaviour for different initial densities (c.f., **Figure 5.3**).

Calculations with  $K_0 = 0.49$  are also plotted on **Figure 5.21**. The  $K_0$  condition has little affect for smooth foundations, while it is quite significant for rough foundations. The effect of  $K_0$  on dense samples cannot be discussed further due to numerical calculation problems.

The effects of  $e$  and  $K_0$  are also significant for the behaviour of fully smooth footings on calcareous sand (**Figure 5.22**). The mobilised bearing capacity factors of all samples increase with increasing displacements and no particular limit load can be found. It is well reflected in the results of triaxial drained shear tests in **Figure 5.4**.

Maximum bearing capacity factors for siliceous sand as well as mobilised  $N_\gamma$  values at a displacement of 10 % of the diameter for calcareous sand are presented against the initial void ratio in **Figure 5.23**. The results of centrifuge model tests are also plotted: Okamura et al. (1997) for Toyoura siliceous sand ( $\gamma' = 9.6 \text{ kN/m}^3$ ,  $D = 1.5\text{-}3 \text{ m}$ ,  $e_0 = 0.65$ ); Finnie (1993) for Goodwyn calcareous sand ( $\gamma' = 7 \text{ kN/m}^3$ ,  $D = 3\text{-}10 \text{ m}$ ,  $e_0 = 1.3$ ). It is found that the bearing capacity factors increase with increasing density (decreasing voids ratio) for both sands. However, the rate of increase is very high for the siliceous sand but smaller for the calcareous sand.

### 5.3.7 Discussion

It can be concluded that the MIT-S1 model replicates reasonably well the typical deformation mechanisms for siliceous sands. The shapes of the incremental horizontal displacement contours are in good agreement with the mesh from the method of characteristics obtained using the ABC computer software (Martin, 2003). This appears consistent with the constant peak friction angle at small stress level as shown in **Figure 5.6**. The applicability of the conventional bearing capacity formulae for small foundations on siliceous sand can be explained by the MIT-S1 model.

The peak friction angles are strongly affected by the void ratio at small stress levels. This is reflected by analysing the shallow foundation with different representative void ratios. Several researchers have attempted to assess this effect on the shallow foundation responses using non-associated Mohr-Coulomb models (e.g. Griffiths, 1982; Frydman and Burd, 1997; Potts and Zdravkovic, 2001; Erickson and Drescher, 2002). Potts and Zdravkovic (2001) conducted several FE analyses for strip and circular foundations, varying the dilation angle from zero, as might be appropriate for loose sand to a fully associated value equal to the friction angle, as is assumed in classical bearing capacity solutions. It was shown that the bearing capacity calculated by the Mohr-Coulomb model is relatively insensitive to the angle of dilation. However, for non-associated flow rule conditions, much greater settlement is needed in order to mobilise the bearing capacity. Such inconsistencies compared with the MIT-S1 model results may be due to the limited capability to simulate the compression characteristics of sands by using a non-associated Mohr-Coulomb model.

The deformation mechanisms for calcareous sand are totally different to that of siliceous sand. The incremental displacement vectors and volumetric strain contours present strong evidence that the shallow foundation response on calcareous sand is dominated by a punching shear deformation mechanism, as suggested by Vesic (1975). It can be concluded that the MIT-S1 model is able to distinguish between the characteristic differences of the deformation of both siliceous and calcareous sands.

Semple (1988) suggested that a unique relationship between void ratio and bearing capacity may exist. The MIT-S1 model results in **Figure 5.23** may be used to derive a

unique exponential correlation with siliceous and calcareous sand results. However, Nauroy and Golightly (1991) indicated that the trend of greater bearing capacities for siliceous sand compared with that for calcareous sand was not always true, because the bearing pressure for calcareous sand generally increases with increasing penetration depth. This also raises an obvious question on to what strain level is appropriate for the assessment of bearing resistance on calcareous sand. This will be discussed in the next chapter.

## 5.4 COMPARISON BETWEEN THE RESPONSES OF LARGE SCALE SHALLOW FOUNDATIONS ON SILICEOUS AND CALCAREOUS SANDS

Shallow foundation systems with a diameter over 100 m and an area in excess of 10,000 m<sup>2</sup> have frequently been designed in offshore engineering (e.g. for gravity base structures) (Watt, 1978; Randolph and Erbrich, 2000). However, the performance of such large scale shallow foundations is still questionable because the potential of centrifuge modelling is limited for simulating extremely large prototype scales. Numerical modelling must often be relied on to assess the performance of large foundations.

This section describes the behaviour of shallow foundations with a diameter of 100 m on siliceous and calcareous sands. The numerical conditions are similar to the analyses of a 10 m diameter footing, as presented in **Section 5.3**, except for the value of effective unit weight,  $\gamma'$ , which has been taken 10 times higher, avoiding the need to modify the finite element meshes (as explained in **Section 4.2.2**). Thus the increase in the foundation size is simulated simply by increasing the initial stress level.

### 5.4.1 Pressure-displacement curves

**Figure 5.24** shows  $N_y$  and  $\delta/D$  relationships for 100 m diameter smooth and rough footings on siliceous sand. The 10 m diameter results are also plotted for comparison. The bearing pressure for the large scale rough footing shows no peak value but rather increases continuously with increasing penetration depth. It will be shown later that this is because the compression component dominates the bearing response increasingly as

the foundation size increases. For the 100 m diameter smooth footing case, however, an ultimate bearing capacity is still observed although it needs much larger vertical displacement than for the small footing. It is worth noting that the effect of roughness for larger foundations is much smaller. This appears to be because the deformation mechanisms on siliceous sand progressively shift forwards punching shear with increasing size of foundation.

The bearing responses on calcareous sand with different foundation sizes show similar trends but the 100 m diameter foundation shows a more linear response (**Figure 5.25**), and the mobilised  $N_y$  for the 100 m case is smaller.

#### **5.4.2 Deformation mechanisms**

As mentioned above, a transformation in the mechanisms from small to large foundations may be seen, in particular for rough footings on siliceous sand. **Figure 5.26** shows that at a penetration of 10% of the diameter the amount of surface heave reduces significantly with increasing diameter. Also the large foundation response shows a compressive punching shear deformation mechanism at  $\delta/D = 20\%$ . However, for the smooth footing analysis (**Figure 5.27**), a classical rupture failure pattern with surface heave is still evident for the 100 m diameter calculations although more obvious downward deformations are exhibited at shallower penetration.

The incremental displacement vectors for 10 m and 100 m diameter footings on calcareous sand show almost identical deformation patterns at all penetration levels (**Figure 5.28**). The soils beneath the footings compress almost in a one-dimensional way and this may allow simulation of the footing behaviour on calcareous sand using a simple 1-D compression theory.

#### **5.4.3 Incremental horizontal displacement contours**

In the analyses of 10 m diameter footings, it was found that the incremental horizontal displacement contours compared well with the characteristic lines of the classical rupture failure patterns. The contours for the 100 m diameter rough footing analyses in **Figure 5.29** are, however, developed to significantly greater depth. It is interesting to

note that the shapes of contours are similar to those for calcareous sand as shown in **Figure 5.14**. In **Figure 5.30**, however, the shape of contours for 100 m diameter smooth footings are still similar to the Hill-type mechanism because the bearing response reaches an ultimate state.

The contours for the 100 m diameter footing on calcareous sand (**Figure 5.31**) are similar to those for the 10 m diameter. It is evident that the punching shear deformation mechanism for shallow foundations on calcareous sand is independent of the foundation size, at least for moderate to large foundations.

#### 5.4.4 Volumetric strain distributions

**Figures 5.32** and **5.33** compare the volumetric strain contours for 100 m diameter fully rough and smooth footing analyses with the 10 m diameter analyses on siliceous sand. The volumetric strains for the 100 m diameter cases are larger (9.75 % for rough footing and 13.5 % for smooth footing) beneath the footing than for the 10 m diameter foundations.

For the calcareous sand analyses, the cumulative volumetric strains are more than doubled for a foundation size increase of 10 times larger (**Figure 5.34**).

#### 5.4.5 Void ratio and mean effective stress relationship from integration points

Results of void ratio and mean effective stress relationships from integration points can also evaluate the significance of volumetric response with increasing diameters. **Figure 5.35** and **5.36** compares  $e$ - $\ln p'$  relationships for both 10 m and 100 m diameter fully rough and smooth footing analyses on siliceous sand. The same integration points are chosen for both analyses so that initial stresses for the 100 m analyses increase due to scaling. The significant development of volume reduction can be found for the centre points. Near surface and footing edge points for the 100 m foundation still show dilative response.

**Figure 5.37** shows  $e$ - $\ln p'$  relationships for calcareous sand. Significant void ratio reduction is noticed for the centre points. Points that had similar initial state, i.e. Centre

point 1 for 100 m foundation and centre point 2 for 10 m foundation, show that the void ratio reduction beneath the 100 m foundations is much greater than for the 10 m foundation. This is further evidence that 1-D compression theory is suitable for the shallow foundation behaviour on calcareous sand.

#### **5.4.6 Effects of void ratio and $K_0$**

**Figure 5.38** presents  $N_\gamma - \delta/D$  relationships for the 100 m diameter fully rough and smooth foundations for various void ratios. It is found that the effects of void ratio and  $K_0$  are still significant. All samples for the rough footing analyses show a monotonic increase in the mobilised  $N_\gamma$  with increasing displacement, with no apparent ultimate bearing resistance, even for the dense samples. On the other hand, the  $N_\gamma - \delta/D$  responses for the smooth footing analyses reach an ultimate bearing capacity except for the initially loose sample ( $e_0 = 0.9$ ). The effect of  $K_0$  for the smooth footings is more significant than for the 10 m diameter results (**Figure 5.21**).

However, the mobilised  $N_\gamma$  values for the 100 m diameter footings on calcareous sand with different densities are normally less than 10 and the response trends are nearly insensitive to the density (**Figure 5.39**).

The effects of void ratio and  $K_0$  are more obvious by plotting the  $N_\gamma$  values against the representative void ratio (**Figure 5.40**). Most of the pressure-displacement curves shown in **Figure 5.38** and **5.39** do not reach an ultimate bearing capacity so that the mobilised  $N_\gamma$  are obtained from a normalised displacement of 10 %. Significant  $N_\gamma$  reductions with increasing diameter and void ratio are noticed apart from the 100 m diameter foundation on calcareous sand, where the  $N_\gamma$  values become nearly independent of the void ratio.

#### **5.4.7 Parametric study**

As mentioned in **Section 4.5**, the sensitivity of the MIT-S1 model parameters could be different for larger foundation analyses. This subsection carries out parametric studies of the MIT-S1 model parameters on 100 m diameter foundations on siliceous and

calcareous sands. The parameters  $p'_{ref}$ ,  $m$ ,  $\phi'_{mr}$  and  $np$  which were found to be the most critical parameters for the small foundation analyses are examined.

**Figure 5.41** shows investigations of the effects of model parameters in terms of pressure-displacement curves for a 100 m diameter smooth foundation on siliceous sand. All parameters still affect the bearing response significantly. It was mentioned in **Section 4.5** that when the foundation becomes larger, the effect of the parameters associated with shear response ( $m$ ,  $\phi'_{mr}$ ,  $np$ ) would be reduced, whereas the effect of the compression parameter ( $p'_{ref}$ ) would be large due to the development of the compression component. It may be reasoned that the large and smooth foundations are still showing ultimate bearing capacity due to the dilative component as found in **Figure 5.38(b)**.

The sensitivity analysis of the 100 m diameter footing on calcareous sand shows that the parameters  $p'_{ref}$  and  $m$  have most influence, while the parameters  $\phi'_{mr}$  and  $np$  have little effect (**Figure 5.42**). This result is similar to the analysis for a 10 m diameter foundation.

#### 5.4.8 Discussion

The comparison of the 100 m diameter with the 10 m diameter footing responses on siliceous and calcareous sands reveals that the compressive behaviour gradually dictates the deformation mechanisms. The analyses of 100 m diameter rough footings on siliceous sand led to pressure-displacement curves that increase smoothly without showing any clear ultimate bearing capacity. A punching shear deformation pattern with large volume change beneath the footing develops for this foundation even at large penetration ( $\delta/D \sim 20\%$ ). The insensitivity of the effect of foundation roughness, which is a typical phenomenon for compressive material, is also evident. However, the response of smooth foundations on siliceous sand is still dominated by the shear component. By contrast, most of the deformation patterns for calcareous sand do not change between large and small diameters of foundation, implying that there is little effect of foundation size on the response of shallow foundations on calcareous sand.

It may be concluded that there is a dimensional transition from a classical rupture shear failure mode to a punching shear failure mode for shallow foundations. For circular foundations, it is assumed that such transitions exist between diameters of 10 and 100 m

for rough footings on siliceous sand or for smooth footings on loose siliceous sand, but for diameters of more than 100 m for smooth footings on dense siliceous sand, and less than 10 m for calcareous sand. A more precise definition of the dimensional transition will be discussed in the next section.

## 5.5 THE EFFECT OF FOUNDATION SIZE ON BEARING CAPACITY FACTOR, $N_y$

The most significant influence factor, i.e. foundation size, in terms of the bearing capacity factor,  $N_y$  is investigated. The foundation size effect on  $N_y$  has been explained as due to stress dependency (De Beer, 1963; Hettler and Gudehus, 1988; Kusakabe et al., 1991) and is associated strongly with the stress-dependency of the peak friction angles as discussed in **Section 5.2**. Further numerical investigations using the MIT-S1 model may provide further explanations for these effects and may allow a possible description of the dimensional transition to be deduced in terms of dilative and contractive responses.

### 5.5.1 Siliceous sand

**Figure 5.43** summarises bearing responses from analyses with different footing sizes of fully smooth shallow circular footings on siliceous sand, by plotting relationships between a)  $N_y - \delta/D$  for  $e_0 = 0.8$  (loose), b)  $N_y - \delta/D$  for  $e_0 = 0.65$  (dense), and c)  $N_y - D$  for both loose and dense results. As mentioned in **Section 2.3.3**, the effect of the foundation size has been recognised experimentally as the mobilised  $N_y$  decreases with increasing diameter, but only over a relatively small diameter range (e.g. De Beer, 1963). The numerical predictions using the MIT-S1 model suggest that the foundation size effect exists for large foundations as well.

Moreover, as expected, a transition from dilative to contractive deformations can be seen as the foundation size increases. The smaller foundations tend to show dilative behaviour with clear peak stress, whereas the larger foundations present contractive response and exhibit lower mobilised  $N_y$  values. This is also reflected from the results of drained triaxial tests with different initial void ratios as shown in **Figure 5.2**. In **Figure 5.43(c)**, two  $N_y$  values are shown, one corresponding to the peak value and the other

corresponding to  $\delta/D = 10\%$  (taken only if the  $N_\gamma$  keeps increasing for  $\delta/D$  greater than 10 %). The two  $N_\gamma$  values merge at about 20 m diameter for loose ( $e_0 = 0.8$ ) samples and 60 m diameter for dense ( $e_0 = 0.65$ ) samples (indicated by arrows) and this will be defined as the transition diameter point from dilative to contractive response. This diameter may be referred to as a ‘critical size’ which basically follows the same concept behind the definition of the ‘critical stress’ as described in **Section 5.2**.

Kimura et al. (1985) suggested that the  $N_\gamma$  value reduces with reduction in density (**Figure 2.11**). **Figure 5.43(c)** shows the great variation with density over a wide range of foundation size. The other influence factors such as  $K_0$  and foundation roughness are also significant (**Figure 5.44**). These factors have most influence at small diameters with gradually reducing influence with increasing foundation diameter.

**Figure 5.45** compares the numerical results with centrifuge model tests for circular footings ( $D = 1.5\text{--}3\text{ m}$ ) on Toyoura siliceous sand performed by Okamura et al. (1997). Unfortunately the numerical results could not be obtained for small diameters owing to numerical problems. However both results show the reduction of  $N_\gamma$  with increasing diameter.

### 5.5.2 Calcareous sand

**Figure 5.46** shows bearing responses of fully smooth shallow circular footings on calcareous sand. The results are obtained for two representative densities ( $e_0 = 1.3$  for dense or  $e_0 = 1.9$  for loose) and  $K_0$  conditions (1 or 0.49) applied over a wide range of diameters (1 to 100 m). It is noticed that the effect of foundation size and density are very strong for smaller diameters. The rate of decrease in  $N_\gamma$  becomes gradually lower at larger foundation sizes. The  $N_\gamma$  values for loose samples are nearly constant for diameters of more than 30 m. Physical model results conducted by Finnie (1993) are also shown. The rate of decrease in  $N_\gamma$  is not as dramatic as from the numerical results.

In **Figure 5.46(a)** and **5.46(b)**, none of the analyses exhibits an apparent ultimate state. The calculation for a 1 m diameter foundation on dense calcareous sand was terminated at about 15.5 % normalised displacement. **Figure 5.47** shows incremental displacement vectors and incremental horizontal displacement contours for the 1 m diameter footing

at settlements of 14 and 15.5 % of the diameter. The kinematic responses at 14 % show a punching shear mechanism, similar to **Figure 5.11** and **5.14**. However, the incremental displacement vectors at 15.5 % indicate a large amount of surface heave adjacent the footing. The incremental horizontal displacement increases significantly and forms more of a classical rupture failure pattern. It may be concluded that the critical diameter for the dense calcareous sand may be defined at about 1 m.

### **5.5.3 $N_\gamma$ - D relationship for various sands**

The investigation of the effect of foundation size has also been conducted with respect to the different types of calcareous soils: Dogs Bay calcareous sand and Goodwyn calcareous silt. Effective unit weights are set to 7 kN/m<sup>3</sup> for the Dogs Bay sand and 6 kN/m<sup>3</sup> for the Goodwyn silt.

The  $N_\gamma$  values from the analyses for Dogs Bay sand are shown in **Figure 5.48(a)**. The factor is very high for small diameters and reduces steeply with increasing diameter. This may be deduced from changes in the more significant model parameters such as the higher  $\phi'_{mr}$  and  $np$  (i.e. higher friction angles) and higher  $p'_{ref}$  (i.e. stiffer). Centrifuge model test results by Klotz and Coop (2001) are compared with the MIT-S1 predictions in **Figure 5.48(b)**. It is difficult to prove full consistency between the physical and the numerical results.

The calcareous silt analyses are based on extremely low  $p'_{ref}$  and  $\theta$  values and lead to very low  $N_\gamma$  values even for small foundation sizes (**Figure 5.49**). The  $N_\gamma$  values for loose samples ( $e_0 = 2.7$ ), in particular, are essentially independent of the foundation size. Physical model results (Finnie, 1993) lie between the numerical predictions of loose and dense states. The experimental data also revealed that the  $N_\gamma$  values for calcareous silt are insensitive to the foundation size.

The  $N_\gamma$  - D curves for all materials above are compared in **Figure 5.50**. For small diameters, Dogs Bay sand has the highest bearing capacity, while the Goodwyn silt gives the lowest, except that results for Toyoura sand are not available at smaller diameters. The different trends of calcareous materials may be explained physically due to changes in the grain size distributions as shown in **Figure 3.1**. The uniformly graded

Dogs Bay sand induces stronger material stiffness, while a large amount of fine particles contained in the Goodwyn sand and silt leads to a reduction in stiffness and strength. The  $N_y$  values for different calcareous materials and densities reduce with increasing diameter and merge to a somewhat unified  $N_y$  (of approximately 10), independent of the density, foundation size and material type. On the other hand, the  $N_y$  values for large foundations on siliceous sand are significantly larger than those for calcareous soils.

#### 5.5.4 Discussion

The investigation of the effect of foundation size on bearing capacity raises interesting issues in regard to the shallow foundation performance. Three aspects are most pronounced: a) the extremely small bearing capacity for a wide variety of foundation sizes on highly compressible calcareous soils; b) the unified bearing capacity for large foundations on calcareous materials; and c) the existence of a ‘critical size’.

First of all, the calculated  $N_y$  values for loose Goodwyn calcareous sand and silt are found to be relatively constant, independent of the foundation diameter (**Figure 5.46** and **5.49**). The physical model results performed by Finnie (1993) also show such foundation size-independency. Materials formed by very weak particles and with a large fines content lead to strong compressional deformation mechanisms with low initial stiffness.

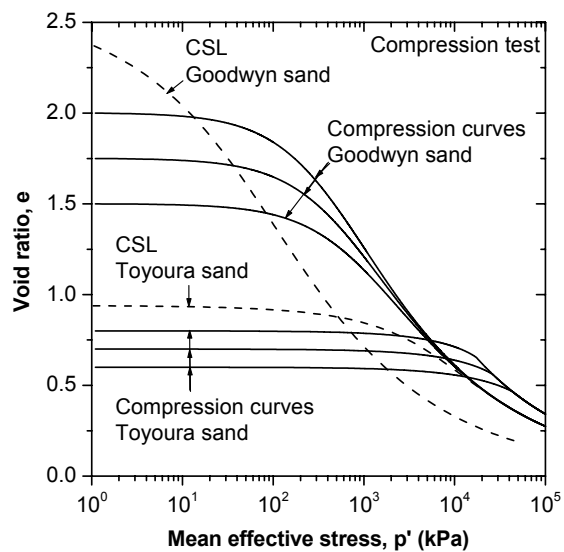
Next, the  $N_y$  values for all calcareous materials decrease dramatically with increasing foundation size and eventually converge to a unified terminal  $N_y$  value as shown in **Figure 5.50**. Development of compressibility (or crushability) with increasing foundation sizes for calcareous materials is the major factor influencing degradation of  $N_y$ , which has mentioned in **Section 5.4**. It may be concluded that the bearing resistance for shallow foundations of more than 100 m diameter on calcareous materials is no longer affected by the variation of initial density and foundation size due to extremely high pressures that destroy the intrinsic properties of the material. For the siliceous sand, an unrealistic large foundation size would be required to achieve the same condition.

Finally, there is an obvious dimensional transition of the deformation mechanisms from the classical rupture shear to punching shear mechanisms. This may be referred to as the

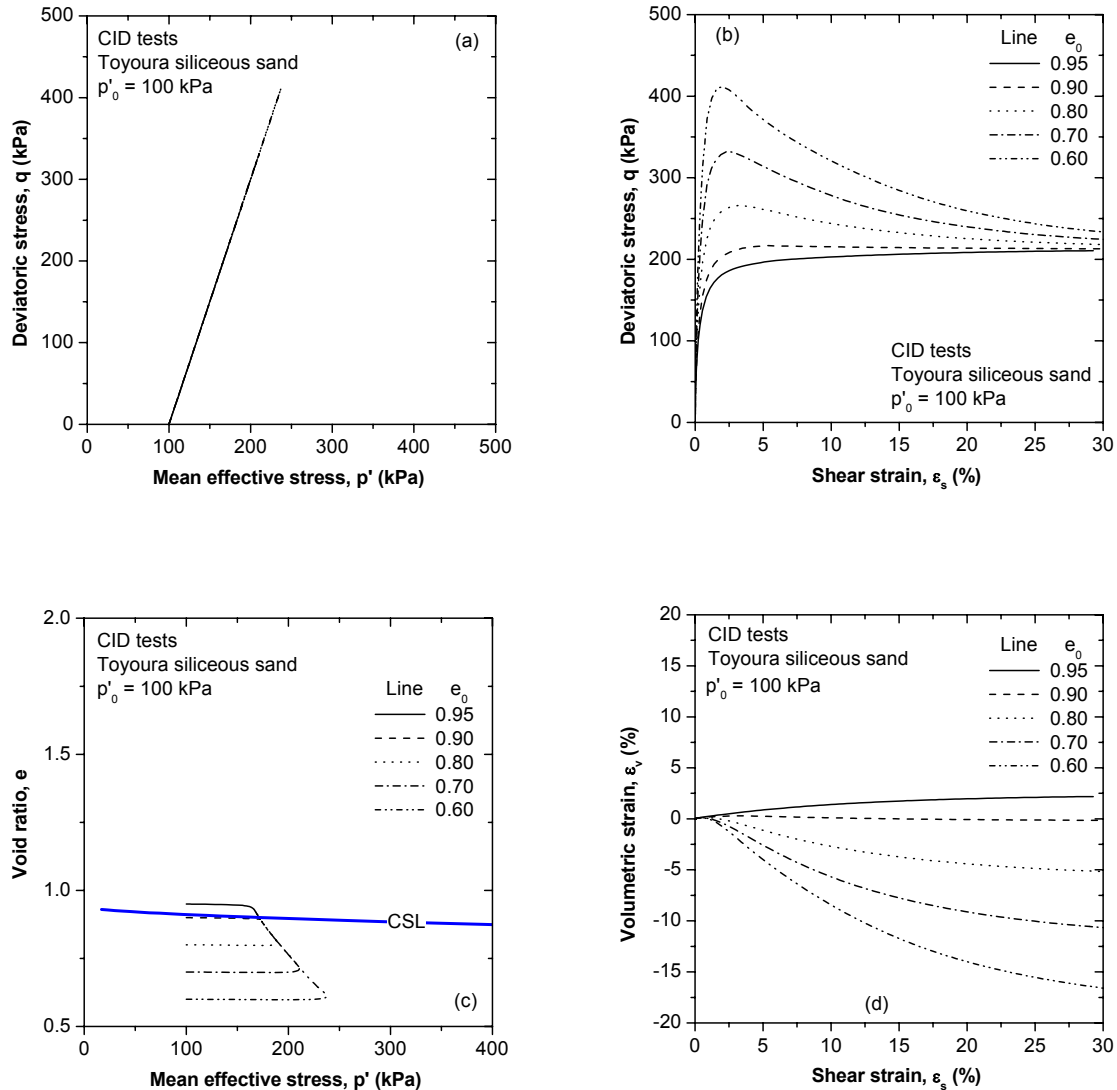
‘critical size’. The critical sizes for smooth foundations on loose and dense siliceous sand can be respectively defined at 20 and 60 m from **Figure 5.43**. They may be assumed as 1.0 m or less for dense Goodwyn samples as in **Figure 5.47**. It may be concluded that pure compression analysis is suitable for shallow foundations greater than the critical size, while the conventional bearing capacity equation is appropriate for foundations smaller than the critical size. Note that the critical size may be associated with the critical stress in **Figure 5.7** which indicates the transition between dilative and contractive behaviours.

## **5.6 CONCLUSIONS**

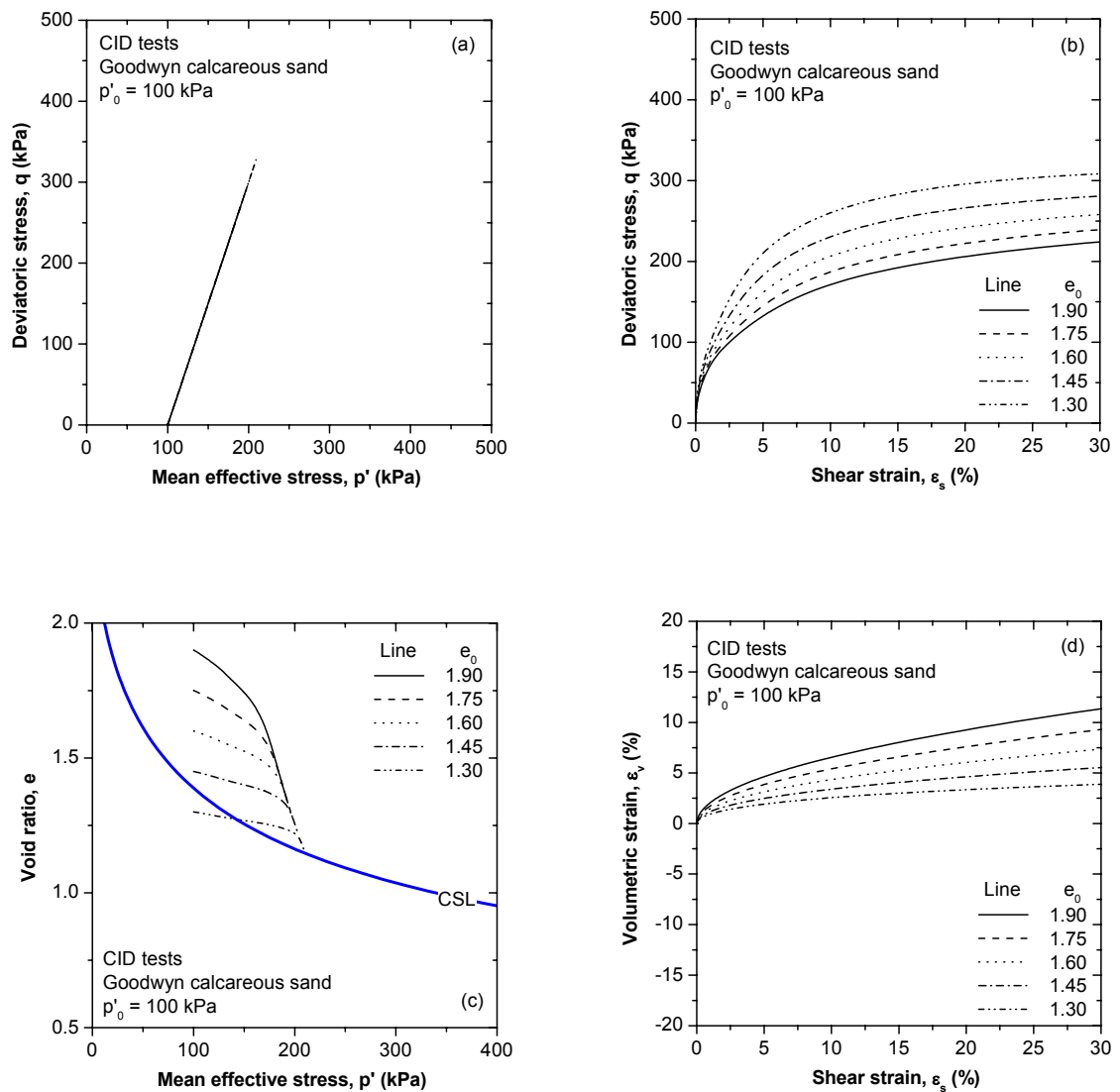
This chapter has presented a numerical examination of the effect of different fundamental geotechnical factors, mainly the density, stress level (or foundation size), inherent anisotropy and material type, on both the element and shallow foundation responses. It was shown in **Figure 5.7** that siliceous sand shows strong dilative response over a wide range of stress, while the dilatancy is much less for calcareous sand. The kinematic features extracted from the MIT-S1 FE analyses highlight the different deformation mechanisms for siliceous and calcareous sands, the classical rapture failure pattern of the former, while a punching shear failure pattern for the latter. It is also found that the foundation deformation on siliceous sand transforms slightly towards a punching shear mechanism with increasing foundation size. A transition of deformation mechanisms from contractive to dilative behaviours, named ‘critical size’, could be identified for both siliceous and calcareous sands. It may be concluded that a simple compression model may allow simulation of the response of shallow foundations which are larger than the critical size.



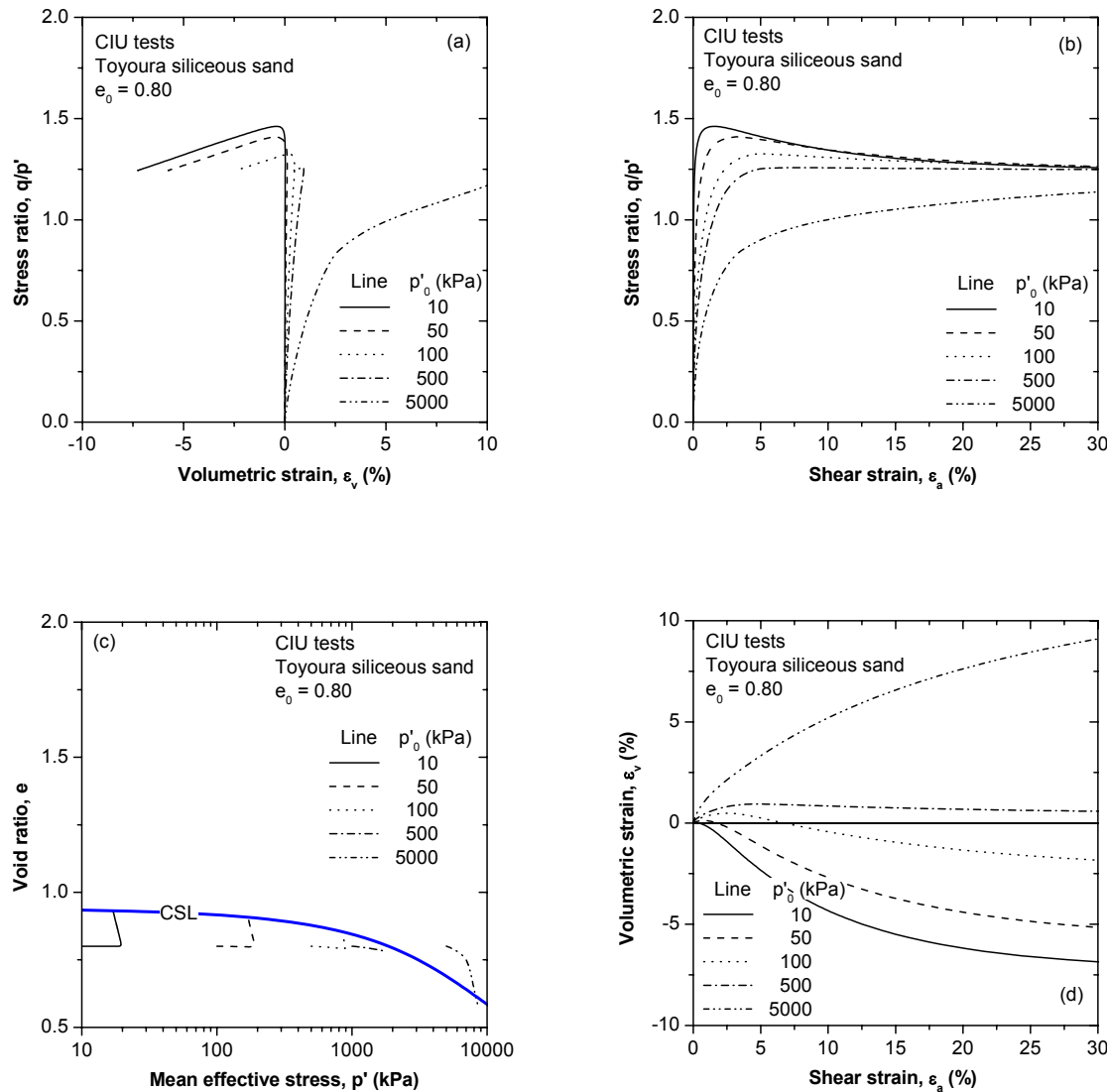
**Figure 5.1: Predictions for compression behaviours and CSLs on siliceous and calcareous sands**



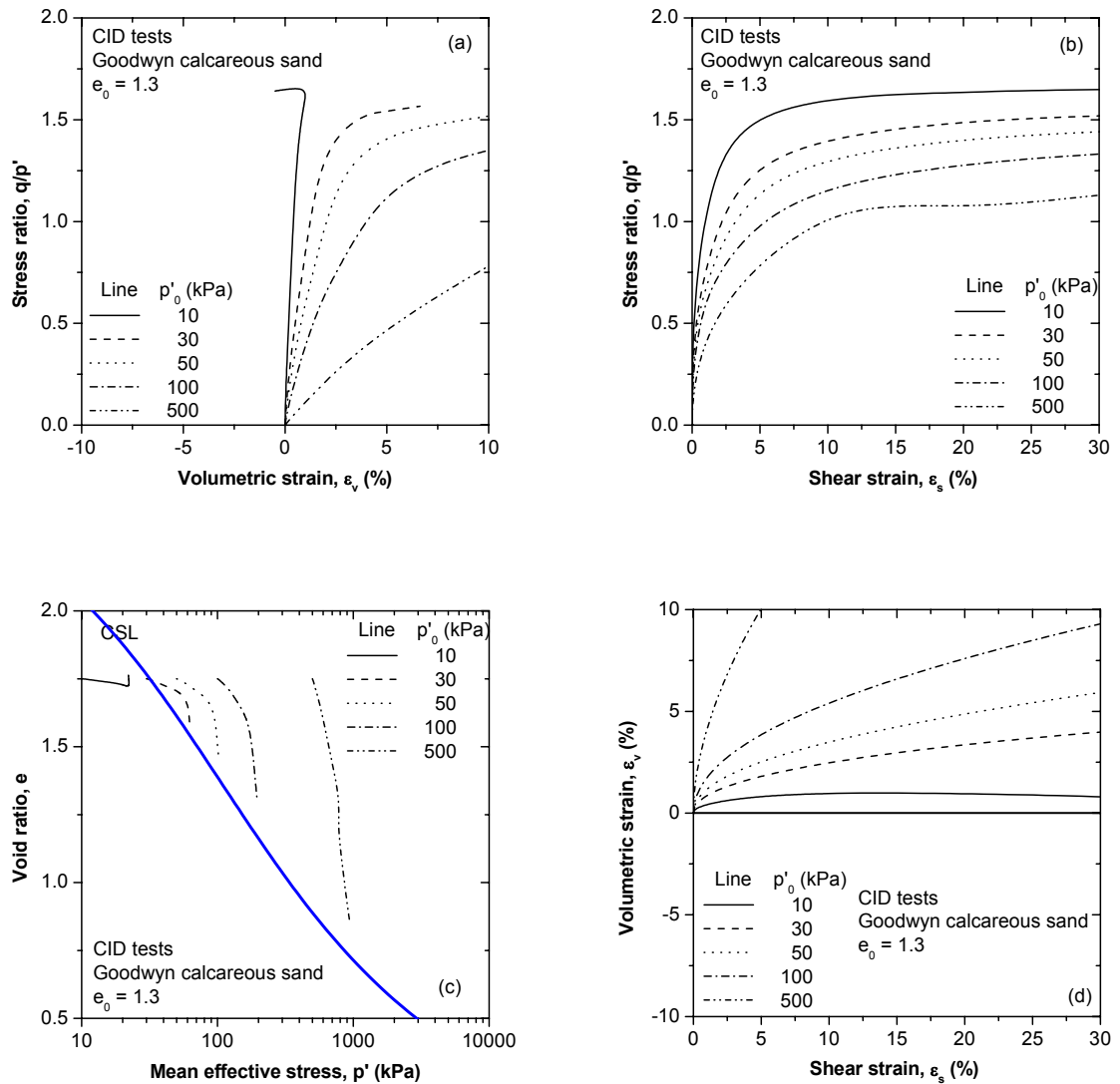
**Figure 5.2: MIT-S1 predictions for triaxial drained shear tests ( $e_0$  = variable,  $p'_0 = 100$  kPa) on siliceous sand**



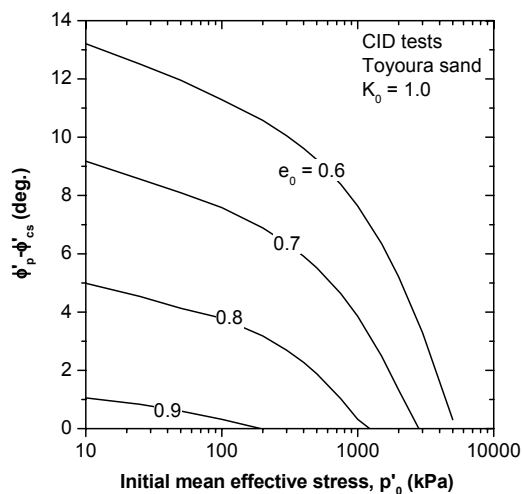
**Figure 5.3: MIT-S1 predictions for triaxial drained shear tests ( $e_0$  = variable,  $p'_0 = 100$  kPa) on calcareous sand**



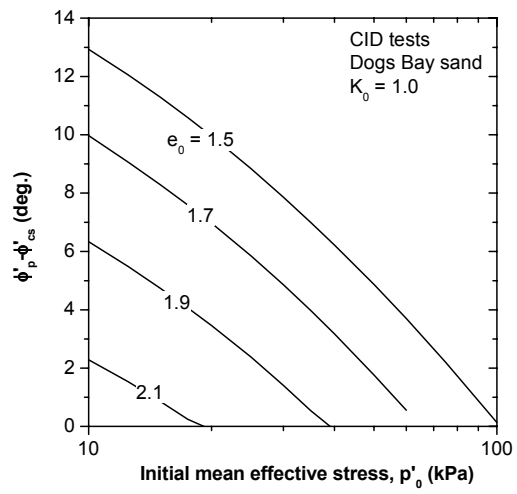
**Figure 5.4: MIT-S1 predictions for triaxial drained shear tests ( $e_0 = 0.8$ ,  $p'_0$  = variable) on siliceous sand**



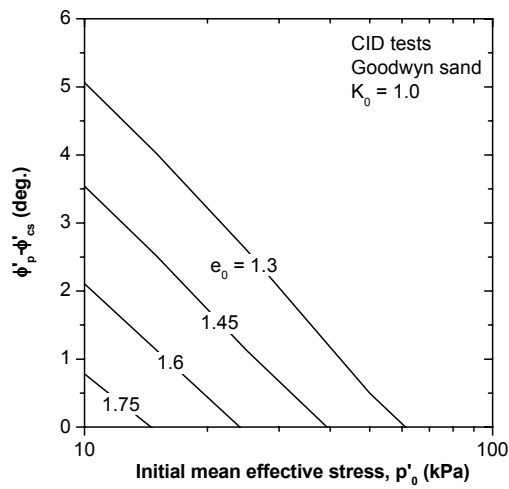
**Figure 5.5: MIT-S1 predictions for triaxial drained shear tests ( $e_0 = 1.3$ ,  $p'_0 = \text{variable}$ ) on calcareous sand**



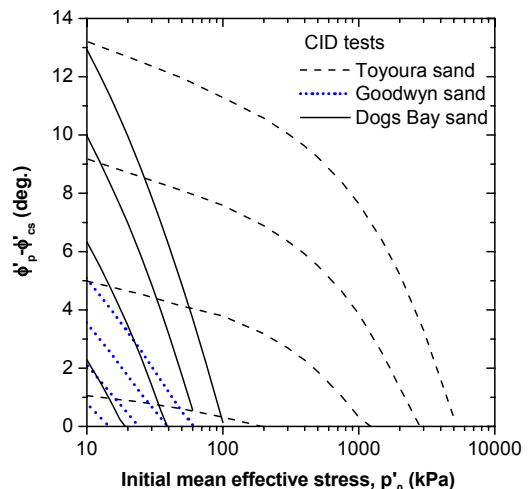
(a) Toyoura sand



1 or 4



(c) Goodwyn sand



(d) All

Figure 5.6: MIT-S1 predictions of  $\phi'_p - \phi'_{cs}$  and initial state relationship for triaxial drained shear tests on siliceous and calcareous sands

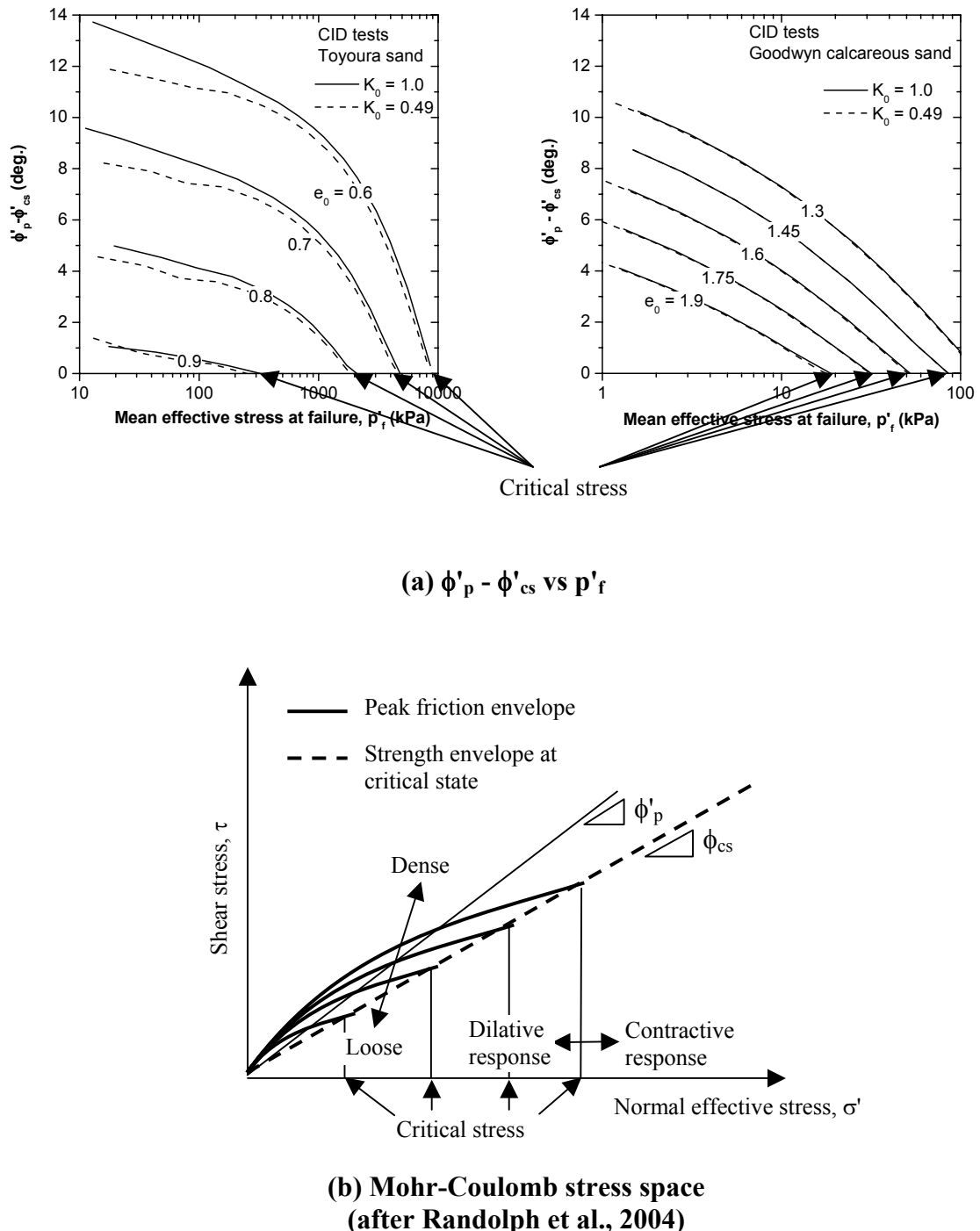
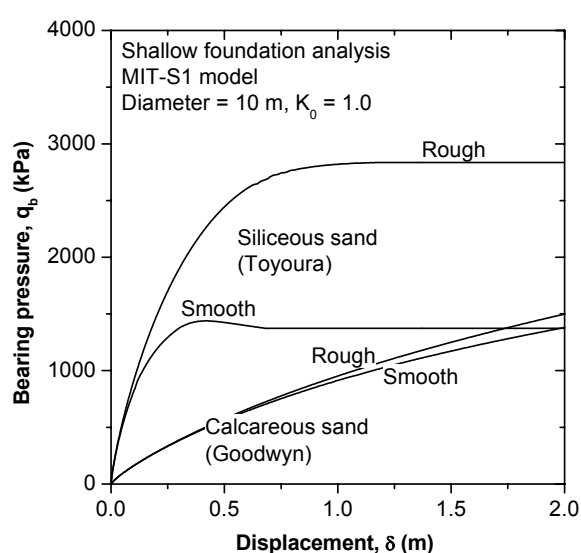
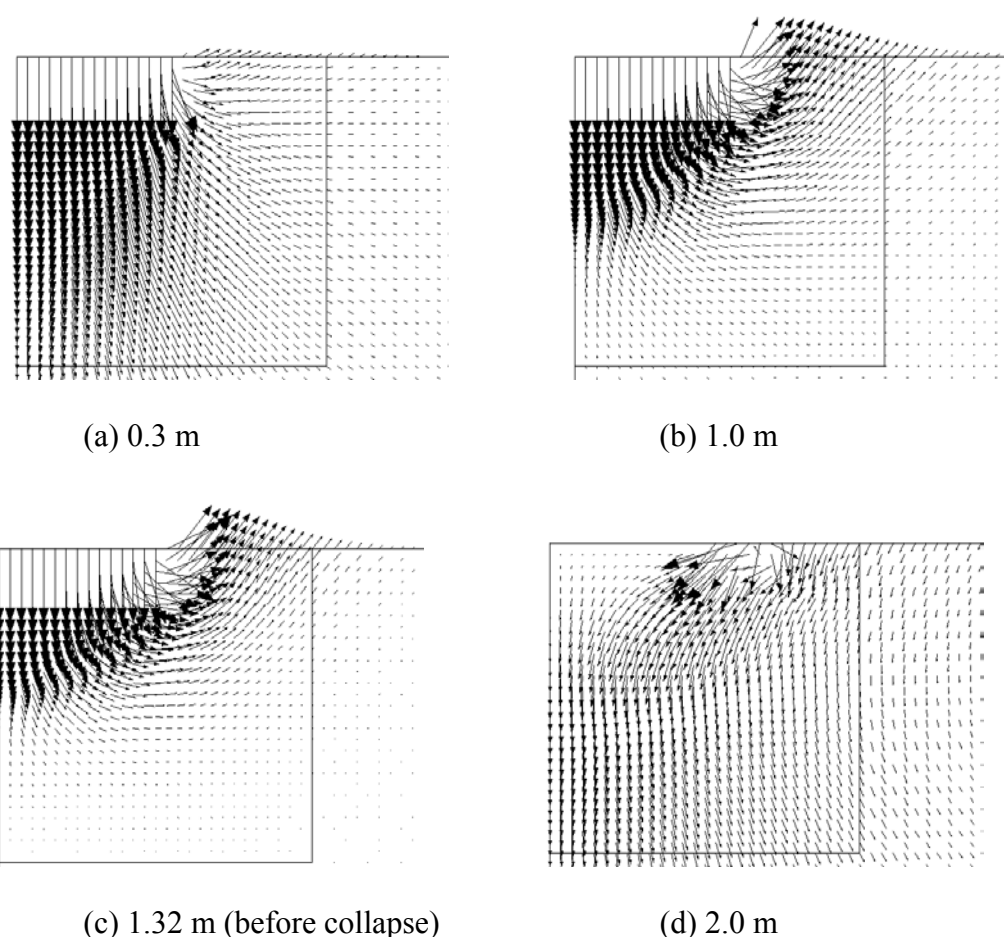
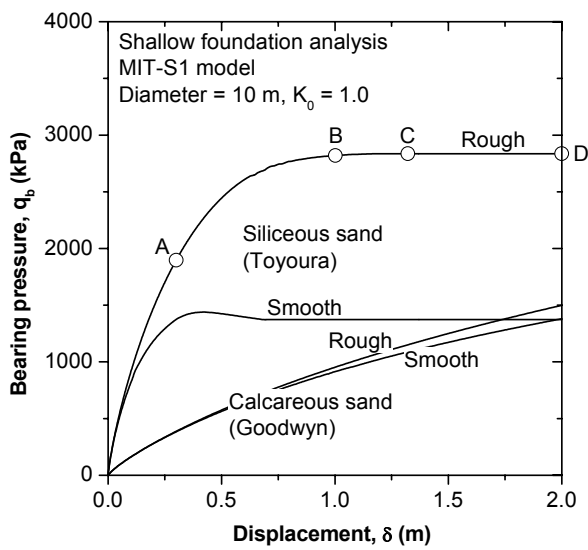


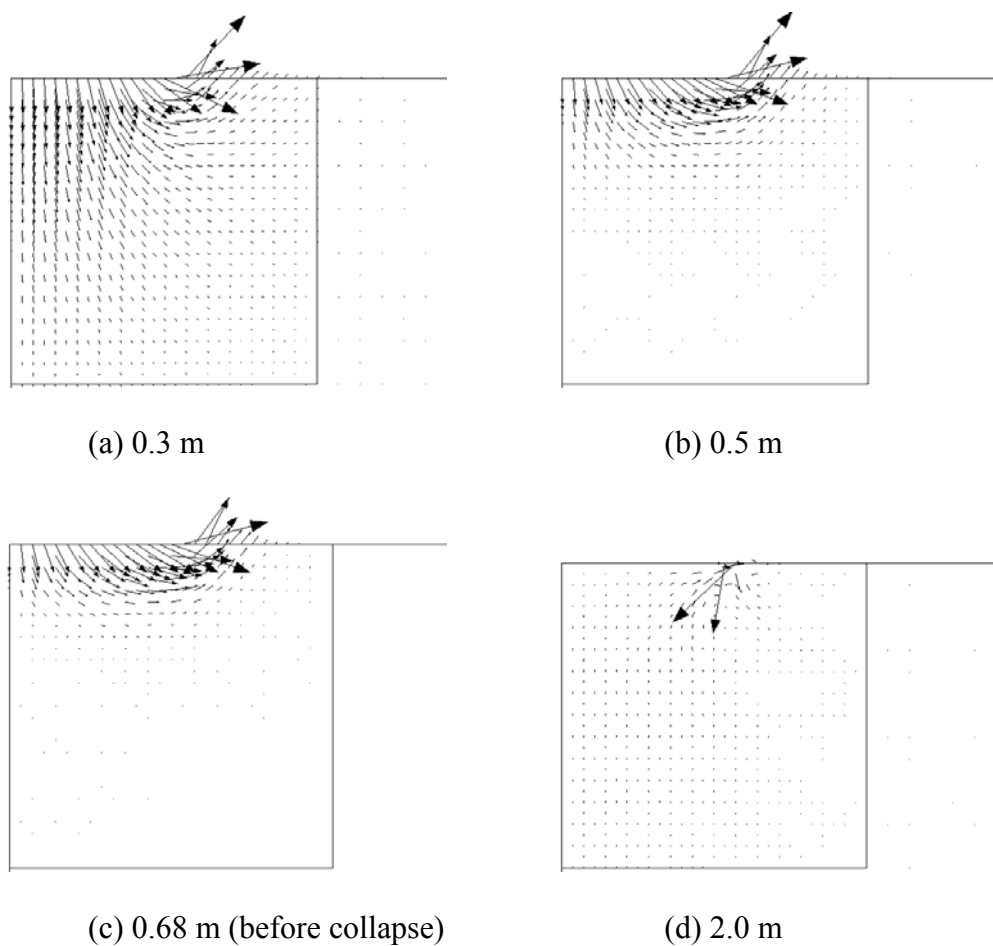
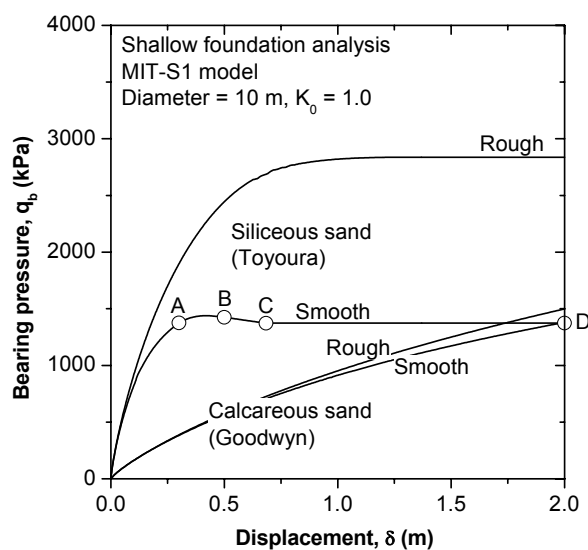
Figure 5.7: Shear strength envelope for siliceous sands



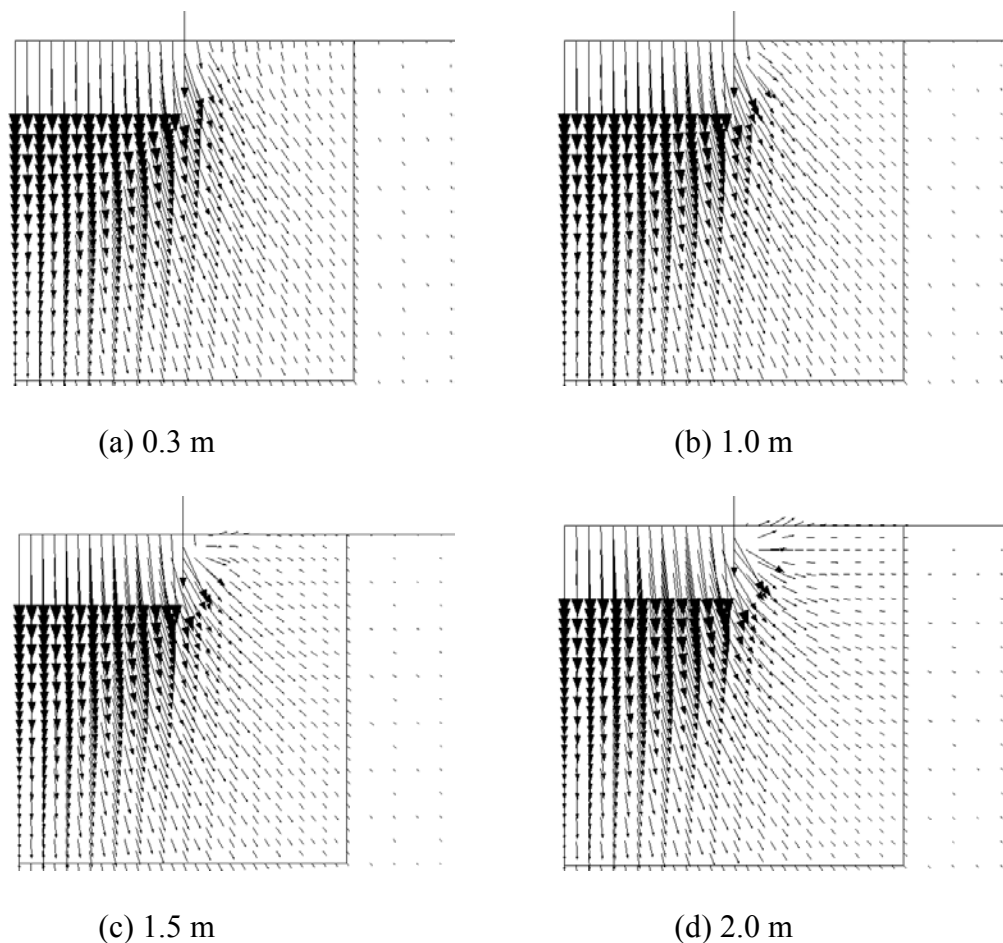
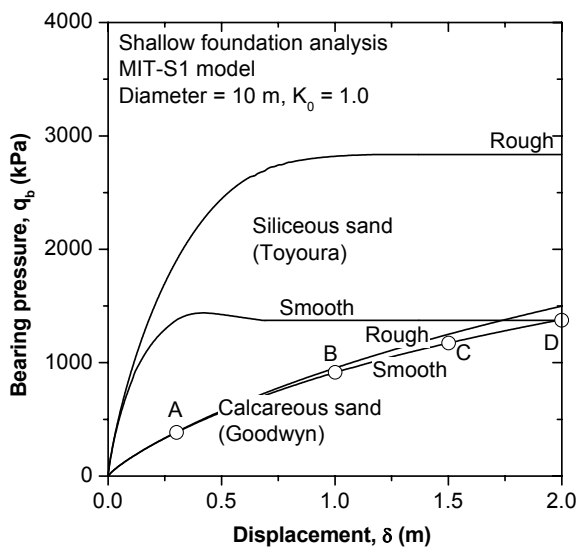
**Figure 5.8: Effects of foundation roughness on MIT-S1 predictions for shallow foundation responses on siliceous and calcareous sands**



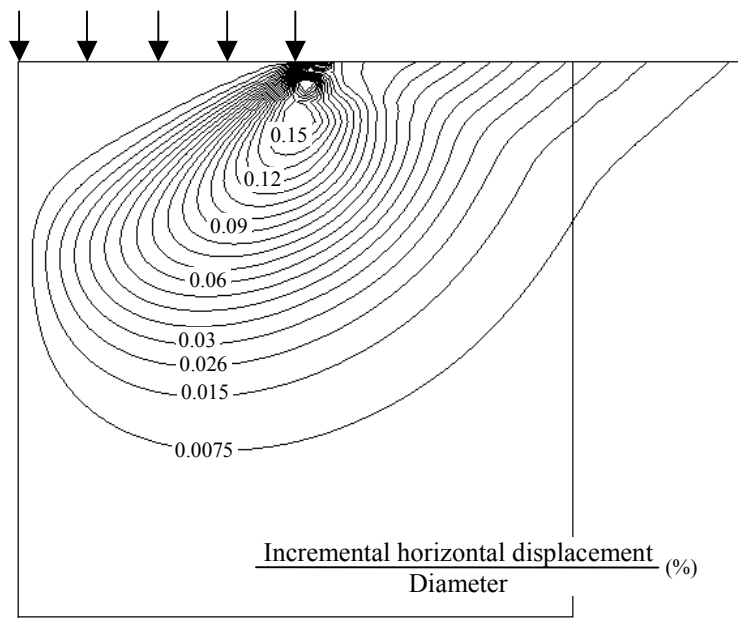
**Figure 5.9: Velocity vectors for shallow rough footing on siliceous sand**



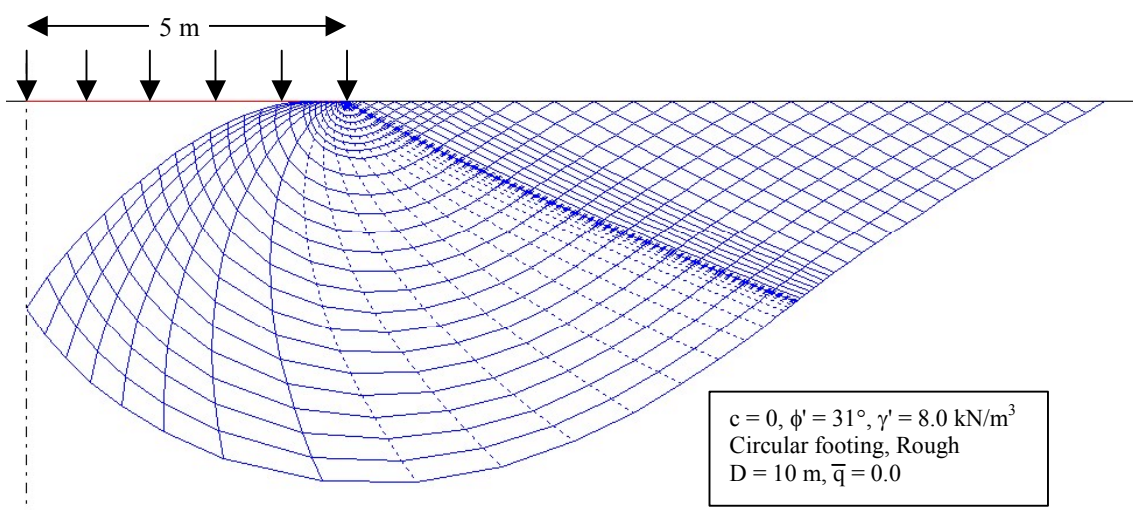
**Figure 5.10: Velocity vectors for shallow smooth footing on siliceous sand**



**Figure 5.11: Velocity vectors for shallow smooth footing on calcareous sand**

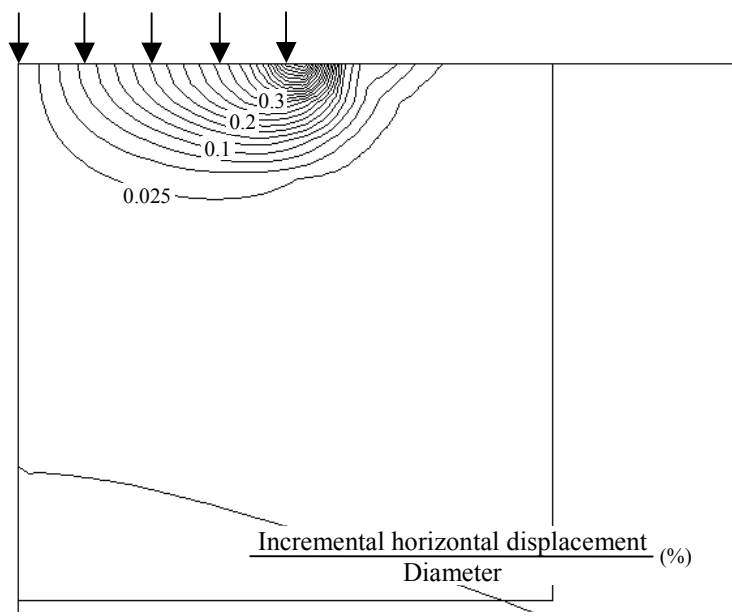


**(a) MIT-S1 model**

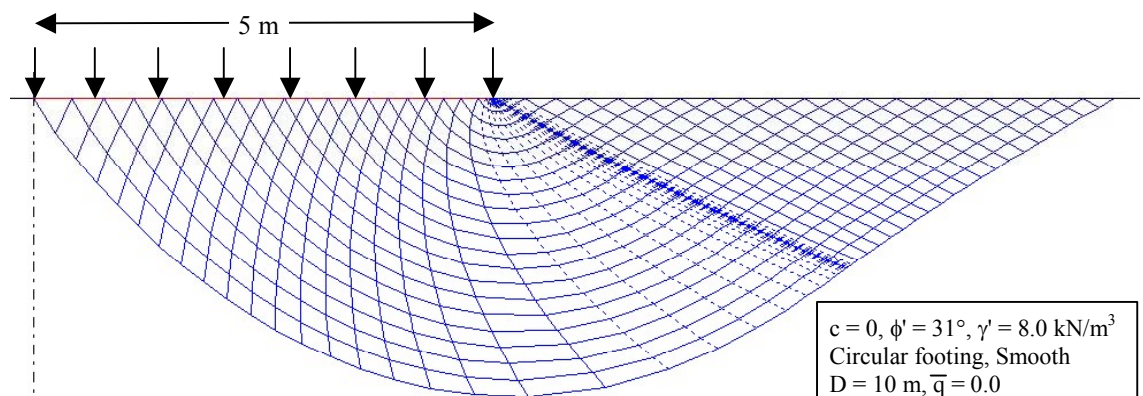


**(b) ABC**

**Figure 5.12: Horizontal velocity contours for shallow rough footing on siliceous sand**

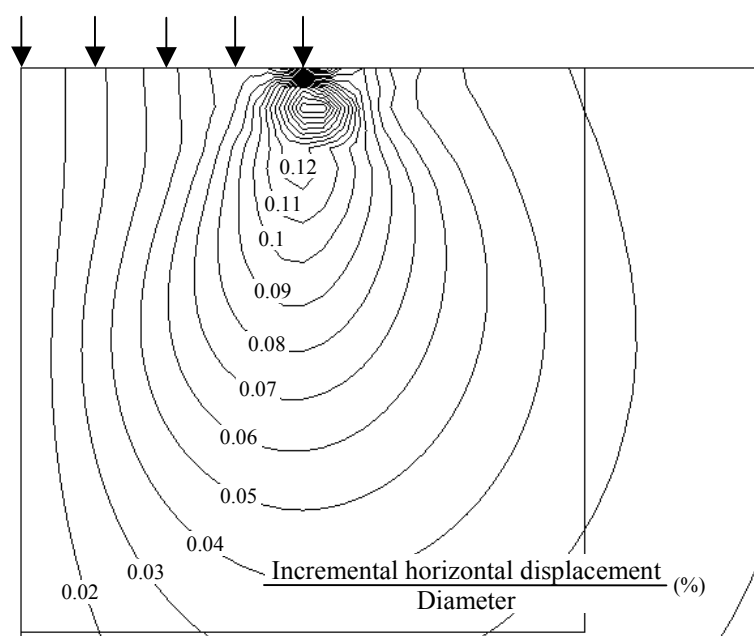


(a) MIT-S1 model

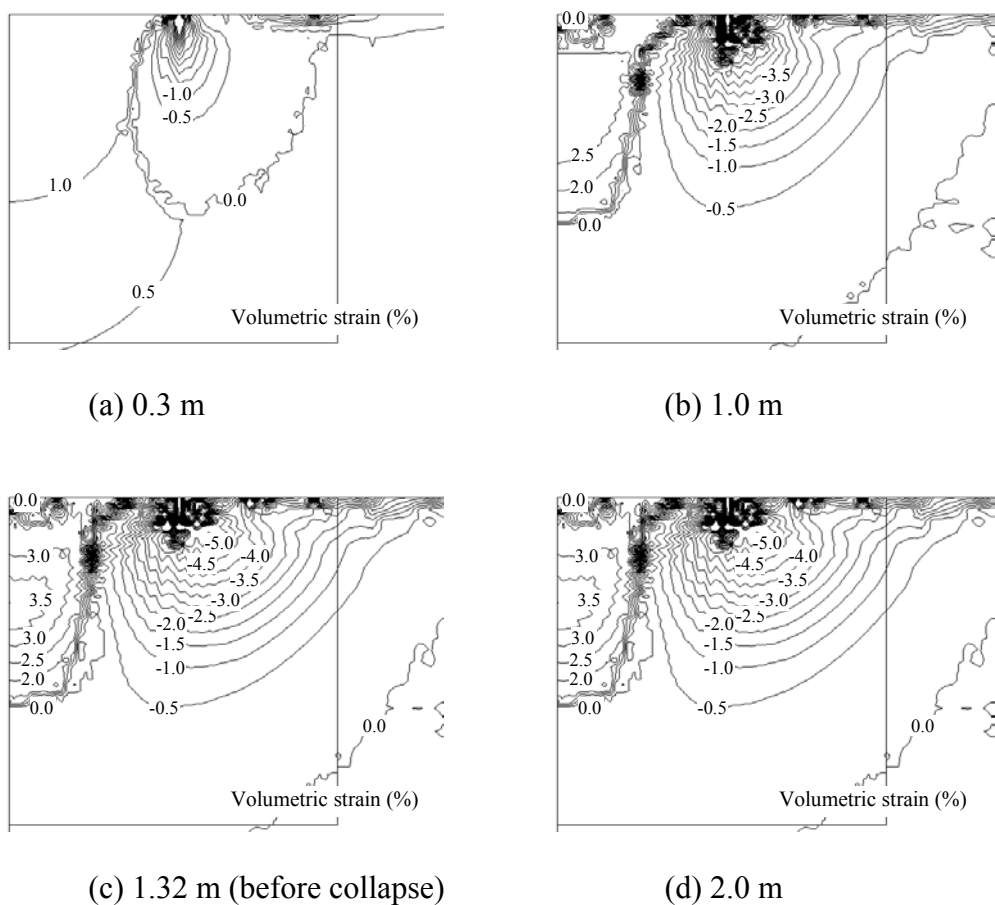
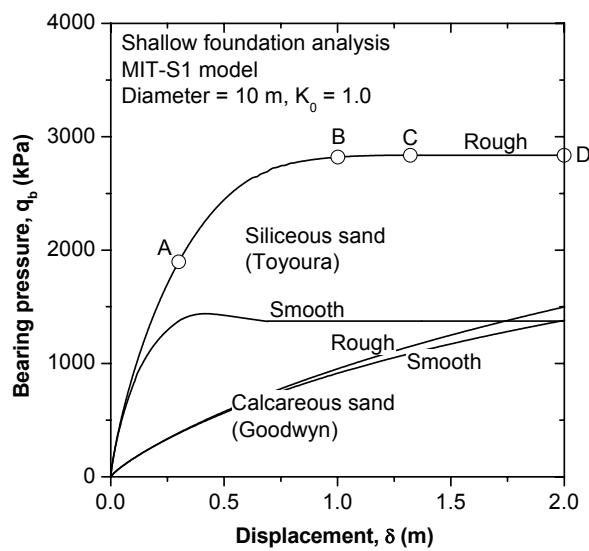


(b) ABC

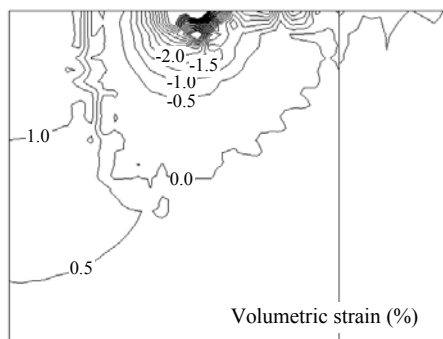
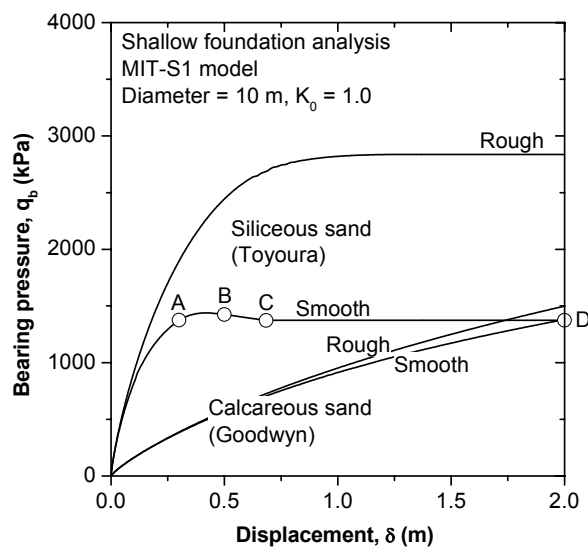
**Figure 5.13: Horizontal velocity contours for shallow smooth footing on siliceous sand**



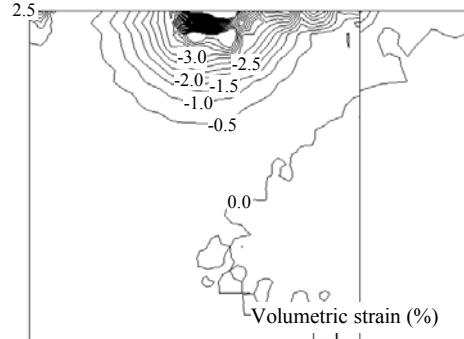
**Figure 5.14: Horizontal velocity contours for shallow smooth footing on calcareous sand**



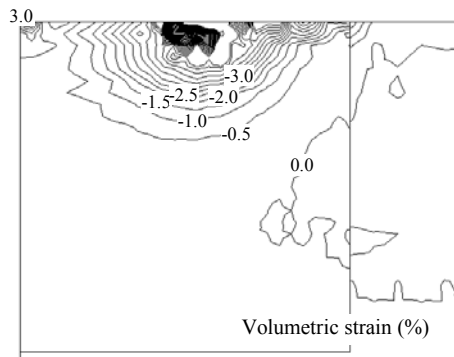
**Figure 5.15:** Volumetric strain contours for shallow rough footing on siliceous sand



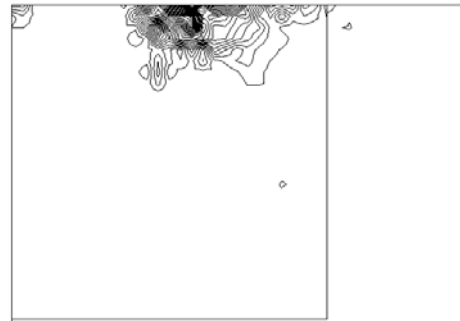
(a) 0.3 m



(b) 0.5 m

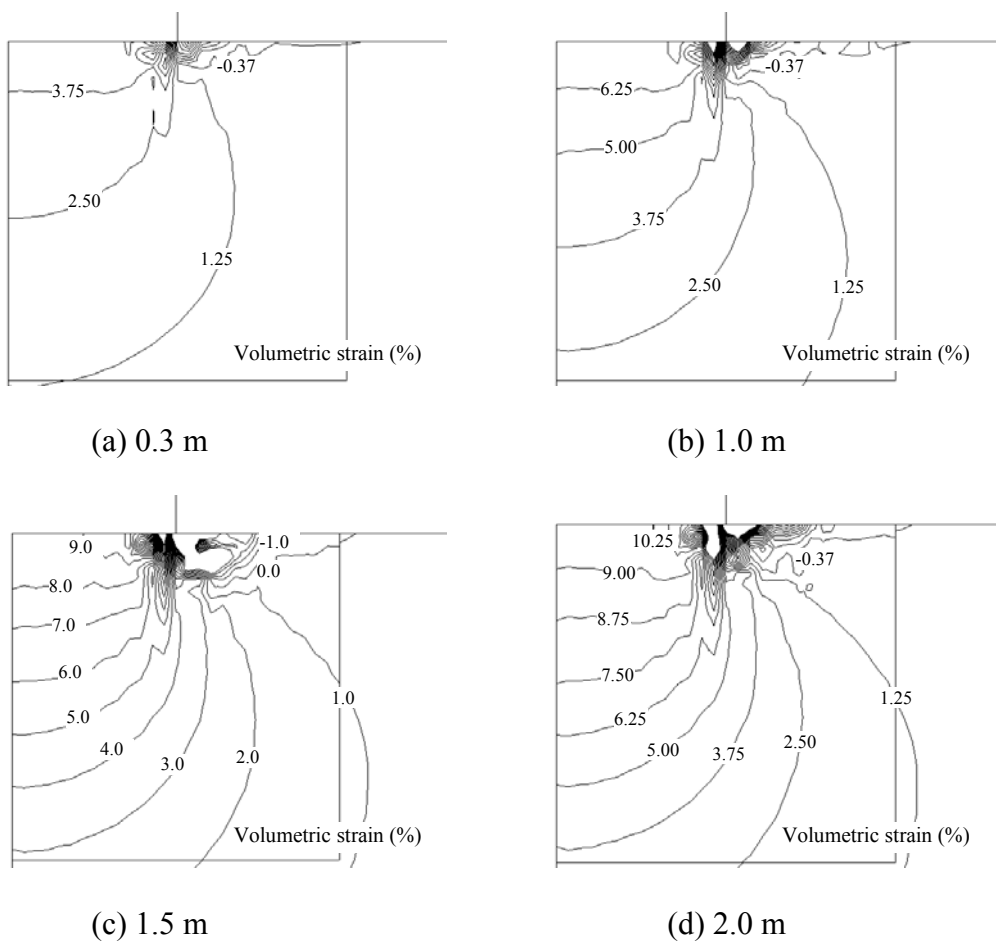
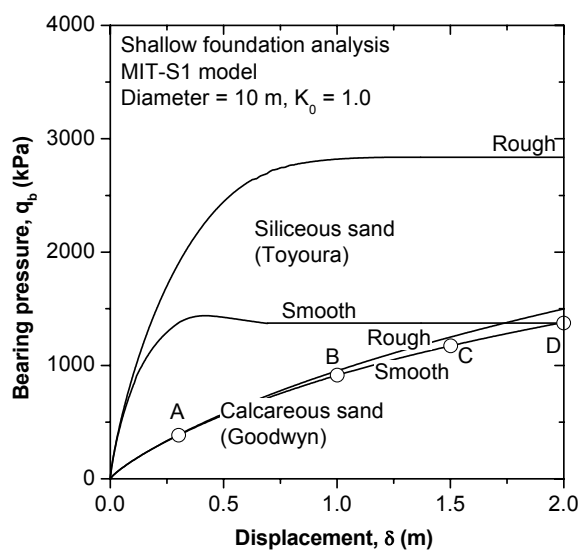


(c) 0.68 m (before collapse)

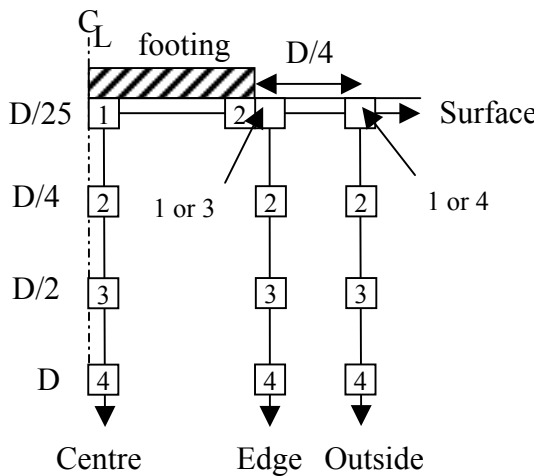
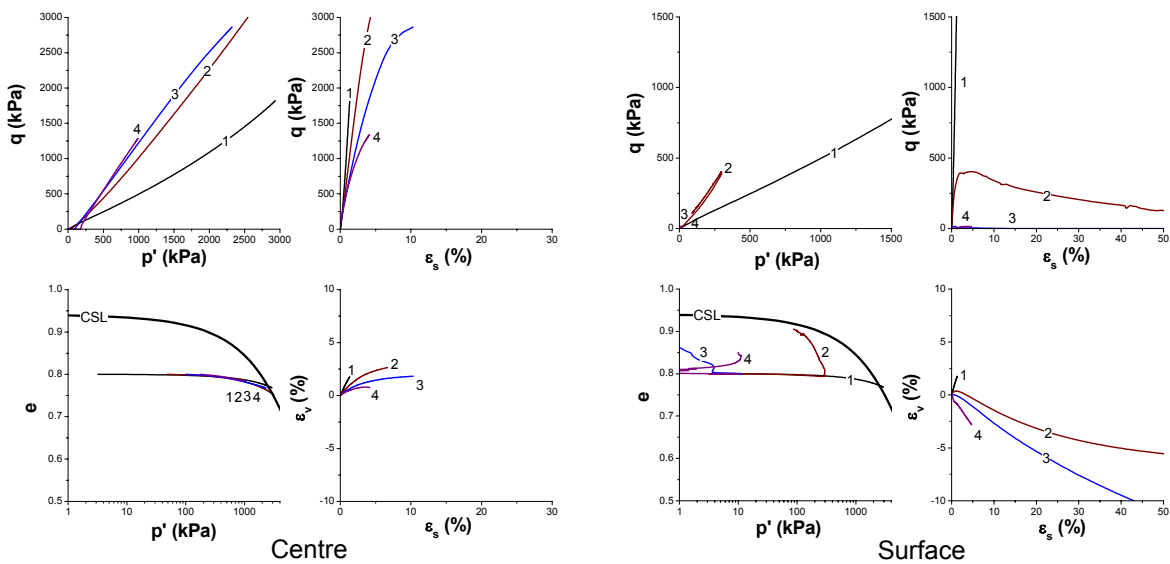


(d) 2.0 m

**Figure 5.16: Volumetric strain contours for shallow smooth footing on siliceous sand**



**Figure 5.17: Volumetric strain contours for shallow smooth footing on calcareous sand**



Toyoura siliceous sand  
 $e_0 = 0.8$   
 Diameter = 10 m  
 $\gamma' = 8 \text{ kN/m}^3$   
 Rough

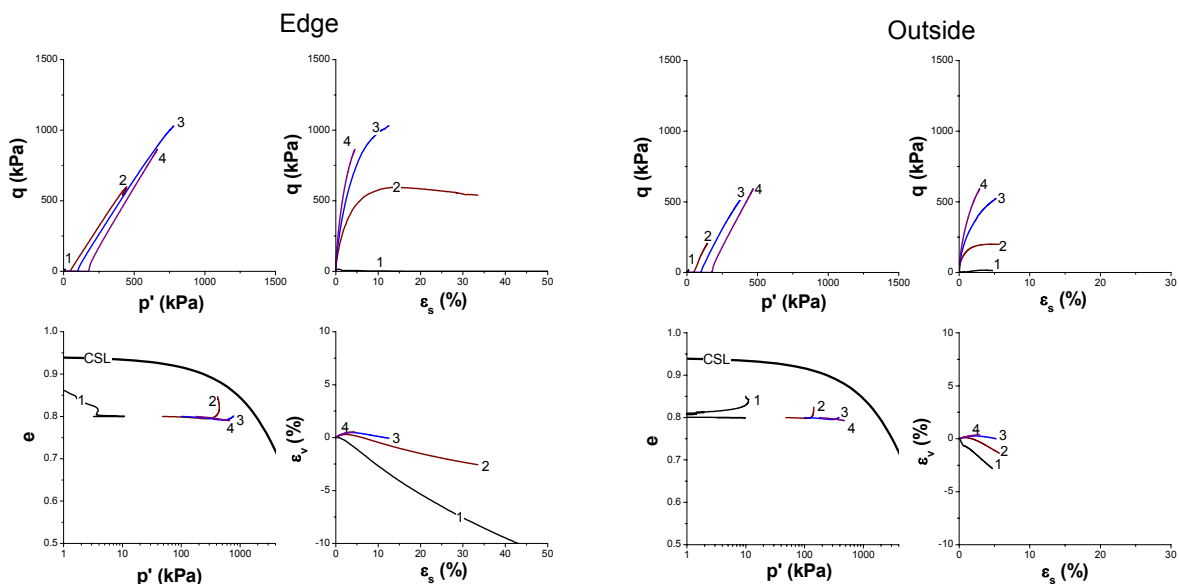
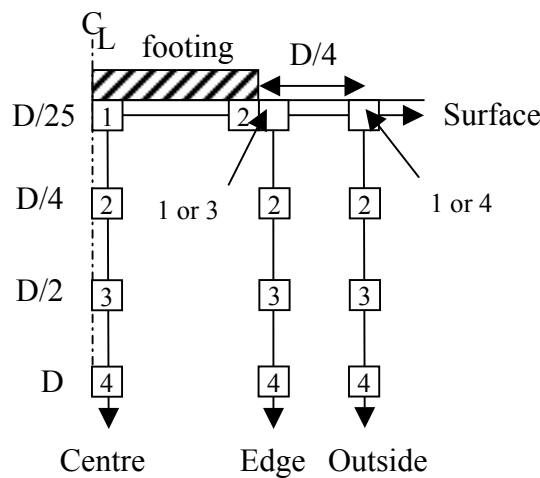
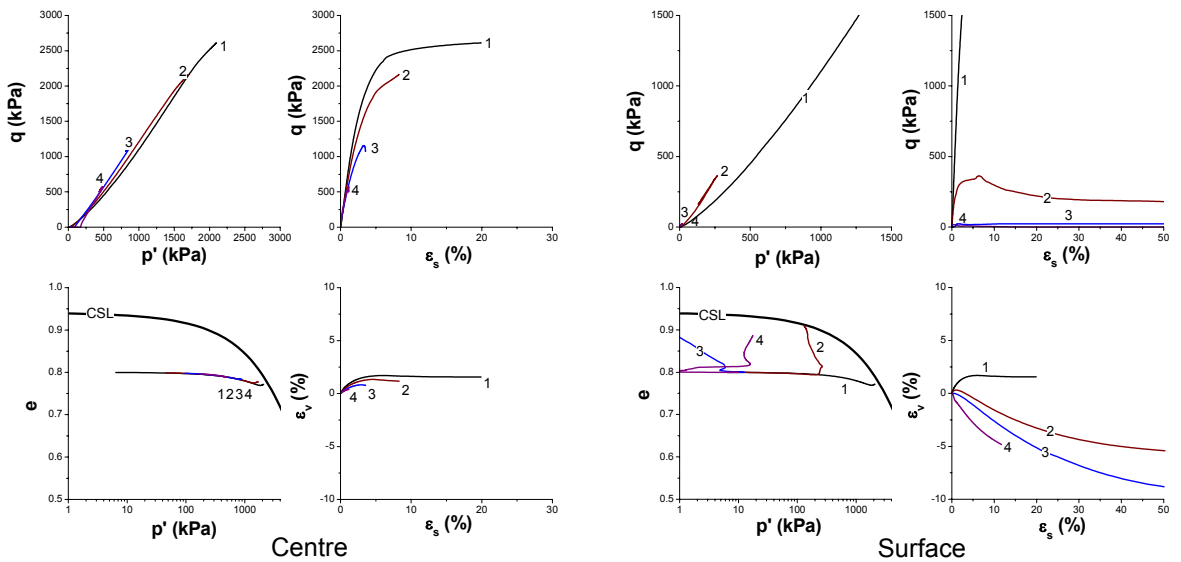
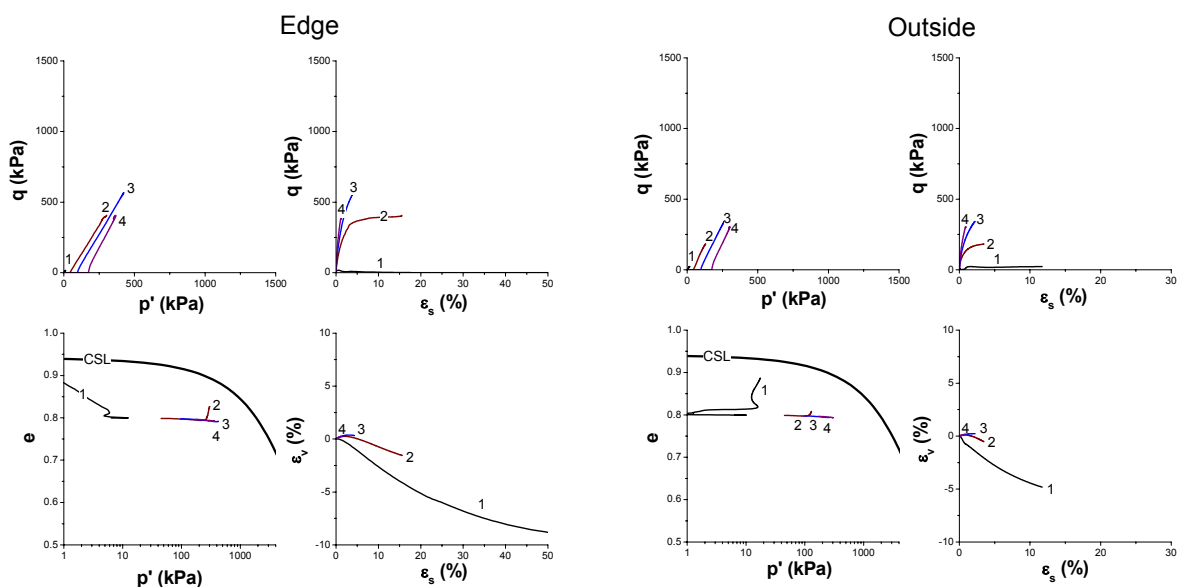


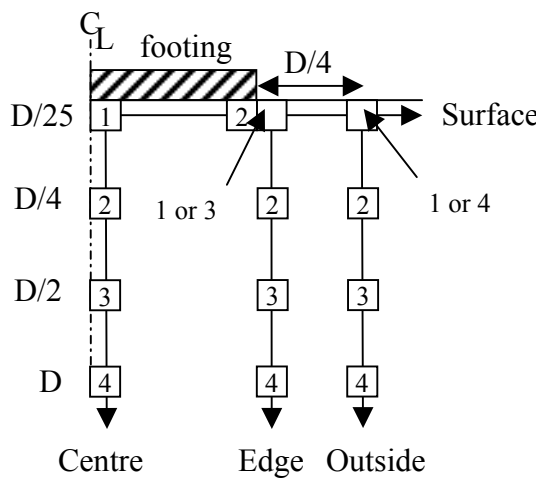
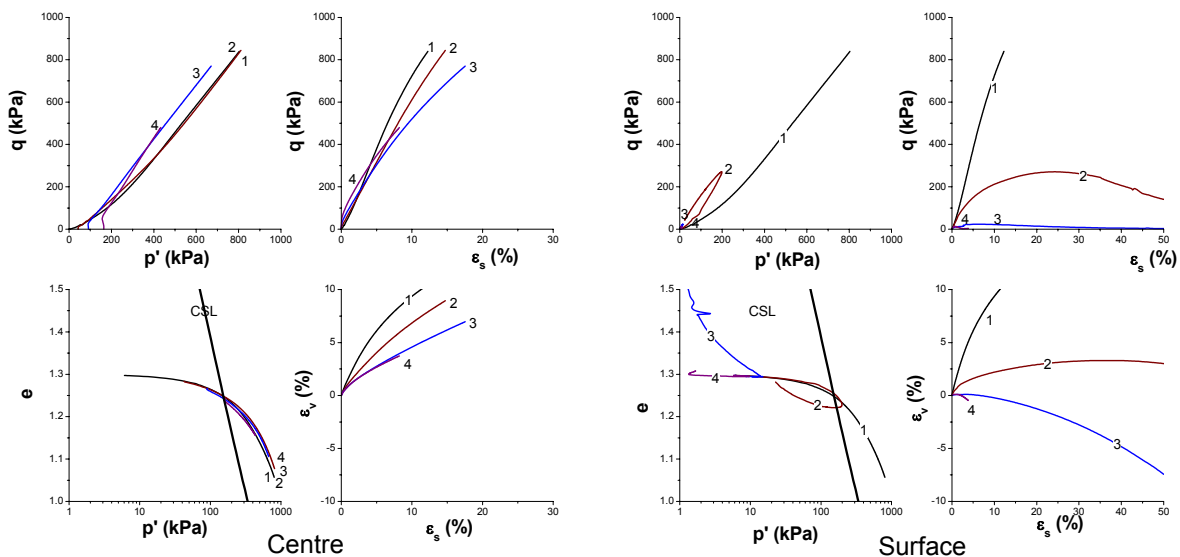
Figure 5.18: Integration point outputs for shallow rough footing on siliceous sand



Toyoura siliceous sand  
 $e_0 = 0.8$   
 Diameter = 10 m  
 $\gamma' = 8 \text{ kN/m}^3$   
 Smooth



**Figure 5.19: Integration point outputs for shallow smooth footing on siliceous sand**



Goodwyn calcareous sand  
 $e_0 = 1.3$   
Diameter = 10 m  
 $\gamma' = 7 \text{ kN/m}^3$   
Smooth  
 $\delta/D = 20 \%$

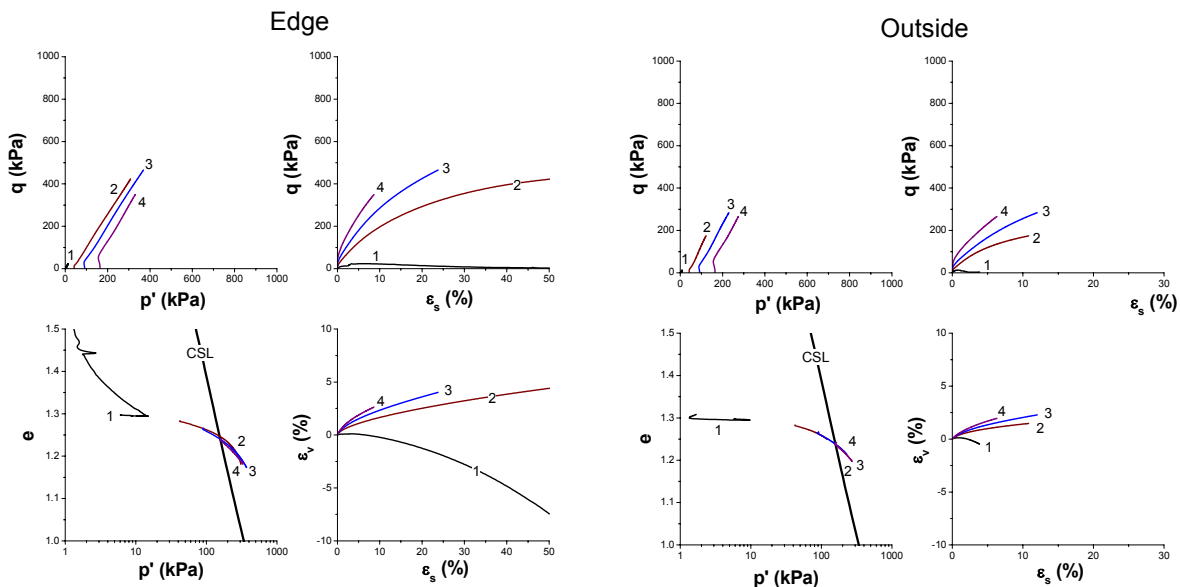
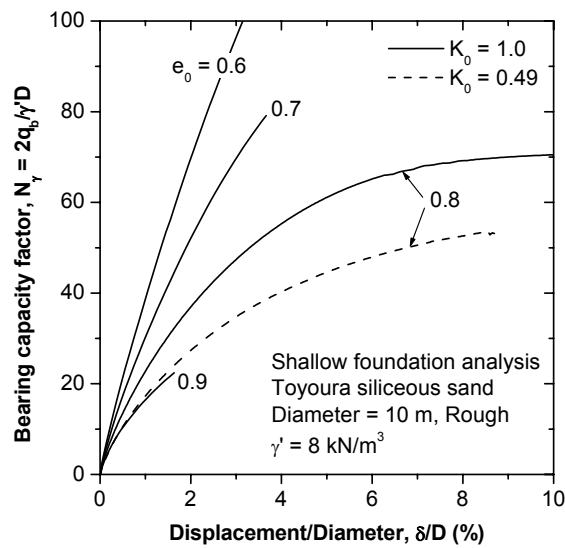
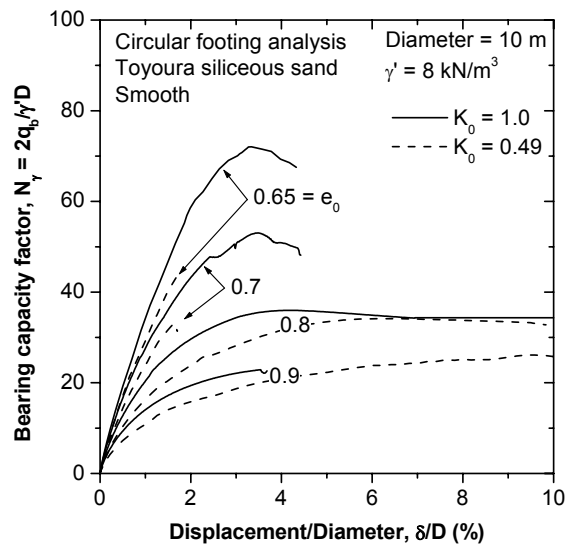


Figure 5.20: Integration point outputs for shallow smooth footing on calcareous sand

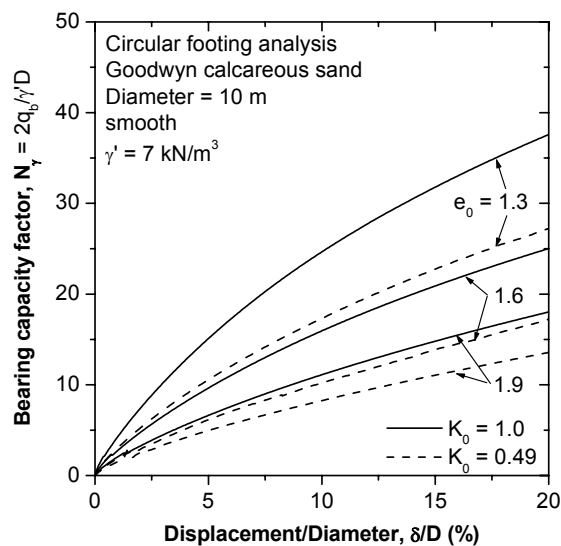


(a) Rough

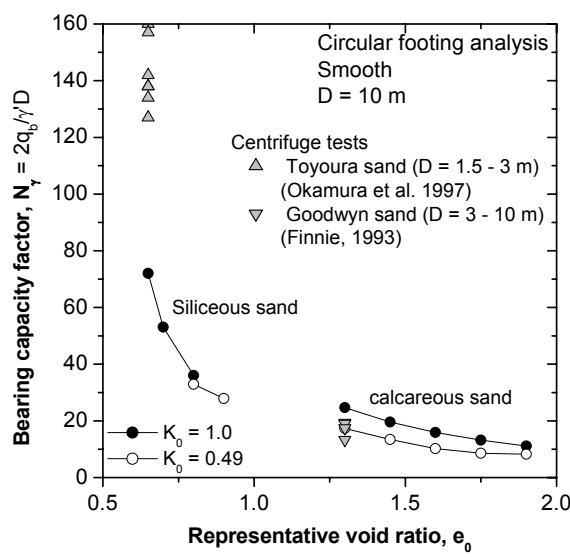


(b) Smooth

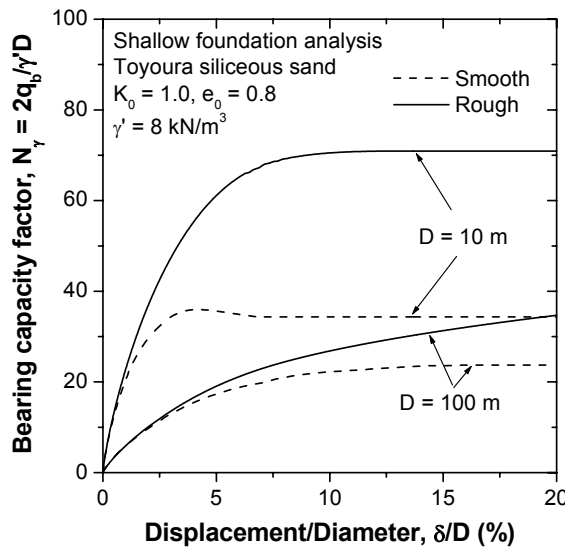
**Figure 5.21: MIT-S1 predictions of shallow foundation responses on siliceous sand with variation of void ratio and  $K_0$**



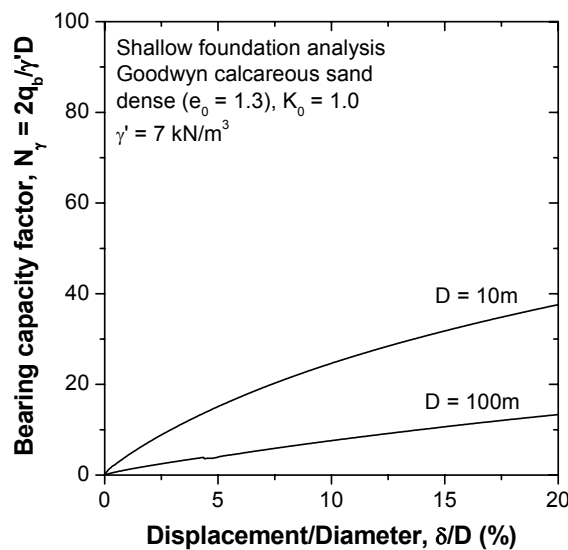
**Figure 5.22: MIT-S1 predictions of shallow foundation responses on calcareous sand with variation of void ratio and  $K_0$**



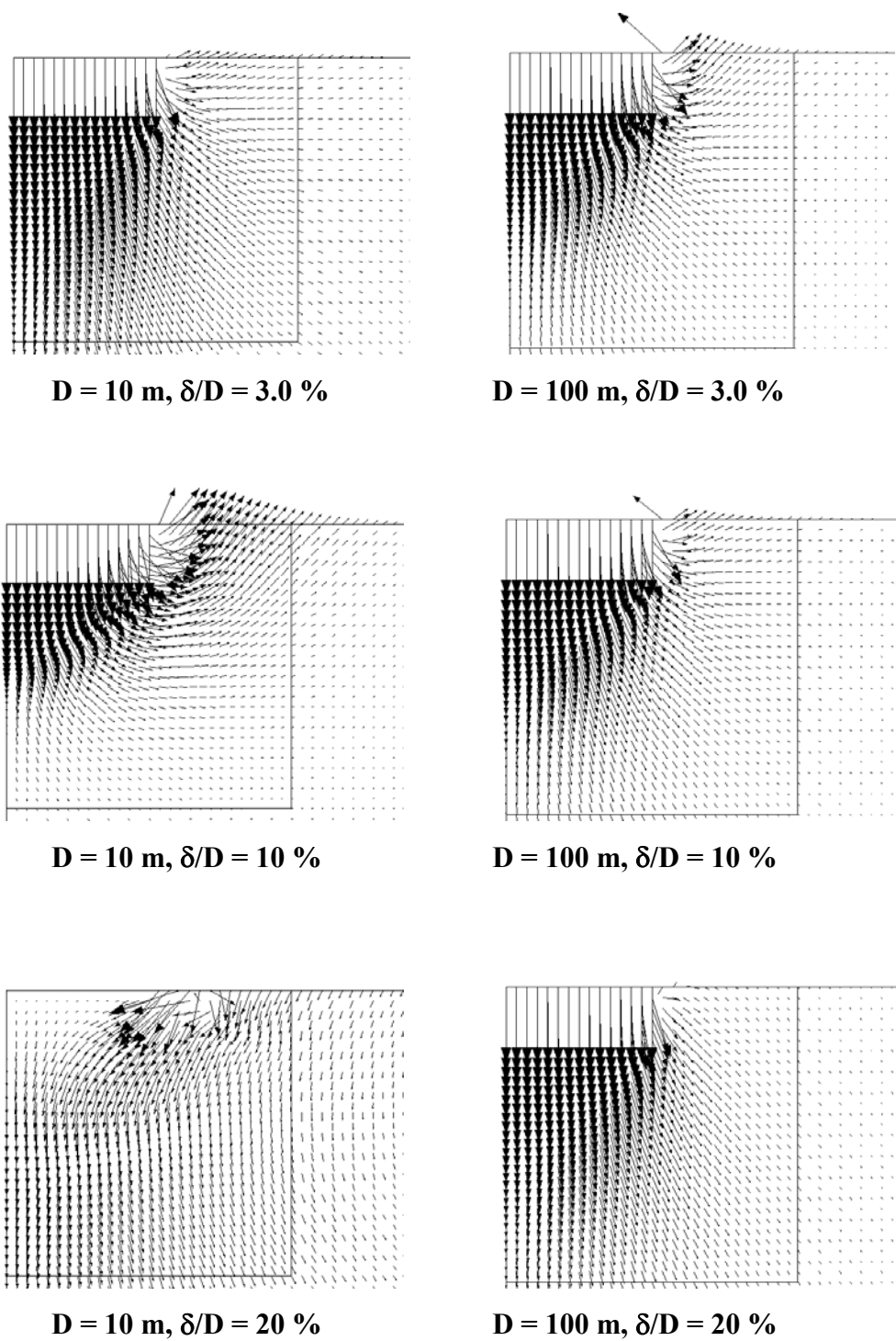
**Figure 5.23:  $N_y$  and void ratio relationship of shallow foundation responses**



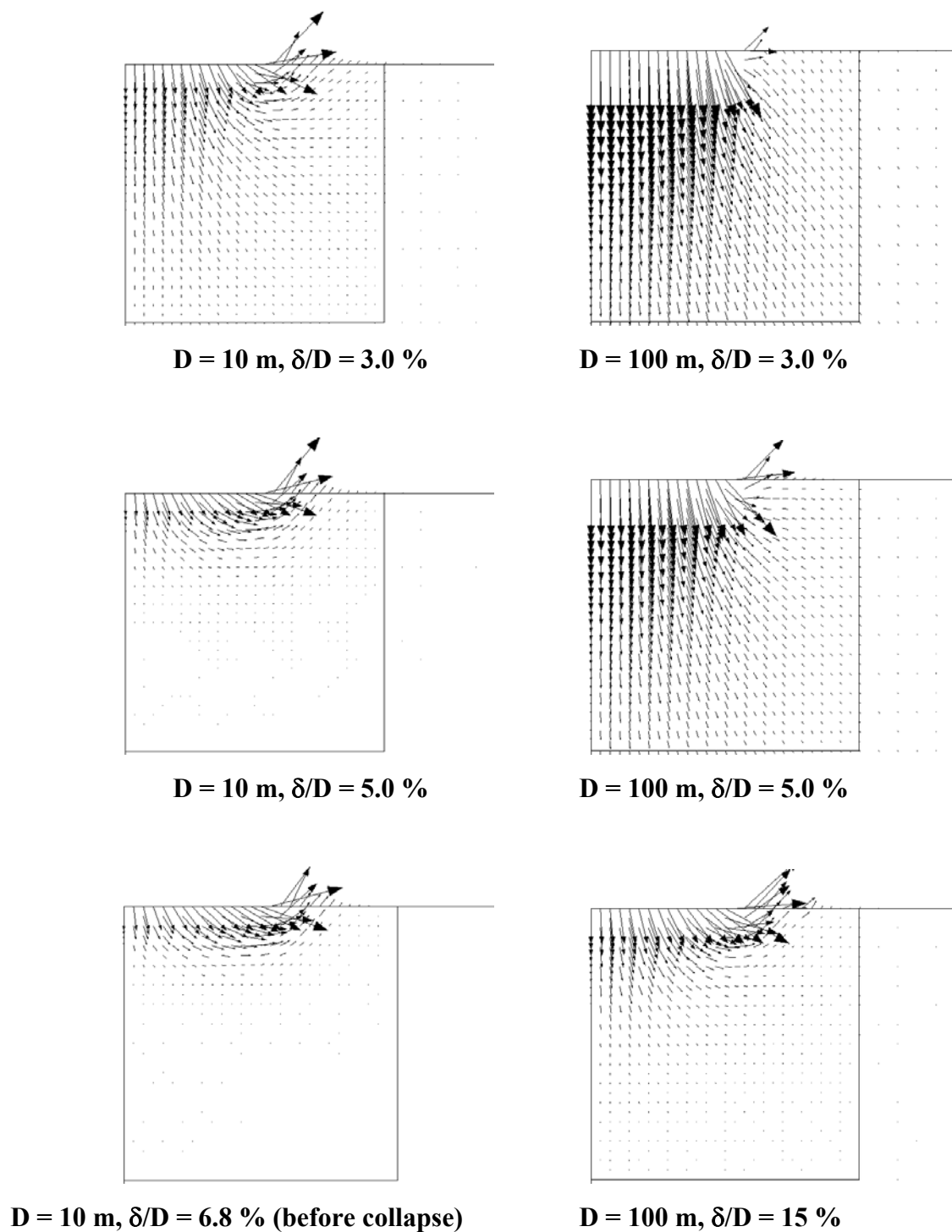
**Figure 5.24: Relationship of  $N_y$  and  $\delta/D$  for 10 and 100 m diameter footings on siliceous sand**



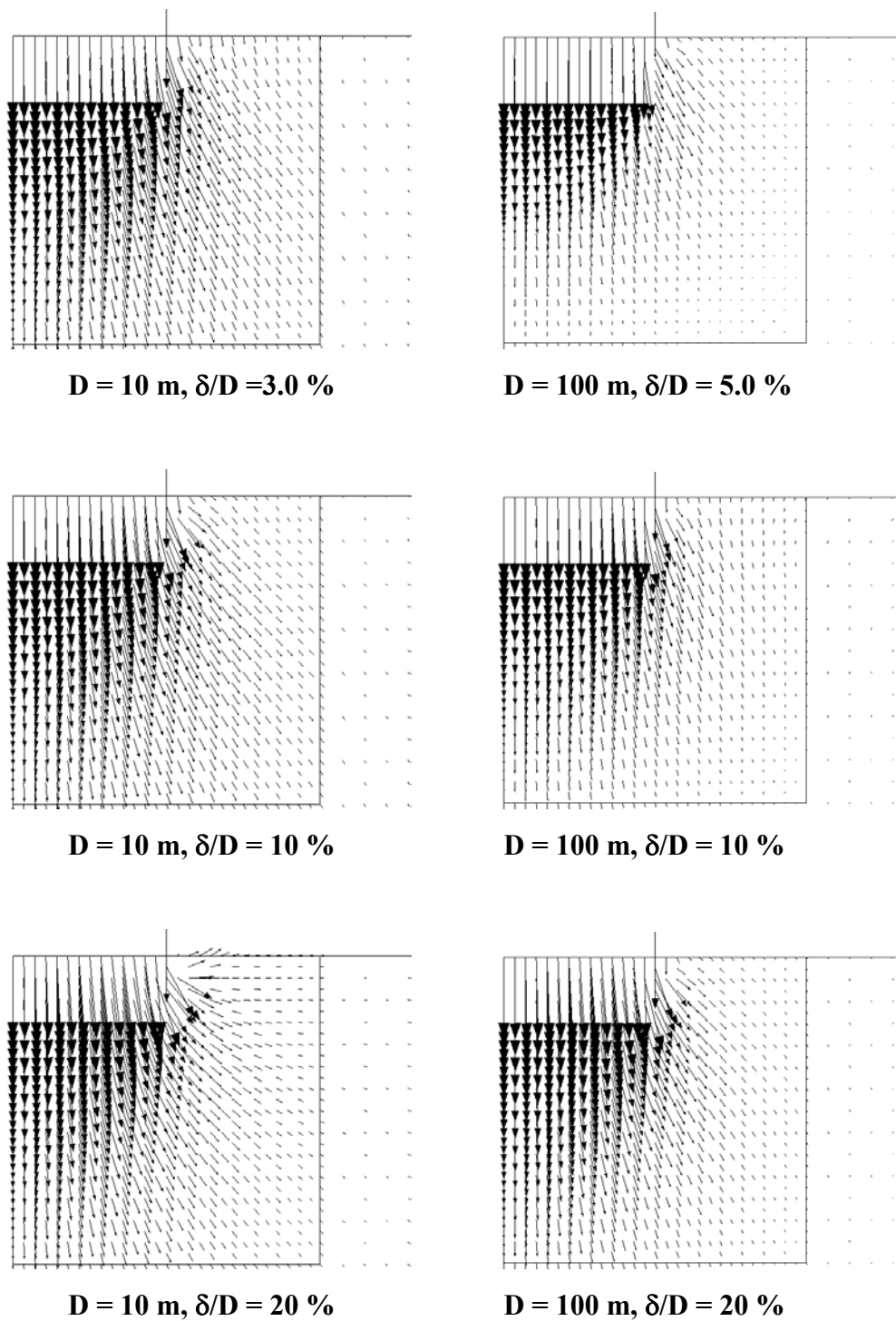
**Figure 5.25: Relationship of  $N_y$  and  $\delta/D$  for 10 and 100 m diameter footings on calcareous sand**



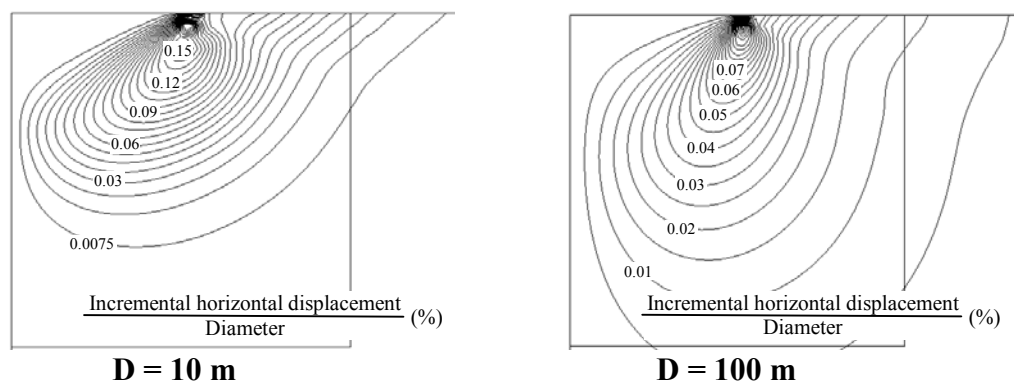
**Figure 5.26: Comparison of velocity vectors for a fully rough 100 m diameter footing with the 10 m diameter on siliceous sand**



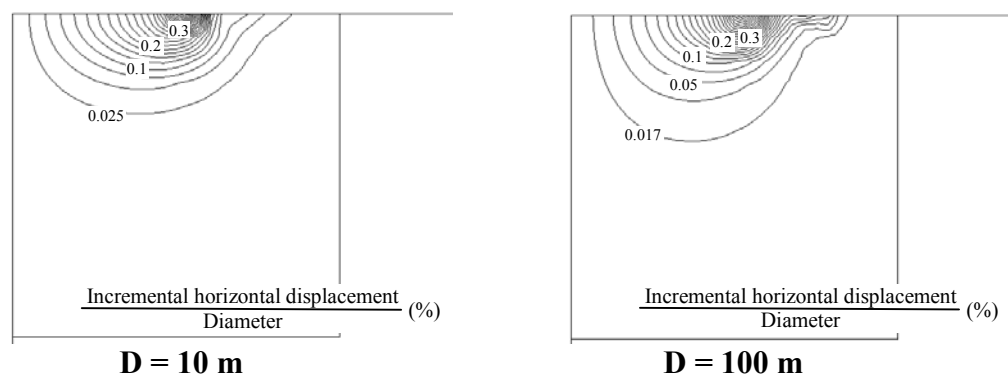
**Figure 5.27: Comparison of velocity vectors for a fully smooth 100 m diameter footing with the 10 m diameter on siliceous sand**



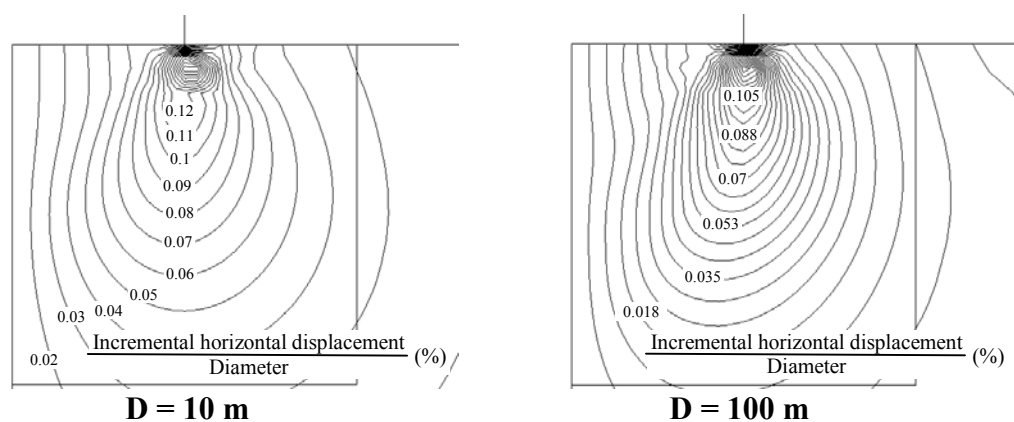
**Figure 5.28: Comparison of velocity vectors for a fully smooth 100 m diameter footing with the 10 m diameter on calcareous sand**



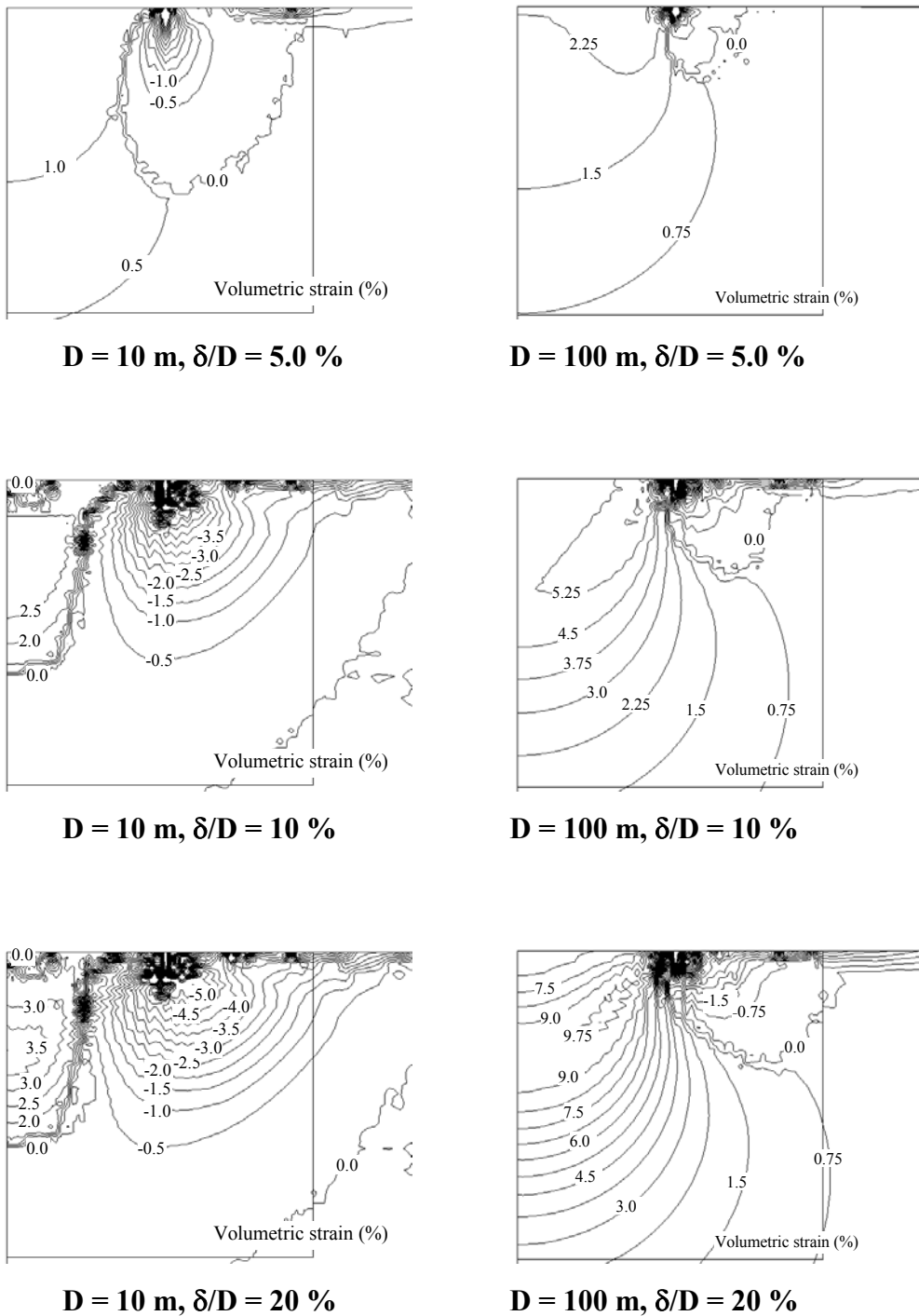
**Figure 5.29: Horizontal velocity contours for a fully rough footing on siliceous sand**



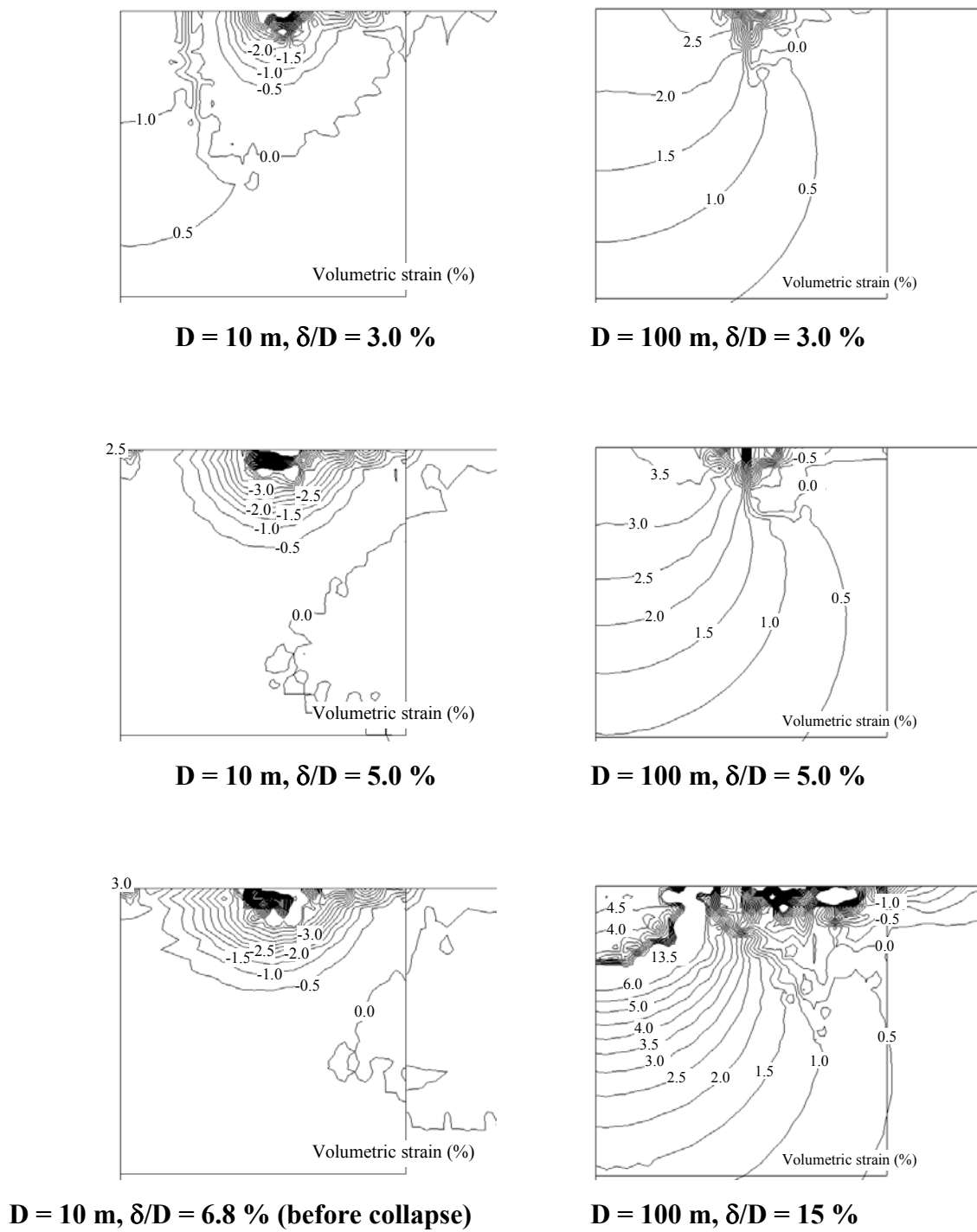
**Figure 5.30: Horizontal velocity contours for a fully smooth footing on siliceous sand**



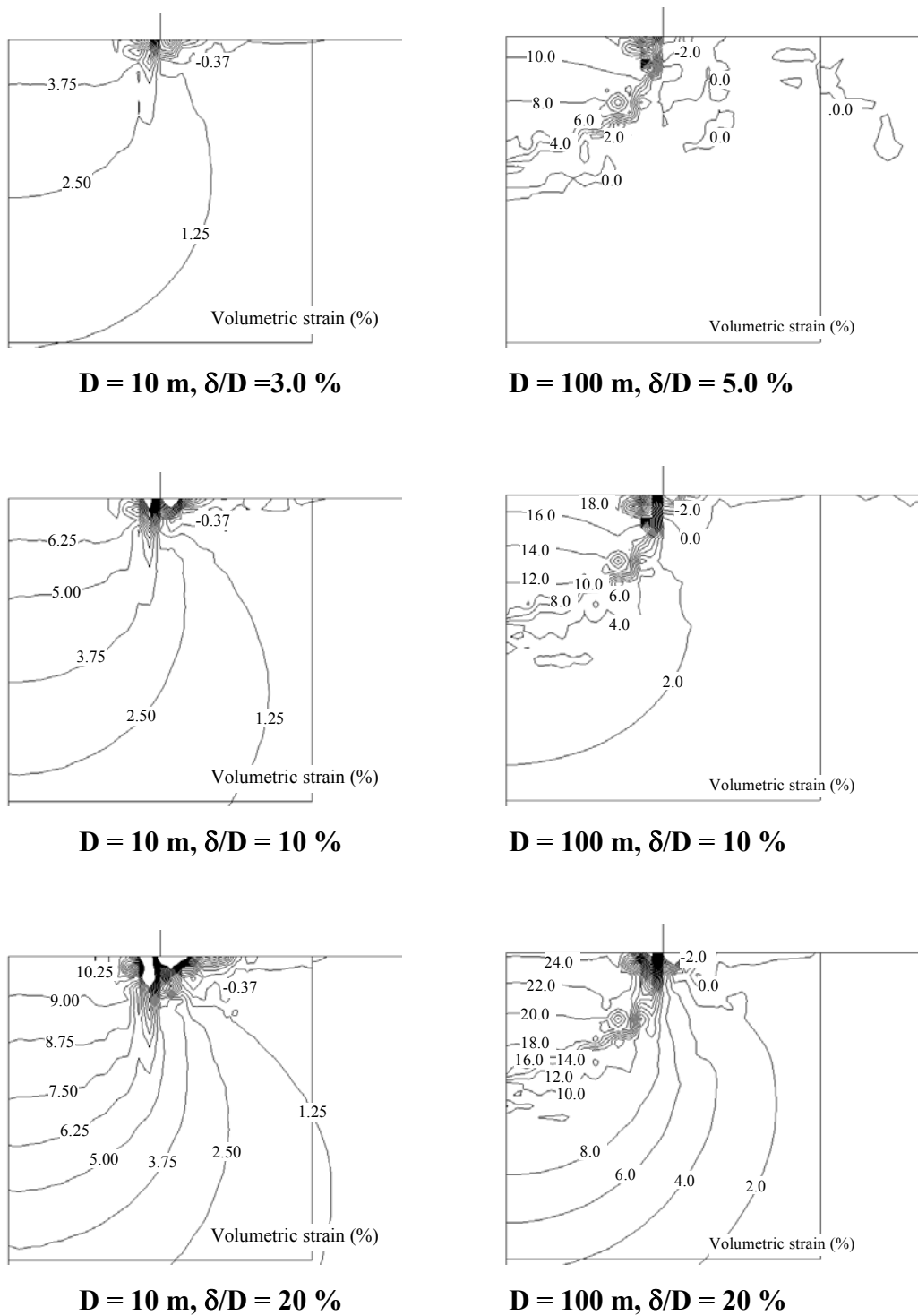
**Figure 5.31: Horizontal velocity contours for a fully smooth shallow footings on calcareous sand**



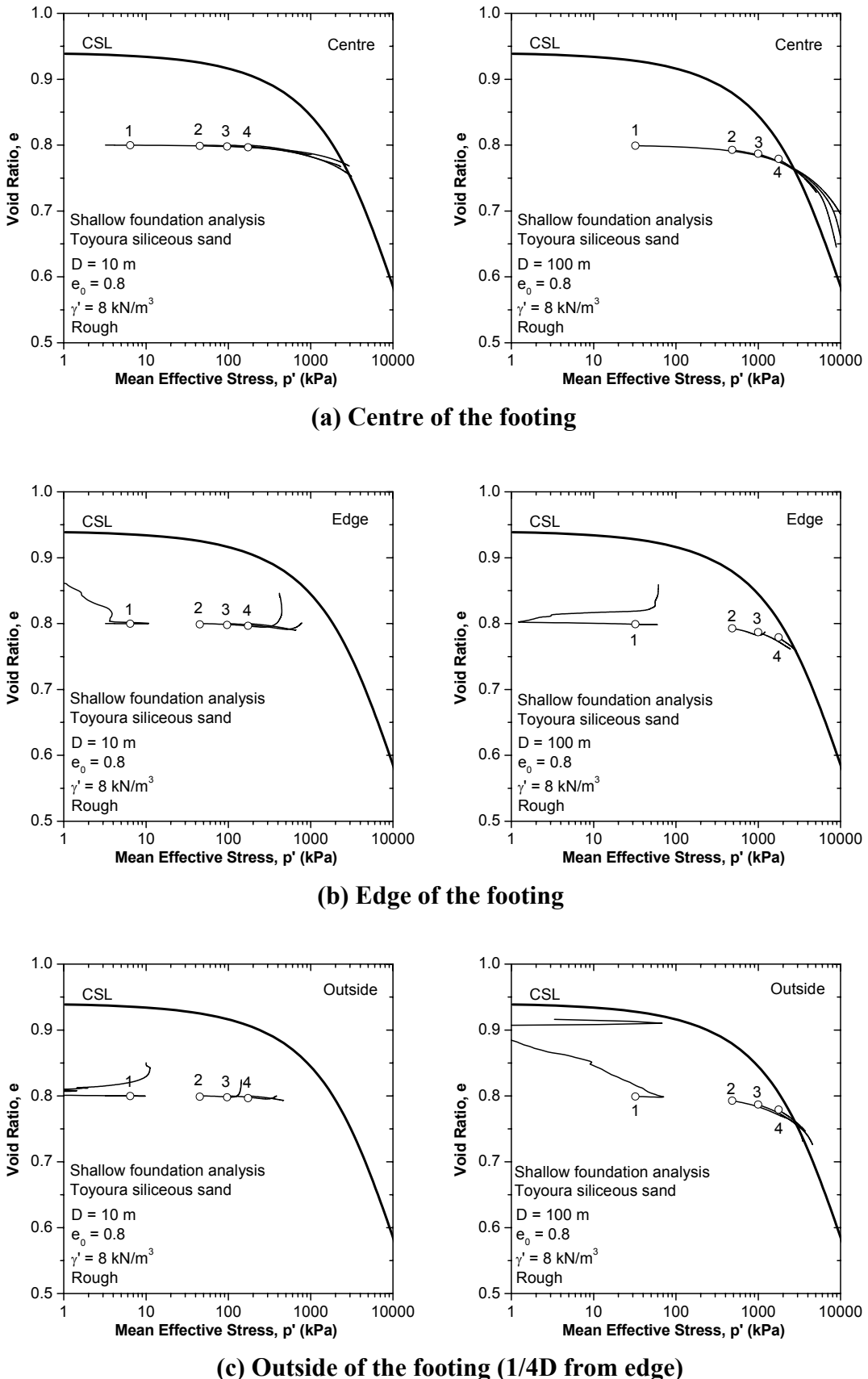
**Figure 5.32: Comparison of volumetric strain contours for a fully rough  $100 \text{ m}$  diameter footing with the  $10 \text{ m}$  diameter on siliceous sand**



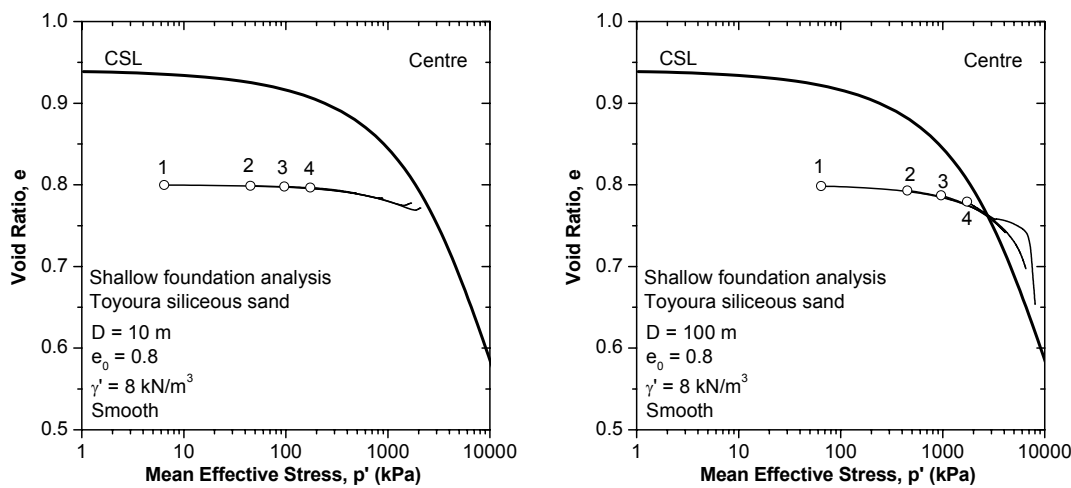
**Figure 5.33: Comparison of volumetric strain contours for a fully smooth 100 m diameter footing with the 10 m diameter on siliceous sand**



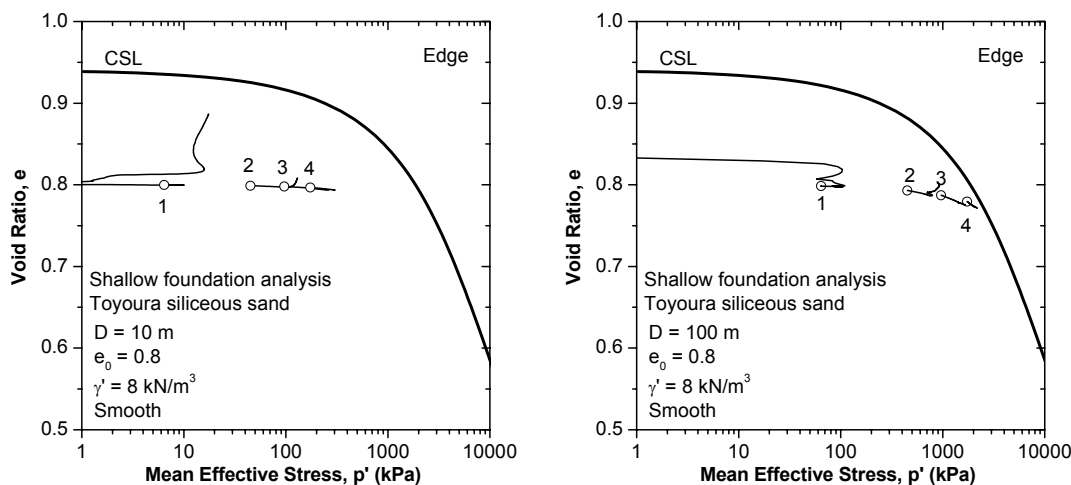
**Figure 5.34: Comparison of volumetric strain contours for a fully smooth 100 m diameter footing with the 10 m diameter on calcareous sand**



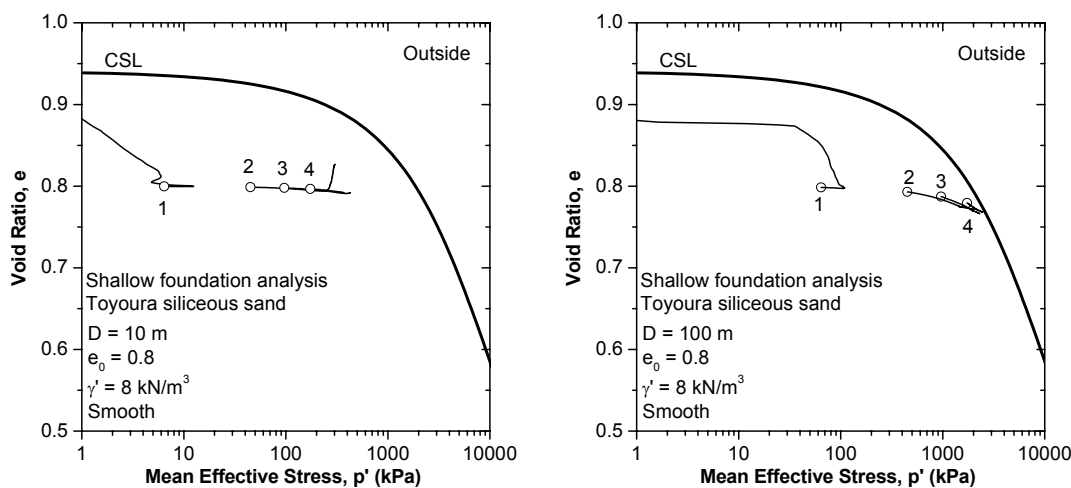
**Figure 5.35: Void ratio and mean effective stress relationship from integration points for shallow rough footing on siliceous sand**



(a) Centre of the footing

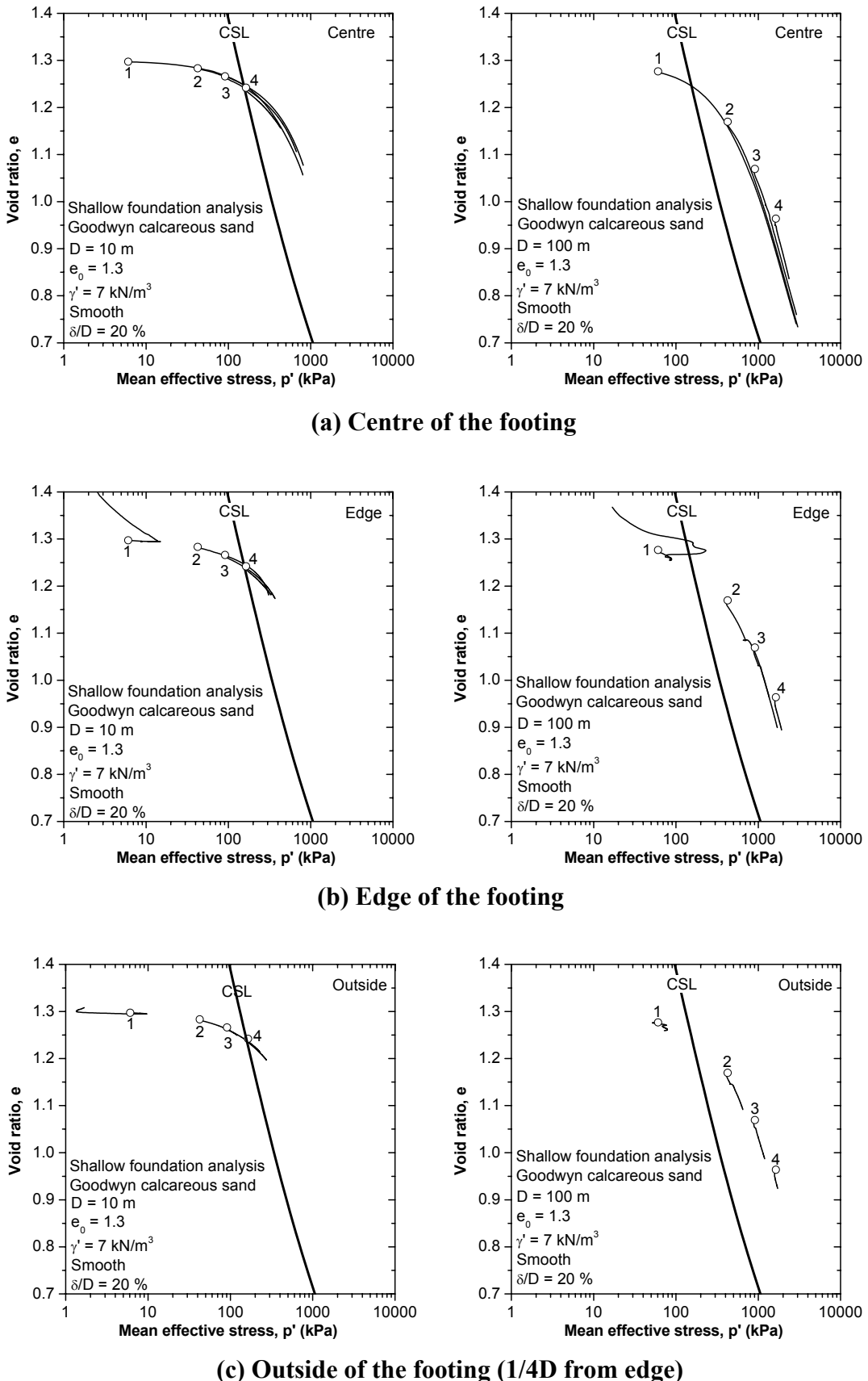


(b) Edge of the footing

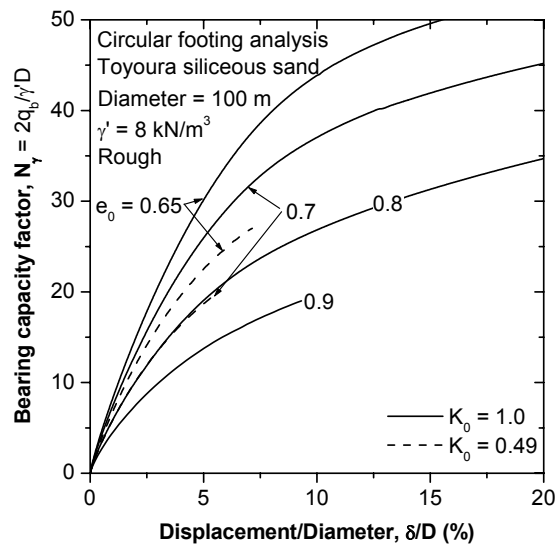


(c) Outside of the footing (1/4D from edge)

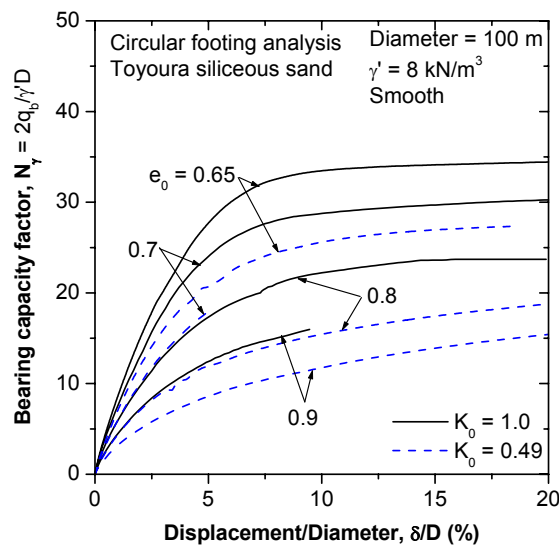
**Figure 5.36: Void ratio and mean effective stress relationship from integration points for shallow smooth footing on siliceous sand**



**Figure 5.37: Void ratio and mean effective stress relationship from integration points for shallow smooth footing on calcareous sand**

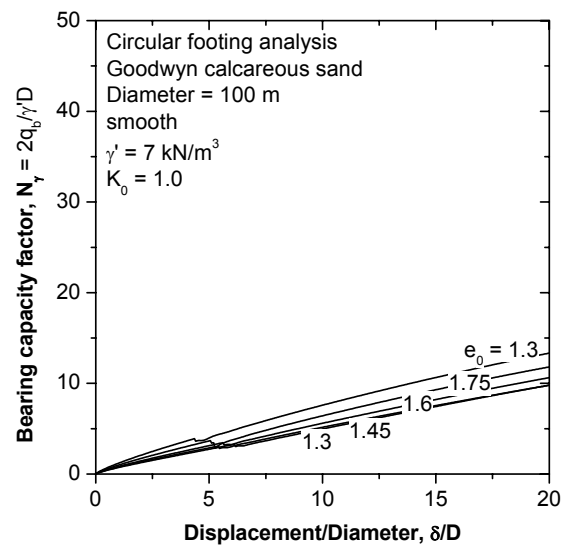


(a) Rough

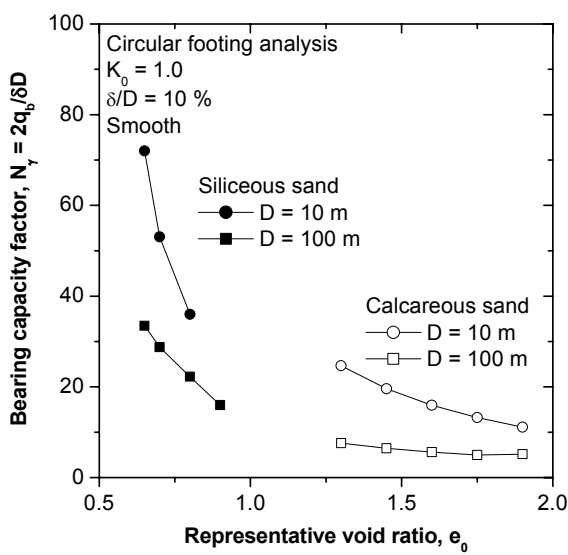


(b) Smooth

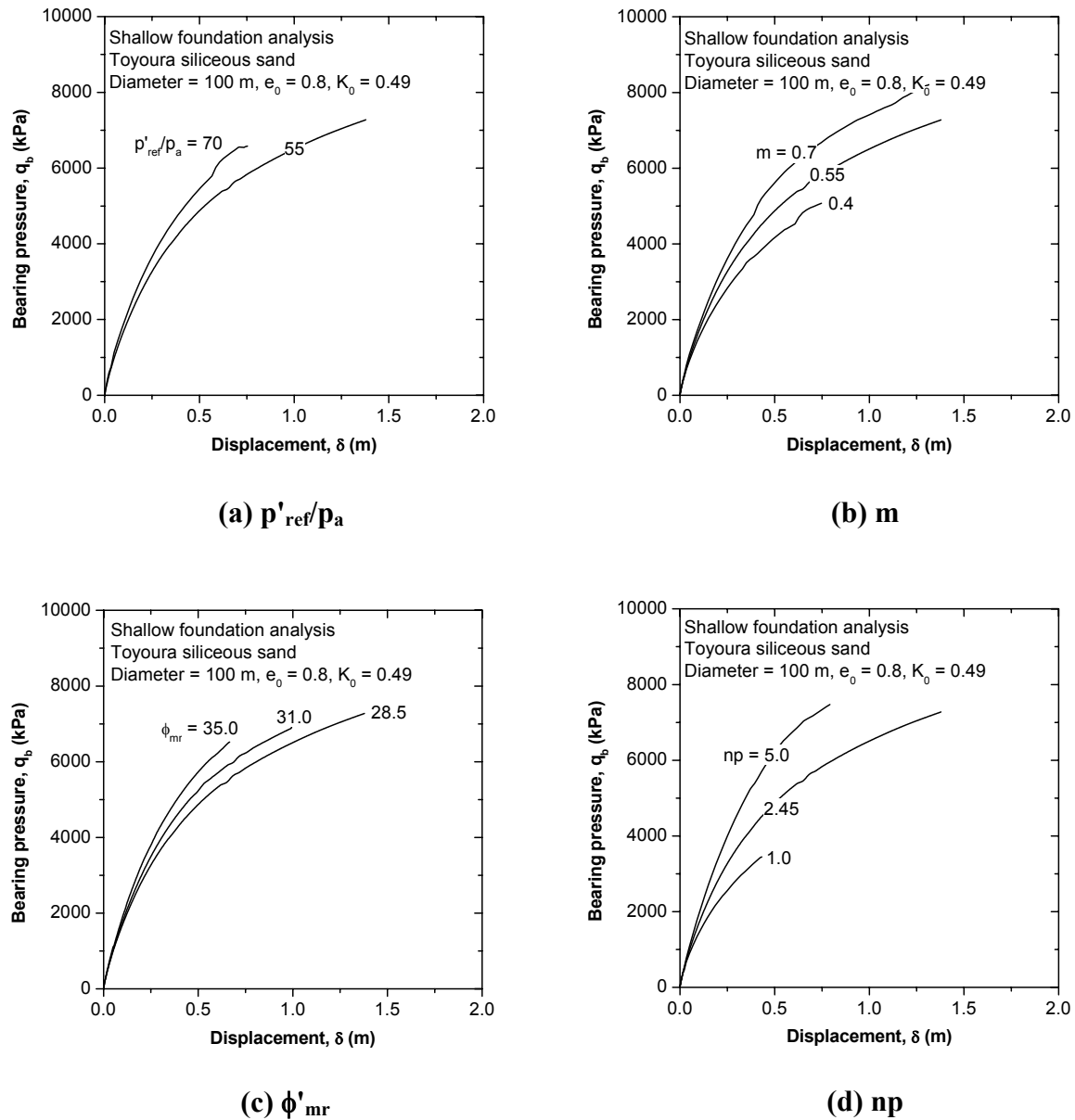
**Figure 5.38: MIT-S1 predictions of 100 m diameter circular foundation responses on siliceous sand with variation of void ratio and  $K_0$**



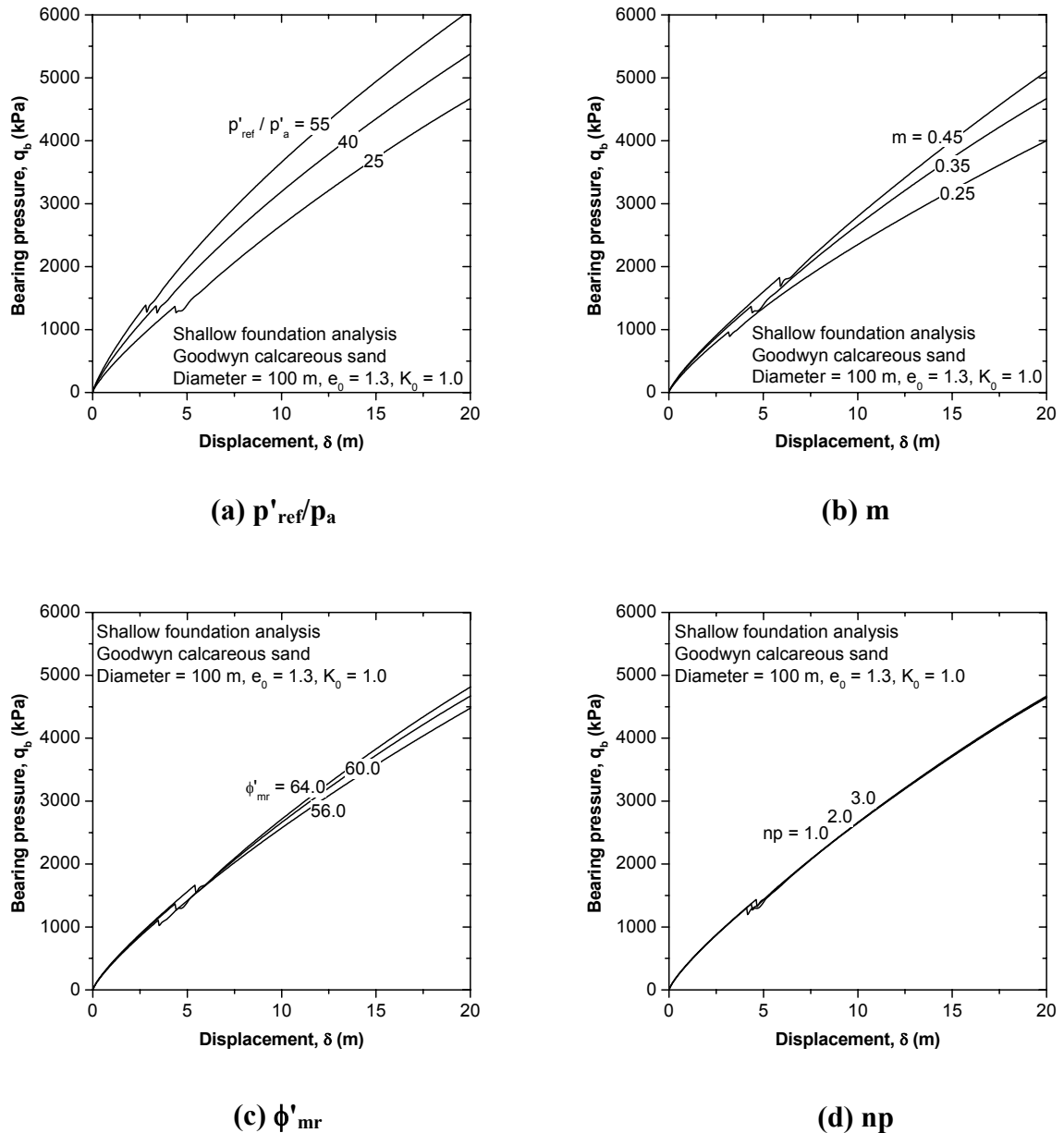
**Figure 5.39: MIT-S1 predictions of 100 m diameter circular foundation responses on calcareous sand with variation of void ratio**



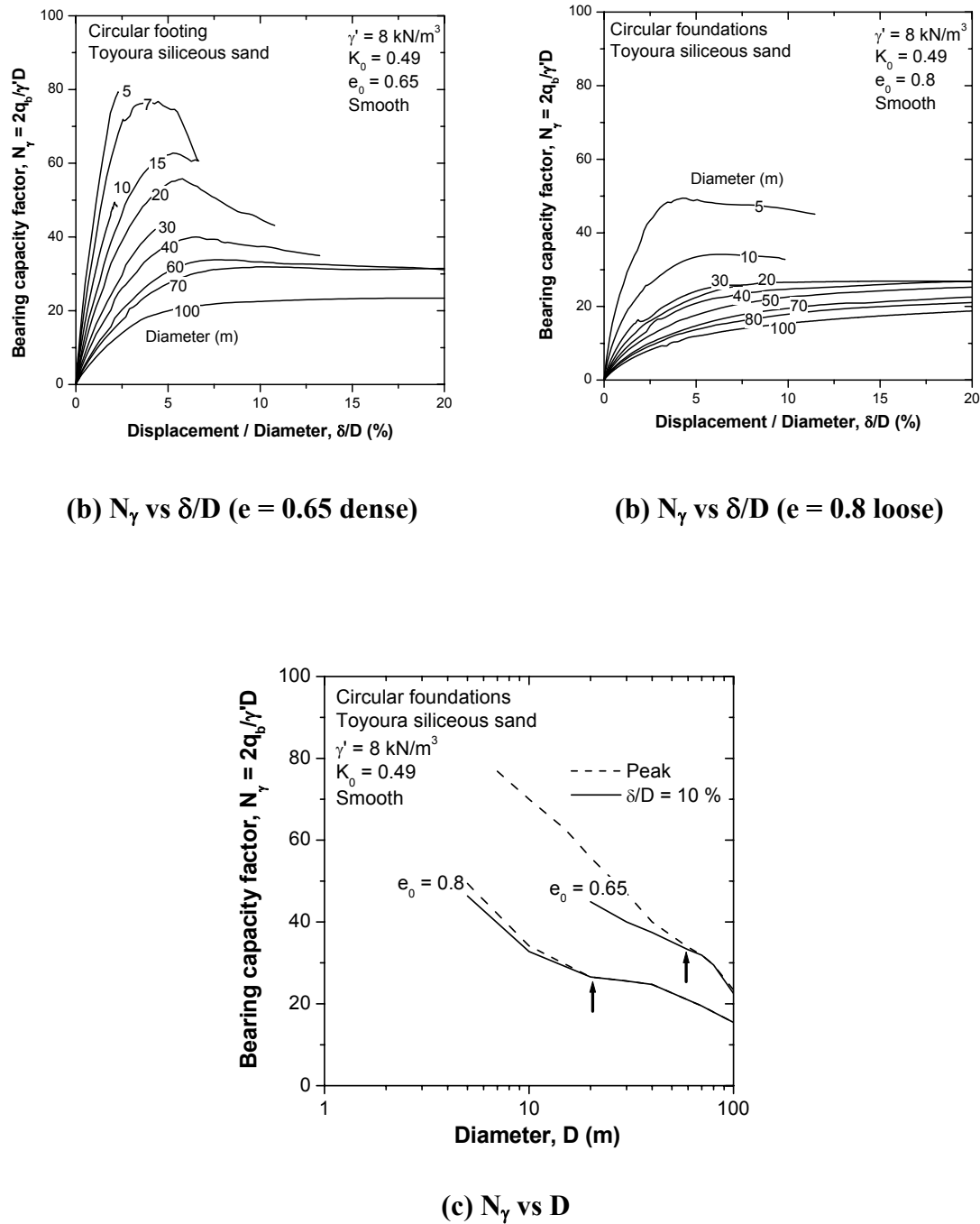
**Figure 5.40: Comparison between 100 m and 10 m diameter shallow foundation responses on  $N_y$  and void ratio space**



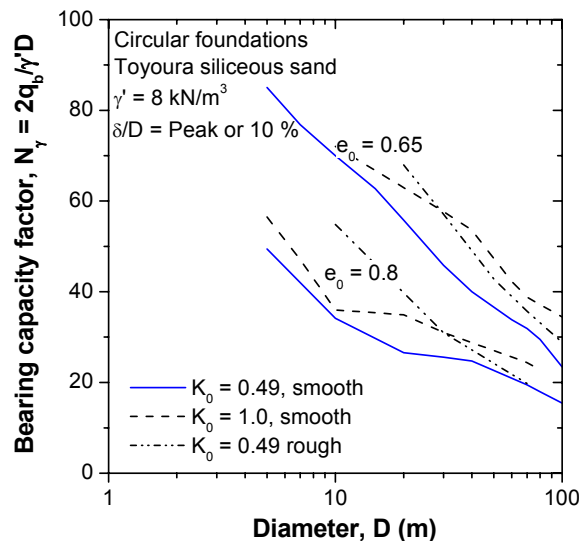
**Figure 5.41: Parametric studies for 100 m diameter footings on siliceous sand**



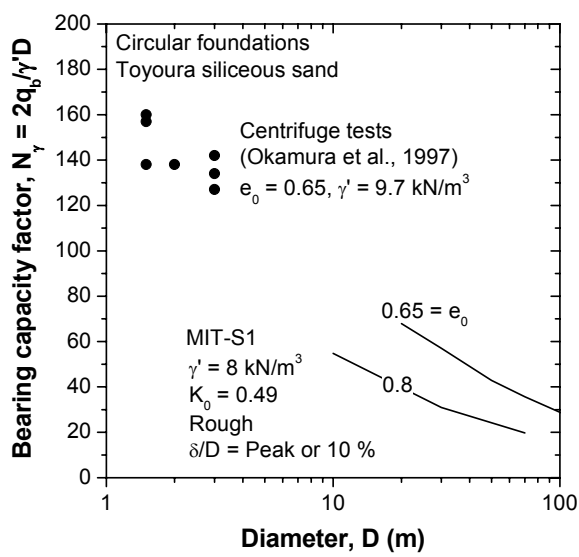
**Figure 5.42: Parametric studies for 100 m diameter footings on calcareous sand**



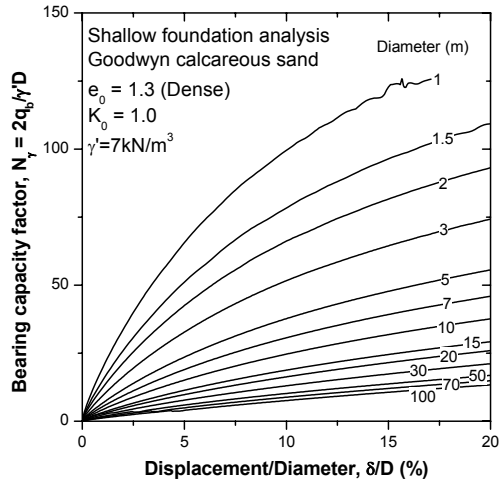
**Figure 5.43: Effects of foundation size and density on shallow circular footings on siliceous sand**



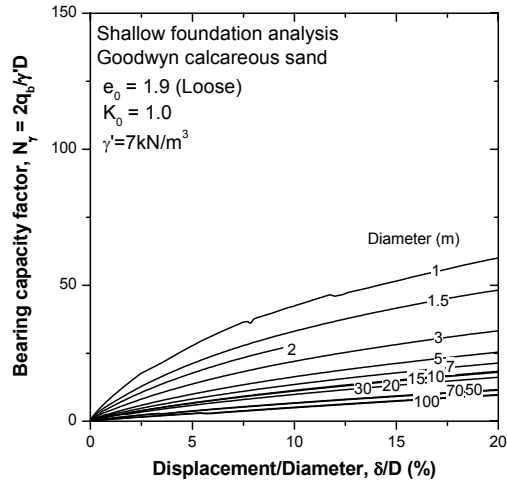
**Figure 5.44: Effects of  $K_0$  and foundation roughness on  $N_y$  -  $D$  relationship of siliceous sand**



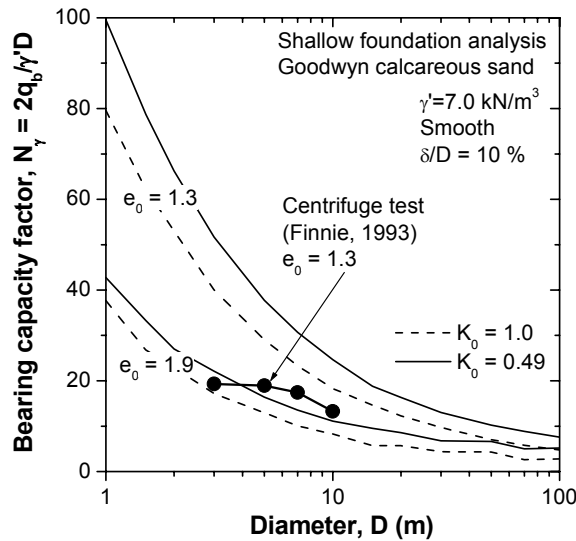
**Figure 5.45: A comparison of  $N_y$  –  $D$  relationship between experimental and numerical results on Toyoura siliceous sand**



(a)  $N_\gamma$  vs  $\delta/D$  ( $e_0 = 1.3$ )

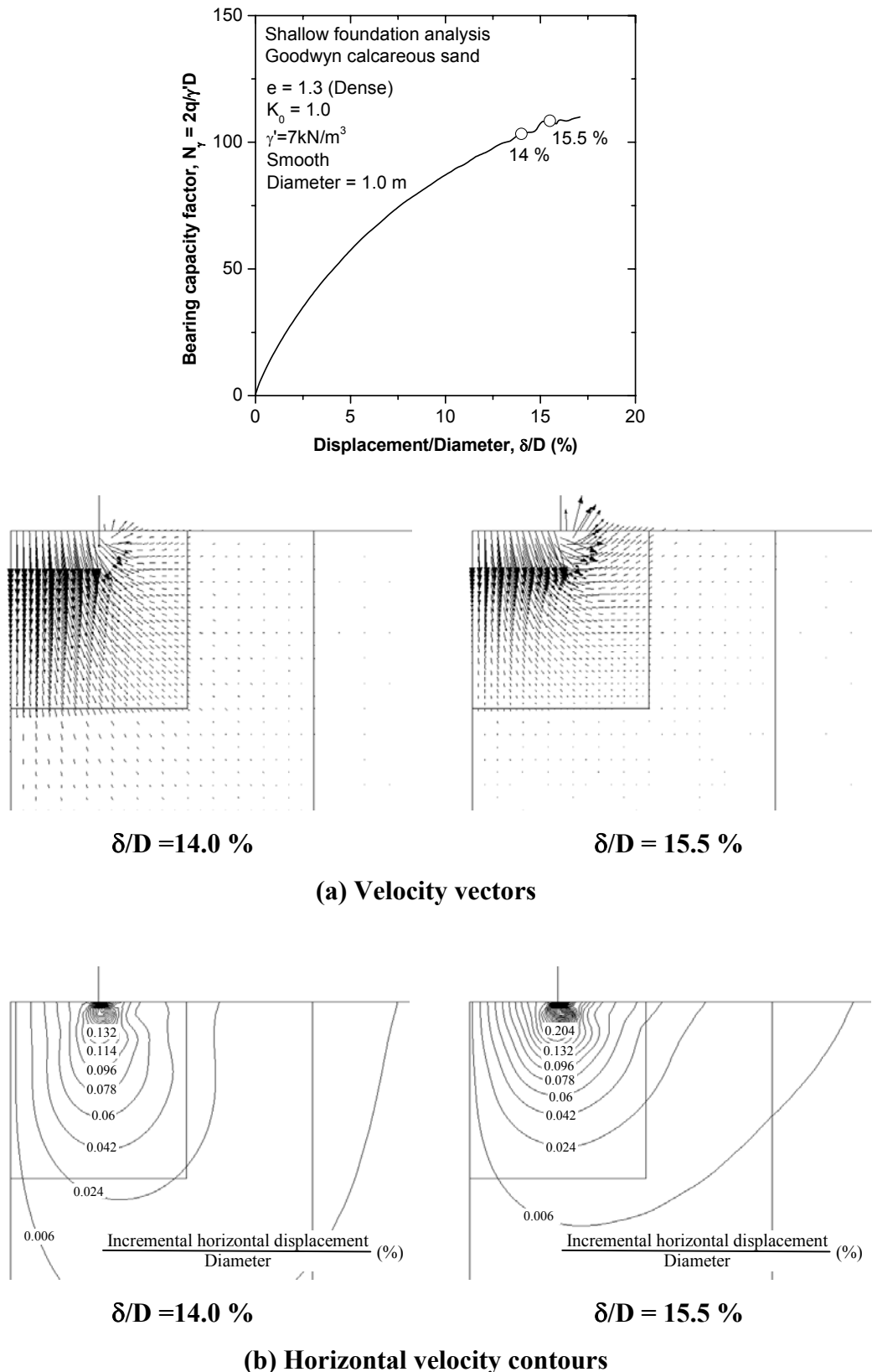


(a)  $N_\gamma$  vs  $\delta/D$  ( $e_0 = 1.9$ )

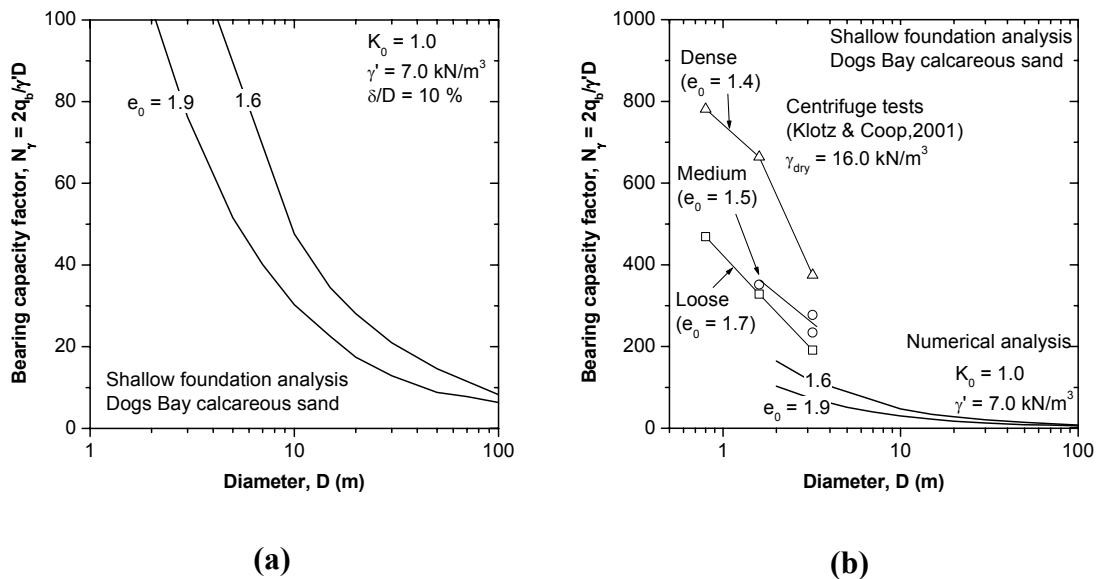


(c)  $N_\gamma$  vs  $D$

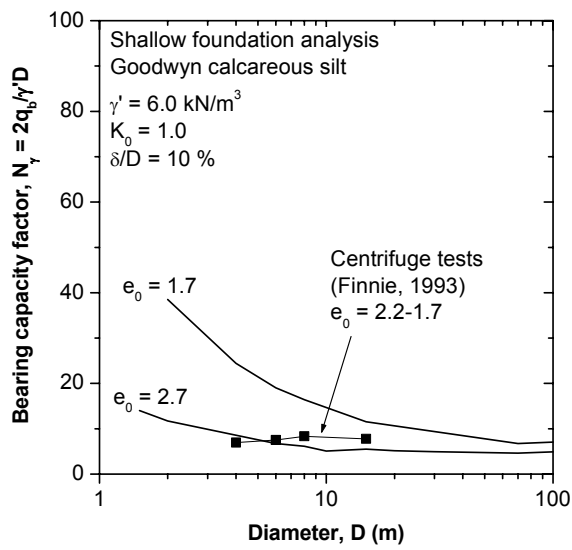
**Figure 5.46: Effect of foundation size on shallow circular footings on calcareous sand**



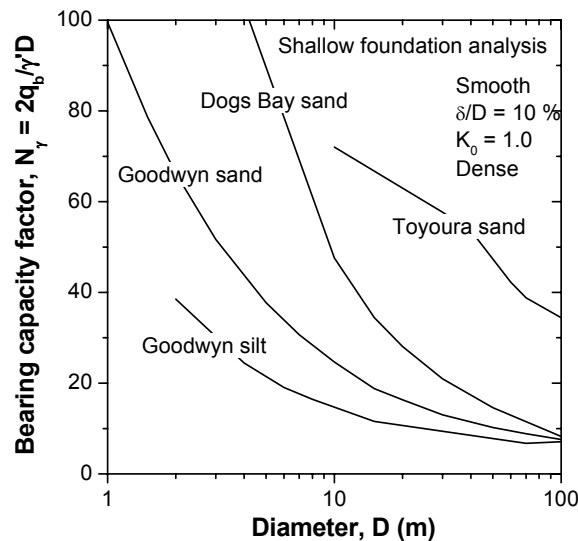
**Figure 5.47: Velocity vectors and horizontal velocity contours for a 1 m diameter footing on calcareous sand**



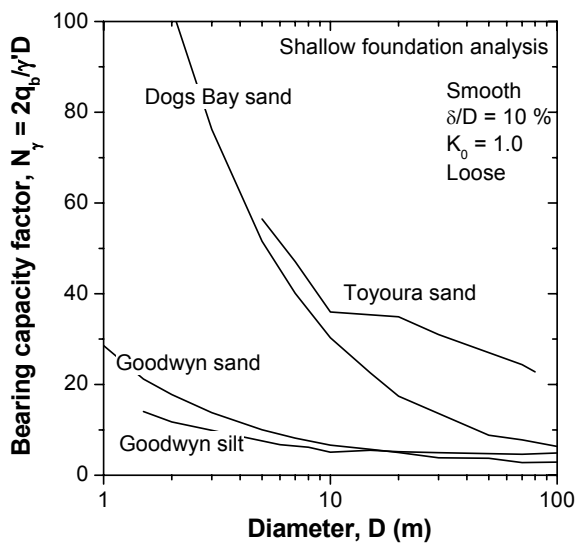
**Figure 5.48: Effects of foundation size and density on shallow circular footings on Dogs Bay calcareous sand**



**Figure 5.49: Effects of foundation size and density on shallow circular footings on Goodwyn calcareous silt**



(a) Dense



(b) Loose

**Figure 5.50: Summary of the effects of foundation size and density on shallow circular footings on various soils**



# **Chapter 6**

## **Analytical methods for Shallow Foundation Response on Calcareous Soil**

### **6.1 INTRODUCTION**

Although the Terzaghi (1943) bearing capacity formula is used almost universally for shallow foundation design, the previous chapter has shown that this formula is suitable only for small foundations on siliceous sands. Randolph et al. (2004) pointed out two major sources of uncertainty in analysing the bearing capacity on sand using the conventional formulae, one being appropriate choice of friction angle for the bearing capacity equation and the other being the interpretation of soil compressibility.

This chapter reveals problems of the choice of friction angle for conventional approaches in terms of a relationship of bearing capacity factor and friction angle. For foundation conditions such as large size foundations, loose samples and compressible materials, other approaches are needed not using the shear parameters but focusing more on the compression characteristics. Two approaches which mainly focus on calcareous materials are described below. First, a simple analysis using a 1-D compression equation is compared with the results from FE simulation for shallow foundations. Second, an analysis using a ‘bearing modulus’ concept proposed by Finnie (1993) (or Finnie and Randolph, 1994a; 1994b) is conducted. Both analyses will provide further information in terms of the soil compressibility.

### **6.2 A COMPARISON BETWEEN THE BEARING CAPACITY FACTOR $N_\gamma$ FROM CONVENTIONAL EQUATIONS, PLASTICITY SOLUTIONS AND FINITE ELEMENT RESULTS**

This section compares the MIT-S1 model results with the bearing capacity factor,  $N_\gamma$ , calculated by: a) a conventional  $N_\gamma$  equation as a function of the friction angle (Brinch

Hansen, 1970); b) a plasticity method based on the method of characteristics (Martin 2003); and c) a numerical analysis using Mohr-Coulomb model (Erickson and Drescher, 2002). For the calcareous sand, the results are also compared with a modified bearing capacity equation (Murff et al., 1992). The discussion will highlight limitations of the conventional approaches for bearing capacity analysis and emphasise those aspects that should be modified.

### 6.2.1 $N_\gamma - \phi'$ relationship for siliceous sand

**Figure 6.1** plots mobilised bearing capacity factor,  $N_\gamma$ , from the MIT-S1 model analysis against the friction angle,  $\phi'$  for the case of 10 m or 100 m diameter, fully rough or smooth shallow circular footings on siliceous sand with isotropic or anisotropic initial stress conditions. The  $N_\gamma$  values are obtained from the analyses with different initial densities as shown in **Figures 5.21** and **5.38**. The friction angles are chosen as the peak friction angle at a mean effective stress of 40 kPa (initial stress at depth of half diameter) in **Figure 5.7** (for  $K_0 = 1$ ,  $\phi' = 41.1^\circ, 39.2^\circ, 35.2^\circ, 31.7^\circ$  and for  $K_0 = 0.49$ ,  $\phi' = 40.4^\circ, 38.6^\circ, 34.9^\circ, 31.6^\circ$  from  $e_0 = 0.65, 0.7, 0.8, 0.9$ , respectively). It is found that the rate of increase  $N_\gamma$  with increasing  $\phi'$  for the 10 m diameter footing is greater than that for the 100 m diameter footing.

The MIT-S1 model results are compared with a conventional bearing capacity equation, plasticity solutions and finite element analysis. The bearing capacity equation for the estimation of the  $N_\gamma$  is taken from Brinch Hansen (1970), with modification for the circular footing as:

$$N_\gamma = 0.75(N_q - 1)\tan\phi' \quad (6.1)$$

where

$$N_q = e^{\pi\tan\phi'} \tan^2\left(\frac{\pi}{4} + \frac{\phi'}{2}\right) \quad (6.2)$$

The  $N_\gamma - \phi'$  envelope of this equation shown in **Figure 6.1** totally underestimates the numerical results for all cases.

The plasticity solution is derived using the computer program, ABC, developed based on the method of characteristics by Martin (2003). The solution from this program is based on standard rigid perfectly plastic isotropic Mohr-Coulomb failure criterion with associated flow rule. Typical characteristic meshes have already been illustrated in **Figures 5.12 or 5.13**. The MIT-S1 model predictions of both rough and smooth footings on dense siliceous sand (high  $\phi'$ ) agree well with the ABC curves, and this is consistent with the consistency in the shape of the incremental horizontal displacement contours in **Figures 5.12 and 5.13**. However, the  $N_y$  values for loose samples (low  $\phi'$ ) are slightly higher than the ABC results. The results for large foundations show lower  $N_y$  values than those from ABC, except for a smooth foundation on the loosest sand.

The MIT-S1 model results are also compared with the numerical analyses performed by Erickson and Drescher, (2002) using the non-associated Mohr-Coulomb model. The figures include two lines based on associated ( $\phi' = \psi$ ) and non-associated ( $\phi' \neq \psi = 0$ ) flow rules for the rough and smooth footings. The FE results for dense samples agree well with the  $\psi = 0$  line; then the results gradually shift towards the  $\phi' = \psi$  envelope with decreasing densities. However, the Mohr-Coulomb FE results give higher  $N_y$  values than the MIT-S1 FE results for large smooth and rough foundations.

Overall, the  $N_y - \phi'$  relationship from the ABC software gives closer results to the FE analyses than obtained from **Equation 6.1**. As shown in **Figure 6.2**, the ABC results for fully smooth foundations agree identically with plasticity solutions by Bolton and Lau (1988). **Figure 6.2** also provides exponential fitting equations of the fully rough and smooth foundations based on the ABC results:

$$N_y = 0.15e^{7\tan\phi'} \text{ (smooth)} \quad (6.3a)$$

$$N_y = 0.15e^{8\tan\phi'} \text{ (rough)} \quad (6.3b)$$

verified for the range of friction angles from  $20^\circ$  to  $40^\circ$ .

### 6.2.2 $N_y - \phi'$ relationship for calcareous sand

**Figure 6.3** shows  $N_y - \phi'$  relationships for 10 m and 100 m diameter fully smooth footings on calcareous sand. The  $N_y$  values are derived for  $\delta/D = 10\%$ . The peak friction angles for loose samples at  $p'_f = 40$  kPa do not exist in **Figure 5.7**, therefore  $p'_f = 10$  kPa is defined as a representative pressure and  $\phi' = 44.6^\circ, 43.1^\circ, 41.7^\circ, 40.4^\circ, 39.6^\circ$  are obtained from the samples for  $e_0 = 1.3, 1.45, 1.6, 1.75, 1.9$ , respectively. The  $N_y$  envelopes from **Equation 6.1** and the ABC program for the smooth footings are also shown. It is found that the calcareous sand results obtained using the MIT-S1 model give much lower  $N_y$  values than the ABC and **Equation 6.1** lines.

Murff et al. (1992) presented an additional modified bearing capacity equation, expressed as:

$$q = \frac{\gamma'D}{2} N_y \left(1 - e^{-\alpha\delta/D}\right) + N_q \gamma' \delta \quad (6.4)$$

The exponential multiplier in the first term in **Equation 6.4** was proposed to allow for sand compression prior to mobilisation of the bearing capacity. Murff et al. (1992) suggested typical  $\alpha$  values of 26 for dense sample ( $\phi' \sim 39^\circ$ ) and 4 for loose sample ( $\phi' \sim 33^\circ$ ) based on  $N_y$  equation proposed by Vesic (1975). **Equations 6.1** and **6.4** has been fitted to the numerical results for  $K_0 = 1$  with an  $\alpha$  value of 6 and for those for  $K_0 = 0.49$  with  $\alpha = 4$ . The  $N_y$  values obtained for the 100 m diameter foundation agree well with  $\alpha = 2$ , which is beyond the suggestion. Although the equation allows considering soil compressibility using the additional settlement parameter, the other factors need to be assessed for analysing the bearing resistance of shallow foundations on compressible sand. Note also that the  $\alpha$  values become smaller when other  $N_y$  equation such as **Equation 6.3** is used.

### 6.2.3 Problems associated with the choice of friction angle

As mentioned in **Section 5.2**, the bearing capacity analyses using conventional equations have an obvious problem for the choice of friction angle. The friction angles chosen above are obtained mostly from the mean effective stress at failure of 40 kPa in

**Figure 5.7.** For a 100 m diameter foundation on siliceous sand, however, the friction angles need to be chosen at 400 kPa. At that stress level, the friction angles decrease significantly to the extent that no peak friction angle can be found for the loose samples. Moreover, peak friction angles for calcareous sands are observed only at very low stress levels or very high densities. It may be concluded that the choice of appropriate friction angles for large foundations, loose samples and calcareous sands is difficult due to the stress level and density dependent of that quantity.

Therefore, alternative approaches are needed to assess the bearing capacity for foundation conditions for which the traditional approach does not work. Two analyses, 1-D compression and bearing modulus are discussed for calcareous sand in the following sections.

### 6.3 ONE-DIMENSIONAL COMPRESSION ANALYSIS FOR SHALLOW FOUNDATIONS ON CALCAREOUS SAND

This section describes simple prediction of shallow foundation response using the MIT-S1 compression model. **Figure 6.4** illustrates a shallow foundation on compressible sand and a 1-D compression test. Shallow foundation responses on calcareous sand show a typical deformation pattern with a bulb of compressed material and a punching shear pattern, very similar to the behaviour in a 1-D compression test. Therefore, a 1-D compression model appears a logical approach.

The methodology is very simple. First, the initial in-situ stress and void ratio at a depth of half of the diameter are defined. Then the MIT-S1 1-D compression calculation (**Equation A.5**) is conducted with the initial state parameters. The initial state values vary with the foundation size and the initial density at the surface ( $p' \sim 0$ ).

**Figures 6.5** compares simulated results for 1-D compression equation with bearing responses of shallow foundations on dense and loose Goodwyn calcareous sands ( $D = 1, 10$  and  $100$  m). The simulations for 100 m diameter foundation responses on both dense and loose samples agree reasonably well with the FE results, while those for 10 and 1 m diameter footings overestimate the FE results. This may be because the FE results which contain the dilative component and exhibit slightly concaved pressure-settlement

response do not agree with the purely compression simulations. It is believed that the FE results agree progressively with the 1-D simulations with increasing foundation size.

The 1-D compression estimations are also compared for other calcareous materials, Dogs Bay calcareous sand and Goodwyn calcareous silt, as shown in **Figures 6.6 and 6.7**. The Dogs Bay analysis does not fit the FE results well, while the Goodwyn silt analysis is in much better agreement with the FE results, in particular for loose conditions.

In summary, 1-D compression analysis is appropriate for extremely large foundations, or very loose and compressible calcareous materials. In these cases, an interpretation of the degree of settlement caused by the punching-shear deformation pattern is a more severe issue for foundation design than the assessment of ultimate bearing capacity. It is not consistent to use a rigid-plastic based method to evaluate the foundation deformation, since these do not occur in the form of a classical rapture pattern. The method should be linked to the deformation mechanism, which is much closer to that of 1-D compression accompanied by punching-shear deformation pattern.

However, deformation response obtained from the 1-D calculation, whereby the pressure increases exponentially with increasing displacement, does not match the quasi-linear shape of the bearing responses computed from the FE analysis. Other approaches are needed for assessing the response for foundations of moderate size and dense calcareous soil conditions.

### **6.4 BEARING MODULUS ANALYSIS FOR SHALLOW FOUNDATIONS ON CALCAREOUS SAND**

The quasi-linear bearing response of foundation on compressible calcareous soil suggests, superficially, that the bearing resistance could be estimated using an approach with  $N_y$  taken as zero and the rate of increase in resistance linked to  $N_q$ . Thus, for a given penetration,  $\delta$ , the bearing resistance would be expressed as:

$$q = N_q \gamma' \delta \quad (6.5)$$

However, the objection to this is that the classical  $N_q$ , derived from a rigid-plastic soil response and a function of the soil strength (or friction angle) has no relationship with the compressional deformation mechanism and punching shear pattern.

Instead, a bearing modulus approach, as suggested by Finnie (1993) (see Finnie and Randolph, 1994a, 1994b), with the bearing modulus linked to the compression parameters for the soil, rather than the strength parameters. This is explained below, with effects of foundation size (or ambient stress level), soil density and  $K_0$  taken into consideration.

#### 6.4.1 Bearing modulus, M

Finnie (1993) found from a series of physical model tests that pressure response for shallow foundations on calcareous sands varied linearly with penetration depth from the surface, and could be expressed in terms of a bearing modulus,  $M$ , which is a secant modulus of the bearing pressure to the equivalent settlement, given by:

$$M = \frac{q_b}{\gamma' \delta} \quad (6.6)$$

**Figure 6.8** shows bearing modulus responses varied with foundation diameters on a) dense and b) loose calcareous sand. The  $M$  values for the smaller foundations gradually decrease with footing penetration, while those for the larger foundations are nearly constant with displacement.

#### 6.4.2 Bearing modulus analysis for Goodwyn calcareous sand

**Figure 6.9** replots  $M$  values at  $\delta/D = 10\% (= M_{10})$  against void ratios and diameters. A semi logarithmic plot of  $M_{10}$  and  $e$  shows that different diameter envelopes can be expressed as proportioned to  $(1 - \ln(e))$ . The  $M_{10}$  results are then plotted normalised by corrections of void ratio and  $K_0$  against  $D$  and indicate a unified power of -0.6 and intercept at  $D = 1$  m of 700. Thus, an estimation of the bearing modulus can be expressed as:

$$M_{10} = 700 \left( \frac{D}{D_{ref}} \right)^{-0.6} (1 - \ln(e)) \left( \frac{1+2K_0}{3} \right) \quad (6.7)$$

where  $D_{ref}$  is a reference diameter ( $= 1$  m). **Figure 6.10** compares estimations of **Equation 6.7** with  $M_{10}$  values from shallow foundation results on Goodwyn calcareous sand. The estimations agree well with the finite element results and express nicely the effects of foundation size, density and  $K_0$ . **Figure 6.11** compares linear pressure-displacement relationships calculated by **Equations 6.6** and **6.7** with numerical results for shallow foundations on Goodwyn calcareous sands. All estimations are in excellent agreement with the FE results except for the case of a 100 m diameter foundation on loose soil where the estimated modulus is 65% of that from the FE result. The settlement limit of 10 % is, therefore, a reasonably representative value for estimating the bearing pressure for compressible sand.

#### 6.4.3 Bearing modulus analysis for Dogs Bay calcareous sand and Goodwyn calcareous silt

This method can also be adapted for the other calcareous materials. The numerical analyses of shallow foundation responses on Dogs Bay sand and Goodwyn silt have been presented previously (e.g., **Figures 5.48** and **5.49**). The same procedure is applied (**Figure 6.12** and **6.13**) and the bearing modulus equations are given by

$$M_{10} = 2500 \left( \frac{D}{D_{ref}} \right)^{-0.7} (1 - \ln(e)) \left( \frac{1+2K_0}{3} \right) \text{ (Dogs Bay sand)} \quad (6.8)$$

$$M_{10} = 500 \left( \frac{D}{D_{ref}} \right)^{-0.5} (1 - \ln(e)) \left( \frac{1+2K_0}{3} \right) \text{ (Goodwyn silt)} \quad (6.9)$$

**Figures 6.14** and **6.15** shows estimations for those sands with comparison to numerical results. The results for Dogs Bay sand overestimate to the FE results, which show significant curvature with penetration. The estimations for Goodwyn silt show excellent fit for 2 and 15 m diameter foundations on dense samples. However, the approach underestimates the response of 100 m diameter foundations on dense silt and all diameter foundations on loose silt. The 1-D compression analysis is more suitable for those cases.

#### 6.4.4 Relationship between bearing modulus equation and MIT-S1 compression parameters

The bearing modulus equations described in previous subsections may ultimately be linked with the compression parameters of the MIT-S1 models such as  $p'_{\text{ref}}$  and  $\theta$  for the sands and silt, which have shown significant influence on the bearing resistance in **Section 4.5**. **Figure 6.16** plots  $M_{10}$  results with different  $p'_{\text{ref}}$  and  $\theta$  values for Goodwyn calcareous sand. The reference diameter  $D_{\text{ref}}$  in **Equation 6.7** may be linked directly with the normalised  $p'_{\text{ref}}$  and expressed as:

$$M_{10} = U \left( \frac{p'_{\text{ref}}}{\gamma' D} \right)^{0.6} \left( 1 - \ln(e) \right) \left( \frac{1 + 2K_0}{3} \right) \quad (6.10)$$

This equation is compared with the FE results in **Figures 6.16** and appropriate U values are then deduced. **Figure 6.17** shows the U values plotted against  $p'_{\text{ref}}$  and  $\theta$ . For a given value of  $\theta$ , the value of U varies linearly with  $p'_{\text{ref}}$ , with a gradient of  $-0.05/p_a$ , where  $p_a$  is atmospheric pressure ( $\sim 100$  kPa). Similarly, for constant  $p'_{\text{ref}}$ , U varies linearly with  $\theta$ , with a gradient of -14. Thus, the U value in **Equation 6.10** can be expressed as:

$$U = 34 - 14\theta - 0.05 \left( \frac{p'_{\text{ref}}}{p_a} \right) \quad (6.11)$$

**Figure 6.18** compares  $M_{10}$  values calculated by **Equations 6.10** and **6.11** with those from the FE results. The estimations agree nicely with the FE results. It is found that the bearing modulus  $M_{10}$  for calcareous sands, unlike the classical  $N_q$  equation (**Equation 6.2**), can be derived as a function of the MIT-S1 compression parameters. Further study of this approach needs to be carried out in the case of other calcareous materials or large diameter foundations on loose siliceous sands.

#### 6.5 DISCUSSION

It is found that the conventional approaches for bearing capacity analysis are suitable only for small size foundations on dense dilative sands, particularly siliceous sand. For

other conditions such as large size foundations, loose samples and compressible materials, other approaches are needed focusing more on the compression characteristics. An analytical boundary between those conditions is associated with a critical size which is mentioned in the previous chapter. Conventional bearing capacity analyses are applicable for foundations smaller than the critical size, while compression analyses are needed for shallow foundations greater than the critical size.

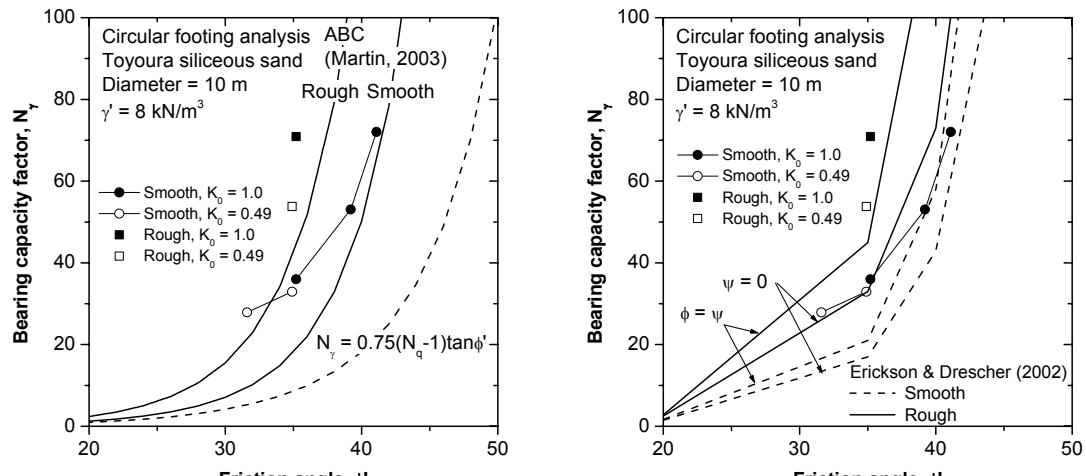
Two analyses for estimating the bearing response on calcareous sands have been proposed, one using a 1-D compression model and the other using the bearing modulus concept. From the investigations, the former is suitable for the extreme case of foundation conditions involving very large foundations on loose, highly compressible soil, while the latter is suitable for moderate size of foundations on dense or medium dense calcareous samples. It may be concluded that the soil compressibility develops significantly with increasing foundation size (or ambient stress level) and void ratio and eventually the shallow foundation responses simply replicate the 1-D compression theory. Moreover, both analyses are associated directly with settlement, thus they can assess the effect of soil compressibility more appropriately than an empirical modification of the bearing capacity factor  $N_y$ , which is based on the strength parameters.

For the bearing modulus analysis, **Equations 6.10** and **6.11** show how the bearing modulus,  $M_{10}$ , is related to the MIT-S1 compression parameters,  $p'_{ref}$  and  $\theta$ , for Goodwyn calcareous sand. It is suggested that the bearing resistance and pressure-displacement response for shallow foundations on compressible sands can be estimated using these compression parameters. More FE analyses, particularly on other compressible sands, need to be carried out to assess the approach further.

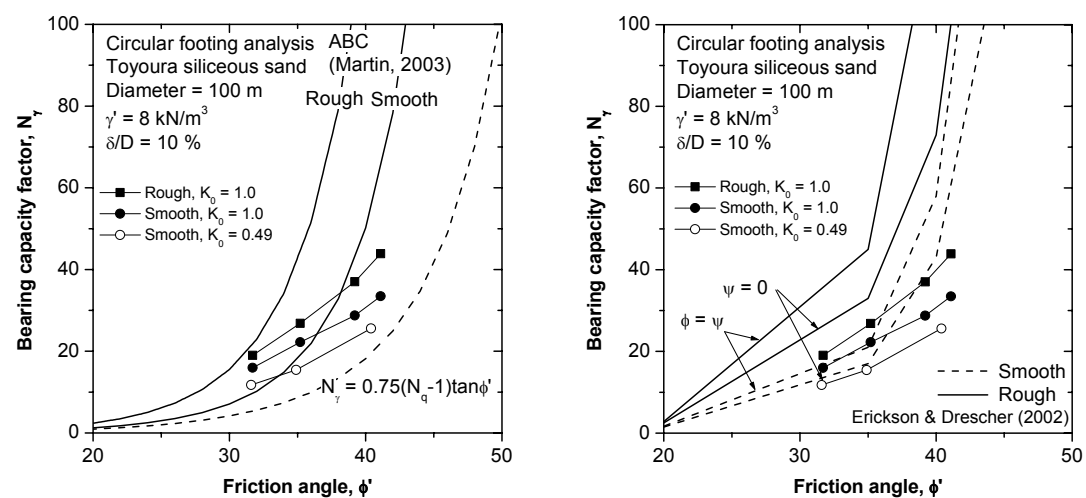
## **6.6 CONCLUSIONS**

The limitations of conventional bearing capacity analyses and the analytical approaches for shallow foundation response on calcareous materials have been discussed, focusing on soil compressibility. It has been shown that the conventional bearing capacity formulae are not applicable broadly because of high stress level and density dependence of the friction angle. For larger foundations, loose samples and compressible materials,

other methods focusing more on the soil compressibility are appropriate. Two analyses, 1-D compression and a bearing modulus approach, are proposed and it has been found that the former is suitable for extreme cases of foundation conditions, while the latter is applicable for moderate cases. For the bearing modulus analysis, the bearing modulus equation can be derived as a function of the MIT-S1 compression parameters, suggesting that a possible route to link the bearing modulus more directly to the compression parameters of the soil.

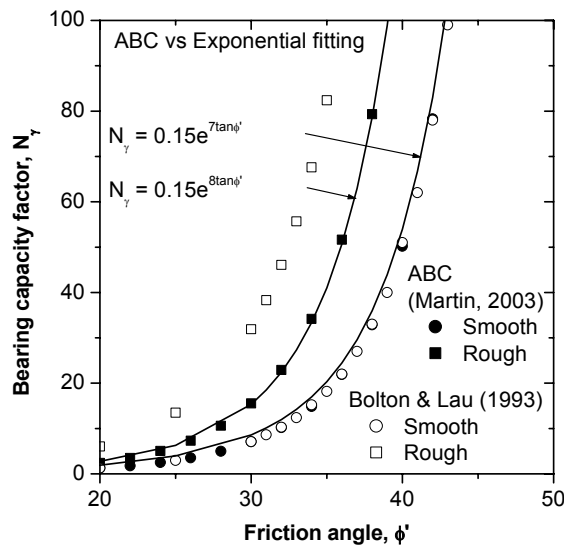


(a) 10 m diameter

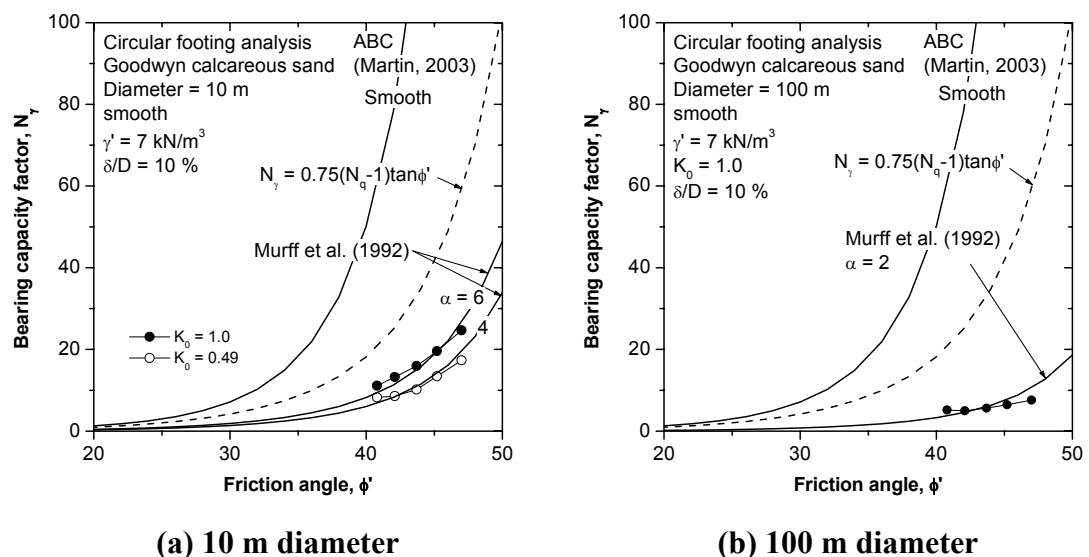


(b) 100 m diameter

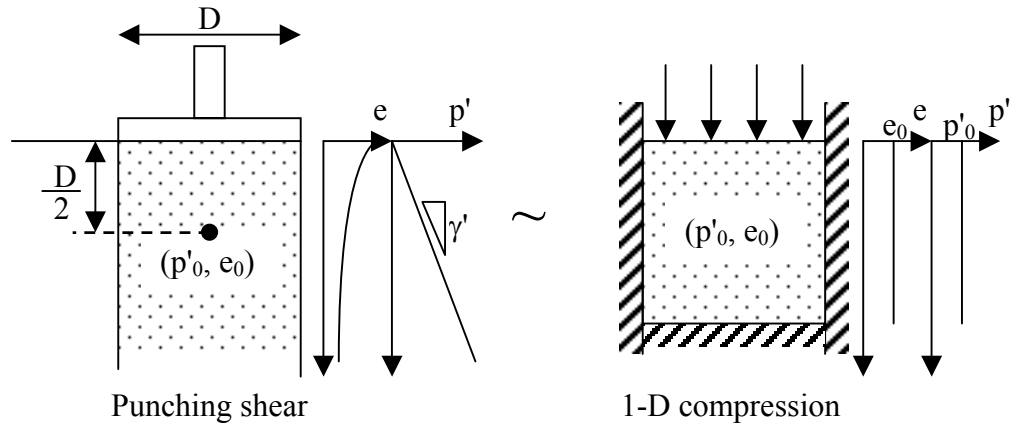
**Figure 6.1:  $N_\gamma$  -  $\phi'$  relationships of the shallow foundations on siliceous sand**



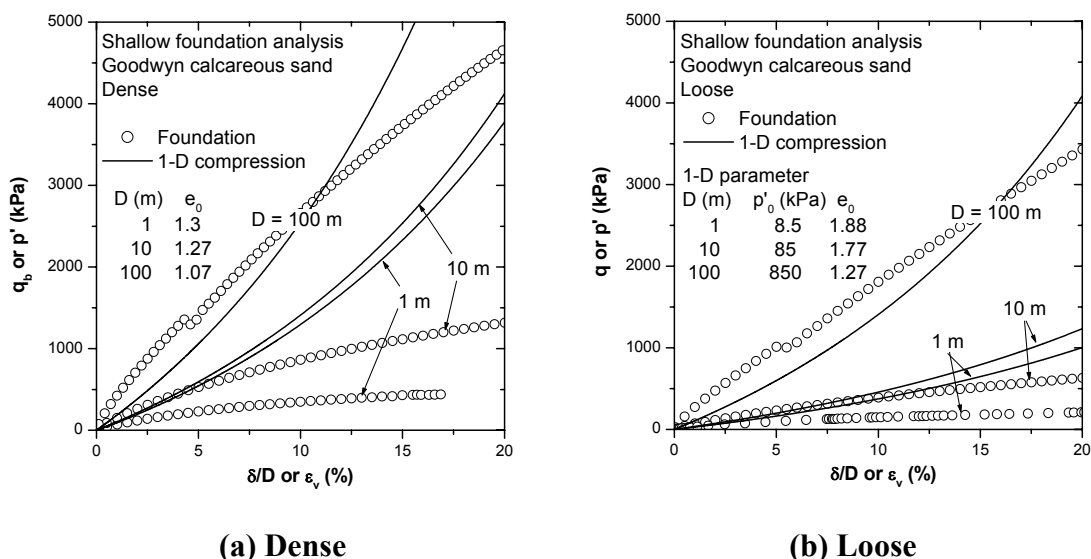
**Figure 6.2: Exponential fitting for ABC and Bolton and Lau plasticity solutions**



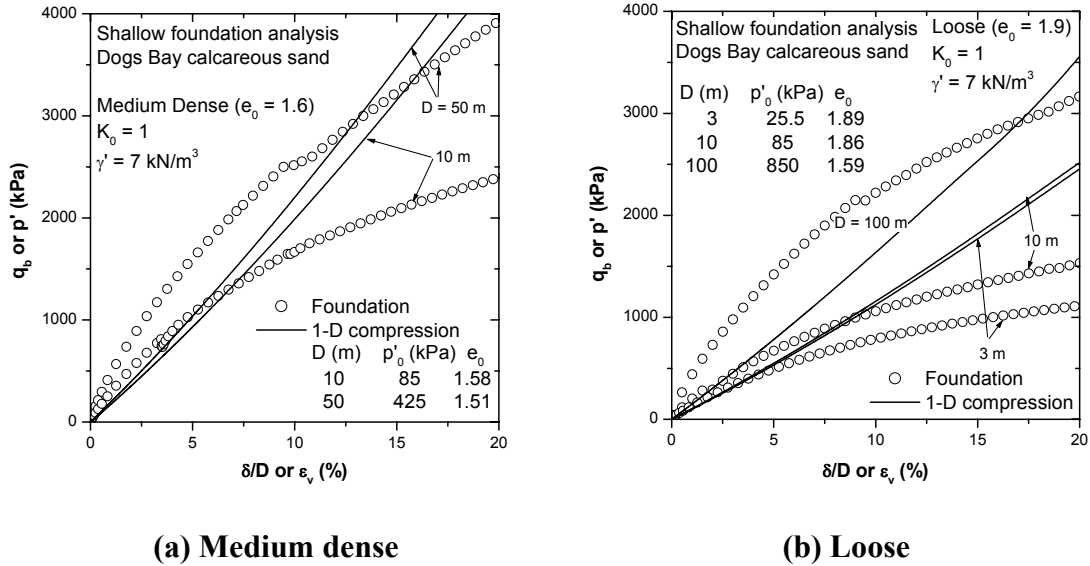
**Figure 6.3:  $N_y$  -  $\phi'$  relationships of the shallow foundations on calcareous sand**



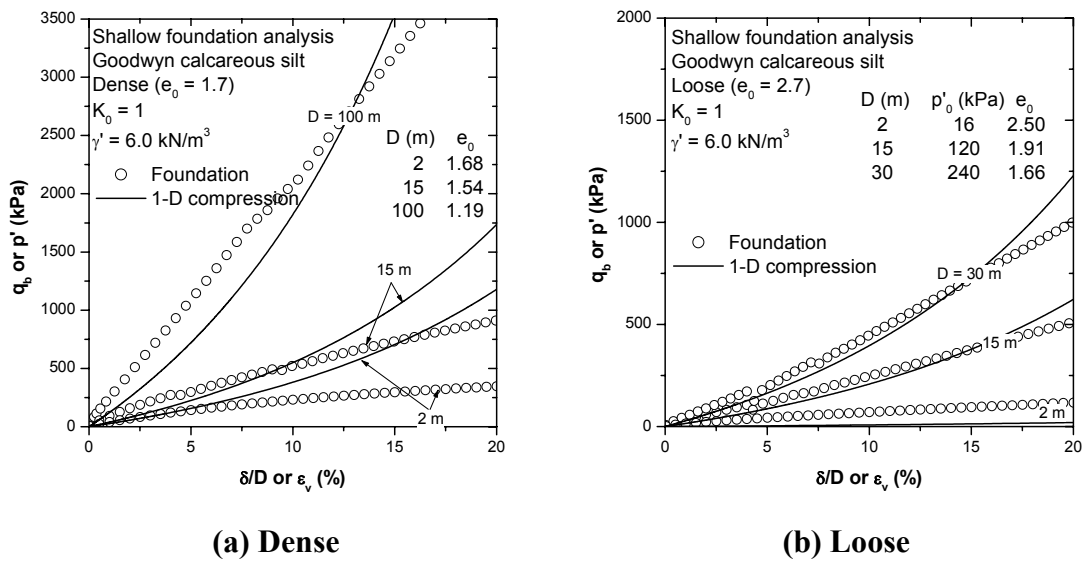
**Figure 6.4: Shallow foundation and 1-D compression**



**Figure 6.5: Estimation of 1-D compression analysis for Goodwyn calcareous sand**

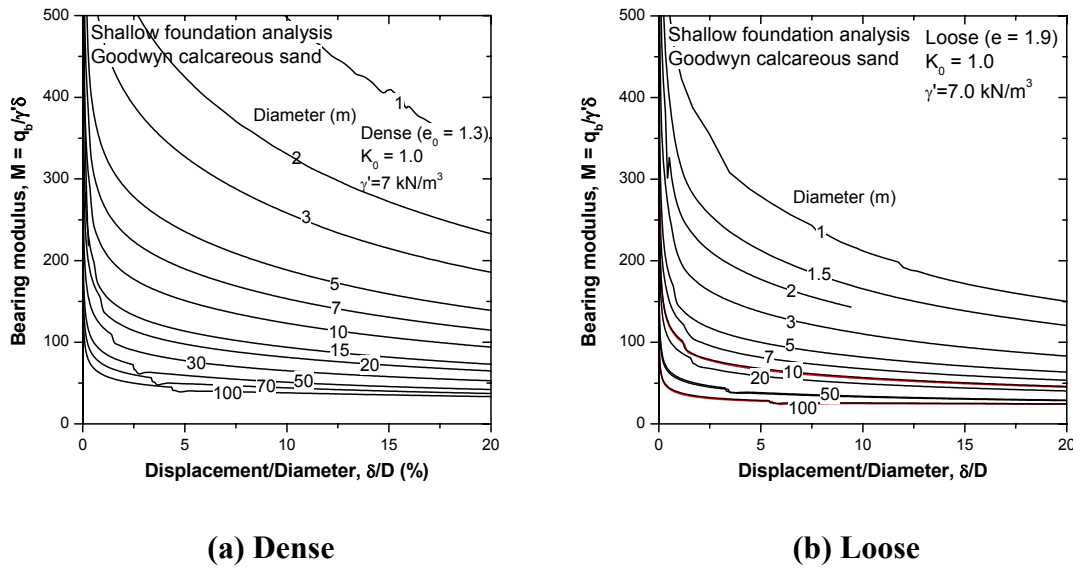


**Figure 6.6: Estimation of 1-D compression analysis for Dogs Bay calcareous sand**

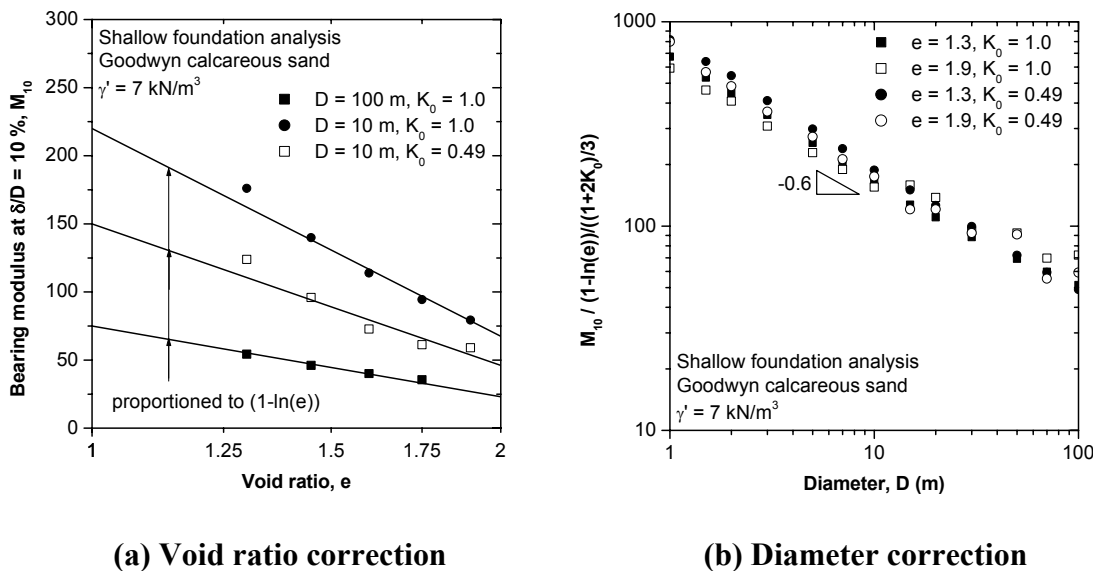


**Figure 6.7: Estimation of 1-D compression analysis for Goodwyn calcareous silt**

## 6. Bearing Capacity Analysis



**Figure 6.8: Bearing modulus for calcareous sands**



**Figure 6.9: Definition of coefficients for bearing modulus estimation for Goodwyn calcareous sand**

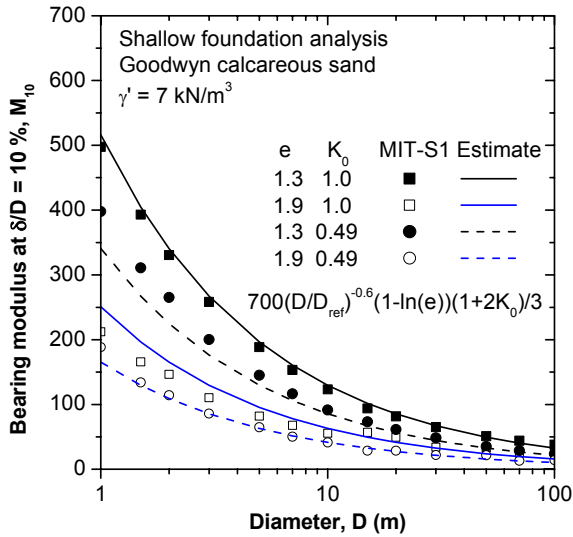
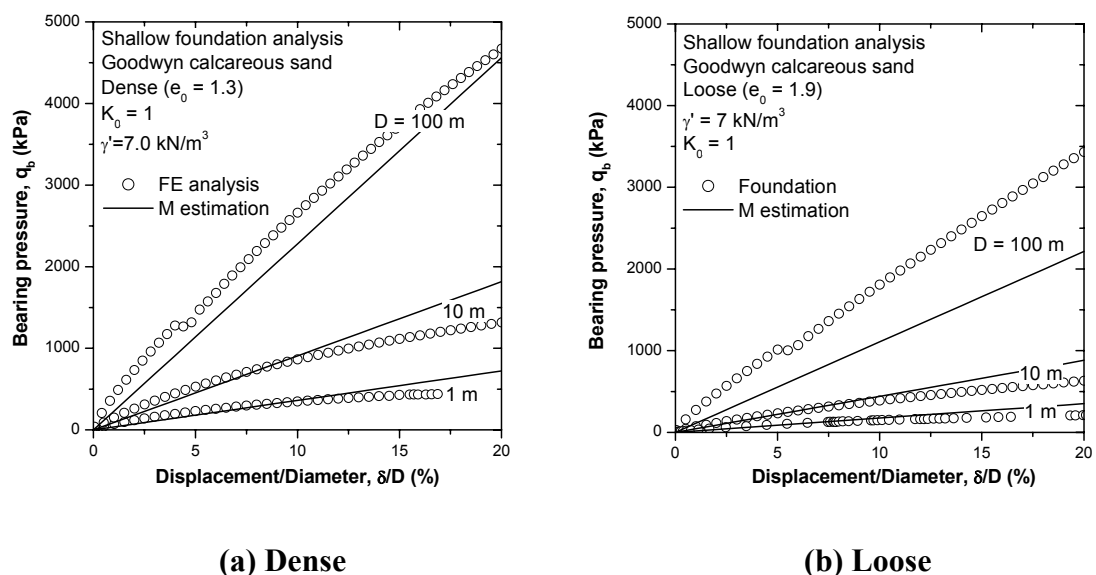
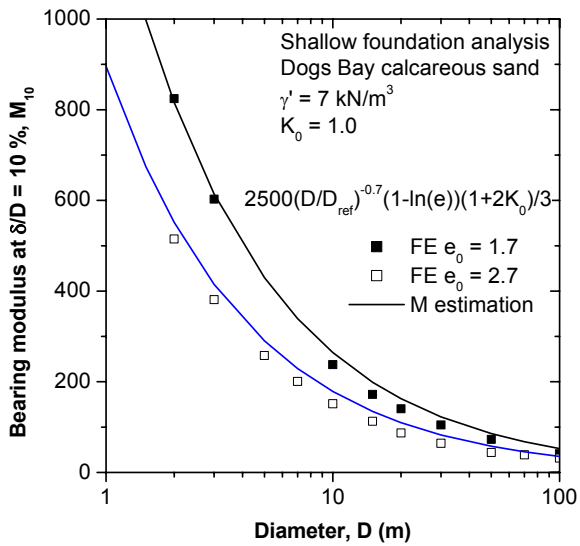
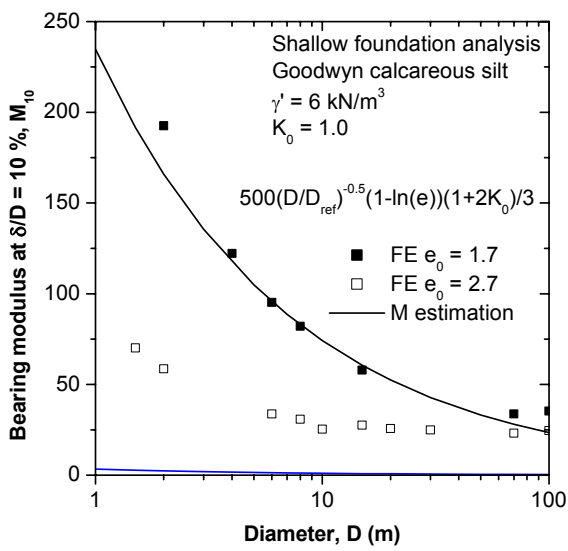

 Figure 6.10:  $M_{10}$  and  $D$  relationship for Goodwyn calcareous sand


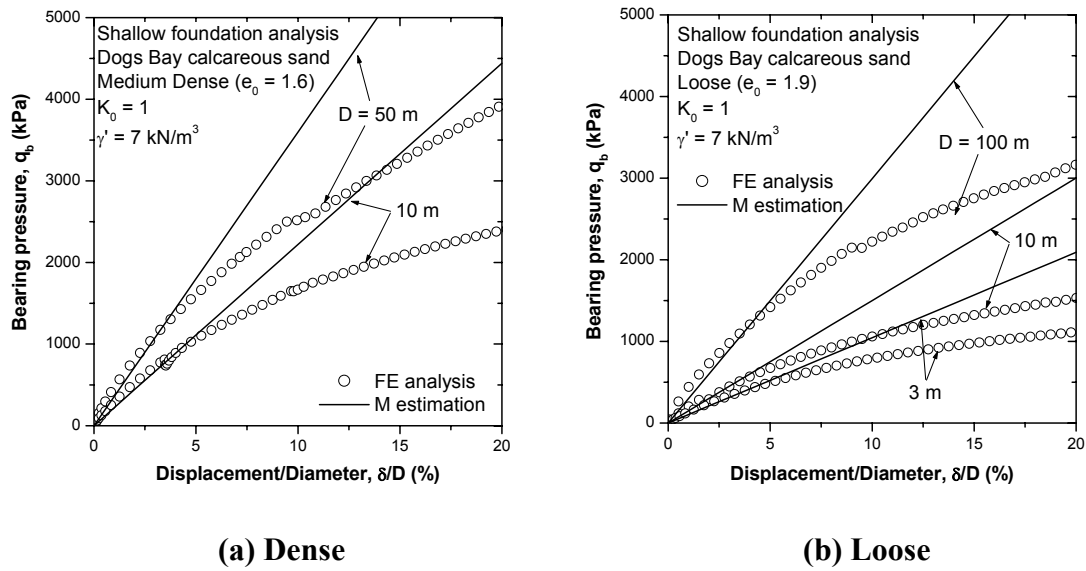
Figure 6.11: Estimation of bearing modulus analysis for Goodwyn calcareous sand



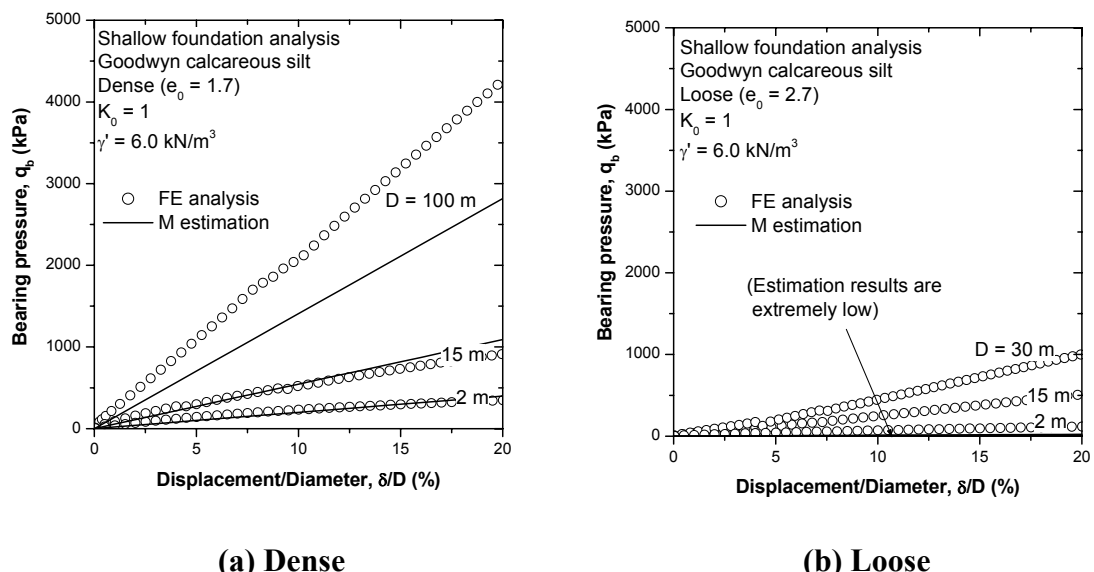
**Figure 6.12: Estimation of bearing modulus analysis for Dogs Bay calcareous sand**



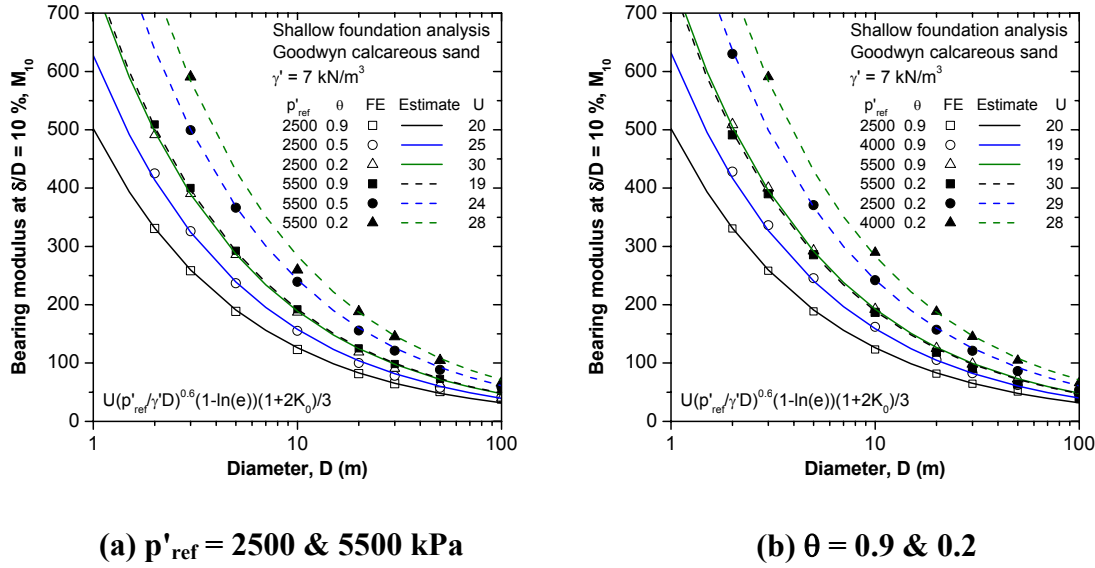
**Figure 6.13:  $M_{10}$  and  $D$  relationship for Goodwyn calcareous silt**



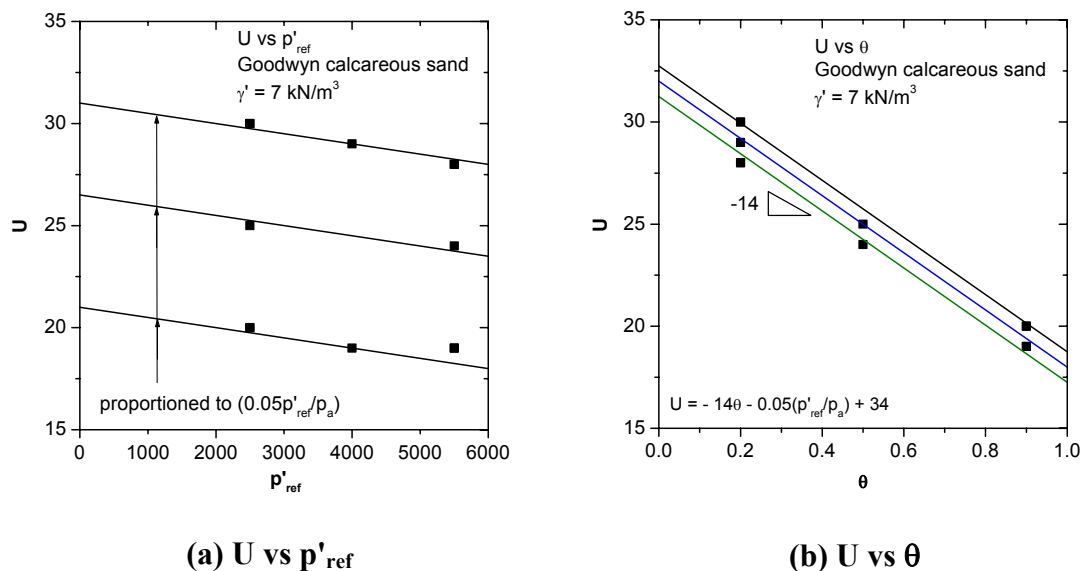
**Figure 6.14: Estimation of bearing modulus analysis for Dogs Bay calcareous sand**



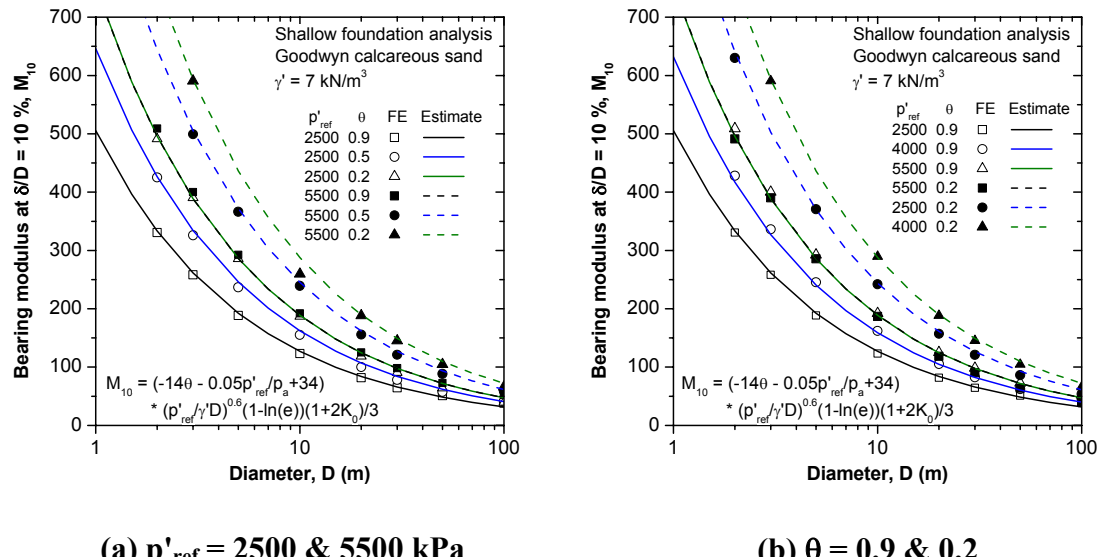
**Figure 6.15: Estimation of bearing modulus analysis for Goodwyn calcareous silt**



**Figure 6.16: Effects of the compression parameters  $p'_{ref}$  and  $\theta$  on the bearing modulus for Goodwyn calcareous sand**



**Figure 6.17: Definition of  $U$  value for bearing modulus estimation for Goodwyn calcareous sand**



**Figure 6.18: Estimation of the bearing modulus equation for Goodwyn calcareous sand**



# **Chapter 7**

## **Conclusions**

### **7.1 CONCLUSIONS**

A numerical investigation of shallow circular foundations resting on various types of soil, namely siliceous and calcareous sands, has been conducted. The MIT-S1 model, which can predict the rate independent behaviour of different types of soils ranging through uncemented sands, silts and clays, has been used to simulate the compression, drained triaxial shear and shallow circular foundation responses on various soils. This section summarises the major findings of this thesis followed by a section describing recommendations found during the study.

#### **7.1.1 MIT-S1 model**

The MIT-S1 model incorporates additional curve fitting parameters for simulating the different mechanical characteristics found in natural soils within a framework of critical state soil mechanics. This model can express many characteristics of soil behaviour such as the non-linear compression curve and critical state line on  $e-\ln p'$  plot, the dilatancy behaviour of sand and the variation of peak friction angle as a function of stress level and density. This model was shown to be fit for the research purpose in this study, in particular the assessment of the bearing response of highly frictional and compressible calcareous sands.

The MIT-S1 model parameters are determined from standard and advanced laboratory test data. This study determined the model parameters for Goodwyn calcareous sand and silt and Dogs Bay calcareous sand and compared them with those for Toyoura siliceous sand which has presented by Pestana (1994). It was found that calcareous sand has much higher friction angle parameters compared with those for Toyoura sand, and that Toyoura and Dogs Bay sands were classified as relatively stiff materials, while Goodwyn sand and silt were classified as softer materials with respect to the

compression parameters. In summary, for foundation analysis primary attention should be given to the selection of the friction angles,  $\phi'_{cs}$  and  $\phi'_{mr}$ , and the compression parameters,  $p'_{ref}$  and  $\theta$ , while the remaining parameters appear to be of secondary importance.

The MIT-S1 model allows distinguishing between foundation response on siliceous and calcareous materials in terms of both the pressure-displacement response and the deformation mechanism based on relatively minor modification of the model parameters. The abilities of three other constitutive models were also examined. They were found to be much less capable in simulating a wide range of soil types and properties and tended to be applicable for only a particular class of soil. The numerical results of pressure-displacement response on siliceous and calcareous sands were compared with published results from physical model tests. The calculations for dense Toyoura and Dogs Bay sands could not be completed beyond a certain load level due to numerical difficulties. However prior to this point, the MIT-S1 predictions agreed satisfactorily with the physical model results. A sensitivity analysis for shallow foundations on siliceous and calcareous sands revealed that the compression parameters  $\theta$  and  $p'_{ref}$  have the greatest effect on the bearing response for both sand types. The shear parameters  $\phi'_{mr}$ , and  $np$  did not affect the response for calcareous sand, but influenced the ultimate bearing resistance for siliceous sand because the parameters dictated the peak friction angle.

### **7.1.2 Effects of soil properties and foundation designs on shallow foundation performance**

A numerical investigation has been conducted on the effects of different fundamental geotechnical factors, mainly the density, stress level (or foundation size), inherent stress anisotropy and material type, on shallow foundation response.

The relationships of peak friction angle against void ratio and mean effective stress showed nicely the effects of initial soil properties as well as the characteristic differences between siliceous and calcareous sands (**Figure 5.6 or 5.7**). It was revealed that siliceous sand has a strong dilatancy contribution over a wide range of stress levels and densities, while dilatancy is evident only at very low stress levels for calcareous

sands. Importantly it was found that the peak friction angles at low to intermediate stress levels for siliceous sand were essentially constant.

Numerical analyses have been carried out for small (10 m) and large (100 m) diameter shallow foundations on siliceous and calcareous sands and the results compared in terms of the kinematic deformation pattern. The deformation mechanisms for small foundations on siliceous sand simulated by the MIT-S1 model were in good agreement with the meshes from the method of characteristics using the ABC program (Martin, 2003). However, the mechanisms for large shallow foundations showed less agreement with conventional bearing capacity analyses because of the increasing development of the compressive punching shear deformation with increasing the foundation size. The calcareous sands, on the other hand, did not fit with the conventional analysis but rather showed a punching shear deformation mechanism accompanied by large volume changes beneath the foundation over a wide range of foundation sizes and densities.

The effects of soil properties were then summarised in terms of the bearing capacity factor,  $N_y$ . It was found that the effects of stress level (foundation size) and density were significant at small diameters then became negligibly small with increasing foundation size on calcareous sands. Moreover, the transitions of deformation mechanisms, namely ‘critical sizes’, are identified clearly for siliceous sand. This boundary suggests that the conventional bearing capacity analyses are applicable for the foundations size less than the critical size, while alternative approaches, focusing mainly on the soil compressibility, are needed for shallow foundations greater than the critical size.

### 7.1.3 Analytical methods for shallow foundations on calcareous sands

The conventional bearing capacity analyses for shallow foundations on various sands have been compared with the MIT-S1 FE results. The conventional  $N_y$  equations and the plasticity and numerical methods based on the Mohr-Coulomb model were applicable only for the smaller foundations on dense or medium dense siliceous sand. It may be concluded that the conventional methods based on a rigid-plastic soil response linked to the soil strength (i.e. friction angle) are not consistent with the shallow foundation response undergoing punching shear pattern. The cases of larger foundations, loose soil conditions and foundations on compressible materials all needed alternative approaches.

Two analyses have been carried out. One approach used the MIT-S1 compression model to compare directly with shallow foundation responses undergoing punching shear. The estimations were in reasonable agreement with extreme cases of foundation conditions, such as very large foundations, loose samples and soft materials. The other approach is based on the bearing modulus proposed by Finnie (1993) and was fit nicely for the quasi-linear pressure-displacement response from FE calculations. Both simple approaches associate directly with the compressional deformation mechanism and the punching shear pattern without using any strength parameters. For the bearing modulus analysis, the bearing modulus equation can be derived as a function of the MIT-S1 compression parameters, suggesting that a possible route to link the bearing modulus more directly to the compression parameters of the soil.

## **7.2 RECOMMENDATIONS FOR FURTHER STUDY**

Several recommendations have emerged from this study and further research is required:

1. Finite element calculations using the MIT-S1 model often terminate due to numerical problem. The finite element implementation of the MIT-S1 model needs improvement, particularly where large dilation occurs (e.g. low stress levels in dense sand). The adaptation of advanced finite element techniques (e.g. large deformation analysis) would also be beneficial in order to model punching shear.
2. The shallow foundation analysis presented in this study is focused on the drained behaviour of freshly deposited uncemented sands. In order to broaden the understanding of shallow foundation response, FE analyses under undrained or partially drained conditions, non-homogeneous layers, and cemented deposits are recommended. Especially for calcareous sand, cementation is frequently observed in practice. The MIT-S1 model could replicate the degree of cementation through appropriate adjustment of compression parameters such as  $p'_{ref}$  and  $\theta$ .

3. The shallow foundation analysis was also restricted to circular foundations resting on the ground surface and subjected only to vertical loading. Different structural footing shapes (strip, square, etc.), foundation types (pipe, spudcan, with skirt, etc.), embedded footings or deep foundations, and loading types (inclined and eccentric) need to be investigated in order to provide a more complete picture of shallow foundation response.
4. The methods based on the soil compressibility proposed in this study have been assessed appropriately for shallow foundation response on calcareous materials. More FE analyses, particularly on other compressible sands, need to be carried out to assess the approaches further
5. The analytical methods described in this thesis are compared mainly with the numerical results. It is recommended that they are also assessed against experimental results in the future, as opportunities arise, perhaps through monitoring of prototype foundation performance.



## **APPENDIX: MIT-S1 MODEL**

The MIT-S1 model was developed as a unified constitutive model for predicting the rate independent behaviour of different types of soils ranging through uncemented sands, silts and clays. The model incorporates additional curve fitting features to simulate the different mechanical characteristics found in natural soils into a framework of critical state soil mechanics. It also enables the behaviour of granular soils to be simulated using a single set of material parameters over a wide range of density and confining stress although the model requires a large number and variety of laboratory data for evaluating the parameters.

The complete MIT-S1 model by Pestana (1994) (or Pestana and Whittle (1999)) includes the following features:

- 1) a unique Limit Compression Curve (LCC) to describe the isotropic hardening of a bounding surface (**Figure A.1**);
- 2) a lemniscate shaped bounding surface (i.e., the yield surface for normally consolidated (freshly deposited) specimens) with non-associated flow rule (**Figure A.2**);
- 3) a rotational hardening function to describe the evolution of the anisotropic stress-strain-strength properties;
- 4) small strain non-linearity in shear;
- 5) non-linear hysteretic response during unload-reload cycles;
- 6) critical state conditions described by an isotropic failure criterion.

These features contribute to the ability of the model to simulate many characteristics of soil behaviour such as non-linear compression curves and critical state lines on e- $\ln p'$  plots, dilatancy behaviour of sands and the variation of peak friction angle as a function of stress level and density.

### **A.1    Compression model**

Pestana and Whittle (1995) proposed a four-parameter elasto-plastic model that is able to predict the non-linear volumetric behaviour of freshly deposited sands over a wide

range of stress level and density. The formulation preserved the advantages of both elasto-plastic behaviour (irrecoverable strains) and power law models (non-linear response). **Figure A.1** illustrates the MIT-S1 compression relationship in  $\ln e - \ln p'$  space.

First, the proposed formulation for elastic response assumes that hydrostatic unloading is elastic but non-linear; thus incremental elastic volumetric strain is given by

$$d\epsilon_v^e = \frac{e}{1+e} \frac{1}{C_b} \left[ \frac{p'}{p_a} \right]^{-1/3} \frac{dp'}{p_a} \quad (\text{A.1.1})$$

where  $e$  is the current void ratio,  $p'$  is the current mean effective stress,  $p_a$  is atmospheric pressure ( $\sim 100$  kPa) and  $C_b$  is a small strain stiffness modulus that must be estimated from laboratory measurements. The constant power,  $1/3$ , is selected mainly from empirical considerations.

Second, the plastic strain is described by a simple mapping rule similar to that used in bounding surface plasticity models (Dafalias and Herrmann, 1982), expressed as:

$$d\epsilon_v^p = \frac{e}{1+e} \left( \rho_c - \frac{(p'/p_a)^{2/3}}{C_b} \right) \left( 1 - \delta_{HS}^\theta \right) \frac{dp'}{p'} \quad (\text{A.1.2})$$

where  $\rho_c$  is the slope of the LCC in  $\ln e - \ln p'$  space (**Figure A.1**) and  $\theta$  is a constant exponent ( $\theta > 0$ ).  $\delta_{HS}$  is the dimensionless distance between the current mean effective stress  $p'$  and the equivalent stress on the hydrostatic LCC,  $p'_b$ , at the same void ratio as:

$$\delta_{HS} = 1 - \frac{p'}{p'_b} \quad (\text{A.1.3})$$

$$p'_b = p'_{ref} \left( \frac{1}{e} \right)^{1/\rho_c} \quad (\text{A.1.4})$$

where,  $p'_{ref}$  is a reference stress at unit void ratio (**Figure A.1**).

Thus, **Equations A.1** and **A.2** are combined for describing the complete incremental elasto-plastic effective stress-strain response in hydrostatic compression:

$$d\varepsilon_v = \frac{e}{1+e} \left[ \frac{\delta_{HS}^\theta}{C_b (p'/p_a)^{1/3}} + \frac{\rho_c}{p'/p_a} (1 - \delta_{HS}^\theta) \right] \frac{dp'}{p_a} \quad (A.5)^1$$

and hence, the tangent bulk modulus, K, is

$$\frac{K}{p_a} = \frac{1+e}{e} \left( \frac{\delta_{HS}^\theta}{C_b (p'/p_a)^{1/3}} + \frac{\rho_c}{p'/p_a} (1 - \delta_{HS}^\theta) \right)^{-1} \quad (A.6)$$

In general, **Equations A.5** and **A.6** cannot be integrated in closed form but can be solved numerically.

## A.2 Bounding surface

A brief illustration of the MIT-S1 model in shear stress and mean effective stress space is shown in **Figure A.2**. The lemniscate shaped bounding surface is expressed as;

$$f = p'^2 \left[ (\eta - b) : (\eta - b) - \zeta^2 \left( 1 - \left( \frac{p'}{\alpha'} \right)^m \right) \right] = 0 \quad (A.7)$$

where,

$$\zeta^2 = c^2 + \mathbf{b} : \mathbf{b} - 2\eta : \mathbf{b} \quad (A.8)$$

---

<sup>1</sup> The model may also be expressed in terms of the vertical effective stress,  $\sigma'_v$ , in order to simulate one-dimensional compression, in corresponding the current (varying) stress ratio,  $K_0$ , and a constant stress ratio in the LCC regime,  $K_{0NC}$ , leading to:

$$\begin{aligned} d\varepsilon_v &= \frac{e}{1+e} \left[ \frac{[(1+2K_0)/3]^{2/3}}{C_b (\sigma'_v / p_a)^{1/3}} \delta_{1D}^\theta + \frac{\rho_c}{\sigma'_v / p_a} (1 - \delta_{1D}^\theta) \right] \frac{d\sigma'_v}{p_a} \\ \delta_{1D} &= 1 - \left( \frac{1+2K_0}{1+2K_{0NC}} \right) \frac{\sigma'_v}{\sigma'_{vb}} \\ \sigma'_{vb} &= \sigma'_{vref} \left( \frac{1}{e} \right)^{1/\rho_c} \end{aligned}$$

For, freshly deposited sands,  $K_0$  may vary from 0.3 to 0.7, while  $K_{0NC} = 0.50 \pm 0.05$ .

$$c^2 = c_a^2 + \left( 3 - \frac{c_a^2}{2} \right) J_{3\eta} \quad (\text{A.9})$$

$$c_a^2 = \frac{8 \sin^2 \phi'_m}{3 + \sin^2 \phi'_m} \quad (\text{A.10})$$

$\eta$  is a current stress ratio vector,  $\alpha'$  is the mean stress at the tip of the bounding surface and  $\mathbf{b}$  is the orientation of the bounding surface. The parameter  $m$  describes the shape of the bounding surface, while  $c$  is defined in terms of a maximum friction angle  $\phi'_m$ , in triaxial compression using a Matsuoka-Nakai generalisation (Matsuoka and Nakai, 1974).  $J_{3\eta}$  is the third invariant of the  $\eta$ .

The maximum friction angle,  $\phi'_m$ , controls the size of the bounding surface on the shear plane. For sand, it is known that the yielding behaviour and a peak friction angle are a function of the current density. Thus, the model indicates that change in shape of the bounding surface is a function not only of a critical state friction angle,  $\phi'_{cs}$ , but also of the current void ratio,  $e$  expressed as:

$$\frac{1}{\tan \phi'_m} = \frac{1}{\tan(45^\circ + \phi'_{cs}/2)} + \left( \frac{1}{\tan \phi'_{mr}} - \frac{1}{\tan(45^\circ + \phi'_{cs}/2)} \right) (e)^{np} \quad (\text{A.11})$$

where  $\phi'_{mr}$  is a reference value of  $\phi'_m$  at a unit void ratio ( $e = 1$ ), and  $np$  is a material constant. Note that  $\phi'_m$  is equal to  $\phi'_{mr}$  for all densities when  $np = 0$  or  $\phi'_{mr} = 45^\circ + \phi'_{cs}/2$ .

Finally, when the stress state is on the bounding surface ( $f = 0$ ), the load direction is given by a yield function gradient  $\mathbf{Q}$  as:

$$\mathbf{Q}_p = \frac{\partial f}{\partial p'} = p' \left[ \left( m\zeta^2 + 2\eta : \mathbf{b} \right) \cdot \left( \frac{p'}{\alpha'} \right)^m - 2\eta : \eta + \left( 9 - \frac{3c_a^2}{2} \right) \left( 1 - \left( \frac{p'}{\alpha'} \right)^m \right) J_{3\eta} \right] \quad (\text{A.12})$$

$$\mathbf{Q}_s = \frac{\partial f}{\partial s} = p' \left[ 2 \left( \eta - \left( \frac{p'}{\alpha'} \right)^m \mathbf{b} \right) - \left( 3 - \frac{c_a^2}{2} \right) \left( 1 - \left( \frac{p'}{\alpha'} \right)^m \right) \frac{\partial J_{3\eta}}{\partial \eta} \right] \quad (\text{A.13})$$

### A.3 Hardening and flow rule

In the MIT-S1 model, there are two hardening laws that change the size and orientation of the bounding surface. First, a rotational hardening referred to Hashighchi (1977) is given by:

$$d\mathbf{b} = \psi \frac{1+\epsilon}{\epsilon\alpha'} \left( \frac{r_x}{m} \langle Q_p d\varepsilon_v^p \rangle + r_y |Q_s : d\varepsilon_s^p| \right) (\eta - \mathbf{b}) \quad (\text{A.14})$$

where,

$$r_x = \frac{k^2 - 2\eta : \mathbf{b} + \mathbf{b} : \mathbf{b}}{k_a^2} \quad (\text{A.15})$$

$$k^2 = k_a^2 + \left( 3 - \frac{k_a^2}{2} \right) J_{3\eta} \quad (\text{A.16})$$

$$k_a^2 = \frac{8 \sin^2 \phi'_{cs}}{3 + \sin^2 \phi'_{cs}} \quad (\text{A.17})$$

$$r_y = (d^2 - 2\eta : \mathbf{b} + \mathbf{b} : \mathbf{b}) \cdot \left( 1 + \left( \frac{\alpha'}{p'} - 1 \right) \delta_{HS}^\theta \right) \quad (\text{A.18})$$

$$d^2 = d_a^2 + \left( 3 - \frac{d_a^2}{2} \right) J_{3\eta} \quad (\text{A.19})$$

$$d_a^2 = \frac{2(1 - K_{0NC})^2}{1 + K_{0NC} + K_{0NC}^2} \quad (\text{A.20})$$

$\Psi$  is a dimensionless material constant that controls the rate of change in anisotropy. The rotational hardening of this model depends on the rate of both the plastic volumetric strain,  $d\varepsilon_v^p$ , and the plastic shear strain,  $d\varepsilon_s^p$ . Parameters  $r_x$  and  $r_y$  impose limits on the principal directions of anisotropy for consolidation along radial effective stress paths and the residual anisotropy for shearing to critical state conditions, respectively.

Second, isotropic hardening derived from the MIT-S1 compression model (**Equation A.5**) is given by:

$$\frac{d\alpha'}{\alpha'} = \frac{(1+e)}{e(\rho_c - \rho_r)(1-\delta_b^0)} \left[ d\varepsilon_v^p + \delta_b^0 \left( \frac{\mathbf{Q}_s : d\varepsilon_s^p}{p'} \right) \right] - \left( \frac{2\mathbf{b} : d\mathbf{b}}{a^2 + \mathbf{b} : \mathbf{b}} \right) \quad (\text{A.21})$$

where

$$\delta_b = 1 - \frac{\alpha'}{p'_b} \left( 1 + \frac{\mathbf{b} : \mathbf{b}}{a^2} \right) = 1 - \frac{\alpha'}{\alpha'_e} \quad 0 \leq \delta_b \leq 1 \quad (\text{A.22})$$

$$a^2 = 24 \left( \frac{\sin \phi'_{cs}}{3 - \sin \phi'_{cs}} \right)^2 \leq 1 \quad (\text{A.23})$$

$$\rho_r = D(1 - \xi^r) + \frac{1 + \omega_s \xi_s}{C_b \left( 1 + \left( \frac{K_{max}}{2G_{max}} \right) \boldsymbol{\eta} : \boldsymbol{\eta} \right)^{1/6}} \left( \frac{p'}{p_a} \right)^{2/3} \quad (\text{A.24})$$

$$\frac{2G_{max}}{K_{max}} = 3 \left( \frac{1 - 2\mu'_0}{1 + \mu'_0} \right) \quad (\text{A.25})$$

$\delta_b$  is a normalised distance of the current bounding surface to the spacing of the LCC (see **Figure A.2**) and generalised the compressibility of sands to non-hydrostatic stress condition. Parameter  $a$  is a shape constant controlling the spacing of the LCC (**Figure A.2**).  $\rho_r$  is the current (tangential) slope of the swelling curve in the compression plane. **Equation A.24** comprises two terms. The first term describes the swelling response for clays and parameters  $D$  and  $r$  control the non-linear behaviour in the compression plane. The second term describes the response for sands and parameters  $\omega_s$  and  $\xi_s$  control small strain non-linearity during undrained shearing. In the case of isotropic consolidation for sands, **Equation A.22** becomes equivalent to **Equation A.5** by neglecting the first term ( $D = 0$ ), assuming no shear strain increment ( $d\varepsilon_s^p = 0$ ) and zero stress ratio ( $\mathbf{b} = 0$ ).

The plastic strain on the bounding surface of this model is described by a non-associated flow rule. The directions of plastic flow are represented as a volumetric component,  $P_p$ , and a deviatoric component,  $\mathbf{P}_s$  as:

$$P_p = \left( k^2 - \boldsymbol{\eta} : \boldsymbol{\eta} \right) \frac{p'}{\alpha'} (1 - \delta_b)^m \quad (\boldsymbol{\eta} : \boldsymbol{\eta} \leq k^2) \quad (\text{A.26a})$$

$$P_p = \left( k^2 - \eta : \eta \right) \frac{p'}{\alpha'} \quad (\eta : \eta > k^2) \quad (\text{A.26b})$$

$$P_s = x P_p \eta + \frac{\zeta^2 |\eta|}{\alpha'} Q_s \quad (\text{A.27})$$

where

$$x = \left( \frac{\rho_c}{\rho_c - \rho_r} \right) \left\{ \frac{1 + 2K_{0NC}}{3(1 - K_{0NC})} - \frac{K}{2G} \left( \frac{\rho_r}{\rho_c} \right) \right\} \quad (\text{A.28})$$

#### A.4 Bounding surface plasticity

The MIT-S1 model has adopted the concept of bounding surface plasticity (Dafalias and Herrmann, 1982) in order to describe the behaviour of overconsolidated samples. For this model, the plastic behaviour at the current (overconsolidated) stress state is linked to that at an image point on the bounding surface (**Figure A.2**). Therefore, a hardening modulus, H, and the volumetric plastic direction, P<sub>p</sub> at the current state is controlled by those at the image point through the mapping rule:

$$P_p = P_p^I (1 - g) + P_p^0 g \quad (\text{A.29})$$

$$H = \langle H^I \rangle + H^0 \frac{g}{1 - g} \left( 1 - \frac{\eta : \eta}{c^2} \right)^{1/2} \quad (\text{A.30})$$

where

$$g = \frac{\alpha' - \alpha'_o}{\alpha' - \alpha'_{oi}} \quad 0 \leq g \leq 1 \quad (\text{A.31})$$

$$P_p^0 = -2|\eta - b| \cdot |\eta| \quad (\text{A.32})$$

$$H_0 = \left( \frac{\rho_r}{\rho_c - \rho_r} \right) \frac{h}{1 - \delta_b^\theta} K_{max}^I |\mathbf{Q}^I| \cdot |\mathbf{P}^I| \quad (\text{A.33})$$

P<sub>p</sub><sup>I</sup>, H<sup>I</sup> and K<sub>max</sub><sup>I</sup> are values of P<sub>p</sub>, H and K<sub>max</sub> at the image point. ⟨ ⟩ are Macaulay brackets. g is a mapping distance of the current stress to the image point. α'<sub>o</sub> and α'<sub>oi</sub> are

sizes of the current loading surface and the loading surface at the initial state, respectively.  $h$  is a dimensionless material constant.

In this study, fresh deposited sand under monotonic loading will mainly be considered. Therefore the current surface and the bounding surface are assumed to be identical ( $\alpha' = \alpha'_0 \rightarrow g = 0$ ). Parameter  $h$  is irrelevant for this condition.

### A.5 Critical state

At the critical state, the stress state must satisfy the yield conditions,  $f = 0$ , hence **Equation A.7** can be written as:

$$\left(\frac{p'}{\alpha'}\right)^m = \frac{c^2 - \eta : \eta}{\zeta^2} = \frac{c^2 - \eta : \eta}{c^2 + \mathbf{b} : \mathbf{b} - 2\eta : \mathbf{b}} \quad (\text{A.34})$$

No further hardening occurs at the critical state ( $\delta_b = 0$ ). The size of the bounding surface is therefore expressed from **Equation A.4** and **A.22** as:

$$\frac{\alpha'}{p'_{\text{ref}}} = \frac{a^2}{a^2 + \mathbf{b} : \mathbf{b}} (e)^{-1/\rho_c} \quad (\text{A.35})$$

Also no rotational hardening ( $d\mathbf{b} = 0$  in **Equation A.14**) requires that the parameter  $r_y$  in **Equation A.18** is zero:

$$r_y = (d^2 - 2\eta : \mathbf{b} + \mathbf{b} : \mathbf{b}) = 0 \quad (\text{A.36})$$

From **Equations A.35**, **A.36** and **A.37**, the expression of the critical state line, CSL can be derived ( $J_{3\eta} = 0$  for  $\eta : \eta = 0$ ) as:

$$\frac{p'}{p'_{\text{ref}}} = \left( \frac{a^2}{a^2 + \mathbf{b} : \mathbf{b}} \right) \left( \frac{c_a^2 - k_a^2}{c_a^2 - d_a^2} \right)^{1/m} (e)^{-1/\rho_c} \quad (\text{A.37})$$

This expression represents an analytical closed form solution for the CSL.

## A.6 Numerical implementation of MIT-S1 model

In this thesis, the MIT-S1 model is incorporated in the finite element code, ABAQUS (ABAQUS, 2003) by means of an ABAQUS user subroutine. In the subroutine, stresses and user-defined variables must be updated and a material Jacobian matrix (tangent stiffness tensor) must be provided. This section firstly presents the MIT-S1 stress-strain relationship with an additional modification for explicit state parameters, such as the void ratio. Then a derivation of the generalised continuum Jacobian is described.

The MIT-S1 model assumes that the yield/bounding function describing plastic behaviour is given by function,  $f$ , expressed as:

$$f(p', s, e, \alpha', \mathbf{b}) = 0 \quad (\text{A.38})$$

where,  $p'$ ,  $s$ ,  $e$  are the state variables defining the current stress and void ratio, and  $\alpha'$ ,  $\mathbf{b}$  are the internal variables (functions of stress history) defining the size and orientation of the bounding surface. From this, increment of the bounding surface can be expressed as:

$$df = \frac{\partial f}{\partial p'} dp' + \frac{\partial f}{\partial s} ds + \frac{\partial f}{\partial e} de + \frac{\partial f}{\partial \alpha'} d\alpha' + \frac{\partial f}{\partial \mathbf{b}} d\mathbf{b} = 0 \quad (\text{A.39})$$

The elasto-plastic hardening modulus,  $H$ , is found from:

$$\dot{H} = -\frac{\partial f}{\partial \alpha'} d\alpha' - \frac{\partial f}{\partial \mathbf{b}} d\mathbf{b} \quad (\text{A.40})$$

and the scalar controlling the magnitude of plastic strains,  $\dot{\Lambda}$  is given by:

$$\dot{\Lambda} = \frac{\left[ KQ_p + \frac{\partial f}{\partial e} (1 + e) \right] \delta \varepsilon_p + 2G \mathbf{Q}_s : \delta \mathbf{e}_s}{H + KQ_p P_p + 2G \mathbf{Q}_s : \mathbf{P}_s} \quad (\text{A.41})$$

The complete elasto-plastic equations are then given by:

$$\begin{Bmatrix} dp' \\ ds \\ de \end{Bmatrix} = \begin{Bmatrix} K(d\varepsilon_p - \dot{\Lambda}P_p) \\ 2G(d\varepsilon_s - \dot{\Lambda}P_s) \\ (1+e)d\varepsilon_p \end{Bmatrix} \quad (A.42)$$

These relations provide updates of the stresses and the void ratio. By means of the additional void ratio term, the MIT-S1 model accomplishes density independency of the input parameters.

Next, the Jacobian matrix for the MIT-S1 model with multiple yielding mechanisms is described. The Jacobian matrix is defined as the change in stress components due to an infinitesimal change in the strain components. The components of the Jacobian can be expressed in terms of its volumetric and deviatoric components:

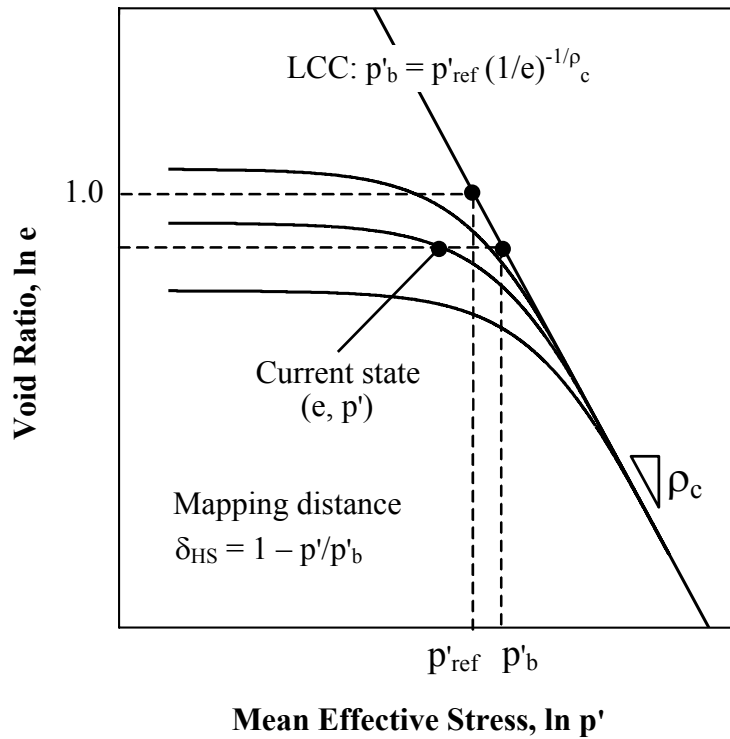
$$J = \begin{bmatrix} J_{00} & J_{0j} \\ J_{i0} & J_{ij} \end{bmatrix} = \begin{bmatrix} \frac{\partial dp'}{\partial d\varepsilon_p} & \frac{\partial dp'}{\partial d\varepsilon_s} \\ \frac{\partial ds}{\partial d\varepsilon_p} & \frac{\partial ds}{\partial d\varepsilon_s} \end{bmatrix} \quad (A.43)$$

The full expression with elastic and plastic, volumetric and deviatoric components is then:

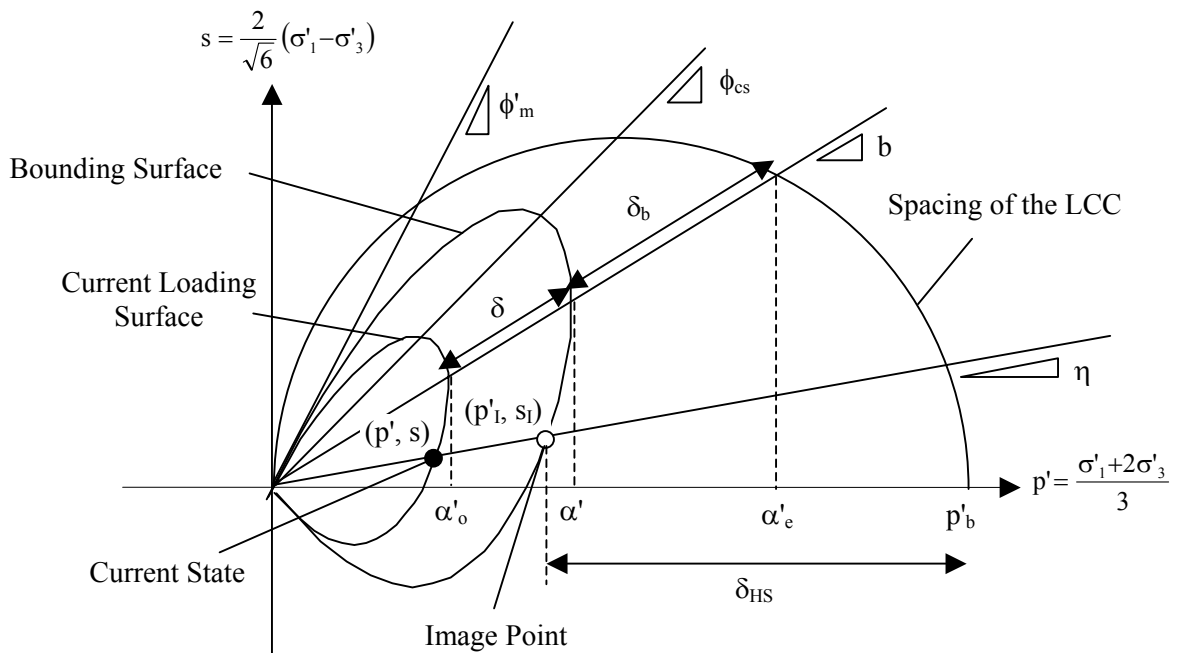
$$J = \begin{bmatrix} K & 0 \\ 0 & 2G \end{bmatrix} = \frac{1}{\Omega} \begin{bmatrix} KKQ_p P_p & 2GKQ_s P_p \\ K2GQ_p P_s & 2GQ_s : P_s \end{bmatrix} \quad (A.44)$$

where

$$\Omega = H + KQ_p P_p + 2GQ_s : P_s \quad (A.45)$$



**Figure A.I.1: MIT-S1 compression model (after Pestana and Whittle, 1995)**



**Figure A.I.2: MIT-S1 model on the shear plane**



## REFERENCES

- ABAQUS (2003). version 6.4-1, Hibbit, Karlsson and Sorensen, Inc.
- Aiban, S. A. (1994). "Verification of shape factors for shallow foundations on sands." *Centrifuge 94*, Vol. 1. Singapore. Balkema, Rotterdam: 547-552.
- Airey, D. W., Randolph, M. F. and Hyden, A. M. (1988). "The strength and stiffness of two calcareous sands." *Engineering for calcareous sediments*, Vol. 1, Perth, Australia: Balkema, Rotterdam: 43-50.
- Allman, M. A. and Poulos, H. G. (1988). "Stress-strain behaviour of an artificially cemented calcareous soil." *Engineering for Calcareous Sediments*, Vol. 1, Perth, Australia: Balkema, Rotterdam: 51-60.
- Asaoka, A., Nakano, M. and Noda, T. (2000). "Superloading yield surface concept for highly structured soil behaviour." *Soils and Foundations*, 40(2): 99-110.
- Asaoka, A., Noda, T., Yamada, E., Kaneda, K. and Nakano, M. (2002). "An elasto-plastic description of two distinct volume change mechanisms of soils." *Soils and Foundations* 42(5): 47-57.
- Been, K. and Jefferies, M. G. (1985). "A state parameter for sands." *Géotechnique*, 35(2): 99-112.
- Been, K., Jefferies, M. G. and Hachey, J. (1991). "The critical state of sands." *Géotechnique*, 41(3): 365-381.
- Baligh, M. M. (1975). "Theory of deep site static cone penetration resistance." *Research Report, R75-56*. Department of Civil Engineering, MIT, Cambridge.
- Bardet, J. P. (1986). "Bounding surface plasticity model for sands." *Journal of Engineering Mechanics, ASCE*, 112(11): 1198-1217.
- Basaran, C. (1994). "A constitutive model for sand." *Computer Methods and Advances in Geomechanics*, Vol. 1. Morgantown, West Virginia. Balkema, Rotterdam: 525-530.
- Bolton, M. D. (1986). "The strength and dilatancy of sands." *Géotechnique*, 36(1): 65-78.
- Bolton, M. D. and Lau, C. K. (1993). "Vertical bearing capacity factors for circular and strip footings on Mohr-Coulomb soil." *Canadian Geotechnical Journal*, 30: 1024-1033.
- Brinch Hansen, J. (1961). "A general formula for bearing capacity." *Danish Geotechnical Institute Bulletin*, No. 11: 38-46.
- Brinch Hansen, J. (1970) "A revised and extended formula for bearing capacity." *Danish Geotechnical Institute Bulletin*, No. 28: 5-11.

- Carter, J. P. and Balaam, N. P. (1995). *AFENA - A Finite Element Numerical Algorithm*, Center for Geotechnical Research, University of Sydney
- Cerato, A. B. (2004). *Scale Effects of Shallow Foundation Bearing Capacity on Granular Material*. PhD thesis, University of Massachusetts, USA.
- Coop, M. R. (1990). "The mechanics of uncemented carbonate sands." *Géotechnique*, 40(4): 607-626.
- Coop, M. R. and Lee, I. K. (1993). "The behaviour of granular soils at elevated stresses." *Predictive Soil Mechanics - Proc. C. P. Wroth Memorial Symposium*, Thomas Telford, London, 186-198.
- Coop, M. R. (2000). "The influence of in-situ state on the behaviour of carbonate sands." *Engineering for Calcareous Sediments*, Vol. 2, Bahrain, Balkema, Rotterdam: 379-400.
- Coop, M. R. and Airey, D. W. (2003). "Carbonate sands." *Characterisation and Engineering Properties of Natural Soils*, Vol. 2. Singapore. Balkema, Rotterdam: 1049-1086.
- Crouch, R. S., Wolf, J. P. and Dafalias, Y. F. (1994). "Unified critical-state bounding-surface plasticity model for soil." *Journal of Engineering Mechanics, ASCE* 120(11): 2251-2270.
- Cuccovillo, T. and Coop, M. R. (1997). "The measurement of local strains in triaxial tests using LVDTs." *Géotechnique*, 47(1): 167-171.
- Dafalias, Y. F. and Herrmann, L. R. (1982). "Bounding surface formulation of soil plasticity". *Soil Mechanics - Transient and Cyclic Loads*. John Wiley & Sons, New York: 253-282.
- Das, B. M. (1995). *Principles of foundation engineering*, Third edition. PWS publishing, Boston.
- De Beer, E. E. (1963). "The scale effect in transposition of the results of deep sounding tests on the ultimate bearing capacity of piles and caisson foundations." *Géotechnique*, 13(1): 39-75.
- Drescher, A. and Mroz, Z. (1997). "A refined superior sand model." *Numerical Models in Geomechanics*, Vol. 1, Montreal, Balkema, Rotterdam: 21-26.
- Dutt, R. N. and Ingram, W. B. (1988). "Bearing capacity of jack-up footings in carbonate granular sediments." *Engineering for Calcareous Sediments*, Vol. 1. Perth, Australia. Balkema, Rotterdam: 291-296.
- Erickson H. L. and Drescher, A. (2002). "Bearing capacity of circular footings." *Journal of Geotechnical and Geoenvironmental Engineering, ASCE*, 128(1): 38-43.

- Finnie, I. M. F. (1993). *Performance of Shallow Foundations in Calcareous Soil*. PhD thesis, University of Western Australia, Australia.
- Finnie, I. M. F. and Randolph, M. F. (1994a). "Bearing response of shallow foundations in uncemented calcareous soil." *Centrifuge 94*, Vol. 1. Singapore. Balkema, Rotterdam: 535-540.
- Finnie, I. M. F. and Randolph, M. F. (1994b). "Punch-through and liquefaction induced failure of shallow foundations on calcareous sediments." *BOSS '94 Behaviour of Offshore Structures*, Vol. 1, Elsevier science: 217-230.
- FLAC - Fast Lagrangian Analysis of Continua. (1993). ITASCA consulting group, Inc., Minneapolis.
- Fookes, P. G. (1988). "The geology of carbonate soils and rocks and their engineering characterisation and description." *Engineering for Calcareous Sediments*, Vol. 2. Perth, Australia. Balkema, Rotterdam: 787-806.
- Fukushima, S. and Tatsuoka, F. (1984). "Strength and deformation characteristics of saturated sand at extremely low pressures." *Soils and Foundations*, 24(4): 30-48.
- Frydman, S. and Burd, H. J. (1997). "Numerical studies of bearing capacity factor,  $N_y$ ." *Journal of Geotechnical and Geoenvironmental Engineering, ASCE*, 123(1): 20-29.
- Gajo, A. and Muir Wood, D. (1999). "Severn-Trent sand: a kinematic-hardening constitutive model: the  $q-p$  formulation." *Géotechnique*, 49(5): 595-614.
- Golightly, C. R. and Hyde, A. F. L. (1988). "Some fundamental properties of carbonate sands." *Engineering for Calcareous Sediments*, Vol. 1. Perth, Australia. Balkema, Rotterdam: 69-78.
- Goto, S., Tatsuoka, F., Shibuya, S., Kim, Y. S. and Sato, T. (1991). "A simple gauge for local small strains measurements in the laboratory." *Soils and Foundations*, 31(1): 169-180.
- Griffiths, D. V. (1982). "Computation of bearing capacity factors using finite elements." *Géotechnique*, 32(3): 195-202.
- Gudehus, G. (1981). *Bodenmechanik*, Stuttgart: Enke
- Gutierrez, M. (2003). "Modeling of the steady-state response of granular soils." *Soils and Foundations*, 43(5): 93-105.
- Hashiguchi, K. (1977). "An expression of anisotropy in a plastic constitutive equation of soils." *9th International Conference of Soil Mechanics and Foundation Engineering*, Vol. 3. Tokyo. Balkema, Rotterdam: 302-305.
- Hashiguchi, K. (1989) "Subloading surface model in unconventional plasticity." *International Journal of Solids and Structures* 25(8): 917-945.

## References

---

- Hettler, A. and Gudehus, G. (1988). "Influence of the foundation width on the bearing capacity factor." *Soils and Foundations*, 28(4): 81-92.
- Houlsby, G. T., Evans, K. M. and Sweeney, M. A. (1988). "End bearing capacity of model piles in layered carbonate soils." *Engineering for calcareous sediments*, Vol. 1, Perth, Australia: Balkema, Rotterdam: 209-214.
- Hsieh, Y. M., Whittle, A. J. and Yu, H. S. (2002). "Interpretation of pressuremeter tests in sand using advanced soil model." *Journal of geotechnical and geoenvironmental engineering, ASCE*, 128(3): 274-278.
- Huang, J. T. (1994). *The Effects of Density and Cementation on Cemented Sands*. PhD thesis, University of Sydney, Australia.
- Ishihara, K. (1993). "Liquefaction and flow failure during earthquakes." *Géotechnique*, 43(3): 351-415.
- Ishihara, K., Tatsuoka, F. and Yasuda, S. (1975). "Undrained deformation and liquefaction of sand under cyclic stresses." *Soils and Foundations*, 15(1): 29-44.
- Islam, M. K. (1999). *Constitutive Models for Carbonate Sand and Their Application to Footing Problems*. PhD thesis, University of Sydney, Australia.
- Ismail, M. A. (2000). *Strength and Deformation Behaviour of Calcite-cemented Calcareous Soils*. PhD thesis, University of Western Australia, Australia.
- Jamiolkowski, H., Lancellotta, R. H. and Lo Presti, D. C. F. (1994). "Remarks on the stiffness at small strains of six Italian clays." *Pre-failure Deformation of Geomaterials*, Vol. 2. Hokkaido, Japan. Balkema, Rotterdam: 817-836.
- Jardine, R. J., Symes, M. J. and Burland, J. B. (1984). "The measurement of soils stiffness in the triaxial apparatus." *Géotechnique*, 34(3): 323-340.
- Jefferies, M. G. (1993). "Nor-Sand: a simple critical state model for sand." *Géotechnique*, 43(1): 91-103.
- Jefferies, M. G. and Been, K. (1987). "Use of critical state representations of sand in the method of stress characteristics." *Canadian Geotechnical Journal*, 24(3): 441-446.
- Joer, H. A. Bolton, M. D. and Randolph, M. F. (2000). "Compression and crushing behaviour of calcareous soils." *International Workshop on Soil Crushability IWSC 99*. Yamaguchi, Japan: 10.1-10.16.
- Jovicic, V. and Coop, M. R. (1997). "Stiffness of coarse-grained soils at small strains." *Géotechnique* 47(3): 545-561.
- Kimura, T., Kusakabe, O. and Saitoh, K. (1985). "Geotechnical model tests of bearing capacity problems in a centrifuge." *Géotechnique*, 35(1): 33-45.

- Klotz, E.U. and Coop, M.R. (2001). "An investigation of the effect of soil state on the capacity of driven piles in sands." *Géotechnique*, 51(9): 733-751.
- Kusakabe, O. (1995). "Foundations". *Geotechnical centrifuge technology*. Chapter 6. Blackie Academic, London: 119-167.
- Kusakabe, O., Yamaguchi, H. and Morikage, A. (1991). "Experiment and analysis on the scale effect of  $N_y$  for circular and rectangular footings." *Centrifuge 91*, Vol. 1. Boulder, Colorado. Balkema, Rotterdam: 179-186.
- Lade, P. V. (1977). "Elasto-plastic stress-strain theory for cohesionless soil with curved yield surfaces." *International Journal of Solids and Structures*, 13: 1019-1035
- Lee, K. L. and Seed, H. B. (1967). "Drained strength characteristics of sands." *Journal of the Soils Mechanics and Foundations Division, ASCE*, 93(SM6): 117-141.
- Le Tirant, P., Fay, J. B., Nauroy, J. F., Meimon, Y. and Lassoudiere, F. (1988). "Centrifuge simulation of the behaviour of a shallow foundation for offshore structure on calcareous sand." *Centrifuge 88*, Vol. 1. Paris. Balkema, Rotterdam: 345-349.
- Manzari, M. T. and Daralias, Y. F. (1997). "A critical state two-surface plasticity model for sands." *Géotechnique*, 47(2): 255-272.
- Mao, X. (2000). *The Behaviour of Three Calcareous Soils in Monotonic and Cyclic Loading*. PhD thesis, University of Western Australia. Australia.
- Martin, C. M. (2003). "New software for rigorous bearing capacity calculations." *International Conference on Foundations*, Dundee: 581-592.
- Matsuoka, H. and Nakai, T. (1974). "Stress-deformation and strength characteristics under three different principal stresses." *Proceedings of Japanese Society of Civil Engineers*, 232: 59-70.
- Mayerhof, G. G. (1953). "The bearing capacity of foundations under eccentric and inclined loads." *3rd International Conference of Soil Mechanics and Foundation Engineering*, Vol. 1. Zurich. Balkema, Rotterdam: 440-445.
- Milliman, J. D. (1974). "Marine carbonate." *Recent Sedimentary Carbonates*, Part 1. Springer-Verlog, New York: 21-29.
- Miura, N., Murata, H. and Yasufuku, N. (1984). "Stress-strain characteristics of sand in a particle-crushing region." *Soils and Foundations*, 24(1): 77-89.
- Miura, N. and Yamanouchi, T. (1975). "Effect of water on the behavior of a quartz-rich sand under high stresses." *Soils and Foundations*, 15(4): 23-34.
- Molenkamp, F. (1981). "Elasto-plastic double hardening model MONOT" *LGM Report CO-218595*, Delft Geotechnics.

- Murff, J. D., Prins, M. D., Dean, E. T. R., James, R. G. and Schofield, A. N. (1992). "Jackup rig foundation modelling." *Proc. 24<sup>th</sup> Annual Offshore Technology Conference*, OTC 6807. Houston: 35-46.
- Nauroy, J. F. and Golightly, C. (1991). "Bearing capacity of a shallow foundation on calcareous sand." *Centrifuge 91*, Vol. 1. Boulder, Colorado. Balkema, Rotterdam: 187-192.
- Nova, K. and Wood, D. M. (1979). "A constitutive model for sand in triaxial compression." *International Journal for Numerical and Analytical Methods in Geomechanics*, 3(3): 255-278.
- Okamura, M., Takemura, J. and Kimura, T. (1997). "Centrifuge model tests on bearing capacity and deformation of sand layer overlying clay." *Soils and Foundations*, 37(1): 73-88.
- Ovesen, N. K. (1975). "Centrifugal testing applied to bearing capacity problems of footings on sand." *Géotechnique*, 25(2): 394-401.
- Pestana, J. M. (1994). *A Unified Constitutive Model for Clays and Sands*. ScD thesis, Massachusetts Institute of Technology, USA.
- Pestana, J. M. and Whittle, A. J. (1995). "Compression model for cohesionless soils." *Géotechnique*, 45(4): 611-631.
- Pestana, J. M. and Whittle, A. J. (1999). "Formation of a unified constitutive model for clays and sands." *International Journal for Numerical and Analytical Methods in Geomechanics*, 23(12): 1215-1243.
- Pestana, J. M., Whittle, A. J. and Salvati, L. A. (2002a). "Evaluation of a constitutive model for clays and sands: Part 1 - Sand behaviour." *International Journal for Numerical and Analytical Methods in Geomechanics*, 26(11): 1097-1121.
- Pestana, J. M., Whittle, A. J. and Gen, A. (2002b). "Evaluation of a constitutive model for clays and sands: Part 1 - Clay behaviour." *International Journal for Numerical and Analytical Methods in Geomechanics*, 26(11): 1123-1146.
- Potts, D. M. and Zdravkovic, L. (2001). *Finite Element Analysis in Geotechnical Engineering: Application*. Thomas Telford Ltd., London.
- Poulos, H. G. and Chua, E. W. (1985). "Bearing capacity of foundations on calcareous sand." *11th International Conference of Soil Mechanics and Foundation Engineering*, Vol. 3. San Francisco. Balkema, Rotterdam: 1619-1622.
- Pu, J. L. and Ko, H. Y. (1988). "Experimental determination of bearing capacity in sand by centrifuge footing tests." *Centrifuge 88*, Vol. 1. Paris, France. Balkema, Rotterdam: 293-299.
- Randolph, M. F. and Erbrich, C. (2000). "Design of shallow foundations for calcareous sediments." *Engineering for Calcareous Sediments*, Vol. 2. Bahrain. Balkema, Rotterdam: 361-378.

- Randolph, M. F., Jamiolkowski, M. B. and Zdravkovic, L. (2004). "Load carrying capacity of foundations." *Advances in Geotechnical Engineering: The Skempton Conference*, Vol.1. Thomas Telford Ltd., London: 207-240.
- Roberts, J. E. and DeSouza, J. M. (1958). "The compressibility of sands." *Proceedings ASTM*, Vol. 58: 1269-1277.
- Schofield, A. N. and Wroth, C. P. (1968). *Critical State Soil Mechanics*. McGraw-Hill Co., London.
- Semple, R. M. (1988). "The mechanical properties of carbonate soils." *Engineering for Calcareous Sediments*, Vol. 2. Perth, Australia. Balkema, Rotterdam: 807-835.
- Sharma, S. S. A. (2004). *Characterisation of Cyclic Behaviour of Calcite Cemented Calcareous Soils*. PhD thesis, University of Western Australia, Australia.
- Sharma, S. S. A., Yamamoto, N. and Fahey, M. (2005). "A numerical study on shear strength-state parameter relationship for sands." *Canadian Geotechnical Journal* (up coming).
- Shibuya, S. and Tanaka, H. (1996). "Estimation of elastic shear modulus in Holocene soil deposits." *Soils and Foundations*, 36(4): 45-55.
- Shibuya, S., Hwang, S. C. and Mitachi, T. (1997). "Elastic shear modulus of soft clays from shear wave velocity measurement." *Géotechnique*, 47(3): 593-601.
- Sloan, S. W. and Randolph, M. F. (1982). "Numerical prediction of collapse loads using finite element methods." *International Journal for Numerical and Analytical Method in Geomechanics*, 6(1): 47-76.
- Smith, I. M., Hicks, M. A., Kay, S. and Cuckson, J. (1988). "Stress-strain behaviour of an artificially Undrained and partially drained behaviour of end bearing piles and bells founded in untreated calcarenite." *Engineering for Calcareous Sediments*, Vol. 2. Perth, Australia. Balkema, Rotterdam: 663-679.
- Sweet, J. (1988). "Estimation of the drained end bearing capacity of calcareous material." *Engineering for Calcareous Sediments*, Vol. 2. Perth, Australia. Balkema, Rotterdam: 655-661.
- Taylor, R. N. (1995). "Centrifuges in modelling: principles and scale effects". *Geotechnical Centrifuge Technology*. Chapter 2. Blackie Academic, London: 19-33.
- Terzaghi, K. (1943). *Theoretical Soil Mechanics*, John Wiley and Sons.
- Ueno, K., Mito, K., Nakatomi, T. and Kusakabe, O. (1994). "Influence of initial conditions on bearing characteristics of sand." *Centrifuge 94*, Vol. 1. Singapore. Balkema, Rotterdam: 541-546.

## References

---

- Ueno, K., Miura, K. and Maeda, Y. (1998). "Prediction of ultimate bearing capacity of surface footings with regard to size effect." *Soils and Foundations*, 38(3): 165-178.
- Verdugo, R. and Ishihara, K. (1996). "The steady state of sandy soils." *Soils and Foundations*, 36(2): 81-91.
- Vesic, A. S. (1963). *Bearing Capacity of Deep Foundations in Sand*. Highway research board (annual meeting).
- Vesic, A. S. (1975). "Bearing capacity of shallow foundations". *Foundation engineering handbook*. Chapter 3. New York, Van Nostrand Reinhold: 121-147.
- Vesic, A. S. and Clough, G.W. (1968). "Behaviour of granular materials under high stresses." *Journal of the Soils Mechanics and Foundations Division, ASCE*, 94(SM3): 661-688.
- Watt, B. J. (1978). "Basic structural systems - a review their design and analysis requirements". *Numerical Methods in Offshore Engineering*. John Wiley & Sons, New York: 1-42.
- Woodside Offshore Petroleum Pty. Ltd. (1988). "Laboratory test data Goodwyn final site investigation." Woodside document No. A1820RC004.
- Yamaguchi, H., Kimura, T. and Fujii, N. (1976). "On the influence of progressive failure on the bearing capacity of shallow foundations in dense sand." *Soils and Foundations*, 16(4): 11-22.
- Yu, H. S. (1998). "CASM: A unified state parameter model for clay and sand." *International Journal for Numerical and Analytical Methods in Geomechanics*, 22(8): 621-653.
- Zadroga, B. (1994). "Bearing capacity of shallow foundations on noncohesive soils." *Journal of Geotechnical Engineering, ASCE*, 120(11): 1991-2008.
- Zhu, F., Clark, J. I. and Phillips, R. (1998). "Bearing capacity of ring foundations under vertical load." *Centrifuge 98*, Vol. 1. Tokyo. Balkema, Rotterdam: 441-446.